Theoretische Physik

Modeling of Deposition Patterns for Complex Liquids

Inaugural-Dissertation
zur Erlangung des Doktorgrades (Dr. rer. nat.)
der Naturwissenschaften im Fachbereich Physik
der Mathematisch-Naturwissenschaftlichen Fakultät
der Westfälischen Wilhelms-Universität Münster

vorgelegt von
Phong-Minh Timmy Ly
aus Münster
2022

Dekan:	Prof. Dr. Michael Rohlfing
Erste Gutachterin:	PD Dr. Svetlana V. Gurevich
Zweiter Gutachter:	Prof. Dr. Uwe Thiele
Tag der mündlichen Prüfung:	_____
Tag der Promotion:	_____

Kurzzusammenfassung

Die Beschichtung und Herstellung dünner Systeme ist essenziell für Anwendungen wie Schutz-schichten oder Halbleiterherstellung. Zwei Modelle für die Beschreibung des dip-coating Ver-fahrens und des Langmuir-Blodgett Transfers (LB transfer) werden hergeleitet und analysiert. In beiden Verfahren wird ein festes Substsrat aus einem Flüssigkeitsbad entzogen und dadurch beschichtet. Bei ersterem beschränken wir uns auf zweikomponentige Mischungen mit flüchtigem Lösungsmittel und nichtflüchtigem gelöstem Material, bei letzterem auf eine flüchtige Flüssigkeit, die mit einer monomolekularen Schicht aus Surfactants bedeckt ist.

Das dip-coating Modell besteht aus symmetrischen Dünnfilmgleichungen für binäre Mischungen, die mit einer Phasenfeld Gleichung gekoppelt sind, um explizit die Ausfällung von gelöstem Ma-terial zu modellieren [XTQ15, XM08, XM11]. Der hydrodynamische Teil beinhaltet Oberflächen-spannungs-, Gravitations, Viskositäts-, Benetzungs-, Verdunstungs- und Mischungseffekte. Das Modell ist für alle Konzentrationen gültig. Dadurch kann Material ausfällen, wenn die Mis-chung übersättigt wird. Ausfällung wird als ein Phasenübergang erster Ordnung modelliert, d.h., eine Nukleationsbarriere muss überwunden werden. Feinheiten der Modellierung, wie z.B. die Wahl der Parameter, Relevanz und Auswirkungen bestimmter Terme und auch die numerischen Verfahren, werden diskutiert. Wir analysieren das vorgeschlagene Modell, indem Schrittweise Mechanismen wie Advektion des Substrats oder Ausfällung eingeschaltet werden und direkte numerische Simulationen durchgeführt werden. Für ruhende horizontale Substrate lassen sich stabile Tropfenlösungen finden, die bei einkomponentigen flüchtigen Flüssigkeiten instabil sind. Simulationen der dip-coating Geometrie mit eindimensionalen (1D) Substraten zeigen homogene und zeitperiodische Kammablagerungen. Letztere erscheinen in einer Vielfalt von Morphologien. Auf einem zweidimensionalen ruhenden Substrat zeigen wir die Ablagerung von Fingern, die spiralförmig Richtung Zentrum des verdunstenden Tropfens wachsen.

Für den LB transfer verwenden wir ein bereits bekanntes, generalisiertes Cahn-Hilliard Modell. Dieses wurde aus einem zweikomponentigen Langwellen-genäherten hydrodynamischen Modell hergeleitet [KGFT12]. Die Ablagerung von Streifen parallel zur Kontaktlinie, bestehend aus sich abwechselnden Surfactantphasen, auch horizontale Streifen genannt, ist über ein breites Geschwindigkeitsintervall des Substrats möglich. Diese Streifen können transversal instabil wer-den und zu Fingern bzw. vertikalen Streifen übergehen. Numerische Pfad Kontinuierung wird für 2D Domänen durchgeführt. Daraus resultiert ein langer Ast bestehend aus 2D Zuständen. Dieser Zweig setzt sich aus einer dichten Ansammlung von Unterästen zusammen. Die meisten 2D Zustände haben eine gebrochene y-Symmetrie (y ist die laterale Richtung) und sind instabil. Unter den stabilen 2D Zuständen mit gebrochener y-Symmetrie befinden sich auch die obenge-nannten Fingerzustände. Einer der Finger-Unteräste überlappt mit dem zeitperiodischen Ast horizontaler Streifen, d.h. sie bilden eine multistabile Region und es besteht ein Zusammenhang zur transveralen Instabilität.

Außerdem wird die Advektionsgeschwindigkeit des Substrats um eine Durchschnittsgeschwindigkeit

periodisch moduliert. Dies führt zur Synchronisation der 2D Zustände mit der Modulationsfrequenz. Die Synchronisation erfolgt lediglich parallel zur Ziehrichtung und wird für horizontale Streifen, schiefe Streifen und Gittermuster beobachtet.

Obwohl die Modelle auf die Beschichtungsverfahren angewendet werden, ist die involvierte Physik relevant für ähnliche musterbildende Systeme und komplexe Flüssigkeiten.

Abstract

Coating of surfaces and fabrication of thin geometries are essential in protective coating, semiconductor fabrication and other applications. We derive and analyze two models for the description of the dip-coating technique and the Langmuir-Blodgett transfer (LB transfer). Both techniques involve pulling a solid substrate out of a liquid bath. We consider binary liquids, in the former case with a volatile solvent and non-volatile solute, in the latter case a volatile liquid covered by a monolayer of surface active molecules (surfactants).

The dip-coating model involves coupling symmetric thin film equations for binary mixtures with a phase-field equation in order to explicitly model the deposition of solute material [XTQ15, XM08, XM11]. The hydrodynamic part includes surface tension, gravity, viscous drag, wetting, evaporation and mixing effects. The model is valid for the full concentration range. This allows the deposition of solute as the liquid becomes oversaturated. Deposition is modeled as a first order phase transition, i.e., a nucleation barrier must be overcome precipitation to occur. Intricacies of the modeling process are discussed, such as parameter choices, relevance and effects of specific terms, and also the numerical scheme. We analyze the proposed model by subsequently turning on mechanisms such as substrate advection or deposition and performing direct numerical simulations. On resting horizontal substrates in the absence of deposition stable droplets are found, which are unstable for one-component volatile liquids. Simulations of the dip-coating geometry on one-dimensional (1D) substrates reveal homogeneous and time-periodic ridge deposits, the latter with a variety of morphologies. On a resting 2D substrate we show the deposition of fingers spiraling towards the center of an evaporating droplet.

The model for the LB transfer is a known generalized Cahn-Hilliard equation derived from two-component lubrication approximated hydrodynamic equations [KGFT12]. The deposition of stripes parallel to the contact line of two alternating surfactant phases, i.e., horizontal stripes, is possible in a wide range of substrate velocities. These stripes can become transversally unstable, transitioning to fingers, also called vertical stripes. Numerical path continuation is performed for 2D domains, revealing a dense cluster of subbranches of mostly unstable states with broken $y-$translation symmetry (y corresponds to the lateral direction). Among the stable 2D states are said finger states. One such subbranch forms a multistable region along with the branch of TPS, indicating a relation to the transversal instability.

In addition, time-periodic forcing is applied to the system by modulating the substrate velocity. Synchronization of the 2D states along the pulling direction is observed for horizontal stripe, oblique stripe and lattice patterns.

Although the models are applied to the mentioned coating techniques, the physics is still relevant for similar pattern forming systems and complex liquids.

Contents

1. Introduction

Modification of a material's surface can change its properties or add new functionality. One way of realizing this is introducing a new material onto the surface. In cases such as thermal barrier [WE99, WHK07, TPMM21], UV resistance/reflective [ZGL07, MHJN+14] or anti-reflection coating [SJJ08, ZYBH+09, SES20], the added material has a protective, but arguably secondary function when the overall product is concerned, whereas in semiconductor fabrication the added material is vital for the functionality of the product. Examples are thin-film solar cells, which convert solar energy into electric or chemical energy [Grä01, Kre09, AP10], organic light-emitting diodes (OLED) displays [TV87, MDBS+19, SFSS19], and field-effect transistors, i.e., building blocks of integrated circuits, to name just a few. Especially organic field-effect transistors (OFET) were a subject of intensive research in the last two decades [Hor98, Muc06, LGSO+10, LGWM+13, LAPM14, LAMB+16, DSZZ19, WWHL+20, JLFH21], see also the extensive review of recent advances in organic semiconductor coating [RARF+20]. In particular, OLED devices can be fabricated via inkjet printing. There, even the piezo-electric printhead itself is the result of a deposition process (micro-electro-mechanical systems, MEMS) [KKLS+12]. Organic layers can also serve as cell membrane models [NPCB+15]. A similarity among these applications is the coating or deposit being *thin*. This is meant in terms of absolute thickness, i.e., microns to nanometers, or relative, i.e., its thickness is smaller than its lateral extent by multiple orders of magnitude [WLLZ+16]. The practical reason for thinness is of course cost, whereas physical reasons vary depending on the application. For example, in optoelectronics the coherence length of light sources requires corresponding thin semiconductor material.

A variety of techniques for creating thin layers exist. In particular, in physical vapor deposition (PVD) the source material is targeted/sputtered with energetic particles (or heated), thereby ejecting(or evaporating) material to be deposited on a separate substrate [CS88, HLBE+06]. In spin-coating, the material is first deposited at the center of the substrate. Coating then occurs by spinning the substrate [Scr88, NGL05]. Whereas, in slot-die coating material is supplied through a precise slot-die onto a moving substrate [DLH16, RSWD+18, KHNK+22].

Often, homogeneous coatings are further processed by patterning. This is for example the case for commercial semiconductor manufacturing. By employing preset masks, patterns are etched into surfaces in lithographic methods [SS07, TLT16, KB20]. Such techniques belong to the so-called *top-down* category. They are precise and highly controllable, however, the procedure is serial, and thus scaling of the apparatus is expensive and time consuming. Alternatives are *bottom-up* methods where the material forms the patterns by following non-equilibrium thermodynamics, without presetting the pattern. This *self-organization* provides advantages in cost and scalability of manufacturing. However, controlling the pattern formation is not as direct as in lithography. Therefore, understanding the underlying, nonlinear physical principles is essential.

In order to support and build on experimental findings, theoretical models are indispensable. They are used for prediction, verification of experimental data and for the systematic under-
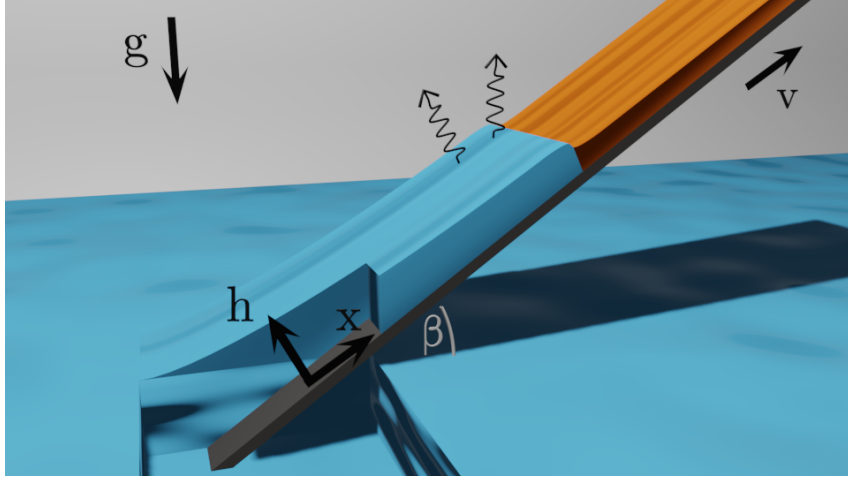
Figure 1.1.: Sketch of a dip-coating setup. A solid substrate is extracted from the liquid bath at an inclination β with velocity v in the x-direction. Gravity acts downwards. The film height h is defined normal to the substrate. Solute is deposited as solvent evaporates.

standing of underlying physical mechanisms. In this thesis we discuss theoretical models for two techniques of thin layer deposition: On the one hand for dip-coating of a binary mixture and on the other for the Langmuir-Blodgett transfer. Both procedures concern deposition of a complex liquid by pulling a solid flat substrate out of a bath. We describe both techniques in the following.

Figure 1.1 shows a sketch of a dip-coating geometry. In dip-coating the liquid is usually a mixture with a volatile solvent. The substrate is immersed in the bath and then extracted. Thus, the liquid coats the substrate while the solvent evaporates. The solute, or nanoparticles in case of a suspension, remain on the substrate. The deposited pattern highly depends on the dynamics of the liquid, especially that of the three-phase contact line, where substrate, liquid and vapor meet. In general the dynamics is governed by factors such as viscous drag due to advection of the substrate, evaporation, wetting of the substrate and capillarity (surface tension). In contrast to one component liquids, the physics of complex liquids is not as well understood. The additional components require consideration of the component interactions. When a volatile component evaporates, the dynamics of the precipitate, i.e., the solid solute, is halted, signifying the importance of non-equilibrium thermodynamics.

A variety of geometries involve deposition from a complex fluid at a three-phase contact line. The morphology of inhomogeneous deposits is diverse, ranging from stripes parallel and perpendicular (also called fingers) to the contact line to labyrinthine, cellular, dendritic, cracked structures und crusts, see [Sta11, Lar14, Thi14, AEZT+18, VSSP+20, LRH22]. A more recent review by Zang et al. is focused on deposition patterns from a volatile sessile droplet [ZTTD+19]. Aside from the dependence of the morphology on solute concentration, droplet volume, vapor pressure, temperature, etc., research is further concerned with other parameters, such as substrate roughness, particle size (in the case of nanoparticle suspensions) [MBN19] and shape [PB19]. Furthermore, externally controlled influences like applying an electric field or substrate vibrations are also investigated in detail [ME18]. The previously mentioned patterns emerge from instabilities such as spinodal/evaporative dewetting, fingering due to Marangoni convection, but also from so-called *stick-slip* motion of the contact line, where the contact line periodically pins/depins at
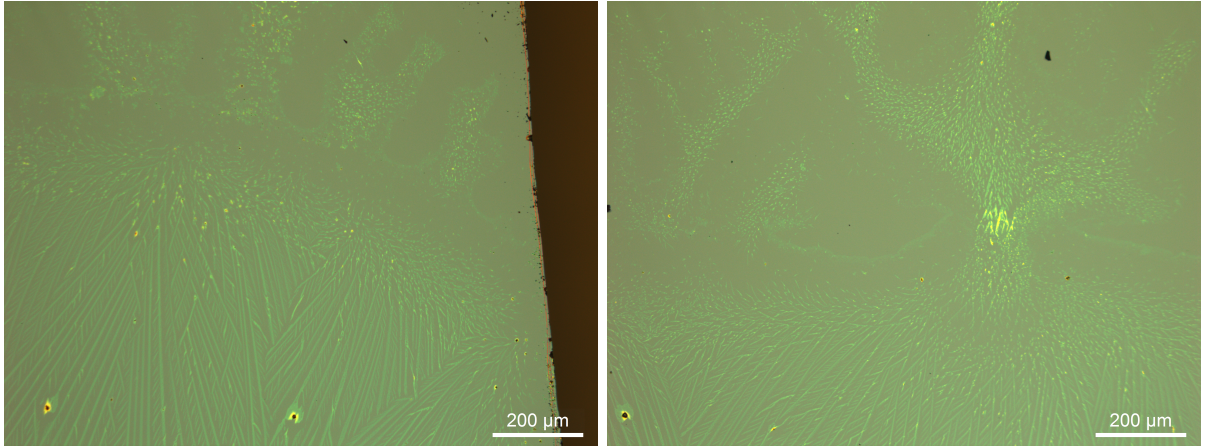
Figure 1.2.: AFM images of DTBDT deposits on Si/SiO2 substrate at transfer velocity $2000 \mu m/s$, provided by Wang et al[WZHT+15]. The DTBDT concentration in the bath is $2 \frac{mg}{ml}$. Evaporation occurs under ambient conditions. The evaporative dewetting in the form of $\sim 100 \mu$m-sized fingers is clearly visible as well as micron sized dendrite formation. The substrate is pulled from bottom to top.

solute particle accumulations[DBDH+97, Dee00].

Upon solvent evaporation the accumulated solute can exhibit a variety of morphologies on a scale smaller than what is directed by hydrodynamics, i.e., the interface and transition between the liquid and solid phase of the solute is of importance as well. In particular, Wang et al. perform dip-coating experiments with the organic semiconductor material DTBDT [LGSO+10, LGWM+13, WZHT+15]. Figure 1.2 shows two atomic force microscopy (AFM) images of irregularly structured deposits after the solvent has evaporated. On a scale of $\sim 100 \mu$m deposit fills out fingers stemming from a dewetting instability. From bottom to top, on a smaller length scale of microns, dendrites with a preferred direction along the pulling direction form. The preferred direction changes to perpendicular to the pulling direction before the onset of the larger scale fingers. Within the fingers, the dendrite branches become much shorter and follow the finger's growth direction. In contrast to striped deposits [GFS07] or flat ones left after a Landau-Levich film evaporates [LL42], dendrites are too fractal to be useful in applications, especially when the branches are as short as in the upper parts of Fig. 1.2. Therefore, increasing the regularity or suppressing the formation of dendrites is sought after. Dendrite formation is a common phenomenon in the formation of microstructures, which is researched in crystal growth and solidification physics [SG70, CCDT+86, HAQ99, UB05, FFDR13]. We give more references of the theoretical literature on complex liquids and dendrite formation in the beginning of Chapter 4.

In order to model the above multiscale phenomenon we propose a model that considers both hydrodynamics and the liquid-solid phase transition of solute during deposition. To this mean we take a symmetric thin-film model for a binary mixture derived by Xu, Thiele and Qian [XTQ15] and couple it to a phase-field equation for precipitation introduced by Xu and Meakin [XM08, XM11]. The theory and model derivation is presented in Chap. 2, while calculations are performed in Chap. 4.

Another technique for the layer deposition is the Langmuir-Blodgett transfer (LB transfer), which is very similar to dip-coating with the key difference being that the deposit is not a material dissolved or suspended in the liquid of the bath but a monolayer of surface active
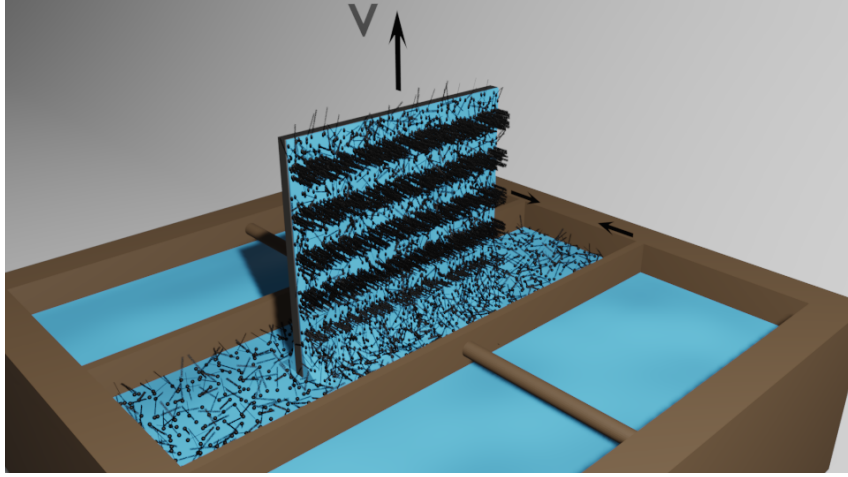
Figure 1.3.: Sketch of the Langmuir-Blodgett transfer. The liquid bath is covered by a monolayer of surfactants. Barriers along the bath surface control the surface pressure. A substrate is vertically extracted from bottom to top, thereby depositing material.

molecules (surfactants) that cover the surface of the bath [Blo35]. Therefore, the deposition of layers of molecular thickness tends to be simpler via the LB transfer than via dip-coating. However, the technique is naturally limited by materials that possess the properties of surfactants, i.e., amphiphilic molecules. Such molecules require a hydrophilic head and a hydrophobic tail. Figure 1.3 shows a sketch of the LB setup. The surface pressure of the monolayer on the bath is controlled by the depicted barriers. Depending on the pressure the monolayer takes on different phases [SR91, RS92, RS92, SR94, GR98]. Here, the molecules on the bath are in the liquid-expanded (LE) phase. The molecules are spread out with the tails pointing away at various angles. The liquid-condensed (LC) phase is the one in which the molecules are densely distributed with their tails pointing perpendicularly away from the substrate. In Fig. 1.3 an example of the deposition of horizontal stripes, i.e., alternating stripes of LE and LC phase parallel to the contact line, is presented [GCF00]. This transition is a result of substrate-monolayer interactions, so-called substrate-mediated condensation (SMC) [SR91]. Both a hydrodynamic thin-film model and one in which the surfactant dynamics is isolated have been formulated in the past [KGF09, KGFC10, Köp11, KGFT12]. We continue investigating the latter one in this thesis with emphasis on patterns on two-dimensional (2D) substrates. The theory and model derivation is presented in Chap. 2, while calculations are performed in Chap. 5.

1.1. Thesis Outline

This thesis is structured as follows. In Chap. 2 we derive the hydrodynamic models for both the dip-coating of a binary mixture as well as the Langmuir-Blodgett transfer in a lubrication approximation of the Navier-Stokes equations. The former model takes into account capillarity, evaporation, wetting and viscous drag. By coupling these equations to a phase-field equation, deposition, i.e., the liquid-solute phase transition, is modeled. In regards to the LB model we go further by reducing the system to a generalized Cahn-Hilliard equation, solely describing the surfactant dynamics close to the phase transition. Chapter 3 describes the numerical techniques

of finite difference method (FDM), finite element method (FEM), Runge-Kutta time integration and numerical path continuation employed in Chapters 4 and 5. In Chap. 4 we evaluate the numerical accuracy and stability of the finite difference methods utilized for direct numerical simulations (DNS). Then, DNS are conducted for the binary mixture model with deposition mechanism by subsequently switching on effects such as evaporation or deposition. The analysis is mostly performed for 1D substrates. The model for the LB transfer is analyzed via numerical path continuation in Chap. 5 and also extended by modulating the velocity of the substrate periodically in time. The calculations are mostly conducted for 2D substrates. Finally, we conclude with a summary and outlook for future directions in Chap. 6.

2. Model Derivation

When interest lies in phenomena occurring on larger than molecular length scales, it can be useful to take a continuum approach. A liquid can be modeled as a continuum. By assuming local equilibrium in neither too large nor small averaging volumes, thermodynamic properties can be locally defined, i.e., the system possesses continuous thermodynamic properties. For the description of nonlinear phenomena, especially pattern formation, theoretical models usually consist of partial differential equations. A paradigm model for fluids are the well-known Navier-Stokes Equations. By extending the Navier-Stokes-Korteweg equations through coupling with a Cahn-Hilliard equation, hydrodynamic flow and phase separation of a binary mixture can be described, also known as *Model H* [HH77]. For large separations between vertical and horizontal length scales the long-wave (lubrication) approximation can be applied to the system to derive a coupled thin-film and Cahn-Hilliard equation[NT10]. By comparison with existing long-wave models Thiele and coworkers formulate thin-film models in gradient dynamics form both for binary mixtures and two layer systems[TAP12, TTL13]. However, the adopted mobilities are only valid in the dilute limit since no interaction between the two components is considered. Xu et al. derive a symmetric gradient dynamics model using Onsager's variational principle and long-wave approximation [XTQ15]. This ensures thermodynamic consistency and leads to diffusive fluxes beyond the dilute limit. We will revisit the NSE and this model after this introductory part of the chapter. The mesoscopic view necessitates the treatment of interfaces which for one can be sharp or for the other diffuse, depending on the modeling approach. In this thesis we are concerned about liquids in contact with a substrate and a gaseous phase. We will see in this chapter that both the liquid-vapor and the substrate-liquid interfaces are treated sharply by imposing corresponding boundary conditions in the long-wave approximation.

Another type of complex fluid is a surfactant-covered liquid as mentioned in the previous Chapter 1. The surfactants undergo a phase transition as well upon Langmuir-Blodgett transfer onto a substrate. It has been shown that the core dynamics can be described by a reduced model corresponding to a generalized Cahn-Hilliard equation, a classic model for phase separation [KGFT12]. Naturally, surfactant-covered liquids can be modeled by thin-film type equations as well. We shall discuss these in this chapter as well.

In dip-coating, solid material remains on the substrate as the liquid becomes oversaturated due to solvent evaporation. This phase transition is called precipitation. While such a solid-liquid interface can also be modeled by a sharp interface, tracking such an interface is computationally cumbersome. Instead, it can be modeled as a *diffuse* interface with finite width. The phase-field ϕ is an order parameter that, as the name suggests, measures the "order" of the material, i.e., its phase. It changes continuously across the interface. This approach does not require explicit tracking. Diffuse interface models are very popular in solidification and crystal growth descriptions but are also utilized in fluid dynamics. For example in liquid-vapor phase transition descriptions [Navier]-Stokes equation and Cahn-Hilliard type equations have been coupled by

a stress tensor contribution. In this case, the "phase-field" is simply the mass density and therefore a physical quantity [NZ95, AMW98, DY99, PP00]. Note that models with a phase-field not associated with the density, but coupled to the flow field of a NSE, exist as well, called *advected field method*[BDSK+99, AG20]. Phase-field models are very popular in the fields of solidification, binary and multicomponent multi-phase alloys, dendrite formation, solid-solid phase transformation, grain growth, liquid crystals and electrochemical reactions. See the reviews [SS08, Emm08, Ste09, ABKK+09, Ste13, KT16] and references therein. The works by Folch et al. include periodic forcing by an electric field [FCH00, FTBC+01], also see [FCHR99b] for phase-field modeling of two-phase flow in a Hele-Shaw geometry. Stewart and coworkers describe vapor deposition of thin metallic films[SS16, SS18, SD20]. Recently, phase-field models have been integrated with machine learning in search for high computational performance, see the introduction of [HMD22]. We shall mention phase-field crystal models, which utilize atomic density fields, as another class of diffuse-interface models[EPBS+07]. We recommend Mathis Plapp's reviews as well as Provatas and Elder's book for an introduction to phase-field modeling and further reading [Pla12, Pla15, PE10].

This chapter is structured as follows: Beginning with the Navier-Stokes equations, the lubrication approximation is demonstrated for a simple, partially wetting liquid in Sec. 2.1. In Sec. 2.2 the gradient dynamics description is introduced, leading to the symmetric thin-film description of a binary mixture in Sec. 2.3. In order to model precipitation of solute from a binary mixture, the phase-field method is presented in Sec. 2.4 which is then combined with the binary mixture model in Sec. 2.5. Finally, another two-component system, the Langmuir-Blodgett transfer, is modeled by reducing a two component thin film model to a generalized Cahn-Hilliard equation in Sec. 2.6.

Note, that in this thesis variables denoted by $\sim$ are dimensional or, in the case of functions, have dimensional arguments. However, most dimensional parameters are not denoted by $\sim$ for readability. All dimensionless variables are not denoted by $\sim$ either. Vectorial variables, excluding the Nabla-Operator, are written in bold symbols whereas matrices, i.e., second-order tensors, are underlined. When in doubt, dimensional analysis can be performed or the List of Recurrent Symbols can be consulted.

2.1. Hydrodynamic Derivation of the Thin-Film Equation

2.1.1. Navier-Stokes Equations

Consider a Newtonian fluid of constant density without body forces. The Navier-Stokes equations then read

$$\tilde{\rho}\frac{D\tilde{\mathbf{u}}^{(3)}}{D\tilde{t}} = \tilde{\rho}(\partial_{\tilde{t}}\tilde{\mathbf{u}}^{(3)} + \tilde{\mathbf{u}}^{(3)} \cdot \tilde{\nabla}^{(3)}\tilde{\mathbf{u}}^{(3)})$$

$$= -\tilde{\nabla}^{(3)}\tilde{p} + \tilde{\nabla}^{(3)} \cdot \left[\eta \left(\tilde{\nabla}^{(3)}\tilde{\mathbf{u}}^{(3)} + \left(\tilde{\nabla}^{(3)}\tilde{\mathbf{u}}^{(3)} \right)^{\mathsf{T}} \right) \right], \tag{2.1}$$

$$\tilde{\nabla}^{(3)} \cdot \tilde{\mathbf{u}}^{(3)} = 0, \tag{2.2}$$

$$\tilde{\rho} = const., \tag{2.3}$$

for the flow field $\tilde{\mathbf{u}}^{(3)}(\tilde{\mathbf{x}}^{(3)}, \tilde{t}) = (\tilde{u}_{\tilde{x}}, \tilde{u}_{\tilde{z}}, \tilde{u}_{\tilde{z}})$, fluid density $\tilde{\rho}$, pressure field $\tilde{p}$ and dynamic viscosity η. Whenever operators or fields depend on all three spatial coordinates $(\tilde{x}, \tilde{y}, \tilde{z})$ they are denoted

by a superscript "(3)", otherwise, there is no $\tilde{z}$-dependency. We also identify the stress tensor $\underline{\tilde{\sigma}}$

$$\underline{\tilde{\sigma}} = -\tilde{p}\underline{I} + \eta \left(\tilde{\nabla}^{(3)} \tilde{\mathbf{u}}^{(3)} + \left(\tilde{\nabla}^{(3)} \tilde{\mathbf{u}}^{(3)} \right)^{\mathsf{T}} \right). \tag{2.4}$$

We assume that $\eta = const$. See App. A.1.1 for a short derivation of the compressible Navier-Stokes equations from which the incompressible ones directly follow [SK61, Lea07].

In many situations of interest liquids are bounded by a solid substrate and surrounding gas. Therefore, general boundary conditions are needed. For the solid-liquid interface no-slip and no-penetration conditions are commonly applied

$$\left. \tilde{\mathbf{u}}^{(3)} \right|_{\tilde{z}=0} = 0. \tag{2.5}$$

For the liquid-gas interface the *kinematic condition* holds. Assuming that no mass transport occurs through this interface, the height $\tilde{h}(\tilde{\mathbf{x}}, \tilde{t})$ of the liquid-gas interface is governed by

$$\tilde{u}_{\tilde{z}} = \partial_{\tilde{t}} \tilde{h} + \tilde{\mathbf{u}} \cdot \tilde{\nabla} \tilde{h}, \qquad\qquad \text{at } \tilde{z} = \tilde{h}. \tag{2.6}$$

See App. A.1.2 for a derivation. Further, the force balance at the interface needs to be considered as well

$$\left(\underline{\tilde{\sigma}} - \underline{\tilde{\sigma}}_{\text{gas}} \right) \cdot \mathbf{n}^{(3)} = \gamma \tilde{\kappa} \mathbf{n}^{(3)} + \tilde{\Pi}(\tilde{h}) \mathbf{n}^{(3)} \tag{2.7}$$

with the stress tensor of the gas phase $\underline{\tilde{\sigma}}_{\text{gas}}$, interface normal $\mathbf{n}^{(3)}$, surface tension γ, mean curvature $\tilde{\kappa}$ and disjoining pressure $\tilde{\Pi}$. The first expression on the right-hand side is the Laplace pressure while $\tilde{\Pi}(\tilde{h})$ is introduced as another pressure contribution. It vanishes for large film heights $\tilde{h}(\tilde{\mathbf{x}}, \tilde{t})$ and takes into account the solid-liquid interaction between liquid and substrate for very thin films. This term is discussed more in detail in Sec. 2.1.3. The presented derivation will lead to a very basic thin-film equation, e.g., tangential stresses are not considered due to the disregard of Marangoni effects.

2.1.2. Lubrication Approximation

The lubrication approximation is useful when it is possible to separate the vertical and lateral length scales of the problem at hand. It allows for the description of thin films without solving the NSE and even reduces the dimensionality of the problem. To this end the incompressibility condition (2.2) is rewritten as

$$\partial_{\tilde{z}} \tilde{u}_{\tilde{z}} = -\tilde{\nabla} \cdot \tilde{\mathbf{u}}, \tag{2.8}$$

where $\tilde{u}_{\tilde{z}}$ is the velocity component in the $\tilde{z}$-direction, and integrated along the height of the liquid

$$\left. \tilde{u}_{\tilde{z}} \right|_{\tilde{z}=\tilde{h}} = -\int_0^{\tilde{h}} \tilde{\nabla} \cdot \tilde{\mathbf{u}} \, \mathrm{d}\tilde{z} \tag{2.9}$$

while making use of Eq. (2.5). This expression can then be inserted into the kinematic condition (2.6), followed by applying the Leibniz integral rule and Eq. (2.5) once again

$$\partial_{\tilde{t}} \tilde{h} = -\int_0^{\tilde{h}} \tilde{\nabla} \cdot \tilde{\mathbf{u}} \, \mathrm{d}\tilde{z} - \left. \tilde{\mathbf{u}} \right|_{\tilde{z}=\tilde{h}} \cdot \tilde{\nabla} \tilde{h} \tag{2.10}$$

$$= -\tilde{\nabla} \cdot \int_0^{\tilde{h}} \tilde{\mathbf{u}} \, \mathrm{d}\tilde{z} \tag{2.11}$$

$$= -\tilde{\nabla} \cdot (\tilde{h}\bar{\tilde{\mathbf{u}}}) \tag{2.12}$$

$$\bar{\tilde{\mathbf{u}}} := \frac{1}{\tilde{h}} \int_0^{\tilde{h}} \tilde{\mathbf{u}} \, \mathrm{d}\tilde{z}. \tag{2.13}$$

The mean velocity, defined in the last step, will be determined from lubrication approximation in the following considerations.

The separation of vertical length scale H and lateral X is conducted by non-dimensionalizing the governing equations and introducing a smallness parameter

$$\epsilon = \frac{H}{X}. \tag{2.14}$$

The relevant variables and operators then read

$$\tilde{t} = Tt, \qquad \tilde{\mathbf{x}} = X\mathbf{x}, \qquad \tilde{z} = Hz = \epsilon X z, \qquad \tilde{\mathbf{u}} = \frac{X}{T}\mathbf{u} = U\mathbf{u}, \qquad \tilde{u}_z = \epsilon U u_z, \tag{2.15}$$

$$\frac{\partial}{\partial \tilde{t}} = \frac{1}{T}\frac{\partial}{\partial t}, \qquad \tilde{\nabla} = \frac{1}{X}\nabla, \qquad \frac{\partial}{\partial \tilde{z}} = \frac{1}{\epsilon X}\frac{\partial}{\partial z}, \tag{2.16}$$

with time scale T. We further scale the pressure as

$$\tilde{p} = \frac{\eta}{T\epsilon^2}p. \tag{2.17}$$

Inserting above relations into Eq. (2.1) and identifying the Reynolds number

$$\mathrm{Re} = \frac{\epsilon \tilde{\rho} X^2}{\eta T}, \tag{2.18}$$

results in

$$\partial_t \mathbf{u} + (\mathbf{u} \cdot \nabla + u_z \partial_z)\mathbf{u} = \mathrm{Re}^{-1}\left(-\epsilon^{-1}\nabla p + (\epsilon \Delta + \epsilon^{-1}\partial_z^2)\mathbf{u}\right), \tag{2.19}$$

$$\partial_t u_z + (\mathbf{u} \cdot \nabla + u_z \partial_z)u_z = \mathrm{Re}^{-1}\left(-\epsilon^{-3}\partial_z p + (\epsilon \Delta + \epsilon^{-1}\partial_z^2)u_z\right). \tag{2.20}$$

To lowest order

$$\nabla p = \partial_z^2 \mathbf{u}, \tag{2.21}$$

$$\partial_z p = 0 \tag{2.22}$$

remain. These equations can be utilized to calculate $\bar{\mathbf{u}}$. For that purpose the boundary conditions need to be rescaled as well. Equation (2.5) keeps its form

$$\mathbf{u}|_{z=0} = 0 \qquad u_z|_{z=0} = 0. \tag{2.23}$$

Assuming that $\sigma_{\mathrm{gas}} = 0$, projecting Eq. (2.7) onto normal/tangential vectors $\mathbf{n}^{(3)}/\mathbf{t}^{(3)}$, applying the non-dimensional scaling as above, the boundary conditions then read to lowest order

$$\partial_z \mathbf{u}|_{z=h} = 0 \tag{2.24}$$

$$p|_{z=h} = -\mathrm{Ca}^{-1}\Delta h - \Pi(h). \tag{2.25}$$

We refer to the literature for similar geometries and details [Thi07, ODB97]. In addition, a 3D derivation written in German can be found in [Eng17]. The pressure terms on the right-hand side of Eq. (2.25) are the Laplace pressure and disjoining pressure with Capillary number

$$\mathrm{Ca} = \frac{X\eta}{\epsilon^3 \gamma T}. \tag{2.26}$$

Integrating Eq. (2.21) in z and determining the integration constant with Eq. (2.24) gives

$$\partial_z \mathbf{u} = z\nabla p - h(\nabla p)|_{z=h}. \tag{2.27}$$

Another integration gives

$$\mathbf{u} = \frac{1}{2}z^2\nabla p - zh\,(\nabla p)|_{z=h}. \tag{2.28}$$

Here, the integration constant vanishes due to Eq. (2.23). We take Eq. (2.13) (its dimensionless form is the same), insert Eq. (2.28) and then Eq. (2.25), i.e.,

$$\bar{\mathbf{u}} = \frac{1}{h}\int_0^h \mathbf{u}\,\mathrm{d}z \tag{2.29}$$

$$= \frac{1}{h}\int_0^h \frac{1}{2}z^2\nabla p - zh\,(\nabla p)|_{z=h}\,\mathrm{d}z \tag{2.30}$$

$$= -\frac{h^2}{3}\,(\nabla p)|_{z=h} \tag{2.31}$$

$$= \frac{h^2}{3}\nabla\left(\mathrm{Ca}^{-1}\Delta h + \Pi(h)\right). \tag{2.32}$$

Finally, this expression can be inserted into Eq. (2.12) resulting in the thin-film equation for a simple liquid

$$\partial_t h = -\nabla \cdot \left[\frac{h^3}{3}\nabla\left(\mathrm{Ca}^{-1}\Delta h + \Pi(h)\right)\right]. \tag{2.33}$$

2.1.3. Disjoining Pressure

The state of a liquid wetting a substrate can be roughly divided into three categories depending on the angle θ at the three-phase contact line. They are non-, partially and completely wetting with $\theta = 180°$, $0 < \theta < 180°$, $0°$, respectively. At equilibrium θ_{eq} relates the three surface tensions of each interface as

$$\gamma_{\mathrm{lg}}\cos(\theta_{\mathrm{eq}}) = \gamma_{\mathrm{sg}} - \gamma_{\mathrm{sl}}, \tag{2.34}$$

for a horizontal substrate. This is the famous *Young equation* with surface tensions γ_i for the liquid-gas, solid-gas and solid-liquid interfaces [You05]. The wetting states can be classified by the spreading parameter

$$S = \gamma_{\mathrm{sg}} - (\gamma_{\mathrm{lg}} + \gamma_{\mathrm{sl}}), \tag{2.35}$$

that describes the surface free energy difference between dry and fully covered substrate. $S > 0$ corresponds to wetting while $S < 0$ is partially wetting. Inserting Young's equation results in the *Young-Dupré* equation

$$S = \gamma_{\mathrm{lg}}(\cos(\theta_{\mathrm{eq}}) - 1) := \gamma(\cos(\theta_{\mathrm{eq}}) - 1). \tag{2.36}$$

Young's law holds well for macroscopic liquids, however, for mesoscopic ones, molecular interactions cannot be neglected. These can be represented by an effective potential (wetting energy) $\tilde{f}(\tilde{h})$. We solely use the following form consisting of a long- and short-range contribution in this thesis

$$\tilde{f}(\tilde{h}) = -\frac{A}{2\tilde{h}^2} + \frac{B}{5\tilde{h}^5}, \tag{2.37}$$

$$\tilde{f}(\tilde{h}) \xrightarrow{\tilde{h}\to\infty} 0, \tag{2.38}$$

with coefficients $A > 0$ and $B > 0$, i.e., the partial wetting case. Its derivative is related to the *disjoining pressure* [Der75]

$$\tilde{\Pi}(\tilde{h}) = -\frac{\partial \tilde{f}(\tilde{h})}{\partial \tilde{h}}. \tag{2.39}$$

For this potential, a droplet always sits on a thin adsorption layer (precursor film) [LEGA+88]. The wetting energy of the precursor of height $\tilde{h}_{\mathrm{eq}}$ relates to the spreading coefficient as

$$S = \gamma_{\mathrm{lg}}(\cos(\theta_{\mathrm{eq}}) - 1) \tag{2.40}$$

$$\approx -\frac{1}{2}\gamma\tilde{\vartheta}_{\mathrm{eq}}^2 \stackrel{!}{=} \tilde{f}(\tilde{h}_{\mathrm{eq}}) \tag{2.41}$$

$$\Rightarrow \tilde{\vartheta}_{\mathrm{eq}} = \sqrt{\frac{-2\tilde{f}(\tilde{h}_{\mathrm{eq}})}{\gamma}}. \tag{2.42}$$

Here, we assume small contact angles, which results in the definition of a mesoscopic equilibrium contact angle $\tilde{\vartheta}_{\mathrm{eq}}$.

2.2. Gradient Dynamics Description

It is possible to bring Eq. (2.33) and many other thin-film equations into a gradient dynamics form. Such models conform to a general framework for multiple order parameter fields u_i depending on a single functional $\mathcal{F}$ close to equilibrium [TAP16, Thi18]. Analyzing them in their gradient dynamics form simplifies identifying commonalities between models and allows model extensions while preserving thermodynamic consistency. Let

$$\mathbf{u} = (u_1, u_2, ..., u_m)^{\mathrm{T}} \tag{2.43}$$

be the vector of m scalar order parameter fields. Then

$$\partial_t \mathbf{u} = \nabla \cdot \left[\underline{Q}^{\mathrm{c}}(\mathbf{u}) \nabla \frac{\delta\mathcal{F}}{\delta\mathbf{u}} \right] - \underline{Q}^{\mathrm{nc}}(\mathbf{u}) \frac{\delta\mathcal{F}}{\delta\mathbf{u}} \tag{2.44}$$

denotes their corresponding dynamic equations whereby the first term on the right-hand side represents the conserved and the second term the non-conserved contribution with mobility matrices $\underline{Q}^{\mathrm{c}}$ and $\underline{Q}^{\mathrm{nc}}$, respectively. $\mathbf{u}$, $\underline{Q}$ and $\frac{\delta\mathcal{F}}{\delta\mathbf{u}}$ are tensors in the order parameter space while ∇ acts on coordinate space. The dynamic equation of the i-th order parameter then reads

$$\partial_t u_i = \nabla \cdot \left[\sum_{j=1}^{m} Q_{ij}^{\mathrm{c}} \nabla \frac{\delta\mathcal{F}}{\delta u_j} \right] - \sum_{j=1}^{m} Q_{ij}^{\mathrm{nc}} \frac{\delta\mathcal{F}}{\delta u_j}. \tag{2.45}$$

The mobility matrices have to be symmetric in order to fulfill Onsager's reciprocal relations [Ons31a, Ons31b] and positive definite to ensure a monotonic decrease in $\mathcal{F}$. The latter can be easily shown by calculating

$$
\begin{aligned}
\frac{d}{dt}\mathcal{F}[\mathbf{u}] &= \int_\Omega \frac{\delta\mathcal{F}}{\delta\mathbf{u}} \partial_t \mathbf{u}\,\mathrm{d}^n\mathbf{x} \\
&= \int_\Omega \frac{\delta\mathcal{F}}{\delta\mathbf{u}}\nabla\cdot\left[\underline{Q}^{\mathrm{c}}(\mathbf{u})\nabla\frac{\delta\mathcal{F}}{\delta\mathbf{u}}\right] - \frac{\delta\mathcal{F}}{\delta\mathbf{u}}\underline{Q}^{\mathrm{nc}}(\mathbf{u})\frac{\delta\mathcal{F}}{\delta\mathbf{u}}\,\mathrm{d}^n\mathbf{x} \quad (2.46) \\
&= \int_\Omega \left(-\nabla\frac{\delta\mathcal{F}}{\delta\mathbf{u}}\right)\cdot\left(\underline{Q}^{\mathrm{c}}(\mathbf{u})\nabla\frac{\delta\mathcal{F}}{\delta\mathbf{u}}\right) - \frac{\delta\mathcal{F}}{\delta\mathbf{u}}\underline{Q}^{\mathrm{nc}}(\mathbf{u})\frac{\delta\mathcal{F}}{\delta\mathbf{u}}\,\mathrm{d}^n\mathbf{x} \le 0 \quad (2.47)
\end{aligned}
$$

with n being the spatial dimension. The final step is done with integration by parts assuming Neumann boundary conditions.

2.3. Symmetric Thin-Film Model for Binary Mixtures

For the description of a liquid containing both solvent and solute, two order parameters are required. Making use of Eq. (2.44) and the functional

$$
\tilde{\mathcal{F}}_{\mathrm{bm}}[\tilde{\psi}_1,\tilde{\psi}_2] = \int_\Omega \left\{ \frac{\gamma}{2}|\tilde{\nabla}(\tilde{h})|^2 + \tilde{f}(\tilde{h}) + \tilde{h}\tilde{f}_{\mathrm{FH}}(\tilde{C}_1,\tilde{C}_2) \right\}\mathrm{d}^2\tilde{\mathbf{x}}, \quad (2.48)
$$

on a 2D domain, with a Flory-Huggins type local potential for the concentrations

$$
\tilde{f}_{\mathrm{FH}}(\tilde{C}_1,\tilde{C}_2) = n_{\max}k_B\hat{T}\left[\tilde{C}_1\ln(\tilde{C}_1) + \tilde{C}_2\ln(\tilde{C}_2) - 1 + \chi\tilde{C}_1\tilde{C}_2\right], \quad (2.49)
$$

one can begin to formulate a symmetric model for binary mixtures. $n_{\max}$, k_B, $\hat{T}$ and χ are the particle number density (per volume) of the mixture (counting solvent and solute particles), the Boltzmann constant, the temperature and the mixing parameter, respectively. The order parameter fields are the effective solvent $\tilde{\psi}_1$ and solute thickness $\tilde{\psi}_2$ which are defined by film height

$$
\tilde{h}(\tilde{x},\tilde{y},\tilde{t}) = \tilde{\psi}_1(\tilde{x},\tilde{y},\tilde{t}) + \tilde{\psi}_2(\tilde{x},\tilde{y},\tilde{t}) \quad (2.50)
$$

and concentrations (volume fractions)

$$
\tilde{C}_i = \frac{\tilde{\psi}_i}{\tilde{h}}. \quad (2.51)
$$

Although the $\tilde{C}_i$ are dimensionless, they do depend on dimensional spatial coordinates and are to be distinguished from C_i appearing in non-dimensionalizations which depend on non-dimensional coordinates. The free energy consists of a surface tension term, dewetting energy and mixing energy. Here, the wetting energy is assumed to solely depend on $\tilde{h}$. The conserved equations for $\tilde{\psi}_1$ and $\tilde{\psi}_2$ then read

$$
\partial_{\tilde{t}}\begin{pmatrix}\tilde{\psi}_1\\\tilde{\psi}_2\end{pmatrix} = -\tilde{\nabla}\cdot\begin{pmatrix}\tilde{\mathbf{J}}_1\\\tilde{\mathbf{J}}_2\end{pmatrix} = \tilde{\nabla}\cdot\left[\left(\underline{\tilde{Q}}^{\mathrm{conv}} + \underline{\tilde{Q}}^{\mathrm{diff}}\right)\begin{pmatrix}\tilde{\nabla}\frac{\delta\tilde{\mathcal{F}}_{\mathrm{bm}}}{\delta\tilde{\psi}_1}\\\tilde{\nabla}\frac{\delta\tilde{\mathcal{F}}_{\mathrm{bm}}}{\delta\tilde{\psi}_2}\end{pmatrix}\right], \quad (2.52)
$$

13

with diffusive and convective mobility matrices

$$\underline{\tilde{Q}}^{\text{conv}} = \frac{\tilde{\psi}_1 + \tilde{\psi}_2}{3\eta} \begin{pmatrix} \tilde{\psi}_1^2 & \tilde{\psi}_1\tilde{\psi}_2 \\ \tilde{\psi}_1\tilde{\psi}_2 & \tilde{\psi}_2^2 \end{pmatrix}, \tag{2.53}$$

$$\underline{\tilde{Q}}^{\text{diff}} = \begin{pmatrix} \tilde{Q}^{\text{diff}}_{\tilde{\psi}_1\tilde{\psi}_1} & \tilde{Q}^{\text{diff}}_{\tilde{\psi}_1\tilde{\psi}_2} \\ \tilde{Q}^{\text{diff}}_{\tilde{\psi}_2\tilde{\psi}_1} & \tilde{Q}^{\text{diff}}_{\tilde{\psi}_2\tilde{\psi}_2} \end{pmatrix} = (\tilde{\psi}_1 + \tilde{\psi}_2)\tilde{M} \begin{pmatrix} 1 & -1 \\ -1 & 1 \end{pmatrix}, \tag{2.54}$$

$$\tilde{M} = \frac{\tilde{\psi}_1\tilde{\psi}_2}{(\tilde{\psi}_1 + \tilde{\psi}_2)^2} \frac{1}{n_{\max}\hat{\zeta}}, \tag{2.55}$$

and diffusion coefficient

$$D = \frac{k_B\hat{T}}{\hat{\zeta}}. \tag{2.56}$$

η is the shear viscosity which appeared in Sec. 2.1 and $\hat{\zeta}$ the drag [friction] coefficient [inverse mobility] for diffusive motion. Above definition of the diffusion constant corresponds to the Einstein relation for Brownian motion due to collisions between particles in a solution [Rei65]. The choice of variables $(\tilde{\psi}_1, \tilde{\psi}_2)$ is sensible in contrast to other choices such as $(\tilde{h}, \tilde{\psi})$, with $\tilde{\psi} = \tilde{\psi}_2$, as it allows formal separation of solvent and solute. Fluxes acting solely on one of the components can then be added consistently. Note that the mobility matrices usually contain polynomials of the order parameter fields. Their particular form depends on the boundary conditions at the different interfaces surrounding the liquid and thus are still derived from hydrodynamic equations. Executing the variations results in

$$\partial_{\tilde{t}}\tilde{\psi}_1 = -\tilde{\nabla} \cdot \left\{ \frac{1}{3\eta}\tilde{\psi}_1\tilde{h}^2\tilde{\nabla}\left[\gamma\tilde{\Delta}\tilde{h} - \tilde{f}'(\tilde{h})\right] - D\tilde{h}\left(1 - 2\chi\tilde{C}_1\tilde{C}_2\right)\tilde{\nabla}\tilde{C}_1 \right\}, \tag{2.57}$$

$$\partial_{\tilde{t}}\tilde{\psi}_2 = -\tilde{\nabla} \cdot \left\{ \frac{1}{3\eta}\tilde{\psi}_2\tilde{h}^2\tilde{\nabla}\left[\gamma\tilde{\Delta}\tilde{h} - \tilde{f}'(\tilde{h})\right] - D\tilde{h}\left(1 - 2\chi\tilde{C}_1\tilde{C}_2\right)\tilde{\nabla}\tilde{C}_2 \right\}. \tag{2.58}$$

This model can then be extended by adding more contributions to the free energy or non-conserved fluxes.

2.3.1. Dilute Limit

It can be easily shown that Eq. (2.57)-(2.58) are related to models in the dilute limit, classically derived from hydrodynamic equations. In a dilute mixture solvent rarely meet solute particles. Neglecting solute-solvent interaction, meaning $\chi = 0$, it is possible to write the dynamic equations for film height $\tilde{h}$ and solute concentration $\tilde{C}$ as

$$\partial_{\tilde{t}}\tilde{h} = -\tilde{\nabla} \cdot \left[\frac{\tilde{h}^3}{3\eta}\tilde{\nabla}\left(\gamma\tilde{\Delta}\tilde{h} - \tilde{f}'(\tilde{h})\right) \right], \tag{2.59}$$

$$\partial_{\tilde{t}}\tilde{C} = -\frac{\tilde{h}^2}{3\eta}\tilde{\nabla}\tilde{C} \cdot \tilde{\nabla}\left(\gamma\tilde{\Delta}\tilde{h} - \tilde{f}'(\tilde{h})\right) + \frac{D}{\tilde{h}}\tilde{\nabla} \cdot (\tilde{h}\tilde{\nabla}\tilde{C}). \tag{2.60}$$

Details can be found in appendix Sec. A.2. For example thin-film models used for nanoparticle suspensions have exactly this form if other driving forces such as evaporation, vapor recoil or surface activity are neglected [WCM03]. For a comparison with models that use $(\tilde{h}, \tilde{\psi})$, with $\tilde{\psi} = \tilde{\psi}_2$, as order parameter fields one can directly take Eq. (2.58) and set $\chi = 0$. Adding evaporation then recovers Frastia et al.'s deposition of nanoparticles in a suspension model[FAT11, FAT12]. Fluxes containing $\tilde{h}\tilde{\nabla}\tilde{C}$ on the right-hand side are found in particle-laden thin-film models with gravity-driven flow, too[CBH07].

2.4. Phase-field Modeling

A simple phase-field model for the solidification of a pure substance is formulated from a Ginzburg-Landau type free energy functional such as

$$\tilde{\mathcal{F}}[\tilde{\phi}, \tilde{u}] = \int_{\Omega} \frac{f_{\text{grad}}}{2} |\tilde{\nabla}\tilde{\phi}|^2 + \tilde{f}(\tilde{\phi}, \tilde{u}) \mathrm{d}^2\tilde{\mathbf{x}}, \tag{2.61}$$

with the phase-field $\tilde{\phi}(\tilde{x}, \tilde{y}, \tilde{t})$, normalized temperature $\tilde{u}(\tilde{x}, \tilde{y}, \tilde{t})$, gradient energy coefficient f_{grad} and local potential

$$\tilde{f}(\tilde{\phi}, \tilde{u}) = f_{\text{bar}} f_1(\tilde{\phi}) + \tilde{\lambda}\tilde{u} f_2(\tilde{\phi}), \tag{2.62}$$

$$f_1(\tilde{\phi}) = -\frac{\tilde{\phi}^2}{2} + \frac{\tilde{\phi}^4}{4}. \tag{2.63}$$

For consistency the problem is formulated for a 2D domain. f_{bar} controls the barrier height of the double-well potential, i.e., the nucleation barrier, while $\tilde{\lambda}$ is a coupling parameter, related to the latent heat L and the melting temperature $\hat{T}_m$. f_2 tilts the potential such that one phase is favored over the other. The model then consists of the dynamic phase-field equation

$$\partial_t \tilde{\phi} = -\tilde{Q} \frac{\delta \tilde{\mathcal{F}}}{\delta \tilde{\phi}}, \tag{2.64}$$

with mobility $\tilde{Q}$ coupled to a dynamic equation for an intensive variable, i.e., the temperature follows a diffusion equation to which a source term is added

$$\partial_{\tilde{t}} \tilde{u} = D\tilde{\Delta}\tilde{u} + \frac{1}{2} \partial_{\tilde{t}} f_3(\tilde{\phi}). \tag{2.65}$$

Here, D is the diffusion coefficient. In a dimensional temperature formulation the latent heat would appear in front of the source term as well. This set of equations cannot be directly derived from a total free energy. A framework for developing thermodynamically consistent phase-field models was formulated by Penrose and Fife [PF90] by using an entropy functional and an energy density as order parameter fields. This was then applied by Wang et al. to models for solidification of a pure substance [WSWM+93]. However, this formulation is not used much in practice due to the simplicity and intuitiveness to work with an order parameter such as the temperature that directly controls the phase transition.

In many cases

$$f_2(\tilde{\phi}) = \tilde{\phi} - \frac{\tilde{\phi}}{3} \tag{2.66}$$

and

$$f_3(\tilde{\phi}) = \tilde{\phi} \tag{2.67}$$

are used since $f_2(\tilde{\phi})$ preserves the minima of the double-well potential at ± 1 and Eq. (2.67) keeps the source term as simple as possible. At equilibrium the temperature $\hat{T}$ of the material equals the melting temperature $\hat{T}_m$. Since

$$\tilde{u} = \frac{C_p}{\hat{L}}(\hat{T} - \hat{T}_m) \tag{2.68}$$

with heat capacity C_p at constant pressure, this means $\tilde{u}^* = 0$. Then the interface profile in 1D is a hyperbolic tangent

$$\tilde{\phi}^*(\tilde{x}) = \tanh\left(\frac{\tilde{x}}{\sqrt{2}W}\right) \tag{2.69}$$

of width

$$W^2 = \frac{f_{\text{grad}}}{f_{\text{bar}}}. \tag{2.70}$$

Essentially f_{grad} and f_{bar} control the interface width W. For numerical calculations these parameters are tuned for efficiency but this in turn means that the interface is given a surface energy that is unphysically magnified. However, the relevant physical parameter is actually the surface tension of the interface

$$\gamma_{\text{2D}} = \int\limits_{-\infty}^{\infty} \frac{f_{\text{grad}}}{2}|\partial_{\tilde{x}}\tilde{\phi}^*|^2 + \tilde{f}(\tilde{\phi}^*, \tilde{u}^*)\,\mathrm{d}\tilde{x} = \frac{\sqrt{2}}{3}\sqrt{\tilde{f}_{\text{bar}}f_{\text{grad}}} = \frac{\sqrt{2}}{3}W\tilde{f}_{\text{bar}}. \tag{2.71}$$

Let the surface tension γ_{2D} of a physical system be known, then W can be chosen as desired and $\tilde{f}_{\text{bar}}$ be determined from Eq. (2.71) resulting in a quantitative description. Note, that γ_{2D} has unit of energy per length as the problem is formulated for a 2D domain. On a 3D domain the unit matches the units of surface tensions mentioned in Sec. 2.1.

Before we discuss further (detrimental) effects due to mesoscopic interface thickness, another important method related to phase-field modeling needs to be mentioned: The method of matched asymptotic analysis. In order to obtain a quantitative description phase-field models can be taken to the sharp interface limit pioneered by Caginalp et al. The limit $W \to 0$ recovers the corresponding sharp-interface model [Cag86, CL87, CS91]. However, this limits the validity of the obtained parameter relations since W is taken to the absolute limit which is obviously not done in actual calculations. Karma and Rappel introduced the thin-interface limit which is based on a separation of length scales, requiring the interface width to be much smaller than the other characteristic length scales[KR96, KR98]. This softens the limitations on W, making quantitative calculations more accessible.

Unfortunately, applying the thin-interface limit to solidification models with asymmetric diffusivities for solid and liquid phase, which is closer to reality, shows that more interface width dependend effects become artificially enhanced for mesoscopic widths [Alm99]. These include temperature discontinuity at the interface, interface stretching and surface diffusion. Analogous effects are found for binary alloy models[Kar01]. The temperature discontinuity then corresponds to a discontinuity of the chemical potential, also known as solute trapping. Solute trapping occurs when the interface moves faster than material can be exchanged through the interface. In the case of solidification, if the equilibrium concentration of the solid c_s is smaller than that of the liquid c_l, this would mean that solute cannot move away from the interface into the liquid fast enough in comparison to the interface movement. Therefore, the solid composition will not be at c_s but instead $c_s < c < c_l$. Although a variational phase-field model for binary alloys in which those three effects vanish has yet to be found[EFKP04, Pla12], Plapp showed that, in analogy to the pure substance case, a thermodynamically consistent phase-field approach for binary alloys can be formulated from a grand canonical potential[Pla11]. However, for numerical applicability this approach still requires a so-called "anti-trapping current" in order to counter solute trapping. This additional current modifies the dynamic equations in a non-variational way and further adds another degree of freedom in the form of an interpolation function. This makes

eliminating the effects of spurious interface stretching and surface diffusion possible[EFKP04]. Besides in Plapp's work, the usage of anti-trapping currents has been very popular in quantitative phase-field modeling since its introduction by Karma[Kar01] for example in a quantitative model for dilute binary alloys[RBKD04] with arbitrary solid diffusivities[OM09] or recently for arbitrary two phase binary alloys not limited to slow solidification[BJM18].

Of course, these works are preceded by much earlier models, most notably the WBM model for (non-)isothermal binary alloy solidification which is not independent of interface width and the KKS model which is incorrect for slow solidification rates [WBM92, WBM93, BWMM94, KKS99].

2.4.1. Modeling Dendrites

The description of dendrites is a long-standing topic with roots in microscopic solvability theory. The starting point is a sharp-interface problem similar to the classic Stefan problem. A linear stability analysis of a planar front reveals an instability widely known as the Mullins-Sekerka instability [MS64]. The dispersion relation predicts linear growth that is stabilized by the Gibbs-Thomson effect. Analytic steady-state solutions without capillarity in the form of circular and elliptic paraboloids have been found by Ivantsov[Iva47], Horvay and Cahn[HC61]. Linear stability analysis of the former shows that such needle-like dendrites become unstable in an unending series of tip-splitting in the absence of capillarity[LM78a, LM78b, LM77]. Simulations that include surface tension effects show that for larger surface tension values the tip stabilizes but a sidebranching instability emerges[ML78]. Further results of microscopic solvability theory state that stable growth of dendrites can only exist in the presence of anisotropy and that their growth directions are determined by it. For more information on microscopic solvability theory (or analytical theory of solvability) the reader is referred to a summary in Chapter 5.8 of [PE10] and (detailed) derivations in [Lan80, Lan87] if interested. The anisotropy necessity is found in phase-field models as well. Anisotropic phase-field models have been presented by Kobayashi et al. as early as 1986 while simulation results are published in [Kob93]. The review by Singer-Loginova and Singer contains an overview on core solvability theory advances[SS08]. First quantitative comparisons between solvability theory and phase-field model have been done in the previously mentioned paper by Karma and Rappel [KR96], later verified and improved by Provatas et al[PGD98]. See the reviews and recommendations mentioned in the introduction of this chapter for more (recent) literature on phase-field descriptions of dendrite formation. In this thesis a distinction between *fingers* and *(an-)isotropic dendrites* is made. We identify the latter by the presence of tip-splitting, side branching etc. Anisotropy manifests itself by the presence of primary dendrites, i.e., clear fingers of larger length scale from which side branches of clearly smaller scale grow. Isotropic dendrites will be called seaweed structures synonymously.

2.4.2. Mullins-Sekerka Instability

The planar front of a solidifying material can become unstable, leading to the formation of fingers. This is known as the *Mullins-Sekerka instability* [MS64]. The dispersion relation of linear perturbations can be derived for the solidification of a pure liquid. There, temperature $\hat{T}$ corresponds to the order parameter field. The derivation is very similar when the solidification [precipitation] of a dilute but oversaturated binary liquid is considered [CCR92]. Then, the concentration $\tilde{C}$ of the impurity is the order parameter field. We consider the case of purely diffusive and isothermal

dynamics:

$$\partial_{\tilde{t}} \tilde{C}_i = D_i \tilde{\Delta} \tilde{C}_i, \qquad\qquad i = s, l, \qquad (2.72)$$

$$\mathbf{n} \cdot \left(D_l \tilde{\nabla} \tilde{C}_l - D_s \tilde{\nabla} \tilde{C}_s \right) = \left(\tilde{C}_s - \tilde{C}_l \right) \tilde{\mathbf{v}} \cdot \mathbf{n} \qquad\qquad \text{at } \tilde{\mathrm{x}} = \tilde{\xi}, \qquad (2.73)$$

$$\tilde{C}_s = K \tilde{C}_l \qquad\qquad \text{at } \tilde{\mathrm{x}} = \tilde{\xi}, \qquad (2.74)$$

$$\hat{T}_l = \hat{T}_m + m_l \tilde{C}_l - \frac{\hat{\gamma} \hat{T}_m}{\tilde{\rho} \hat{L}_m} \kappa \qquad\qquad \text{at } \tilde{\mathrm{x}} = \tilde{\xi}. \qquad (2.75)$$

s and l denote quantities in the solid and liquid phase, respectively. $\mathbf{n}$ is the interface normal pointing into the liquid, $\tilde{\mathbf{v}}$ the velocity of the interface, $\tilde{\xi}$ the interface position, $\tilde{\kappa}$ the curvature of the interface and K the equilibrium segragation coefficient, denoting the ratio of the liquidus and solidus slopes m_i in the phase diagram of the mixture. Further, $\hat{\gamma}$, $\tilde{\rho}$, $\hat{L}_m$ and $\hat{T}$ are surface energy, density (equal in both phases), latent heat per unit mass and melting temperature of the pure solvent, respectively. Equation (2.73) reflects solute conservation and (2.75) the Gibbs-Thomson relation, i.e., the melting temperature shifts when the interface is curved (Laplace pressure). This model is a prime example of a sharp interface model. For simplicity, we confine the problem to the $\tilde{x}$-$\tilde{y}$ plane, where $\tilde{y}$ denotes the lateral direction, where each phase is homogeneous and $\tilde{x}$ the direction of the propagating solidification front. We impose the following conditions

$$\tilde{C}_s \xrightarrow{\tilde{x} \to -\infty} C_\infty, \qquad\qquad \tilde{C}_l \xrightarrow{\tilde{x} \to \infty} C_\infty, \qquad\qquad \tilde{C}_i \xrightarrow{\tilde{x} \to 0} C_{\mathrm{eq},i}, \qquad (2.76)$$

with C_∞ being the solute concentration at infinity and $C_{\mathrm{eq},i}$ the local equilibrium solute concentration of the liquid[solid] at a planar interface. The planar front solution is found by solving for steady states in the comoving frame:

$$\tilde{C}_l^* = C_\infty + (C_{\mathrm{eq},l} - C_\infty) e^{-\frac{\tilde{v}}{D_l} \tilde{x}}, \qquad\qquad \tilde{C}_s^* = K C_{\mathrm{eq},l}. \qquad (2.77)$$

We perform a linear stability analysis of these steady states by making the Ansatz

$$\tilde{C}_i(\tilde{x}, \tilde{y}) = \tilde{C}_i^* + \epsilon \tilde{C}_{ik}^{(1)}(\tilde{x}) b(\tilde{t}, \tilde{y}), \qquad (2.78)$$

$$\tilde{\xi}(\tilde{y}, \tilde{t}) = \epsilon \tilde{\xi}_{\tilde{k}}^{(1)} b(\tilde{t}, \tilde{y}), \qquad (2.79)$$

$$\text{with } b(\tilde{t}, \tilde{y}) = e^{\tilde{\omega} \tilde{t}} e^{i \tilde{k} y}. \qquad (2.80)$$

After some algebra, only keeping perturbations up to $\mathcal{O}(\epsilon)$, setting $K = 1$ and assuming that the wavelength of the perturbation is much smaller than the diffusive length scale

$$\tilde{k} \gg \frac{\tilde{v}}{D_i}, \qquad (2.81)$$

also called the *quasi-stationary approximation*, we arrive at

$$\tilde{\omega} = \tilde{k} \tilde{v} \left[1 - \tilde{k}^2 d_c d_d (1 + n) \right]. \qquad (2.82)$$

The effective parameters capillary length d_c, diffusive length scale in the liquid d_d and ratio of the diffusivities n are defined as:

$$d_c = \frac{\hat{\gamma} \hat{T}_m}{\tilde{\rho} \hat{L}_m m_l \Delta C}, \qquad d_d = \frac{D_l}{\tilde{v}}, \qquad n = \frac{D_s}{D_l}, \qquad \text{with } \Delta C = C_{\mathrm{eq},s} - C_{\mathrm{eq},l}. \qquad (2.83)$$
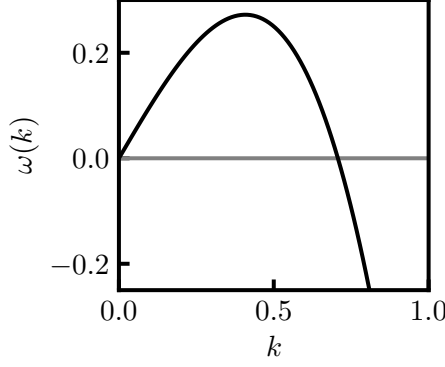
Figure 2.1.: Dispersion relation $\tilde{\omega}(\tilde{k})$ of the Mullins-Sekerka instability for $v = d_c = d_d = n = 1$.

See App. A.7 for details of the derivation. A plot of the dispersion relation in Fig. 2.1 shows the linear destabilization of long wavelengths and the stabilization of short ones by capillarity. A fluid analogon of this instability exists, the *Saffman-Taylor instability* [ST58, LC00], where a less viscous fluid displaces a more viscous one in a porous medium. Fingers of the former protrude into the latter with a faster velocity than a planar interface would have. This phenomenon is also called *viscous fingering*.

2.4.3. Xu and Meakin Model

In Sec. 2.5 a phenomenological model that includes precipitation for a volatile binary mixture will be formulated. Here, we present the phase-field model that motivates the equation for the phase-field used later on. The phase-field model for dendritic precipitation of solute under diffusive flux investigated in [XM08, XM11] consists of a non-conserved equation for the phase-field $\tilde{\phi}(\tilde{x}, \tilde{y}, \tilde{t})$

$$\partial_{\tilde{t}}\tilde{\phi} = -\frac{1}{\tau}\frac{\delta\tilde{\mathcal{F}}_{\mathrm{xm}}}{\delta\tilde{\phi}} - \frac{\varepsilon^2}{\tau}\tilde{\kappa}|\tilde{\nabla}\tilde{\phi}| \tag{2.84}$$

$$\tilde{\mathcal{F}}_{\mathrm{xm}}[\tilde{\phi}, \tilde{c}] = \int\limits_{\Omega} \left(\frac{\varepsilon^2}{2}(\tilde{\nabla}\tilde{\phi})^2 + f_{\mathrm{xm}}\right)\mathrm{d}^2\tilde{\mathbf{x}} \tag{2.85}$$

$$f_{\mathrm{xm}}(\tilde{\phi}, \tilde{c}; \lambda) = f_1(\tilde{\phi}) + \lambda f_2(\tilde{\phi})\tilde{c} \tag{2.86}$$

$$= (1 - \tilde{\phi}^2)(\lambda\tilde{c} - \tilde{\phi}) \tag{2.87}$$

$$f_1(\tilde{\phi}) = -\frac{\tilde{\phi}^2}{2} + \frac{\tilde{\phi}^4}{4} \tag{2.88}$$

$$f_2(\tilde{\phi}) = \tilde{\phi} - \frac{\tilde{\phi}^3}{3} \tag{2.89}$$

$$\tilde{\kappa} = \tilde{\nabla} \cdot \frac{\tilde{\nabla}\tilde{\phi}}{|\tilde{\nabla}\tilde{\phi}|} \tag{2.90}$$

and a diffusion equation for the normalized solute concentration $\tilde{c}(\tilde{x}, \tilde{y}, \tilde{t})$

$$\partial_{\tilde{t}}\tilde{c} = D_{\mathrm{xm}}\tilde{\Delta}\tilde{c} + \alpha\partial_{\tilde{t}}\tilde{\phi}\left(1 + \frac{D_{\mathrm{xm}}\tilde{\Delta}\tilde{\phi} - \partial_{\tilde{t}}\tilde{\phi}}{\tilde{k}_r|\tilde{\nabla}\tilde{\phi}|}\right). \tag{2.91}$$

$\tilde{\phi} = -1$ corresponds to solid and $\tilde{\phi} = 1$ liquid phase while $\tilde{c} = \frac{\tilde{C} - C_{\mathrm{eq}}}{C_{\mathrm{eq}}}$ is the concentration normalized by the local equilibrium concentration C_{eq}. D_{xm} is the diffusion constant, τ a characteristic time scale related to the particle mobility, ε a characteristic length scale related to the interface thickness and λ the dimensionless coupling parameter. α relates solute and solid densities (parts per volume) during phase transition. Notice that the functional has unit of length^2. The local potential f_{xm} is made up of a double-well potential f_1 and an odd polynomial coupling to $\tilde{c}$, that maintains the extrema, f_2. Note, that the extremum

$$\tilde{\phi}^* = \lambda \tilde{c}, \qquad (2.92)$$

may become larger than 1. At $\tilde{\phi}^* = 1$ the curvatures of the colliding extrema swap, see Fig. 2.2. The decrease or increase in $\tilde{c}$ upon precipitation or dissolution is modeled by the source terms in Eq. (2.91). Since $\tilde{\phi} = -1$ represents the solid phase, $\partial_t \tilde{\phi}$ is positive when precipitation occurs. Therefore, calling the expressions on the right-hand side of Eq. (2.91) source terms is correct. If $\tilde{C}$ is larger than C_{eq} or equivalently $\tilde{c} > 0$, precipitation is favored. Technically, negative $\tilde{c}$ are allowed but in such cases the tilt of f_{xm} reverses and the excess material dissolves again such that $\partial_t \tilde{\phi} > 0$ and thus $\tilde{c} > 0$ again.
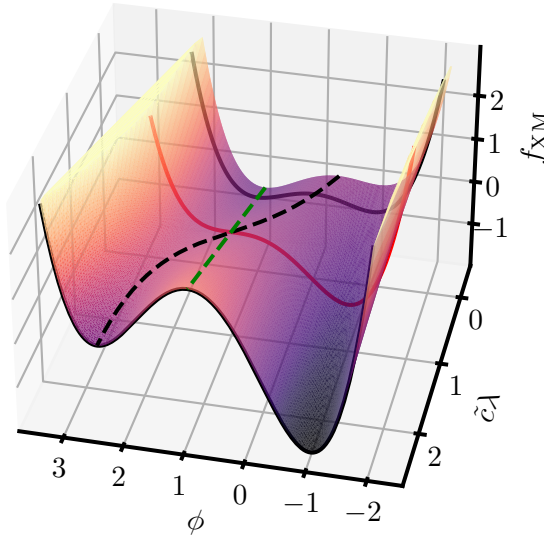
Figure 2.2.: Surface plot of the local potential of the phase-field $f_{\mathrm{xm}}(\tilde{\phi}, \lambda \tilde{c})$, see Eq. (2.87). The symmetric double-well potential at $\tilde{c}\lambda = 0$ is marked in solid black. As $\tilde{c}\lambda$ increases, the potential is tilted such that $\tilde{\phi} = -1$ becomes the global minimum. $\tilde{\phi} = \lambda \tilde{c}$ is marked by the dashed black line. The local maximum becomes a local minimum as $\tilde{c}\lambda$ increases, i.e., the linear stability of two steady states interchanges, corresponding to a transcritical bifurcation at $\tilde{c}\lambda = 1$, marked by a red solid line. The liquid phase $\tilde{\phi} = 1$ is denoted by a green dashed line.

Relations obtained from asymptotic analysis can be used in order to link microscopic interface parameters and physical quantities. Xu and Meakin show that this model converges to appropriate

sharp-interface equations in the thin-interface limit which results in the following relations:

$$\alpha = \frac{1}{2bk_c} \, . \tag{2.93}$$

k_c is a stoichiometric coefficient of order unity, which gives the relative numbers of molecules that take part in a chemical reaction and

$$b = \frac{C_{\text{eq}}}{\tilde{\rho}_s} \tag{2.94}$$

is the ratio between equilibrium concentration C_{eq} with a flat solid surface and the density of the solid $\tilde{\rho}_s$. The microscopic parameters can be related to $\tilde{k}_r$ by

$$\tau = \alpha\lambda\frac{\varepsilon^2}{D_{\text{xm}}} \left(\frac{5}{3} + \frac{\sqrt{2}D_{\text{xm}}}{\tilde{k}_r\varepsilon} \right) \tag{2.95}$$

$\tilde{k}_r$ is the reaction rate coefficient for the precipitation [dissolution] process. Nevertheless, we proceed by non-dimensionalizing the model with diffusive time scale and interface width as length scale

$$T = \frac{\varepsilon^2}{D_{\text{xm}}} \qquad X = \varepsilon, \tag{2.96}$$

resulting in

$$\partial_t\phi = \frac{1}{\text{Pe}_{\text{xm}}} \left(\Delta\phi - \partial_\phi f_{\text{xm}}(\phi, c, \lambda) - \kappa|\nabla\phi| \right), \tag{2.97}$$

$$\partial_t c = \Delta c + \alpha\partial_t\phi \left(1 + \frac{\Delta\phi - \partial_t\phi}{D_a s|\nabla\phi|} \right), \tag{2.98}$$

with Péclet number Pe_{xm}

$$\text{Pe}_{\text{xm}} = \frac{\tau D_{\text{xm}}}{\varepsilon^2}, \tag{2.99}$$

Damköhler number D_a

$$D_a = \frac{k_r}{s}, \tag{2.100}$$

and the ratio of characteristic interface thickness to diffusive length scale $s = \frac{\varepsilon}{l}$. See A.3 for details on the non-dimensionalization. Note, that although $\tilde{\phi}$ and $\tilde{c}$ are dimensionless, they do depend on dimensional spatial coordinates and time, therefore, the order parameter fields depending on dimensionless arguments are distinguished by (ϕ, c). In conjunction, Eq. (2.95) can be rewritten as

$$\lambda = \frac{\text{Pe}_{\text{xm}}}{\alpha \left(\frac{5}{3} + \frac{\sqrt{2}}{sD_a} \right)} \xrightarrow{D_a \to \infty} \frac{3}{5}\frac{\text{Pe}_{\text{xm}}}{\alpha} \, . \tag{2.101}$$

The case of precipitation limited by diffusion, i.e., negligible interface kinetics, is obtained when $D_a \to \infty$. , that then the second source term in Eq. (2.98) vanishes. The majority of phase-field models solely use $\sim \partial_t\phi$ for the source term. Here, the second term is added to take into account the discontinuity of the concentration at the interface in the thin-interface limit. Most phase-field models take this into account by formulating bulk free energies separately for each phase [Pla11]. At this point we would like to remind the reader that at locations, where $\phi = -1$ solute has precipitated, c is not necessarily 0. Therefore, solution above/around the precipitate

is still present. Furthermore, ϕ is only an indicator function and does not give information on for example the amount of precipitate.

Finally, let us discuss the curvature term $\kappa|\nabla\phi|$ in Eq. (2.97). It counters curvature-driven interface motion and is used in few phase-field models. The reason being that many models usually strife to be quantitative and therefore take into account interface kinetics. Here, our intention is to implement a phase-field model that is as simple as possible but still allows the formation of dendrites. Therefore, interfaces will converge locally to hyperbolic tangents unaffected by curvature making the phase-field solely as a means of tracking the solid/liquid interface. This counter term was first introduced by Folch et al. [FCHR99b, FCHR99a] and has been used in other works such as [BMLV03, BM03, BRSB+04].

2.5. Complex Liquid with Precipitation Mechanism

2.5.1. Coupling Complex Liquid Flow to the Phase-Field Equation

Thin-film models are able to describe fingering patterns such as the large scale ones appearing in Fig. 1.2 [Sch89, SH96, Kal00, ESR00, LGP02, Aja05]. However, the deposited small scale dendrites possess a clear directional preference and strinkingly straight main branches. Without anisotropy, thin-film models cannot describe dendrite formation as mentioned in Sec. 2.4.1. Even if anisotropy was somehow introduced into the hydrodynamic equations, it would only affect the, here, larger scale dewetting fingers. Thus, a second fingering instability, ideally leading to dendrites, on a smaller scale must be included in the model. In this section, we combine the phase-field equation with the equations for binary mixtures of Sec. 2.3 in order to primarily include convective and evaporative fluxes. Assuming that the process occurs at almost saturated pressure and is therefore limited by phase transition, the rate of evaporation $\tilde{J}_{\text{evap}}$ then depends on the difference in chemical potentials [partial pressures] $\tilde{\mu}_l$ and $\tilde{\mu}_g$ of liquid and gas phase [LGP02, Aja05, Thi10, KGFC10, TTP12, FAT12, WTGK+15]

$$\tilde{J}_{\text{evap}} = -E_v\left(\tilde{\mu}_l - \tilde{\mu}_g\right) \tag{2.102}$$

$$\tilde{\mu}_l = \frac{\delta\tilde{\mathcal{F}}_{\text{bm}}}{\delta\tilde{\psi}_1}. \tag{2.103}$$

Related reviews are [CG10, SSVR11, Erb12, Thi14]. Also, see the recent preprint on the crossover between diffusion-limited and phase transition-limited regimes [HDJT22]. In this thesis we will synonymously refer to $\tilde{J}_{\text{evap}}$ as the evaporative flux for convenience, even though it is technically a rate of change. E_v characterizes the strength of evaporation. Furthermore, $\tilde{\mu}_g$ is assumed to be constant in time and space. This kind of evaporative flux can be well implemented in a variational formalism. The dynamic equations then read

$$\partial_t\begin{pmatrix}\tilde{\psi}_1\\\tilde{\psi}_2\end{pmatrix} = -\tilde{\nabla}\cdot\begin{pmatrix}\tilde{\mathbf{J}}_{1,c}\\\tilde{\mathbf{J}}_{2,c}\end{pmatrix} + \begin{pmatrix}\tilde{J}_{\text{evap}}\\\tilde{J}_{\text{source}}\end{pmatrix}$$

$$= \tilde{\nabla}\cdot\left[\left(\underline{\tilde{Q}}^{\text{diff}} + \underline{\tilde{Q}}^{\text{conv}}\right)\begin{pmatrix}\tilde{\nabla}\frac{\delta\tilde{\mathcal{F}}_{\text{bm}}}{\delta\tilde{\psi}_1}\\\tilde{\nabla}\frac{\delta\tilde{\mathcal{F}}_{\text{bm}}}{\delta\tilde{\psi}_2}\end{pmatrix}\right] + \begin{pmatrix}-E_v\left(\frac{\delta\tilde{\mathcal{F}}_{\text{bm}}}{\delta\tilde{\psi}_1} - \tilde{\mu}_g\right)\\\alpha\tilde{h}\partial_{\tilde{t}}\tilde{\phi}\end{pmatrix} \tag{2.104}$$

$$\partial_{\tilde{t}}\tilde{\phi} = -\frac{1}{\tau}\frac{\delta\tilde{\mathcal{F}}_{\text{xm}}}{\delta\tilde{\phi}} - \frac{\varepsilon^2}{\tau}\tilde{\kappa}|\tilde{\nabla}\tilde{\phi}| \tag{2.105}$$

$$\partial_{\tilde{t}}\tilde{\zeta} = -\alpha(\tilde{\psi}_1 + \tilde{\psi}_2)\partial_{\tilde{t}}\tilde{\phi} \tag{2.106}$$

In the diffusive phase-field models presented in Sec. 2.4, 2.4.3 $\partial_{\tilde{t}}\tilde{\phi}$ contributes as a non-conserved flux to the solute concentration, the expression needs to be adjusted according to $\tilde{\psi}_2 = \tilde{C}_2 \cdot \tilde{h}$ for the solute thickness analogue, properly relating amount of deposit with reduction in solute thickness. The reader will have realized that the second order source term is neglected, i.e., we consider the limit of instantaneous reaction rates or neglect interface kinetics.

Since for coating applications the profile of the deposit is of interest and the solute is extracted from the fluid upon deposition, a means of tallying up the amount of deposit is required by introducing the effective deposit thickness $\tilde{\zeta}$. Its dynamics do not follow that of the liquid anymore and simply corresponds to the sink to the source term, this likewise means that the equation is only coupled one way. Naturally, there is no restriction on introducing effects such as diffusion for the deposit in future model extensions. Further, we choose a slightly different local potential in $\tilde{\mathcal{F}}_{\mathrm{xm}}$:

$$f_{\mathrm{xm}}(\tilde{\phi}, \tilde{C}_2; \lambda) = f_1(\tilde{\phi}) + \lambda f_2(\tilde{\phi})(\tilde{C}_2 - C_{\mathrm{eq}}). \tag{2.107}$$

This is simply a parameter choice as the concentration factor can be normalized by C_{eq} or λ redefined. However, $\tilde{C}_i$ and C_{eq} are volume fractions, $|\tilde{C}_2 - C_{\mathrm{eq}}| \leq 1$, therefore, a normalization by C_{eq} does not seem necessary.

Due to the complexity of this system, we will not attempt a matched asymptotic analysis within the thin interface limit mentioned in Sec. 2.4. Therefore, parameters such as α or λ become phenomenological in nature. Thus, we aim for qualitative and order of magnitude agreement in obtained pattern scales. Then one may use the phenomenologic parameters for fitting purposes. At this point we emphasize the usage of separate functionals $\tilde{\mathcal{F}}_{\mathrm{bm}}$ and $\tilde{\mathcal{F}}_{\mathrm{xm}}$, meaning that to this date no total free energy functional is known for this system. Thus, not only is the dynamics non-conserved but it is also non-variational.

In order to reduce the number of parameters we proceed by non-dimensionalization and introducing effective parameters. Length, height, time and energy scales X, H, T and F with equilibrium height $\tilde{h}_{\mathrm{eq}}$ and contact angle $\tilde{\vartheta}_{\mathrm{eq}}$

$$X = \sqrt{\frac{3}{5}\frac{\tilde{h}_{\mathrm{eq}}}{\tilde{\vartheta}_{\mathrm{eq}}}}, \qquad H = \tilde{h}_{\mathrm{eq}}, \qquad T = \frac{9\eta\tilde{h}_{\mathrm{eq}}}{25\gamma\tilde{\vartheta}_{\mathrm{eq}}^4}\left(=\frac{X^4\eta}{H^3\gamma}\right), \tag{2.108}$$

$$F = \gamma\tilde{h}_{\mathrm{eq}}^2, \qquad \tilde{h}_{\mathrm{eq}} = \left(\frac{B}{A}\right)^{\frac{1}{3}}, \qquad \theta_{\mathrm{eq}} = \sqrt{\frac{-2\tilde{f}(\tilde{h}_{\mathrm{eq}})}{\gamma}} = \sqrt{\frac{3}{5}\frac{A}{\gamma}\frac{1}{\tilde{h}_{\mathrm{eq}}}}, \tag{2.109}$$

are introduced leading to the non-dimensional equations

$$\partial_t\psi_1 = -\nabla\cdot\left\{\frac{1}{3}\psi_1 h^2\nabla\left[\Delta h - f'(h)\right] - \mathrm{Pe}^{-1}h\left(1 - 2\chi C_1 C_2\right)\nabla C_1\right\}$$
$$- \Omega\left[-\Delta h + f'(h) + \Upsilon\left(\ln(C_1) - 1 + \chi C_2^2\right) - \mu\right], \tag{2.110}$$

$$\partial_t\psi_2 = -\nabla\cdot\left\{\frac{1}{3}\psi_2 h^2\nabla\left[\Delta h - f'(h)\right] - \mathrm{Pe}^{-1}h\left(1 - 2\chi C_1 C_2\right)\nabla C_2\right\} + \alpha h\partial_t\phi, \tag{2.111}$$

$$\partial_t\phi = \sigma\left(\Lambda^{-2}\Delta\phi - \partial_\phi f_{\mathrm{xm}}\left(\phi, C_2 - C_{\mathrm{eq}}; \lambda\right) - \Lambda^{-2}\kappa|\nabla\phi|\right), \tag{2.112}$$

$$\partial_t\zeta = -\alpha h\partial_t\phi, \tag{2.113}$$

with wetting potential $f(h)$ and precursor height h_p

$$f(h) = -\frac{1}{2h^2} + \frac{1}{5h^5}, \qquad h_p = 1. \tag{2.114}$$

Specifically, the effective parameters are

$$\mathrm{Pe}^{-1} = \frac{\eta}{h_{\mathrm{eq}}^2 n_{\max}\hat{\zeta}} \Upsilon = \frac{3}{5}\frac{k_B\hat{T}\eta}{\hat{\zeta}h_{\mathrm{eq}}\theta_{\mathrm{eq}}^2\gamma}, \tag{2.115}$$

$$\Omega = \frac{3}{5}\frac{\eta}{h_{\mathrm{eq}}\theta_{\mathrm{eq}}^2}E_v, \tag{2.116}$$

$$\Upsilon = \frac{3}{5}n_{\max}k_B\hat{T}\frac{h_{\mathrm{eq}}}{\gamma\theta_{\mathrm{eq}}^2}, \tag{2.117}$$

$$\mu = \frac{3}{5}\frac{h_{\mathrm{eq}}}{\gamma\theta_{\mathrm{eq}}^2}\mu_g, \tag{2.118}$$

$$\sigma = \frac{9\eta h_{\mathrm{eq}}}{25\gamma\theta_{\mathrm{eq}}^4\tau}, \tag{2.119}$$

$$\Lambda = \sqrt{\frac{3}{5}\frac{h_{\mathrm{eq}}}{\theta_{\mathrm{eq}}\varepsilon}}. \tag{2.120}$$

The inverse Peclét number Pe^{-1} relates convective and diffusive time scales, Ω convective and evaporative time scales, Υ is a ratio between thermal and surface energy density, μ a non-dimensional chemical potential (pressure), σ is a time scale ratio between convection and particle mobility, while finally Λ relates length scale of dewetting and the solutal interface. Details can be found in appendix Sec. A.4.

2.5.2. Generalization to the Dip-coating Geometry

In a dip-coating geometry the substrate is inclined which requires consideration of gravitational effects. Writing Eq. (2.110)-(2.113) in their flux form and supplementing gravitational terms, the modified equations read

$$\partial_t \begin{pmatrix} \psi_1 \\ \psi_2 \end{pmatrix} = -\nabla \cdot \begin{pmatrix} \mathbf{J}_{1,c} \\ \mathbf{J}_{2,c} \end{pmatrix} + \begin{pmatrix} J_{\mathrm{evap}} \\ J_{\mathrm{source}} \end{pmatrix}$$
$$= \nabla \cdot \left[\left(\underline{Q}^{\mathrm{diff}} + \underline{Q}^{\mathrm{conv}}\right) \begin{pmatrix} \nabla\frac{\delta\mathcal{F}}{\delta\psi_1} \\ \nabla\frac{\delta\mathcal{F}}{\delta\psi_2} \end{pmatrix} \right] + \begin{pmatrix} -\Omega\left(\frac{\delta\mathcal{F}_{\mathrm{bm}}}{\delta\psi_1} - \mu\right) \\ \alpha h(\partial_t\phi) \end{pmatrix}, \tag{2.121}$$

$$\partial_t\phi = -\sigma\frac{\delta\mathcal{F}_{\mathrm{xm}}}{\delta\phi} - \frac{\sigma}{\Lambda^{-2}}\kappa|\nabla\phi|, \tag{2.122}$$

$$\partial_t\zeta = -\alpha h\partial_t\phi, \tag{2.123}$$

with functionals

$$\mathcal{F} = \mathcal{F}_{\mathrm{bm}} + \mathcal{F}_g$$
$$= \int_\Omega \left\{ \frac{1}{2}h^2 + f(h) + \frac{1}{2}gh^2 + gh\beta x + \Upsilon\left[\psi_1\ln(C_1) + \psi_2\ln(C_2) - h + \chi\frac{\psi_1\psi_2}{h}\right]\right\}\mathrm{d}^2\mathbf{x} \tag{2.124}$$

$$\mathcal{F}_{\mathrm{xm}} = \int_{\Omega} \left(\frac{1}{2} \Lambda^{-2} (\nabla \phi)^2 + f_{\mathrm{xm}} \right) \mathrm{d}^2 \mathbf{x}. \tag{2.125}$$

The contribution $\mathcal{F}_g$ accounts for hydrostatic pressure and, if the substrate is inclined, the potential energy depending on inclination β and effective gravitational acceleration g. Note the change from $\mathcal{F}_{\mathrm{bm}}$ to $\mathcal{F}$ in the conserved fluxes $\mathbf{J}_{i,c}$ and the unchanged $\mathcal{F}_{\mathrm{bm}}$ in the evaporative flux. This is due to the fact that gravity is required to model inclined substrates but numerically reasonable g are exaggerated in comparison to reality. The gravitational contribution to the evaporative flux is therefore neglected. Up to here, the equations describe the dynamics for a resting substrate. In a dip-coating geometry the substrate moves with constant dragging velocity $\mathbf{v} = (v, 0)$. Since the interesting dynamics occur in the vicinity of the solution bath, it is imperative to introduce advection terms in order to stay in the laboratory frame. Above equations then become

$$\partial_t \psi_1 = -\nabla \cdot \left\{ \frac{1}{3} \psi_1 h^2 \nabla \left[\Delta h - f'(h) - g(h + \beta x) \right] + \mathbf{v} \psi_1 - \mathrm{Pe}^{-1} h \left(1 - 2\chi C_1 C_2 \right) \nabla C_1 \right\}$$
$$- \Omega \left[-\Delta h + f'(h) + \Upsilon \left(\ln(C_1) - 1 + \chi C_2^2 \right) - \mu \right], \tag{2.126}$$

$$\partial_t \psi_2 = -\nabla \cdot \left\{ \frac{1}{3} \psi_2 h^2 \nabla \left[\Delta h - f'(h) - g(h + \beta x) \right] + \mathbf{v} \psi_2 - \mathrm{Pe}^{-1} h \left(1 - 2\chi C_1 C_2 \right) \nabla C_2 \right\}$$
$$+ \alpha h (\partial_t \phi + \mathbf{v} \cdot \nabla \phi), \tag{2.127}$$

$$\partial_t \phi = \sigma \left(\Lambda^{-2} \Delta \phi - \partial_\phi f_{\mathrm{xm}} \left(\phi, C_2 - C_{\mathrm{eq}}; \lambda \right) - \Lambda^{-2} \kappa |\nabla \phi| \right) - \mathbf{v} \cdot \nabla \phi, \tag{2.128}$$

$$\partial_t \zeta = -\alpha h (\partial_t \phi + \mathbf{v} \cdot \nabla \phi) - \mathbf{v} \cdot \nabla \zeta. \tag{2.129}$$

The additional effective parameters read

$$g = \frac{\tilde{\rho} X^2}{\gamma} \tilde{g} = \frac{3}{5} \frac{\tilde{\rho} \tilde{h}_{\mathrm{eq}}^2}{\gamma \tilde{\vartheta}_{\mathrm{eq}}^2} \tilde{g}, \tag{2.130}$$

$$\beta = \frac{X}{H} \tilde{\beta} = \sqrt{\frac{3}{5}} \frac{1}{\tilde{\vartheta}_{\mathrm{eq}}} \tilde{\beta}. \tag{2.131}$$

$\tilde{\rho}$ is the constant mass density of the fluid, $\tilde{g}$ the gravitational acceleration and $\tilde{\beta}$ the small inclination angle. See appendix Sec. A.4.5-A.4.6 for details. Note, how Eq. (2.129) can be substituted into Eq. (2.127), thereby formally eliminating the dependence of $\partial_t \psi_2$ on ϕ, emphasizing the nature of the phase-field as a mathematical tool. In the stationary case this substitution would allow a reduction of the governing equations to two fields if one were to make assumptions about the ζ profile.

2.5.3. Boundary Conditions

For calculations on a resting horizontal substrate we implement either periodic or Neumann boundary conditions. For the dip-coating calculations the following boundary conditions are implemented

$$\psi_i = C_{i,0} h_0, \qquad \partial_x \psi_i = -C_{i,0} \beta, \qquad \phi = \phi_0, \qquad\qquad \text{at} \quad x = 0; \quad i = 1, 2 \tag{2.132}$$

$$\partial_x \psi_i = 0, \qquad \partial_{xxx} \psi_i = 0, \qquad \partial_x \phi = 0, \qquad \partial_x \zeta = 0 \quad \text{at} \quad x = L_x \tag{2.133}$$

with

$$C_{1,0} = C_1(x = 0, t = 0) = 1 - C_2(x = 0, t = 0) = 1 - C_{2,0}. \tag{2.134}$$

The liquid bath has some homogeneous solvent or solute concentration $C_{i,0}$ and the corresponding Dirichlet boundary conditions for the effective layer thicknesses are easily formulated. The condition for the slope can be adopted from the case of a simple liquid. There,

$$\partial_x h(x = 0) = -\beta. \tag{2.135}$$

It can be shown that the individual slopes are distributed very similarly

$$\partial_x \psi_i = \partial_x (C_i h) = h \partial_x C_i + C_i \partial_x h,$$
$$\xrightarrow{x=0} \partial_x \psi_i(x = 0) = h \underbrace{\partial_x C_i(x = 0)}_{0} + C_i \partial_x h(x = 0),$$
$$= -C_i \beta.$$

In this thesis "concentration" refers to solute concentration if not stated otherwise, shortening the notation to $C_2 = C$ and $C_{2,0} = C_0$. In the 2D case periodic boundaries are applied in the lateral direction y. Further, Eq. (2.126)-(2.129) and above boundary conditions are called the *full model*.

2.5.4. Initial Conditions

Throughout Chapter 4 a couple of different initial conditions are utilized for direct numerical simulations. For the dip-coating geometries a meniscus, i.e., hyperbolic tangent, is exclusively used for the liquid, i.e.,

$$h(x, y, 0) = h_0 - (h_0 - h_p) \tanh\left(\beta \frac{x}{h_0 - h_p}\right) \tag{2.136}$$

with $h_0 = 20$, $h_p = 1$ if not stated otherwise. If the liquid is a mixture, the effective thicknesses are determined from a homogeneous concentration distribution

$$\psi_i(x, y, 0) = C_{i,0} h(x, y, 0). \tag{2.137}$$

For the full model the phase-field is initialized in the liquid phase as

$$\phi(x, y, 0) = 0.99 + \text{ white noise} \tag{2.138}$$

and the effective deposit thickness as

$$\zeta(x, y, 0) = 0. \tag{2.139}$$

Sessile droplets are mostly initialized by a parabolically shaped cap of radius R of the form

$$h(x, y, 0) = \begin{cases} -\frac{\vartheta_{\text{eq}}^2}{4(h_0 - h_p)} r^2 + h_0 & \text{for } r \leq R \\ h_p & \text{else,} \end{cases} \tag{2.140}$$

$$R = \frac{2(h_0 - h_p)}{\vartheta_{\text{eq}}} \tag{2.141}$$

with maximum droplet height h_0 and short hand notation

$$r = \sqrt{\left(x - \frac{L_x}{2}\right)^2 + \left(y - \frac{L_y}{2}\right)^2}.$$ (2.142)

The contact angle is approximated by the equilibrium contact angle for an infinite droplet

$$\vartheta_{\text{eq}} = \sqrt{-2f(h_p)}.$$ (2.143)

See appendix Sec. A.6 for a derivation. If not stated otherwise the following values hold: $h_0 = 20$ and $C_0 = 0.3$.

The presented model is investigated in Chapter 4 mostly by means of direct numerical simulations (DNS). After evaluating the numerical scheme in Sec. 4.1-4.3 and giving an example of a full model simulation 4.4, the focus lies in submodels, where gravity, substrate advection, deposition or convection are turned off 4.3-4.7. Therein, the main portion of the analysis concerns a volatile sessile droplet on a flat 1D substrate, i.e., $\alpha = g = 0$. Finally, the full model is analyzed for 1D and exemplary for a 2D substrate in Sec. 4.8.

2.6. Liquid Covered by Insoluble Layer of Surfactants

Previously, we presented descriptions for mixtures consisting of a solute and solvent. The former being dissolved in the latter or deposited on the substrate without further interactions. With the presented additions the model describes the dynamics of a dip-coating process. Another coating process is the so-called *Langmuir-Blodgett transfer* (LB transfer). This technique utilizes a different type of complex fluid comprised of molecules active on the surface of a liquid, so-called *surfactants*. We briefly present the model describing the Langmuir-Blodgett transfer developed and used in [KGF09, KGFC10, KGF11, KGFT12]. This set of dynamic equations was derived hydrodynamically by Köpf et al. employing NSE, lubrication approximation and an advection-diffusion equation for the surfactant dynamics[KGF09, KGFC10]. Here, we present the model in its gradient dynamics form to emphasize its thermodynamic consistency as well as the generality of Eq. (2.44) [TAP12, TAP16]. The free energy functional

$$\tilde{\mathcal{F}}[\tilde{h}, \tilde{\Gamma}_p] = \int_{\Omega} \left\{ \tilde{f}(\tilde{h}) + \tilde{f}_{\text{surf}}\left(\frac{\tilde{\Gamma}_p}{\xi}, \tilde{h}\right)\xi + \frac{\kappa_{\text{surf}}}{2}\left(\tilde{\nabla}\frac{\tilde{\Gamma}_p}{\xi}\right)^2 \frac{1}{\xi} \right\} \mathrm{d}^2\tilde{\mathbf{x}}$$ (2.144)

depends on the film height $\tilde{h}$ and projected surfactant concentration $\tilde{\Gamma}_p$ with wetting energy $\tilde{f}(\tilde{h})$, local free energy of the surfactants and an associated gradient energy term with constant κ_{surf} [TAP12, WTGK+15]. $\tilde{\Gamma}_p$ is a projection of the surfactant concentration $\tilde{\Gamma}$ onto the plane of the substrate since a local change in $\tilde{\nabla}\tilde{h}$ alters the liquid surface and thus changes $\tilde{\Gamma}$ "without any surfactant transport"

$$\tilde{\Gamma}_p = \xi\tilde{\Gamma}, \qquad \xi = \sqrt{1 + |\tilde{\nabla}\tilde{h}|^2} \approx 1 + \frac{1}{2}|\tilde{\nabla}\tilde{h}|^2.$$ (2.145)

The variation is therefore applied with respect to $\tilde{\Gamma}_p$ and not to $\tilde{\Gamma}$ in order to ensure independence of the order parameter fields during variation. The local free energy of the surfactants

$$f_{\text{surf}}(\tilde{\Gamma}, \tilde{h}) = \sum_{i=0}^{4} F_i(\tilde{\Gamma} - \tilde{\Gamma}_{\text{cr}})^i + \tilde{\lambda}_{\text{SMC}}\tilde{f}(\tilde{h})(\tilde{\Gamma} - \tilde{\Gamma}_{\text{cr}})$$ (2.146)

consists of a fourth order polynomial in $\tilde{\Gamma} - \tilde{\Gamma}_{\mathrm{cr}}$, representing a double-well potential for first order phase transitions and a term that models the so-called *substrate-mediated condensation* with constants F_i and $\tilde{\lambda}_{\mathrm{SMC}}$, respectively [SR91, RS92]. $\tilde{\Gamma}_{\mathrm{cr}}$ is the critical surfactant concentration. The SMC-term describes substrate-monolayer interactions and can be chosen to be modeled with the wetting energy, tilting the double-well potential towards the condensed phase for $\tilde{h} \to \tilde{h}_p$. Further, this choice means that such a phase transition occurs on length scales similar to the substrate-liquid interaction [KGFC10]. Applying Eq. (2.144)-(2.146), the mobility matrix

$$\underline{\tilde{Q}} = \begin{pmatrix} \frac{\tilde{h}^3}{3\eta} & \frac{\tilde{h}^2 \tilde{\Gamma}}{2\eta} \\ \frac{\tilde{h}^2 \tilde{\Gamma}}{2\eta} & \frac{\tilde{h}\tilde{\Gamma}^2}{\eta} + D_{\mathrm{surf}}\tilde{\Gamma} \end{pmatrix} \tag{2.147}$$

with dynamic viscosity η and molecular mobility D_{surf}, an evaporation term analogous to the one presented in Sec. 2.5.1

$$\tilde{J}_{\mathrm{evap}} = -E_v \left(\tilde{\mu}_l - \tilde{\mu}_g \right), \tag{2.148}$$

$$\tilde{\mu}_l = \frac{\delta \tilde{\mathcal{F}}}{\delta \tilde{h}}, \tag{2.149}$$

and substrate advection to Eq. (2.44) gives the dynamic equations of the system

$$\partial_{\tilde{t}} \tilde{h} = -\tilde{\nabla} \cdot \left\{ \frac{\tilde{h}^3}{3\eta} \tilde{\nabla} \left[\tilde{\nabla} \cdot (\tilde{\gamma} \tilde{\nabla} \tilde{h}) - \tilde{f}'(\tilde{h}) \right] + \frac{\tilde{h}^2}{2\eta} \tilde{\nabla} \tilde{\gamma} + \tilde{\mathbf{v}} \tilde{h} \right\} + \tilde{J}_{\mathrm{evap}}, \tag{2.150}$$

$$\partial_{\tilde{t}} \tilde{\Gamma} = -\tilde{\nabla} \cdot \left\{ \frac{\tilde{h}^2 \tilde{\Gamma}}{2\eta} \tilde{\nabla} \left[\tilde{\nabla} \cdot \left(\tilde{\gamma} \tilde{\nabla} \tilde{h} \right) - \tilde{f}'(\tilde{h}) \right] + \left(\frac{\tilde{h}\tilde{\Gamma}}{\eta} + D_{\mathrm{surf}} \right) \tilde{\nabla} \tilde{\gamma} + \tilde{\mathbf{v}} \tilde{\Gamma} \right\} \tag{2.151}$$

where the order parameter field for the surfactant concentration remains to be $\tilde{\Gamma}$. Both equations possess a convective term with forms very similar to Eq. (2.57)-(2.58) with two main differences: One, the mobilities are not symmetric, two, the (generalized) surface tension

$$\tilde{\gamma} = \tilde{f}_{\mathrm{surf}} - \tilde{\Gamma} \partial_{\tilde{\Gamma}} \tilde{f}_{\mathrm{surf}} - \frac{\kappa_{\mathrm{surf}}}{2} \left(\tilde{\nabla} \tilde{\Gamma} \right)^2 + \kappa_{\mathrm{surf}} \tilde{\Gamma} \tilde{\Delta} \tilde{\Gamma} \tag{2.152}$$

is not constant, leading to additional contributions such as the *Marangoni convection* $\frac{h^2}{2\eta} \tilde{\nabla} \tilde{\gamma}$. See [TAP12] for details on the derivation, including approximations that are not mentioned here.

2.6.1. Generalized Cahn-Hilliard Model for the Langmuir-Blodgett Transfer

Direct numerical simulations show that after an initial transient the meniscus remains almost static while $\tilde{\Gamma}$ forms a variety of patterns. Even artificially freezing the former, i.e., setting $\partial_{\tilde{t}} \tilde{h} = 0$ does not impede this process [KGFC10, KGF11, KGFT12, Köp11]. This indicates that the $\tilde{h}$ dependence of the SMC-term and thus the meniscus shape of $\tilde{h}$ can be translated to a spatially dependend external field in the free energy. Further, both $\tilde{h}$ and $\tilde{\Gamma}$ equations share the same generalized pressure terms. These are minimal after said transient and are thus less important for the surfactant pattern formation. Overall it is possible to reduce this system to a Cahn-Hilliard type equation in order to focus on a minimal description of the pattern forming mechanisms [KGFT12]. The dynamic equation for the surfactant concentration c then reads

$$\partial_t c = \nabla \cdot \left(M(c) \nabla \frac{\delta \mathcal{F}}{\delta c} + \mathbf{v} c \right), \tag{2.153}$$

$$\mathcal{F}[c] = \int_\Omega \frac{1}{2}|\nabla c|^2 + f(c)\mathrm{d}^2\mathbf{x}, \tag{2.154}$$

$$f(c) = \frac{c^4}{4} - \frac{c^2}{2} + \lambda_{\mathrm{SMC}}\zeta_{\mathrm{SMC}}(\mathbf{x})c, \tag{2.155}$$

$$M(c) = 1. \tag{2.156}$$

with free energy $\mathcal{F}[c]$ consisting of a gradient energy term and the local potential takes the form of a double-well tilted by an external field $\zeta_{\mathrm{SMC}}(\mathbf{x})$ with strength λ_{SMC}, modeling the substrate-mediated condensation. The model has been extensively analyzed by means of path continuation in [KT14]. Here, the simplest mobility $M(c) = 1$ is chosen. Notice that similar to the phase-field equation in Sec. 2.4.3-2.5.2 the local minima of the double-well potential are again at $c = \pm 1$ and the tilt is coupled linearly in the concentration. However, unlike before, the condensed phase is denoted by $c > 0$ and the expanded by $c < 0$. The form of $\zeta_{\mathrm{SMC}}(\mathbf{x})$ can be motivated by the shape of $\tilde{h}$ in the hydrodynamic model after the transient. A meniscus possesses large film heights as the liquid bath is approached, thus the wetting energy is negligible there. $\tilde{f}(\tilde{h})$ then rapidly increases as the meniscus transitions in space to the flat precursor and stays constant at $\tilde{f}(\tilde{h}_p)$. Thus, a step-like function is reasonable for ζ_{SMC}. Here, we choose a hyperbolic tangent

$$\zeta_{\mathrm{SMC}}(\mathbf{x}) = -\frac{1}{2}\left[1 + \tanh\left(\frac{x - x_s}{l_s}\right)\right] \tag{2.157}$$

with meniscus position x_s and width of the transition region l_s. The dynamic equation then reads

$$\partial_t c = \Delta\left[-\Delta c - c + c^3 + \lambda_{\mathrm{SMC}}\zeta_{\mathrm{SMC}}(\mathbf{x}) - \mathbf{v}c\right], \qquad \mathbf{v} = (v, 0)^T. \tag{2.158}$$

Since material is provided from a bath exactly like in the dip-coating model a Dirichlet boundary condition is imposed on the left side of the domain

$$c = c_0, \qquad \partial_{xx}c = 0, \qquad \text{at } x = 0, \tag{2.159}$$

$$\partial_x c = 0, \qquad \partial_{xxx}c = 0, \qquad \text{at } x = L_x. \tag{2.160}$$

Since gravity is not modeled here, no inclination needs to be imposed either. Instead, the curvature is set to vanish and the right boundary behaves non-reflecting. Periodic or Non-reflecting conditions are imposed in the y-direction depending on the scenario. Note, that for large domain sizes the particular set of conditions far from the bath are not strict since boundary effects are negligible then. The works cited above employ vanishing first and second derivatives

$$c = c_0, \qquad \partial_{xx}c = 0, \qquad \text{at } x = 0, \tag{2.161}$$

$$\partial_x c = 0, \qquad \partial_{xx}c = 0, \qquad \text{at } x = L_x. \tag{2.162}$$

First steps towards a mathematical analysis of models of this form by proving existence, uniqueness of solutions, continuous dependence on initial data and showing the existence of a global attractor for small advection velocities are made in [BDM19]. If not stated otherwise, the initial condition

$$c(\mathbf{x}, t = 0) = c_0 + \frac{1}{2}\left(1 + \tanh(x - x_s)\right)\left(1 - c_0\right) \tag{2.163}$$

with or without white noise is employed in calculations concerning this model.

In Chapter 5 we extend existing research by putting emphasis on transversal instabilities in 2D geometries and time-periodic forcing. The analysis is performed by means of numerical path continuation and DNS. The numerical schemes for all calculations are presented in the next Chapter 3.

3. Numerical Methods

Analytically solving nonlinear PDEs is often difficult or impossible without approximations. In this chapter numerical methods utilized in this thesis for solving PDEs are presented. For more mathematically rigorous derivations we refer to the cited literature below. In Sec. 3.1 and 3.2 spatial discretization methods are presented. Time integration schemes are not outlined and only named since the basic principles are the same as for spatial discretization and information is readily available in the literature.

3.1. Finite Difference Method

Numerically solving PDEs of the form

$$\partial_t \mathbf{u} = \mathbf{R}\left[t, \mathbf{u}, \nabla \mathbf{u}, ...\right] \tag{3.1}$$

requires discretizing the occuring operators, in particular the derivatives since they involve infinitesimal quantities. The Finite Difference Method (FDM) is a very intuitive way of discretizing derivatives. A one dimensional (spatial) first derivative of some component u at position x is defined as the limit

$$u'(x) = \lim_{x \to 0} \frac{u(x + \Delta x) - u(x)}{\Delta x}. \tag{3.2}$$

For a multi-component variable $\mathbf{u}$ the derivative is simply the vector of each component's derivative. Since space cannot be sampled down to infinitesimal distances, one settles for finite Δx. Thus, the domain is described by a grid. In this section, we focus on rectangular (a line in 1D) grids of uniform spacing $\Delta x = \frac{L}{N} = const.$, with domain size L and number of grid points N. The idea of FDM is to approximate the exact derivative $u'(x)$ by only function values $u(x)$ at local grid points surrounding x

$$u'_{\text{FDM}}(x) = \sum_i a_i u(x_i) =: \sum_i a_i u_i. \tag{3.3}$$

x_i can be exactly at the center x, nearest neighbors $x \pm \Delta x$, next neigherst neighbors $x \pm 2\Delta x$, etc. $u'(x)$ is related to the FDM approximation by

$$u'(x) = u'_{\text{FDM}}(x) + \mathcal{O}(\Delta x^p) \tag{3.4}$$

since the approximation approaches the exact function for $\Delta x \to 0$, with p being the order of FDM approximation. This becomes clearer when Taylor expanding u_i for small Δx around x as

$$u(x + \Delta x_i) = u(x) \pm u'(x)(\Delta x_i) + \frac{1}{2}u''(x)(\Delta x_i)^2 + \mathcal{O}(\Delta x_i^3), \qquad i = 0, 1, ..., n-1 \tag{3.5}$$

with

$$\Delta x_i \in \{\pm \Delta x, \pm 2\Delta x, ...\} \tag{3.6}$$

depending on the stencil choice. Inserting Eq. (3.5) into (3.4) gives an equation with n unknown coefficients a_i and m derivatives of u. For a second order approximation of $u'(x)$ with a symmetric stencil of size $n = 3$ the equation reads

$$
\begin{aligned}
u'_{\text{FDM}}(x) =& a_0 u(x) + a_1 \left[u(x) + u'(x)\Delta x + \frac{u''(x)}{2}(\Delta x)^2 + \mathcal{O}(\Delta x^3) \right] \\
&+ a_2 \left[u(x) - u'(x)\Delta x + \frac{u''(x)}{2}(\Delta x)^2 + \mathcal{O}(\Delta x^3) \right] \\
=& u(x)\,(a_0 + a_1 + a_2) + u'(x)\Delta x\,(a_1 - a_2) + \frac{u''(x)}{2}(\Delta x)^2\,(a_1 + a_2) + \mathcal{O}(\Delta x^3)
\end{aligned} \tag{3.7}
$$

This expression can be rearranged to

$$u'(x)\Delta x(a_1 - a_2) = u'_{\text{FDM}}(x) - u(x)\,(a_0 + a_1 + a_2) - \frac{u''(x)}{2}(\Delta x)^2(a_1 + a_2) + \mathcal{O}(\Delta x^3). \tag{3.8}$$

Each coefficient represents one degree of freedom for which extra conditions can be imposed. We demand that the FDM approximation equals the exact derivative except for a truncation error of $\mathcal{O}(\Delta x^2)$:

$$\Delta x(a_1 - a_2) = 1 \qquad\qquad a_0 + a_1 + a_2 = 0 \qquad\qquad a_1 + a_2 = 0 \tag{3.9}$$

or in other words: Terms not containing $u'(x)$ are to vanish since the exact derivatives cannot be evaluated. Solving this system of equations results in

$$a_0[x] = 0 \qquad\qquad a_1[x - \Delta x] = -\frac{1}{2\Delta x} \qquad\qquad a_2[x + \Delta x] = \frac{1}{2\Delta x}. \tag{3.10}$$

Note that the grid discretization Δx is often omitted when listing stencil coefficients since the power of Δx equals the differentiation order. Although Eq. (3.7) is written like the error between approximation and analytical is of order Δx^3 one needs to take into account that all orders of differentiation are multiplied by the coefficients a_i. Since $a_i \sim \frac{1}{\Delta x}$ here, the actual truncation error is of order Δx^2. Thus, above approximation is a so-called centered second order FDM approximation, centered because the stencil consists of the grid point at x and its nearest neighbors symmetrically. In that sense Eq. (3.2) without the limit would be considered a first order forward FDM approximation. After discretization one is left with a system of ordinary differential equations (ODE) to be solved by a time integration scheme.

The presented scheme can be extended to higher differentiation orders and spatial dimensions. While the lower orders are trivial, it becomes less so at higher ones, especially in 2D. The stencil determines the degrees of freedom and in conjunction with the desired accuracy the order of the Taylor expansion. For example a 4th order approximation of $\frac{\partial^2 u}{\partial x \partial y}(x, y)$ would naively require Taylor expansion to 5th order if one were to neglect all 6th order terms as truncation error. However, this results in an underdetermined system of equations. It turns out that part of the 6th order terms are required to close the system, i.e., the $\frac{\partial^6 u}{\partial x^3 \partial y^3}$ term has to be taken into account as well. This effectively does not change the order of the truncation error, however, the scheme could be considered to be a slightly better than 4th order approximation. Some of the stencils, in particular ones that are found rarer in literature, are listed in the appendix A.15. The

self-derived stencils utilizing a Mathematica script [Wol22] are verified with [Szi04] if listed (note that by definition of the 1D stencils some 2D stencils have sign errors in the book).

Since the computational domain is finite, boundaries need to be treated as well. Typically, so-called *ghost points* are utilized which extend the grid by additional nodes. These affect the derivatives of nodes close to the boundaries as stencils possess a certain "range", cf. Fig. 3.1 (a). In this thesis the "grid" is always meant without the ghost points. The function value at a ghost point is determined from the analytical boundary conditions and possibly values next to the boundary. Take for example the generalized Cahn-Hilliard model for LB-Transfer in Sec. 2.6.1. We employ second order FDM stencils for the spatial operators. The highest order derivative, which is the biharmonic operator Δ^2, is then a centered stencil of "radius 2", meaning that it extends up to the next-nearest neighbors. Therefore, two ghost points are required at each side of the rectangular domain, if one intends to use centered stencils for each grid point. For the ghost points on the bath side the Dirichlet BC is simply implemented by imposing

$$c_{-1} = c(x = -\Delta x) = \hat{c}. \tag{3.11}$$

Since indices are reserved for the discrete grid points, we denote the value of the Dirichlet BC by $\hat{c}$ instead of c_0 as previously. For the Neumann BC we impose

$$\partial_{xx} c_{-1} = \partial_{xx} c(x = -\Delta x) = 0 \tag{3.12}$$

insert the FDM approximation for the derivative and solve for the value at the second ghost point

$$c_{-2} = c(x = -2\Delta x) = 2c_{-1} - c_0 = 2\hat{c} - c_0. \tag{3.13}$$

Notice that technically the boundary conditions are imposed on $x = -\Delta x$. The derivation of other numerical boundary conditions is executed similarly. The Neumann BC of the opposing side results in a system of two equations with two unknowns to be solved. Periodic BC implementation is trivial. In order to have vanishing odd derivatives at a boundary, i.e., non-reflecting, the function values at a boundary can be mirrored, here at $y = 0$ for example,

$$c_{i,-j} = c_j \tag{3.14}$$

with j being the ghost point counter. Since centered stencils of odd derivatives themselves possess opposing signs on opposite sites, see Eq. (3.10), these derivates will then vanish. With this the system possesses sufficient points to allow computation of derivatives in the full grid.

We have shown that each analytical BC can reduce the number of unknowns (ghost points) by one. However, higher order approximations have larger stencils, e.g., the biharmonic operator in fourth order has a radius of three. Since changing the analytical problem for the sake of a numerical scheme is usually not a good approach, we do not consider adding more boundary conditions. Instead, one can resort to so-called "non-centered" stencils. Classically, students are taught about forward and backward differencing where stencils only extend to one direction. These however would not incorporate the ghost points and thus boundary conditions if utilized at the boundaries of the grid. As a compromise one can derive stencils that for example reach further into the bulk but extend at most to two points outside the boundaries, see Fig. 3.1 (b). The scheme presented above is naturally capable of that. Note that using non-centered stencils at the boundaries makes implementation of non-reflecting BC not as simple as in Eq. 3.14. A system of equations such as in Eq. (3.12)-(3.13) has to be solved for the ghost points then.

When deciding on the grid discretization and FDM order, a balance must be struck. The finer

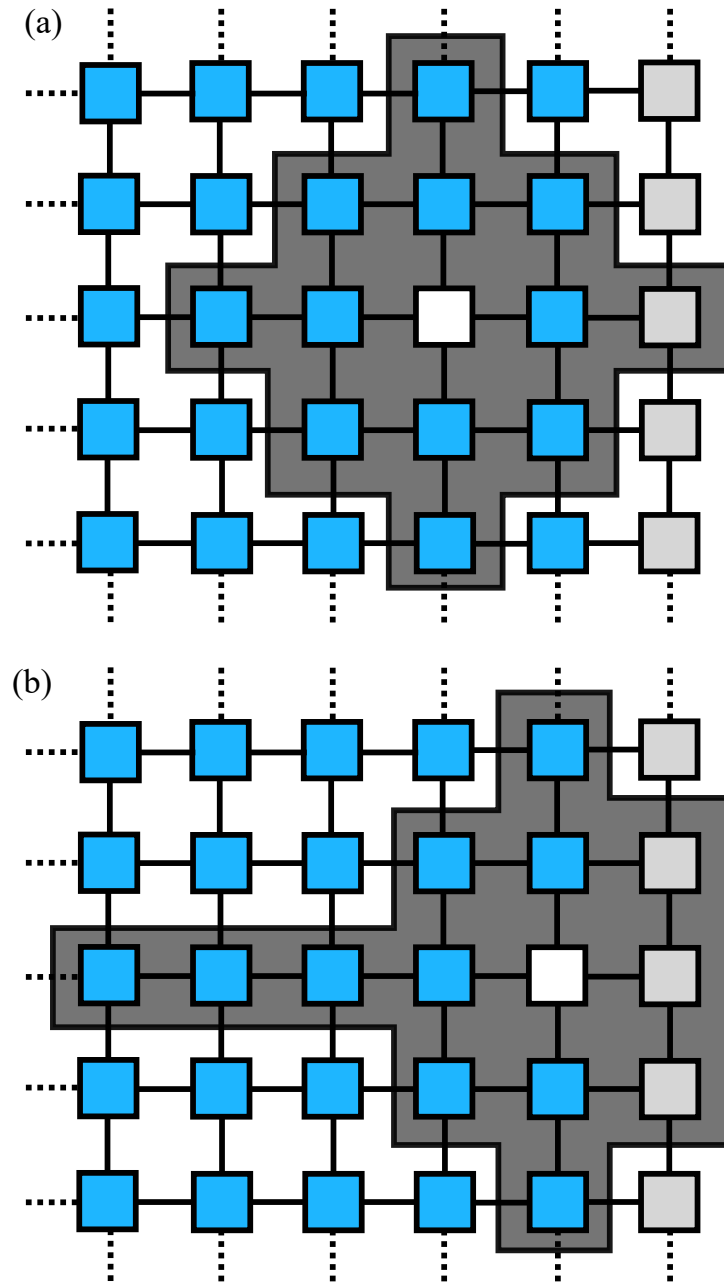Figure 3.1.: Sketches of the boundary of a uniform grid. (a) Evaluation of a two-dimensional derivative at a node (white) within the grid. The ends of the unspecified stencil (dark gray) extend past the boundary, requiring the usage of ghost points (light gray). (b) Evaluation of a two-dimensional derivative even closer to the boundary. Since only one ghost point is utilized a non-centered stencil is applied.

the grid the more closely the sampled data points are arranged both in space and in nodal value. This may lead to loss of significance in for example difference operations, also known as *catastrophic cancellation*, i.e., when two numbers of similar value are subtracted from each other. Thus, the smallest Δx is limited by machine precision. Low ordered approximations possess relatively large truncation errors and may be unfit for the problem from the very start. The error naturally becomes smaller for higher order stencils, however, they possess relatively large coefficients, especially non-centered ones, which furthers loss of significance. Interfaces are prone to instabilities due to large variations of the order parameter and its derivatives. Nonlinearities can increase numerical instability as well. Therefore, truncation errors can be alleviated by higher order stencils , however, loss of significance, needs to be taken into account possibly by improving machine precision (floating point representation). For more details on FDM, especially on convergence, consistency and stability, see [Tho95, LeV07]. Besides going to higher FDM orders, more sophisticated methods that utilize smaller stencils but require more involved derivations for the coefficients exist. They are so-called *essentially non-oscillatory* (ENO) or weighted essentially non-oscillatory (WENO) schemes and can be applied to both FDM and Finite Volume Methods for conserved equations[SO88, ZS16].

3.2. Finite Element Method

Another method of discretization is the *Finite Element Method* (FEM) [Šol05]. In this section, we first present the method for the case of a stationary second order PDE, i.e., Laplace equation, and then extend the scheme to time-dependent problems. The scheme can be adopted for higher order PDEs by defining auxiliary fields. Instead of the strong form used in the previous section, the PDE is solved in its weak form

$$r := \int_\Omega \mathrm{R}[u, \nabla u, \Delta u] \phi_{\text{test}}(\mathbf{x}) \, \mathrm{d}\mathbf{x} \tag{3.15}$$

$$= \int_\Omega \left[\Delta u + f(\mathbf{x}) \right] \phi_{\text{test}}(\mathbf{x}) \, \mathrm{d}\mathbf{x} = 0 \tag{3.16}$$

with weighted residual r. Here, we consider the simple homogeneous boundary condition

$$u = 0 \qquad \qquad \text{on } \partial\Omega. \tag{3.17}$$

We look for solutions that satisfy Eq. (3.16)-(3.17) for any *test function* $\phi_{\text{test}}(\mathbf{x})$ that satisfy the homogeneous boundary condition as well. First, it is useful to reduce the maximum order of differentiation by integration by parts

$$r = \int_\Omega \left[-\nabla u \cdot \nabla \phi_{\text{test}} + \nabla \cdot (\phi_{\text{test}} \nabla u) + f(\mathbf{x}) \phi_{\text{test}}(\mathbf{x}) \right] \, \mathrm{d}\mathbf{x} \tag{3.18}$$

$$= \int_\Omega \left[-\nabla u \cdot \nabla \phi_{\text{test}} + f(\mathbf{x}) \phi_{\text{test}}(\mathbf{x}) \right] \, \mathrm{d}\mathbf{x} + \int_{\partial\Omega} \phi_{\text{test}} \nabla u \cdot \mathbf{n} \, \mathrm{d}\sigma. \tag{3.19}$$

$$= \int_\Omega \left[-\nabla u \cdot \nabla \phi_{\text{test}} + f(\mathbf{x}) \phi_{\text{test}}(\mathbf{x}) \right] \, \mathrm{d}\mathbf{x} \tag{3.20}$$

Since the test functions vanish on $\partial\Omega$ the surface integral vanishes as well. The *Galerkin method*, which the FEM is a special case of, expands both solution u and test fuctions ϕ_{test} in a set of functions $\varphi(\mathbf{x})$ that form a complete basis

$$u(\mathbf{x}) = \sum_{i=1}^{\infty} U_i \varphi_i(\mathbf{x}) \qquad \phi_{\text{test}}(\mathbf{x}) = \sum_{i=1}^{\infty} \Phi_i \varphi_i(\mathbf{x}) \tag{3.21}$$

with coefficients U_i and Φ_i. The residual then reads

$$r = \int_{\Omega} \left[-\sum_{i,j=1}^{\infty} \Phi_i U_j \nabla\varphi_j \cdot \nabla\varphi_i + f(\mathbf{x}) \sum_i^{\infty} \Phi_i \varphi_i \right] \, \mathrm{d}\mathbf{x} \tag{3.22}$$

$$= \sum_i^{\infty} \Phi_i \int_{\Omega} \left[-\sum_{j=1}^{\infty} U_j \nabla\varphi_j \cdot \nabla\varphi_i + f(\mathbf{x})\varphi_i \right] \, \mathrm{d}\mathbf{x} \tag{3.23}$$

$$=: \sum_i^{\infty} \Phi_i r_i. \tag{3.24}$$

It must vanish for any test function and therefore coefficients Φ_i. In other words, coefficients U_j that solve the system of algebraic equations

$$0 = r_i(U_1, \ldots) = -\sum_{j=1}^{\infty} \left(U_j \int_{\Omega} \nabla\varphi_j \cdot \nabla\varphi_i \, \mathrm{d}\mathbf{x} \right) + \int_{\Omega} f(\mathbf{x})\varphi_i \, \mathrm{d}\mathbf{x} \tag{3.25}$$

solve the Poisson equation. The residual (3.20) has a symmetric form as both u and ϕ_{test} appear as first order derivatives in the first term. Therefore it is sufficient to demand basis functions and their first derivatives to be square integrable which is reflected in Eq. 3.25. We will not go into details on Sobolev spaces. In practice the sums must be cut off so

$$u(\mathbf{x}) = \sum_{i=1}^{M} U_i \varphi_i(\mathbf{x}) \qquad \phi_{\text{test}}(\mathbf{x}) = \sum_{i=1}^{M} \Phi_i \varphi_i(\mathbf{x}), \tag{3.26}$$

resulting in M unknown coefficients U_i with M equations r_i to be solved. The equations can then be solved by Newton's method which requires calculating the Jacobian

$$J_{ij} = \frac{\partial r_i}{\partial U_j} = \int_{\Omega} \nabla\varphi_j \cdot \nabla\varphi_i \, \mathrm{d}\mathbf{x} \tag{3.27}$$

Note that the Jacobian is in general not independent of U_j as residuals can be nonlinear in the coefficients U_j. The right-hand side expression is often abbreviated by the *stiffness matrix*

$$K_{ij} = \int_{\Omega} \nabla\varphi_j \cdot \nabla\varphi_i \, \mathrm{d}\mathbf{x}. \tag{3.28}$$

Evaluation of r_i and J_{ij} requires solving M and M^2 integrals. In the Finite Element Method basis functions are chosen that simplify these calculations. They are so-called *shape functions*

which have finite support, i.e., zero almost everywhere. Shape functions in one spatial dimension can be for example Lagrangian polynomials centered around each grid point x_i such that

$$\varphi_i(x_j) = \delta_{ij} \tag{3.29}$$

where δ_{ij} is the Kronecker delta. Thus, the coefficients U_i represent the nodal values of the solution

$$u(x_i) = U_i. \tag{3.30}$$

The simplest and commonly used shape functions are piecewise linear both in 1D and in higher dimensions. The above integrals then only need to be calculated around each node.

Implementation of boundary conditions can be done in multiple ways. They can be weakly imposed by adding a penalty term to the right-hand side of the PDE [JS09] or strongly applied by directly fixing the corresponding nodal values. Note that for strongly imposed non-zero Neumann BC the test functions are not required to fulfill homogeneous BC and the surface integral in Eq. (3.19) does not vanish.

Let us include time dependency now [LB13], i.e.

$$\partial_t u(\mathbf{x}, t) = \Delta u + f(\mathbf{x}) \tag{3.31}$$

and the coefficients of the expansion become time-dependent since the shape functions are constant in time

$$u(\mathbf{x}, t) = \sum_{i=1}^{M} U_i(t) \varphi_i(\mathbf{x}). \tag{3.32}$$

The residuals then read

$$r_i = -\sum_{j=1}^{\infty} \left(\dot{U}_j M_{ij} + U_j K_{ij} \right) + \int_{\Omega} f(\mathbf{x}) \varphi_i \, \mathrm{d}\mathbf{x} \tag{3.33}$$

where we identify the *mass matrix* and b_i

$$M_{ij} = \int_{\Omega} \varphi_i \varphi_j \, \mathrm{d}\mathbf{x}, \qquad b_i = \int_{\Omega} f(\mathbf{x}) \varphi_i \, \mathrm{d}\mathbf{x}. \tag{3.34}$$

Written in vector notation

$$0 = -\mathbf{M}\dot{\mathbf{U}} - \mathbf{K}\mathbf{U} + \mathbf{b} \tag{3.35}$$

This ODE can be solved with a time integration scheme.

3.3. Numerical Stiffness

For time-dependent problems numerical instability can express itself by exponentially growing modes, finite oscillatory modes or by the inconsistently used term *numerical stiffness*. Often, stiffness is used as a property classifying a differential equation when it is difficult to solve by explicit time-stepping. Both spatial and temporal explicit discretization perturb the system at each time step due to the introduced local truncation errors. These can result in transients of small time scales that quickly relax back to the smooth solution. This can occur repeatedly throughout the simulation or only in a few time intervals [Spi96, LeV07]. In this thesis we frequently use the term *stiffness* and refer to an adaptive time step size Δt that suddenly becomes significantly smaller as the system becoming *stiff*, i.e., in a certain time interval. Although implicit methods tend to be more stable, they too, are not fully numerically stable.

3.4. Numerical Path Continuation

Direct numerical simulations (DNS) are very illustrative for the dynamics of a system. However, simulation times can be considerably long and it is difficult to obtain a satisfactory overview of the solution space. A very powerful tool is numerical path continuation in which entire branches in solution space are calculated. These are usually stable and unstable steady states, the latter of which are inaccessible by DNS. Let $\mathbf{G}(\mathbf{u}, \lambda)$ denote the right-hand side of a system of ODEs, which can be a result of FDM or FEM discretization. The elements of $\mathbf{u}$ are then the nodal values of the order parameter field. Steady states solve

$$0 = \mathbf{G}(\mathbf{u}, \lambda) \tag{3.36}$$

with a control parameter λ. In this section, we sketch the *pseudo-arclength continuation* [Kel77, KN87]. Although it is possible to calculate solution branches by varying λ, it is difficult to continue past saddle-node bifurcations. Changing the parametrization of the branch to a pseudo-arclength s solves this problem and brings other benefits with it. A solution is then characterized by

$$\mathbf{v}(s) = (\mathbf{u}(s), \lambda(s)). \tag{3.37}$$

and a discrete solution branch is denoted by $\mathbf{v}(s_i) = \mathbf{v}_i$ where s_i is the arclength of the previous continuation step with index i for the following parametrization/constraint/normalization

$$N(\mathbf{u}, \lambda, s) = \partial_s \mathbf{u}(s_i) \left[\mathbf{u}(s) - \mathbf{u}(s_i) \right] + \partial_s \lambda(s_i) \left[\lambda(s) - \lambda(s_i) \right] - (s - s_i) = 0. \tag{3.38}$$

We can then calculate a solution branch by varying s with step size Δs, make an initial guess and apply Newton's method to

$$P(s) = \begin{pmatrix} \mathbf{G}(\mathbf{u}, \lambda, s) \\ N(\mathbf{u}, \lambda, s) \end{pmatrix} = 0 \tag{3.39}$$

at each step. The Jacobian of the extended system reads

$$\partial_{\mathbf{v}} P(s) = \begin{pmatrix} \partial_{\mathbf{u}} \mathbf{G} & \partial_\lambda \mathbf{G} \\ \partial_{\mathbf{u}} N & \partial_\lambda N \end{pmatrix} \tag{3.40}$$

with $\partial_{\mathbf{u}} \mathbf{G}$, $\partial_\lambda \mathbf{G}$, $\partial_{\mathbf{u}} N$, $\partial_\lambda N$ being the Jacobian of the original right-hand side (square matrix), a column vector, row vector and scalar, respectively. For $s = s_i$ the Jacobian simplifies to

$$\partial_{\mathbf{v}} P(s_i) = \begin{pmatrix} 0 & \partial_\lambda \mathbf{G}(\mathbf{u}(s_i), \lambda(s_i), s_i) \\ \partial_s \mathbf{u}(s_i) & \partial_s \lambda(s_i) \end{pmatrix}. \tag{3.41}$$

The initial Newton guess of the next continuation step $\mathbf{v}^0(s_{i+1})$ is predicted by

$$\mathbf{v}^0(s_{i+1}) = \mathbf{v}^0(s_i) + \Delta s \frac{\partial_s \mathbf{v}(s_i)}{|\partial_s \mathbf{v}(s_i)|}. \tag{3.42}$$

Superscripts denote Newton iterations and subscripts continuation steps in this section. The tangent direction $\partial_s \mathbf{v}$ is calculated by solving

$$\frac{d}{ds} P(s_i) = \partial_{\mathbf{v}} P(s_i) \partial_s \mathbf{v}_i + \partial_s P(s_i) = 0. \tag{3.43}$$

Notice that the tangent is calculated at s_i, while the Newton algorithm evaluates the Jacobian at s_{i+1}. The framework can be extended to find linear stability analysis, bifurcations, time-periodic orbits [NS15] etc.

3.5. Utilized Tools

Direct numerical simulations are mostly run with a GPU parallelized CUDA code [NVI22]. The base code is provided by Markus Wilczek and Walter Tewes. Due to the point and stencil-wise discretization of FDM, implementation in parallelized computing is very natural since the evaluation of the PDE at one grid point can be handled by one thread. For time integration an adaptive Runge-Kutta Dormand-Prince (RKDP) method is utilized. A fourth order Lax-Wendroff scheme was tested, however, it had worse convergence than the FDM-RKDP scheme, not shown here. Otherwise, a FEM based library oomph-lib with implicit time-stepping is adopted [HH06]. For numerical path continuation the also FEM-based package pde2path is employed[UWR14, Uec18, Uec21]. Note, that both the pde2path and oomph-lib calculations in this thesis use piecewise linear shape functions. The former imposes boundary conditions weakly whereas the latter does so strongly as mentioned in Sec. 3.2.

4. Dynamics of Binary Mixture Flow and Deposition

In systems concerning complex liquids, or in our case, binary mixtures with volatile solvents, both the liquid and the deposit can form patterns. By formulating models that are as minimal as possible, researchers can single out which model components are required for particular mechanisms and the formation of certain patterns. Highly regular stripes parallel to the contact line can be obtained when the contact line undergoes periodic pinning and depinning, also known as *stick-slip* motion. In the well-known coffee stain experiment, diverging solvent evaporation leads to an increase in nanoparticle concentration at the contact line[DBDH+97, Dee00]. These particles jam and physisorb onto the substrate, pinning the contact line. When the solvent continues to evaporate capillary flow supplies material from the center leading to the formation of a ring deposit. As the capillary force exceeds the pinning force the contact line depins and the cycle repeats, resulting in concentric rings[Gen85, BDG10]. Stick-slip motion can be modeled by a concentration-dependent dynamic viscosity such as in the thin-film model presented by Frastia and coworkers [FAT12]. There, an evaporation front and deposition patterns are extensively numerically investigated on 1D substrates. In the related context of gelation Okuzono et al. present droplet profiles for a pinned drop leaving basin, crater and mound type deposits with a step-like evaporation rate[OKD09]. Ring deposits are found during the evaporation of thin films in cylindrical geometry as well [WCM03]. The periodic accumulation of particles at the contact line has also been shown in Lattice Boltzmann calculations [CMS13]. Similar to [XTQ15] Onsager's variational principle is utilized to derive models with contact line friction for (multi) ring deposits of drying droplets by assuming a parabolic shape [MD16, HWMD17, WYQ18, WMD18, JYWM20, YJLD+21]. Chalmers et al. show in a DDFT model that a coffee-ring like effect occurs in the absence of convection as well due to aggregation and phase separation [CSA17], while Zigelman et al. investigate oscillatory wetting-dewetting motion of the contact line [ZAM19]. See also Erbil's recent review on the dependency of the contact angle on the moving contact line [Erb21].

Lattice gas models including evaporation and diffusion can describe fingering in nanoparticle deposits [YR06, VTPS+08]. Dynamic density functional theory (DDFT) shows that jamming of discrete particles is not necessary for fingering to occur, vanishing diffusivity on dry spots is enough. Weaker particle-liquid or stronger particle-particle interaction makes the fingering instability stronger and can lead to demixing in the bulk ahead of the receding contact line[TVAR+09, RAT11]. Note that other deposition patterns such as labyrinthine, cellular, or sawtooth structures have been simulated as well [TVAR+09, Sta11, RAT11, Thi14] and can appear on multiple scales[SMPM+08]. Similar to the dilute models mentioned in the introduction of Sec. 2 a long-wave model is utilized by Diez et al. to describe demixing and dewetting in alloys which are usually treated by means of phase-field equations[DGGR+21].

The mentioned works mainly consider passive geometries, i.e., the droplet or film rests. In controlled (active) setups part of the dynamics is *controlled* [HL12]. This can result in more regular patterns in comparison to passive geometries. For example the inclination of a substrate, on which liquid flows down, controls the influence of gravity. In such a geometry a capillary ridge can become transversally unstable resulting in the formation of liquid fingers[Sch89, SH96]. Dip-coating is another controlled setup. Similar to the stick-slip motion mentioned above, the contact line can periodically advance and recede on the substrate due to competition between viscous drag, capillarity and gravity. This can lead to liquid ridges (stripes) parallel to the contact line detaching from it. Depending on the velocity of the pulled substrate three prominent liquid states can be found: A front with static contact line position, a dynamically moving contact line that ejects stripes and steady flat films, known as Landau-Levich solutions [LL42, SADF07, SZAF+08, ZSE09, GLFD+16, TWGT19]. Analytical, direct numerical and bifurcation studies of single component thin film models for dip-coating are, for example, presented in the following references[CSE12, TGT14, GTHT14, WZCT+17, MMT21]. However, real experiments mostly employ mixtures consisting of volatile and non-volatile components. In the simplest case, the mentioned liquid patterns are directly reflected in the deposit morphology. Doumenc, Guerrier (and Dey) analyze steady and periodic states of a binary mixture in a dip-coating geometry with diffusion-limited evaporation without disjoining pressure or for a fully wetting substrate [DG10, DG13, DDG16]. Their results include morphological phase diagrams.

In the mentioned thin-film models[WCM03, OKD09, FAT12] the deposit is identified by the absence of solvent or the concentration in the precursor. As derived in Sec. 2.5.2 we model the solutal solid-liquid phase transition by coupling a phase-field equation to the hydrodynamic ones and describe the effective deposit thickness by a fourth order parameter field $\zeta(\mathbf{x})$. In this chapter we mainly perform direct numerical simulations (DNS) on 1D substrates and briefly on a 2D substrate. The analysis is divided into submodels by subsequently switching on effects such as evaporation or deposition. In Sec. 4.1-4.3 some numerical challenges are addressed followed by a preliminary look on the full model in Sec. 4.4. The dynamics of a volatile sessile droplet are presented in Sec. 4.5-4.6 with emphasis on the development of the solute concentration profile. The instability of the solutal solid-liquid interface is shown in Sec. 4.7 for diffusion-limited precipitation from a nucleus. Finally, the full model is analyzed in Sec. 4.8. Except for Sec. 4.2 and 4.7 two types of (un)controlled geometries are chosen for the investigation: A sessile volatile droplet on a horizontal substrate and a dip-coating geometry. Section 4.3, 4.5 and 4.6 consider the former while Sec. 4.1, 4.4 and 4.8 the latter.

4.1. Choice of FDM Order and Numerical Boundary Conditions

Most simulations in this chapter are performed with models discretized by the finite difference method (FDM). A general presentation of the method can be found in Sec. 3.1. For the sake of efficiency and exactness the order of the stencils and concurrently the number of ghost points (GP) need to be chosen. We consider, for example, the thin-film equation for a non-volatile simple liquid (TFE) in a dip-coating geometry as obtained by rescaling Eq. (2.33) or using $\partial_t h = \partial_t \psi_1 + \partial_t \psi_2$ with Eq. (2.126)-(2.127) and $(\Omega, \alpha) = (0, 0)$. In this case, the diffusive contributions of each component cancel out, leaving

$$\partial_t h = -\nabla \cdot \left[\frac{h^3}{3} \nabla \left(\Delta h - f'(h) - g(h + \beta x) \right) + \mathbf{v}h \right] \tag{4.1}$$

with film height h, wetting energy $f(h)$, effective gravitational acceleration g, effective substrate inclination β and transfer velocity $\mathbf{v} = v\mathbf{e}_x$. In this section, two different sets of boundary conditions are considered, labeled by the number of ghost points (GP) used in the implementation

$$h(0) = h_0, \qquad \partial_x h(0) = -\beta, \qquad \partial_{xxx}\psi_1(0) = 0; \qquad\qquad \text{(3GP)}$$
$$h(0) = h_0, \qquad \partial_x h(0) = -\beta. \qquad\qquad\qquad\qquad\qquad\qquad\quad \text{(2GP)}$$

Remember, that $x = 0$, i.e., the left hand side of the domain, denotes the bath side. In all cases, Neumann boundary conditions are used on the right-hand side of the domain. In a simple second order implementation the operators div, grad and Δ are represented by centered stencils covering nearest neighbor grid points. Then, three ghost points/numerical boundary conditions (3GP) per boundary are required in order to retain centered stencils all over the grid. A corresponding
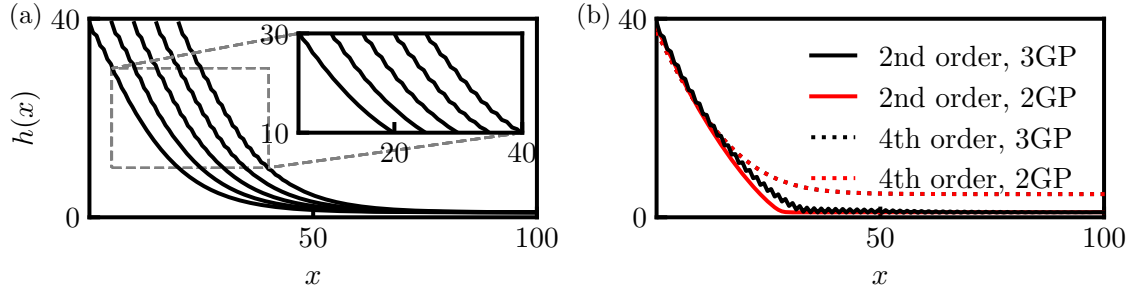

Figure 4.1.: Snapshots of height profiles for a simple dragged meniscus at different orders of FDM and number of ghost points [numerical boundary conditions]. The operators are discretized according to Eq. (4.1) for second order and Eq. (4.2) for 4th order FDM. The left boundary conditions are chosen from Eq. (3GP)-(2GP). See Sec. 2.5.4 for the initial condition. Only the left section of the domain is shown. (a) second order FDM with 3 GP at very early times, the profiles are shifted by $\Delta x_{\text{shift}} = 5$ each for visualization. A numerical instability develops starting from the left boundary. (b) The same solution after longer times is depicted as a solid black line. It is compared with second order FDM and 2 GP (solid, red), 4th order and 3 GP (dotted, black), 4th order and 2 GP (dotted, red). Aside from the numerical instability, the missing overlap of the curves are likely due to mass conservation errors. The parameters are $h_0 = 40$, $g = 0.001$, $v = 0.2$, $\beta = 2$, $L_x = 320$. $N_x = 400$ for second order FDM and $N_x = 240$ for 4th order FDM.

example solution at early times is shown in Fig. 4.1 (a). One observes that a numerical instability on the scale of the grid resolution starts at the left and extends to the right. Later it covers the whole domain, as depicted by the solid black line in panel (b), suggesting that the left boundary conditions are problematic. Such an instability is briefly mentioned in the beginning of Sec. 3.3. However, the simulation is not stiff here, indicating that the time scale of this transient is not too different from the physical time scale. By using forward and backward differences close to the boundaries for the Laplacian it is possible to drop the required number of ghost points to two. This prevents the emergence of the instability as shown by the red solid line showing that the third boundary condition is the destabilizing factor. Note that, in second order, extrapolating the slope to the third ghost point leads to the instability as well (not shown). However, this should not lead to the conclusion that overdetermination by a numerical boundary condition

is problematic since (3GP) has been used in previous works (in a FEM implementation on the simple thin-film equation) [Tew13]. This can be demonstrated by switching to 4th order stencils and compare (3GP) with (2GP) again, see Fig. 4.1 (b). One can see that both solutions, depicted by the dotted black/red (overlapping) lines, are numerically stable. This indicates that the third boundary condition being of second order acts destabilizing. Note that for the 4th order (3GP) implementation the right-hand side of Eq. (4.1) is rewritten by evaluating the divergence and gradient terms which allows minimal usage of asymmetric stencils close to the boundaries

$$\partial_t h = -h^2 \nabla h \cdot \left(\nabla \Delta h - \nabla f'(h) - g(\nabla h + \beta \mathbf{e}_x) \right) - \frac{h^3}{3} \left(\Delta^2 h - \Delta f'(h) - g \Delta h \right) + \mathbf{v} \cdot \nabla h. \quad (4.2)$$

This means that if numerical instabilities develop at the boundaries it is possibly due to the numerical boundary condition being of too small order. In addition to the above, the advection term is discretized by an asymmetric stencil instead of a centered one, in order to treat a different numerical instability. This is discussed in more detail in Sec. 4.8.1. The discrepancy in film height between second and 4th order (2GP) is likely due to mass conservation errors.

4.2. Mass Conservation

Having established the boundary conditions and number of ghost points for the dip-coating geometry, next we investigate the mass conservation depending on the FDM order. As the simulation domain is moving with the substrate, observable time scales are limited by the domain size which hides mass conservation problems. Therefore, a resting horizontal substrate is considered here and in the next section. For simplicity, we use periodic boundary conditions. Figure 4.2 (a) shows the time evolution of the mean film height

$$\bar{h}(t) := \frac{1}{L_x L_y} \int h(x, y, t) \, \mathrm{d}x \mathrm{d}y \quad (4.3)$$

of a perturbed flat film of initial height $h_0 = 2.5$ for different orders of FDM implementations and two choices of the discretizations of the terms involving the wetting energy $f(h)$. It is convenient for the implementation to express all operators as derivatives of h

$$\partial_t h = -h^2 \nabla h \left(\nabla \Delta h - f''(h) \nabla h \right) - \frac{h^3}{3} \left(\Delta^2 h - \Delta h f'''(h) - (\nabla h)^2 f''(h) \right). \quad \text{(Form-A)}$$

We label corresponding simulations by "A". Three different sets of FDM orders are investigated: 4th order stencils that are mostly centered except for the points right next to the boundaries, 6th order inner stencils with 4th order ones next to the boundaries and centered 6th order stencils only. All simulations using (Form-A) show significant loss of mass independent of the FDM order, as indicated in Fig. 4.2 (b) where a space-time plot of the first set is shown. The film dewets into multiple droplets that start to coalesce but quickly lose mass over time. However a change in implementation can improve the mass conservation by switching to (Form-B)

$$\partial_t h = -h^2 \nabla h \left(\nabla \Delta h - \nabla f'(h) \right) - \frac{h^3}{3} \left(\Delta^2 h - \Delta f'(h) \right) \quad \text{(Form-B)}$$

which is analogous to Eq. (4.2). The spatial derivatives of $f'(h)$ are not evaluated by chain rule. The mass is conserved better but there is an increase in mass over longer time scales. A space-time plot of a (Form-A)-simulation with fourth order FDM is shown in Fig. 4.2 (c). There, the
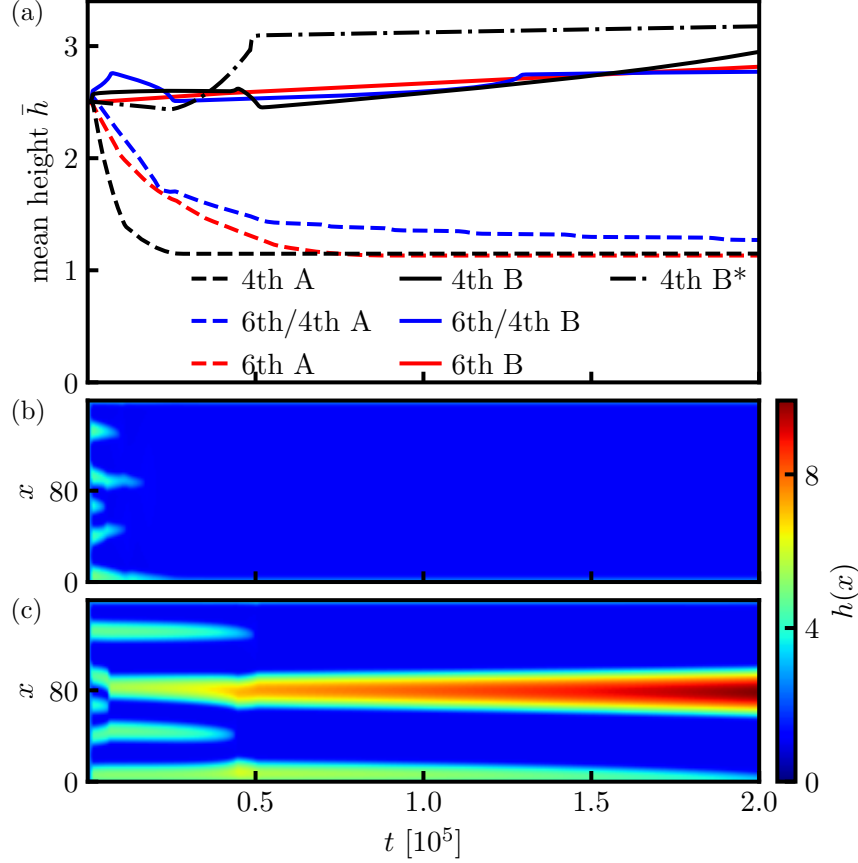
Figure 4.2.: DNS of a dewetting flat film of a simple liquid described by Eq. (4.1) with periodic boundary conditions in 1D. The initial height is $h_0 = 2.5$ with white noise of amplitude $\hat{\eta} = 0.05$. (a) Time evolution of mean height $\bar{h}$ for different FDM orders and discretization schemes for spatial derivatives of $f'(h)$. Black: 4th order stencils. Blue: 6th order inner stencils/ 4th order stencils next to and on boundaries. Red: 6th order centered stencils over the full domain. Dashed and solid lines show simulations with discretizations according to Eq. (Form-A) and (Form-B), respectively. The former exhibits significant loss of mass while the latter retains mass gain over large time scales. The grid resolution is $\Delta x = 1$ while **4th B*** is calculated with $\Delta x \approx 0.77$. (b) Space-time plot of **4th A**. (c) Space-time plot of **4th B**.

droplets coalesce which is clearly visible in panel (a) by sudden jumps in $\bar{h}$. The improvement in mass conservation is at least related to the additional truncation error in (Form-A) over (Form-B) because the Laplacian is split up in two operators:

$$\Delta h f'''(h) + (\nabla h)^2 f''(h) \leftrightarrow \Delta f'(h). \tag{4.4}$$

In addition, loss of significance (cf. final paragraph of Sec. 3.1) occurs less due to fewer arithmetic operations. Mass is best conserved using solely centered 6th order FDM stencils over the full domain, including the boundaries. Unfortunately, such a setup is only possible when periodic boundary conditions are applied. In other cases asymmetric stencils need to be used at the

boundaries due to the limited number of ghost points. The 6th order asymmetric stencils contain larger coefficients than their centered counterparts and unfortunately can result in precision errors even with double precision float numbers. Therefore, considering how mass is preserved according to (a) the decision lies between 6th order inner/4th order outer stencils or 4th order stencils only. The former is more precise while the latter has simpler implementation and less computational cost.

Grün and Rumpf show the equivalence between Finite Volume and Finite Element Method for the thin-film equation for certain meshes and developed thereby mass and nonnegativity preserving numerical schemes with implicit Euler time stepping by choosing an appropriate numeric (discrete) mobility [Grü99, GR00, GR01]. This mobility takes the form of a harmonic mean between half-step next neighbor grid points as shown parallel by Zhornitskaya and Bertozzi with a similar ansatz. They proof second order accuracy for FDM schemes with implicit time-stepping which is utilized Diez et al. for thin-film flow with capillarity and gravity [ZB00, DKB00, DK02]. Adopting this mobility for their binary mixture model Karpitschka and coworkers show that a droplet with volatile solvent can maintain a quasi-stationary apparent contact angle through interplay of Marangoni, capillary, diffusive and evaporative flow [KLR17]. Note, that they discretize space non-uniformly by means of FVM and integrate in time with an operator-splitting scheme[GLR02]. A Finite Difference Method without the mentioned discrete mobility is utilized by Diez and Kondic to simulate dewetting of a thin-film with capillarity, gravity and disjoining pressure[DK07]. They resort to high grid resolutiona and quadruple precision in order to avoid numerical noise. While Karpitschka and Riegler resort to central differences of 8th order[KR14]. Doumenc and Guerrier consider a long-wave binary mixture model without disjoining pressure with second order FDM on an adaptive mesh and implicit time stepping[DG10, DG13]

In this chapter we mostly adopt 4th ordered stencils with (Form-B) unless stated otherwise. Considering the results from Fig.4.2 (a), a finer resolution of $\Delta x \approx 0.77$ seems to be better at conserving mass than $\Delta x = 1$ in non-coalescing situations. An attempt at a more efficient implementation using the logarithmic transformation $u = \log(h)$ did not result in a noticeable performance gain.

4.3. Hyperbolicity of Binary Mixture Equations

Another type of numerical instability can occur when turning to more complex systems. In this section, we consider a binary mixture described by Eq. (2.126)-(2.127) in the case of a sessile droplet on a horizontal substrate without evaporation or precipitation, i.e., $g = v = \Omega = \alpha = 0$. The detailed analysis is presented in Sec. 4.5. Figure 4.3(a) shows the final frame of a time simulation in which a droplet approaches an equilibrium state. Diffusion is turned off, that is $\mathrm{Pe}^{-1} = 0$. Therefore, we expect $C(\mathbf{x}, t) = const. = C_0$. While the height profile (black) relaxes as expected, the concentration field (blue), however, develops a numerical instability at the contact line. Panel (b) shows the time evolution of the maximal deviation of the concentration from the initial value C_0. It is depicted for various values of Pe^{-1} showing that the deviation increases for $\mathrm{Pe}^{-1} < 10^{-3}$, thus, this parameter region should be avoided on these time scales. This threshold likely depends on the other system parameters, however, it can serve as an estimate. The growth of numerical perturbations is related to the hyperbolicity of the convective flux, i.e., a finite propagation velocity of perturbations. The parabolic diffusive terms stabilize the numerical instability [Tho95, LS06].
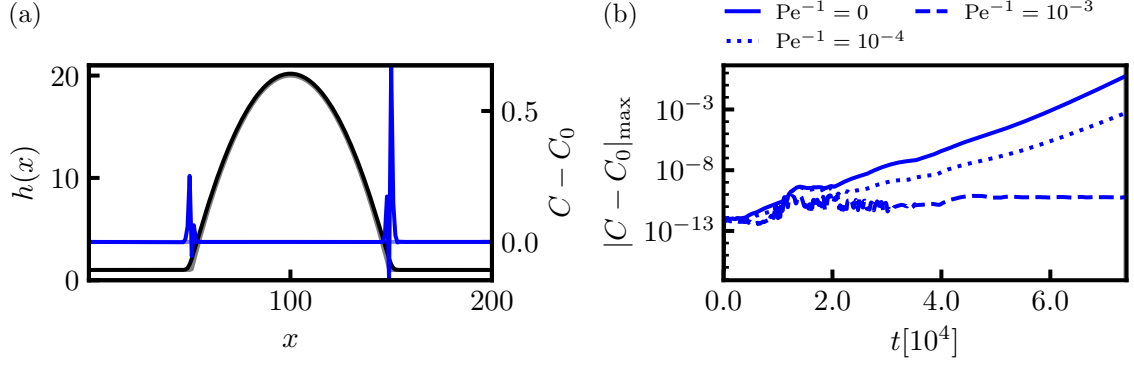
Figure 4.3.: (a) Final snapshot of a sessile droplet of a binary mixture described by Eq. (2.126)-(2.127). The film height h (black, left axis) and deviation of solute concentration C from initial concentration C_0 (blue, right axis) are depicted. The initial condition (slightly visible in gray) is a parabolically shaped cap, see Eq. (2.140). The other parameters are: $\text{Pe}^{-1} = g = v = \Omega = \alpha = 0$, $\chi = 1.5$, $h_0 = 20$, $L = 200$, $N = 192$. (b) Time evolution of the maximum concentration deviation (blue) for other inverse Peclét numbers $\text{Pe}^{-1} = 0, 10^{-4}, 10^{-3}$.

4.4. Full Model – First Look

At this point we motivate the subsequent studies of individual model parts by giving a first impression of the behavior of the full model, that describes the dip-coating of a binary mixture with volatile solvent and a solute that can precipitate. The considered dynamic equations are

$$\partial_t \psi_1 = - \nabla \cdot \left\{ \frac{1}{3} \psi_1 h^2 \nabla \left[\Delta h - f'(h) - g(h + \beta x) \right] + \mathbf{v} \psi_1 - \text{Pe}^{-1} h \left(1 - 2\chi C_1 C_2 \right) \nabla C_1 \right\}$$
$$- \Omega \left[- \Delta h + f'(h) + \Upsilon \left(\ln(C_1) - 1 + \chi C_2^2 \right) - \mu \right] \tag{4.5}$$

$$\partial_t \psi_2 = - \nabla \cdot \left\{ \frac{1}{3} \psi_2 h^2 \nabla \left[\Delta h - f'(h) - g(h + \beta x) \right] + \mathbf{v} \psi_2 - \text{Pe}^{-1} h \left(1 - 2\chi C_1 C_2 \right) \nabla C_2 \right\}$$
$$+ \alpha h (\partial_t \phi + \mathbf{v} \nabla \phi) \tag{4.6}$$

$$\partial_t \phi = \sigma \left(\Lambda^{-2} \Delta \phi - \partial_\phi f_{\text{xm}} \left(\phi, C_2 - C_{\text{eq}}; \lambda \right) - \Lambda^{-2} \kappa |\nabla \phi| \right) - \mathbf{v} \nabla \phi \tag{4.7}$$

$$\partial_t \zeta = - \alpha h (\partial_t \phi + \mathbf{v} \nabla \phi) - \mathbf{v} \nabla \zeta. \tag{4.8}$$

The order parameter fields are effective solvent thickness ψ_1, effective solute thickness ψ_2, phase-field ϕ and effective deposit thickness ζ. It is possible to switch between (ψ_1, ψ_2) and (h, C) without loss of generality. Parameters that do not appear in the previous sections are the inverse Peclét number Pe^{-1}, mixing parameter χ, effective evaporation rate Ω, effective osmotic pressure Υ, chemical potential of the gas phase μ, source strength α, time scale ratio σ and length scale ratio Λ. Taking into account the results of previous sections, a simulation is run for a 2D substrate and the result is shown in Fig. 4.4.

Snapshots are taken at times of significant change in the height or concentration profiles, increasing time from top to bottom. The upper surface represents film height h with colors indicating the solute concentration C. Below, the effective thickness of the deposit ζ is shown. In the
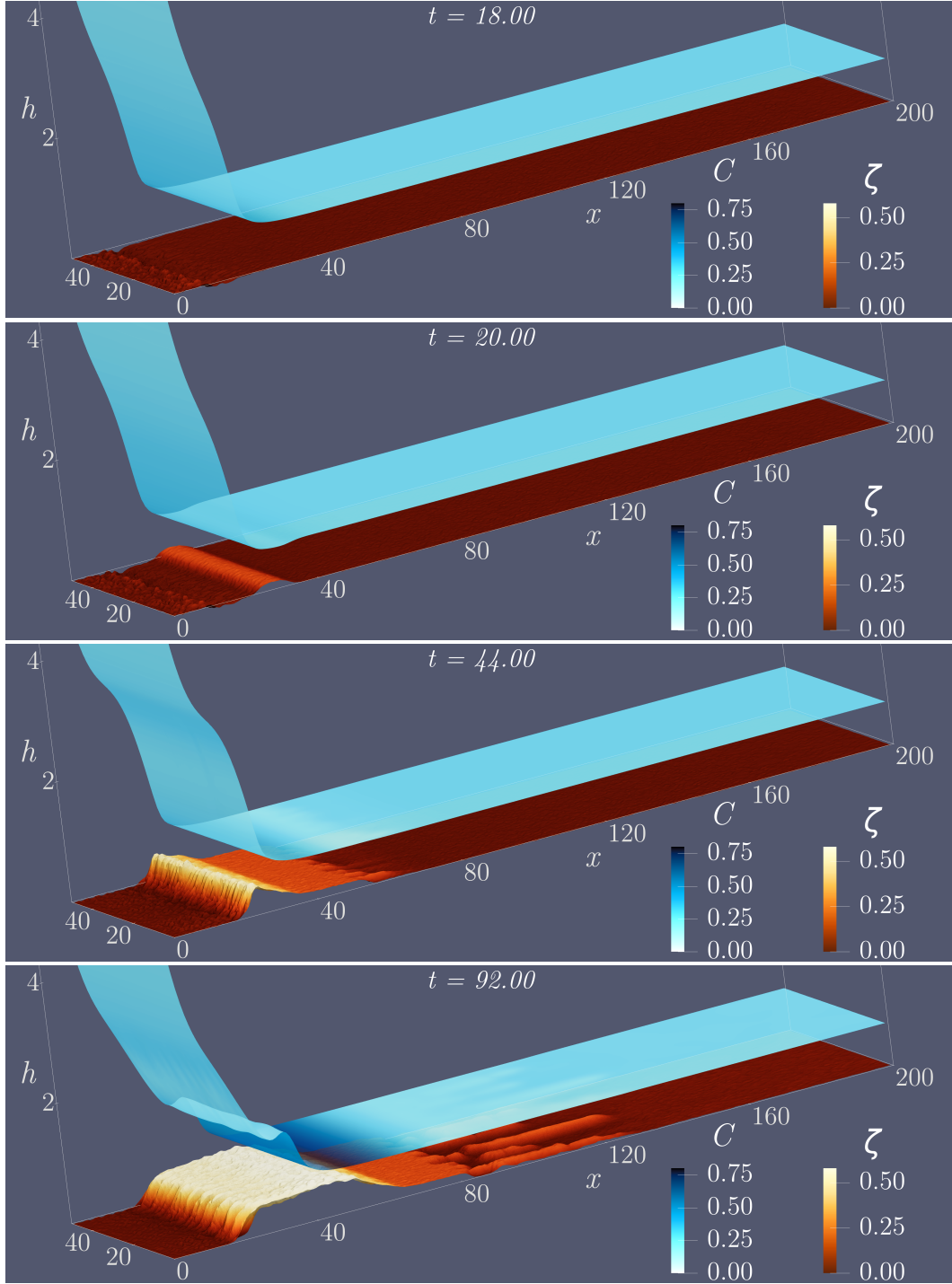
Figure 4.4.: Snapshots from a simulation of a volatile binary mixture on a 2D plate out of a liquid bath at times $t \in \{18, 20, 44, 92\}$ described by Eq. (2.126)-(2.129). The upper surface represents the film height h, with a color scheme representing the solute concentration C. The lower surface represents the effective deposit thickness ζ, both, in height and color. The initial condition for the height profile is a meniscus, see Sec. 2.5.4. The system parameters are $L_x = 200$, $L_y = 50$, $N_x = 256$, $N_y = 64$, $h_0 = 15$, $C_0 = 0.3$, $C_{\text{eq}} = 0.35$, $v = 0.6$, $g = 10^{-3}$, $\beta = 2$, $\text{Pe}^{-1} = 1$, $\chi = 1.5$, $\Omega = 0.008$, $\Upsilon = 1$, $\mu = -6$, $\alpha = 0.1$, $\lambda = 15$, $\Lambda = 1$ and $\sigma = 1$.
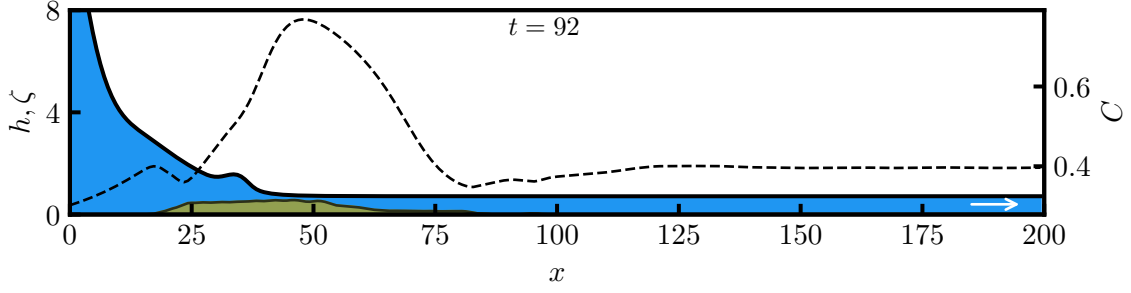
Figure 4.5.: One-dimensional cross-section at the center of the final snapshot in Fig. 4.4. The film height h, solute concentration C and deposit thickness ζ are shown in blue, dashed black and olive, respectively. The substrate is pulled towards the right (white arrow). The solution is shown close to the numerical instability due to stiffness. See caption of Fig. 4.4 for further information.

beginning, the meniscus deforms due to the extraction of liquid by advection. Meanwhile, solvent evaporates leading to a local increase in C, see the slightly yellow region in front of the meniscus at $t = 18$. When C has sufficiently increased, solute is deposited (cf. $t = 20, 44, 92$). ϕ is initialized with some white noise, i.e., lateral perturbations exist, triggering the formation of fingers in the deposit at $t = 92$, part of which are even detached. Unfortunately, this is when the system becomes very stiff and the simulation cannot be continued.

More issues become apparent in the 1D cross-section of (h, ζ, C, ϕ) in Fig. 4.5. We observe that C is maximal outside the contact line, within the precursor film. The deposit thickness is below the precursor height. However, it is uncertain whether these factors are the origin of stiffness. To better understand the issue, in the following sections we break down the full model into submodels. The full model is then revisited in Sec. 4.8.

4.5. Volatile Droplet of a Binary Mixture

The increase in solute concentration followed by the onset of precipitation within the precursor is a point of concern. The precursor should mainly serve as a mathematical tool to avoid the moving contact line problem. Thus, the maximal solute concentration should occur within the droplet. The purpose of this section is the analysis of a two-field submodel in a passive geometry, i.e., a sessile droplet of a volatile binary mixture. This corresponds to the full model with $g = \alpha = \partial_t \phi = \partial_t \zeta = 0$. The considered model is

$$
\begin{aligned}
\partial_t \psi_1 = -\nabla \cdot &\left\{ \frac{1}{3} \psi_1 h^2 \nabla \left[\Delta h - f'(h) \right] - \mathrm{Pe}^{-1} h \left(1 - 2\chi C_1 C_2 \right) \nabla C_1 \right\} \\
&- \Omega \left[-\Delta h + f'(h) + \Upsilon \left(\ln(C_1) - 1 + \chi C_2^2 \right) - \mu \right]
\end{aligned}
\tag{4.9}
$$

$$
\partial_t \psi_2 = -\nabla \cdot \left\{ \frac{1}{3} \psi_2 h^2 \nabla \left[\Delta h - f'(h) \right] - \mathrm{Pe}^{-1} h \left(1 - 2\chi C_1 C_2 \right) \nabla C_2 \right\}.
\tag{4.10}
$$

We begin by analyzing the dynamics of droplet evaporation, with emphasis on how the concentration profile develops and the behavior of the precursor. For this purpose DNS and analytical

calculations for stationary states are employed. The simulations are calculated on domain size $L = 200$ and grid points $N = 256$ if not stated otherwise. Figure 4.6 shows the time evolution of an evaporating droplet. Film height h (left axis) is depicted in gray scale on panels (a) to (h) while other fields of interest are depicted in color (right axis). The color grading denotes increasing times t. The liquid evaporates across the full domain resulting in a concentration
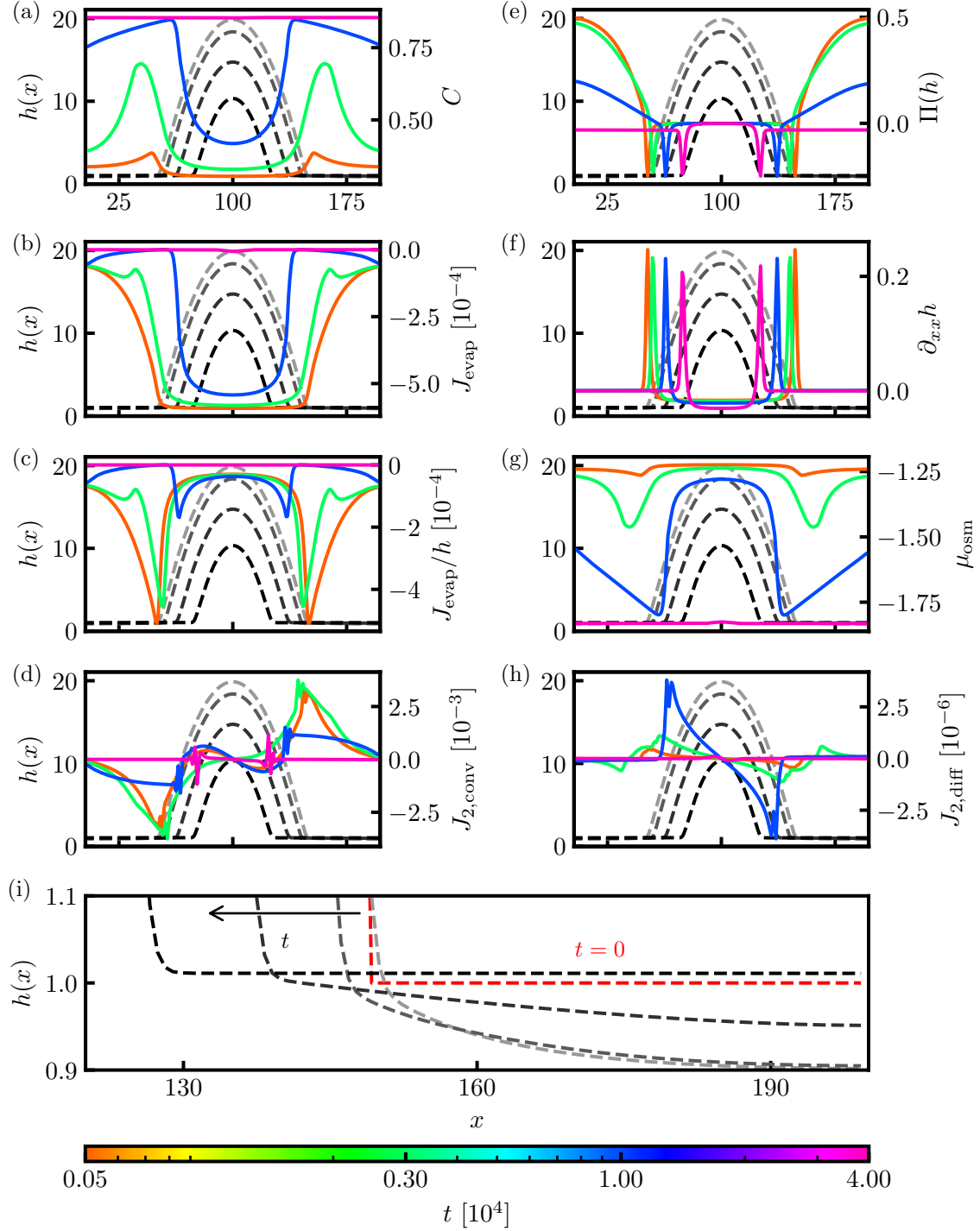
Figure 4.6.: Time evolution of a sessile droplet of a volatile binary mixture described by Eq. (2.126)-(2.127) with $g = 0$, $v = 0$, $\alpha = 0$. Film height h (left axis, grayscale) and other quantities (right axis, colored) are depicted at times labeled on the color bar. The gray/black lines follow the same order as the colored ones, i.e., the darker shades correspond to later times. (a) solute concentration C (b) evaporative flux J_{evap} (c) relative evaporative flux J_{evap}/h (d) convective flux of solute $J_{2,\text{conv}}$ (e) disjoining pressure $\Pi(h)$ (f) negative curvature $\partial_{xx}h$ (g) osmotic pressure μ_{osm} (h) diffusive flux of solute $J_{2,\text{diff}}$ (i) zoom of the precursor region. The profile at $t = 0$ is shown in red. See Sec. 2.5.4 for the initial conditions. The remaining parameters are $\text{Pe}^{-1} = 10^{-4}$, $\chi = 1.5$, $\Omega = 0.001$, $\Upsilon = 1$ and $\mu = -1.8$.

maximum developing outside the droplet (panel (a)). The magnitude of the evaporative flux J_{evap} is maximal inside (panel (b)). However, due to the different height ratios, the concentration grows faster outside of the droplet. This is more visible in the relative evaporative flux J_{evap}/h whose maximum magnitude coincides with that of the local concentration $C_{\max}$ at early times ($t = 0.05 \cdot 10^4$, red) (panel (c)). Later, however, $C_{\max}$ resides farther away from the center and $J_{\text{evap}}/h|_{\max}$. This can be attributed to convection occurring from inside the droplet into the precursor after solvent has evaporated there (panel (d)). This indicates that the precursor is not flat and is verified with the disjoining pressure $\Pi(h)$ which can also be viewed as a mapping of h (panel (e)). The precursor height initially lowers to ≈ 0.9 from $h_p(t = 0) = 1$, develops a gradient and then approaches constant height $h_p > 1$ (panel (i)). Equilibrium is thus achieved by the interplay of convection and evaporation. For completeness, we also provide in (f) a plot of $\partial_{xx}h$.

For panels (g) and (h) the mixing terms in Eq. (4.9)-(4.10) are discussed in more detail in the following. The osmotic pressure

$$\mu_{\text{osm}}(C, \Upsilon, \chi) := \Upsilon \left(\ln(1 - C) - 1 + \chi C^2 \right) \tag{4.11}$$

not only appears in the evaporative flux but is also related to the diffusivities in Eq. (4.9)-(4.10) by

$$1 - 2\chi(1 - C)C = (1 - C)\mu'_{\text{osm}}. \tag{4.12}$$

$\mu_{\text{osm}}/\Upsilon$ is shown as a function of C in Fig. 4.7 for several $\chi \in \{0..5\}$. The sign of the diffusivity (4.12) determines whether solute and solvent mix [demix] by diffusion [anti-diffusion], i.e., the point of marginal stability. A linear stability analysis of homogeneous states (h_0, C_0) shows that the change in stability is determined from the curvature of the local potential of the compositions Eq. (2.49)

$$f''_{\text{FH}}(C_0) = 1 - 2\chi(1 - C_0)C_0 \overset{!}{=} 0. \tag{4.13}$$

Thus, anti-diffusion cannot be resolved numerically as the corresponding linear growth mode diverges to infinity with increasing wavenumber, see App. A.4. This means that the values of (χ, C) are limited and marked by the gray or white regions in Fig. 4.7. Since all C values between 0 and 1 should be allowed and anti-diffusion is to be avoided, an appropriate χ is any $\chi < 2$, which follows from setting $1 - 2\chi(1 - C)C > 0$. We have chosen $\chi = 1.5$ here and it stays fixed for all DNS in this chapter. This corresponds to a monotonic dependence of the osmotic contribution on the solute concentration: As C increases μ_{osm} decreases and diverges as
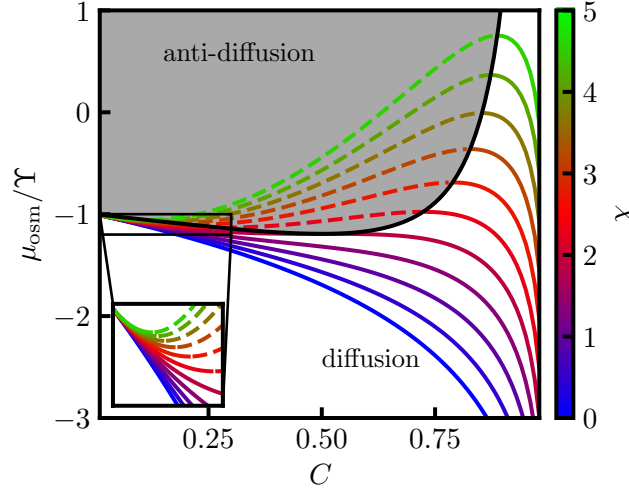
Figure 4.7.: Osmotic contribution $\mu_{\mathrm{osm}}/\Upsilon = \ln(1 - C) - 1 + \chi C^2$ to the evaporation rate for $\chi \in \{0..5\}$. $\mu_{\mathrm{osm}} > 0$ increases the rate of evaporation while $\mu_{\mathrm{osm}} < 0$ decreases it. The region of anti-diffusion is marked in dark gray and diffusion in white. Its boundary is given by $1 - 2\chi(1 - C)C = 0$.

C approaches one. Since $\mu_{\mathrm{osm}}(\chi = 1.5) < 0\,\forall C$, the osmotic pressure purely decreases the rate of evaporation, especially at higher concentrations. This behavior is reflected in panel (g). As C locally grows, the effect becomes more apparent. It slows down the growth of C_{max}, whereas the less concentrated surrounding liquid experiences a relatively higher rate of evaporation due to the weaker osmotic pressure. This, and the relatively small diffusive flux $J_{2,\mathrm{diff}}$ contribute to a broadening of the local maxima of the concentration C (panel (h)). Pe^{-1} is chosen to be relatively small in order to separate the diffusive time scale from the other time scales. The slowing rate of evaporation with increased solute concentration is an expected effect since the solute is non-volatile. This has previously been seen in a convection-diffusion model with evaporation in the context of gelation in spin-coating, however, the phenomenon is attributed to increasing viscosity and skin formation there [BMS89]. Other works employ lubrication approximated models with concentration dependent viscosities in order to investigate drying films and droplets. There, the evaporative flux decreases with increasing solute concentration due to a power law or a quadratic dependence, respectively [SREP01, TVI11]. The aforementioned development of concentration maxima outside of the droplet is unrelated to diffusion. This is verified in App. A.5 by turning off diffusion.

In the end the simulation achieves homogeneous concentration at finite droplet size. Figure A.6 in the appendix shows the rates $\nabla \cdot J$ instead of the fluxes for better quantitative comparison.

In the following we present select parameter studies in order to provide more impressions of the binary mixture system. Figure 4.8(a) shows space-time plots of sessile droplets at constant μ. The chemical potential is varied for each simulation, showing the transition from condensation to evaporation.

For $\mu = 0, 2, 4$ smaller droplets spontaneously condense and then coalesce with the central droplet as more material is added to the system until a flat film remains. Since only the solvent is volatile, the concentration decreases. For longer time scales we expect C to become homogeneous due to mixing. For $\mu = -2, -4$ the droplet does not fully evaporate and approaches a stationary
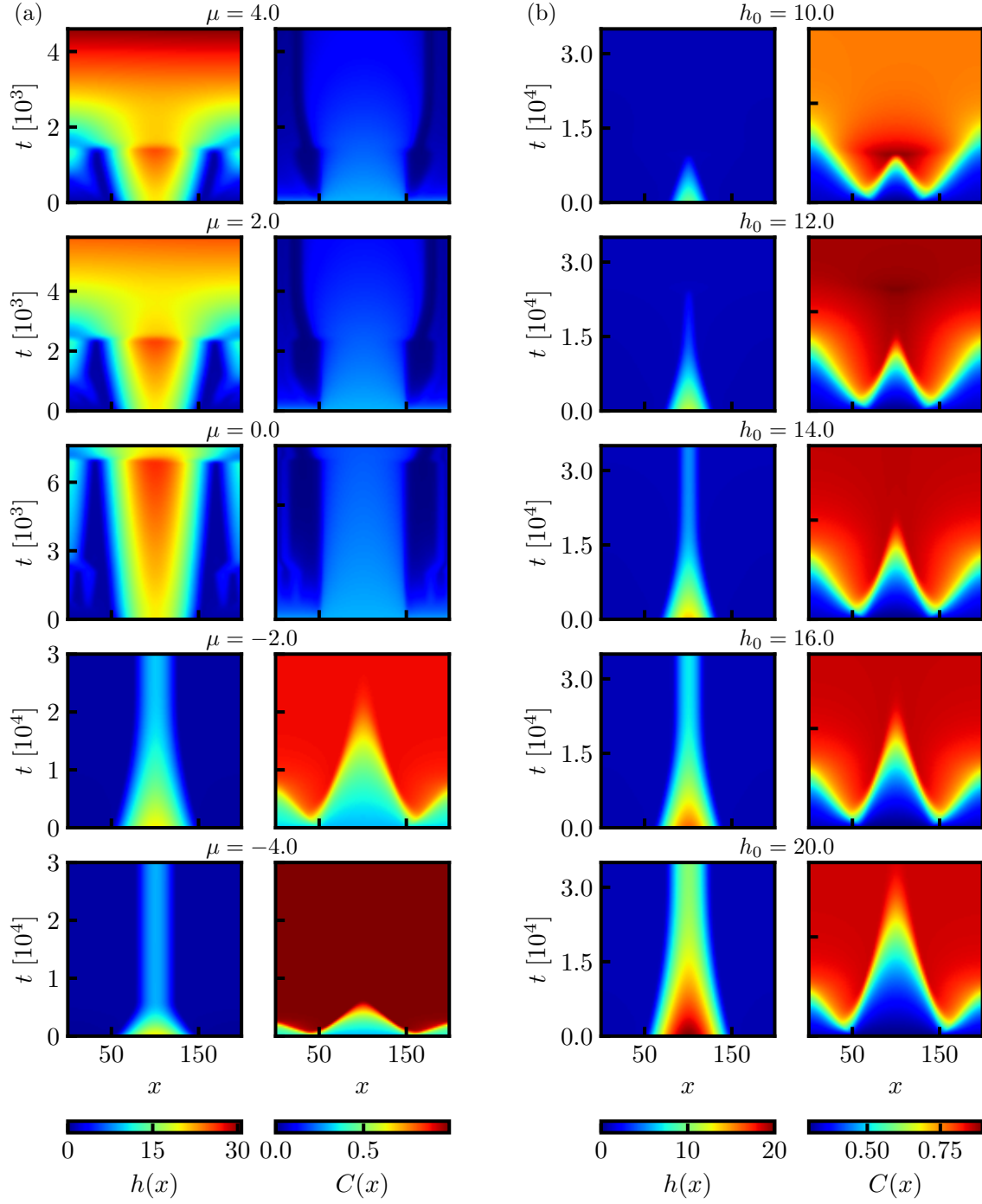
Figure 4.8.: Space-time plots of film height h and solute concentration C for a volatile droplet of a binary mixture on a horizontal substrate described by Eq. (2.126)-(2.127) with $g = 0$, $v = 0$, $\alpha = 0$. See Sec. 2.5.4 for the initial conditions. The common parameters are $\chi = 1.5$, $\mathrm{Pe}^{-1} = 10^{-4}$, $\Omega = 0.001$, $\Upsilon = 1$, $L = 200$ and $N = 256$. (a) Parameter study of $\mu \in \{-4, -2, 0, 2, 4\}$ at $h_0 = 20$. (b) of $h_0 \in \{10, 12, 14, 16, 20\}$ at $\mu = -1.8$.

but smaller droplet. The concentration grows throughout the domain while C_{max} shifts into the precursor region, broadens and approaches a homogeneous profile. Note that the stationary droplet at $\mu = -4$ is smaller than at $\mu = -2$ and the equilibrium concentration is higher. The existence of stationary droplets contrasts with the behavior of the TFE for a simple volatile liquid for which no stable droplet solutions are known. Interestingly, the binary mixture model does not only have stable droplet solutions but they exist over relatively large parameter ranges as well. The major difference is the presence of a second component and concurrently the osmotic pressure that decreases the rate of evaporation. The solute represents an additional degree of freedom that is allowed to adjust, such that evaporation stops, thus resulting in a stable droplet. Note that the time scales shown in Fig. 4.8 (a) are not necessarily equal. Not only do the dynamics slow down when approaching the threshold between evaporation and condensation but, in the case of condensation, material is injected into the system which causes film heights to grow, thereby making the system stiffer. The initial condition selects which stationary solution appears in the dynamics. In Fig. 4.8 (b) the maximum height h_0 is varied, showing that for $h_0 = 10$ the droplet will evaporate to a flat film, while for larger h_0 a stationary droplet remains. We understand this process as follows: As solvent evaporates across the whole domain, material convects from the droplet into the precursor region as discussed previously, i.e., the droplet loses solute by convection and solvent by evaporation. Since solute is conserved, a smaller sized droplet will remain as long as enough material exists for both the droplet and the precursor to maintain the homogeneous equilibrium concentration, otherwise the final state will be a flat film.

It is possible to make some analytical considerations for the stationary droplet solutions. Consider the evaporative flux

$$J_{\text{evap}} = -\Omega \left[-\Delta h + f'(h) + \mu_{\text{osm}}(C) - \mu \right]. \tag{4.14}$$

It must vanish for a stationary solution. For spatially homogeneous C this implies that

$$-\Delta h + f'(h) = const. \tag{4.15}$$

and the convective fluxes vanish as well. For stationary states of constant C the diffusive fluxes are 0, too. Therefore, it is sufficient to analyze $J_{\text{evap}} = 0$. Across a flat film, the precursor region of a droplet or its inflection point all possess vanishing curvature

$$\Delta h = 0. \tag{4.16}$$

We introduce

$$\tilde{\mu} := \mu_{\text{osm}} - \mu \tag{4.17}$$

as a shorthand notation. One can now solve $J_{\text{evap}} = 0$ for h

$$0 = -\Omega \left[f'(h) + \tilde{\mu} \right]. \tag{4.18}$$

The only real results are

$$h_p = \left(\frac{2}{1 + \sqrt{1 + 4\tilde{\mu}}} \right)^{\frac{1}{3}} = \left(\frac{2}{1 + \sqrt{1 + 4 \left(\Upsilon \left(\ln(1 - C) - 1 + \chi C^2 \right) - \mu \right)}} \right)^{\frac{1}{3}} \tag{4.19}$$

$$h_i = \left(\frac{2}{1 - \sqrt{1 + 4\tilde{\mu}}} \right)^{\frac{1}{3}} = \left(\frac{2}{1 - \sqrt{1 + 4 \left(\Upsilon \left(\ln(1 - C) - 1 + \chi C^2 \right) - \mu \right)}} \right)^{\frac{1}{3}}. \tag{4.20}$$
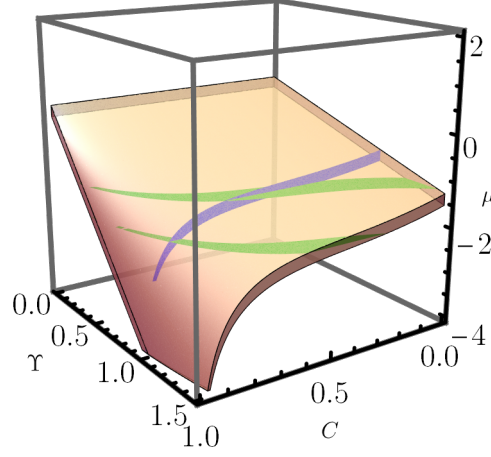
Figure 4.9.: Parameter space of possible stationary droplets with constant concentration C for the volatile binary mixture system. A subset of Eq. (4.21) at $\chi = 1.5$ is shown. Cross-sections at $\Upsilon = 1$ (blue) and $\mu = -1.2, -1.8$ (green) are depicted as well. The parameter set $(\Upsilon, \mu) = (1, -1.8)$ is the same as in Fig. 4.6. Not the full range of C but only $0 \leq C \leq 0.99$ is shown. $\mathcal{D}$ does diverge for all $\Upsilon > 0$ as $C \to 1$.

See Appendix A.8 for intermediate steps. As long as both values exist, stationary droplets exist. It follows that (C, χ, Υ, μ) must be part of the set

$$\mathcal{D} := \{(C, \chi, \Upsilon, \mu) \mid 0 < \sqrt{1 + 4\left(\Upsilon\left(\ln(1 - C) - 1 + \chi C^2\right) - \mu\right)} < 1\}. \tag{4.21}$$

The lower boundary arises from the positivity of the radicand while the upper one from that of the denominator. Figure 4.9 shows a subset of this parameter space for $\chi = 1.5$. At $C = 0$ it is bounded from above by

$$\mu_{\max}(C = 0) = \max(f'(h)) - \Upsilon = \frac{1}{4} - \Upsilon. \tag{4.22}$$

and below by

$$\mu_{\min}(C = 0) = -\Upsilon \tag{4.23}$$

$\Upsilon = 0$ recovers the case of a simple liquid. Overall, the set's μ-range is mostly bounded, except for $C \to 1$. In this limit steady state droplets are only possible for diverging μ. Note that Fig. 4.9 only shows the interval $0 \leq C \leq 0.99$. The divergence of $\mathcal{D}$ for $C \to 1$ does occur for any $\Upsilon > 0$. Cross-sections at $\Upsilon = 1$ (blue), $\mu = -1.8$ and $\mu = -1.2$ (green) are depicted as well showing that the parameter set $(\Upsilon, \mu) = (1, -1.8)$ in Fig. 4.6 allows at most

$$0.846 < C < 0.894 \tag{4.24}$$

which conforms with the measured homogeneous concentration of

$$C = 0.854. \tag{4.25}$$

Judging from Fig. 4.9 stationary droplet solutions with smaller concentrations may exist for higher Υ or μ values. Remember that C is assumed to be homogeneous for above considerations

which means that solutions with inhomogeneous C may exist as well, although it is unlikely due to diffusion and osmosis.

We verify the properties of $\mathcal{D}$ further by performing two more simulations. Figure 4.10 shows how for $(\Upsilon = 0.1, \mu = -4)$ the concentration C approaches unity (panel (a.1)) and the osmotic pressure μ_{osm} diverges ((panel (b.1)), causing the system to become too stiff. If the droplet contains enough solute to supply the precursor and to retain its curvature the final state will still be a droplet, otherwise a flat film will remain. Whereas for $(\Upsilon = 1, \mu = 1)$ in Fig. 4.10 the
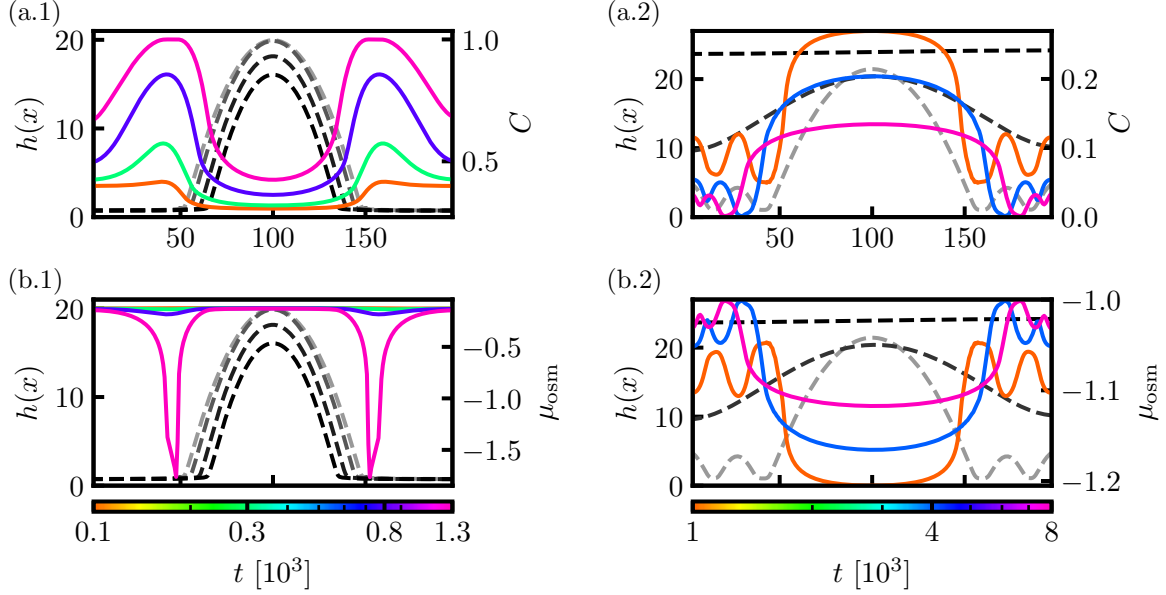

Figure 4.10.: Snapshots from the time evolution of an evaporating droplet of a binary mixture on a horizontal substrate at times labeled on the color bars. The parameter sets are chosen below (1) and above (2) the parameter set of possible steady droplet states shown in Fig. 4.9. Film height (left axis, dashed, black) and (a) solute concentration C (b) osmotic pressure μ_{osm} (right axis, solid, color). The color bars at the bottom map each color to a specific t. The governing equations are Eq. (2.126)-(2.127) with $g = 0$, $v = 0$, $\alpha = 0$. See Sec. 2.5.4 for the initial conditions. The remaining parameters are Pe_1^{-1}, $\mathrm{Pe}_2^{-1} = 1, 10^{-4}$, $\chi = 1.5$, $\Omega = 10^{-3}$, $\Upsilon_1, \Upsilon_2 = 0.1, 1$ and $\mu_1, \mu_2 = -4, 1$.

droplet grows, new droplets condense and then coalesce. Diffusion will eventually equalize C, leaving a flat film of homogeneous concentration, see panel (a.2).

Since the initial condition used here is not a stationary solution and the calculations are done with direct numerical simulations, it is likely that these droplet solutions are stable. The reader is referred to App. A.9 for a stability test in which a droplet solution is perturbed by white noise. Previously, it has been mentioned that μ_{osm} decreases the rate of evaporation. In conjunction with convection, induced by precursor gradients, C_{max} shifts away from the droplet into the precursor region. An interesting case is $\Upsilon = 0$ which turns off the osmotic contribution. Such a simulation is shown in Fig. 4.11. As in previous cases the concentration increases in the contact line region at early times (panel (a)). However, C_{max} clearly shifts into the precursor region due to convection, past old contact line positions (panel (b)). Diffusion smooths out the
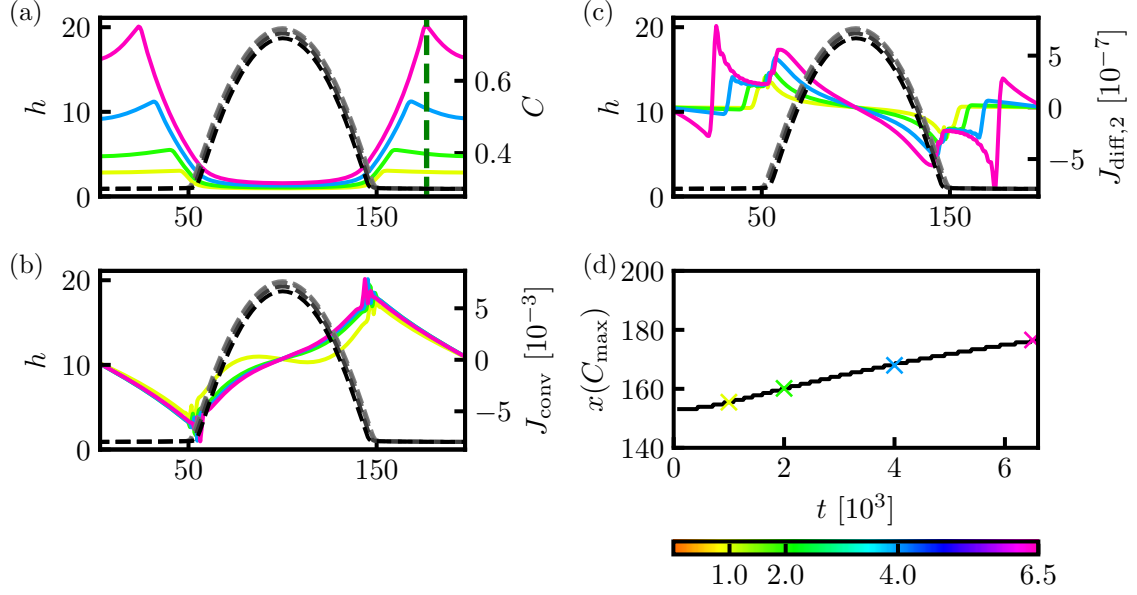
Figure 4.11.: Time evolution of an evaporating droplet of a binary mixture on a horizontal substrate at times labeled on the color bar. (a)-(c) Film height (left axis, dashed, gray scale). The right axis shows (a) solute concentration C (b) convective flux J_{conv} (c) diffusive solute flux $J_{\text{diff},2}$ in colors. (d) Position of right-hand local concentration maximum $x(C_{\text{max}})$. Note, that the step-like behavior is a result of the spatial discretization. $x(C_{\text{max}}, t = 6.5)$ is depicted as a dark green line in (a). The color bar is depicted at the bottom, mapping each color to a specific t. The governing equations are Eq. (2.126)-(2.127) with $g = 0$, $v = 0$, $\alpha = 0$. The remaining parameters are $\text{Pe}^{-1} = 10^{-4}$, $\chi = 1.5$, $\Omega = 10^{-4}$, $\Upsilon = 0$ and $\mu = -1.6$.

concentration profile as can be judged from its sign (panel (c)). As J_{conv} is not changing much in time, $x(C_{\text{max}})$ shifts almost linearly (panel (d)). Note, that the step-like behavior is a result of the spatial discretization. This shows that setting $\Upsilon = 0$ is not a viable option for the prevention of the C_{max} shift. On a side note, the $\Upsilon = 0$ case needs to be specifically treated in the numerical implementation due to the divergence of the logarithmic term.

4.6. Gradients in the Precursor Region

The precursor of a static droplet is flat. In the previous section, we have shown that precursor gradients develop due to the interplay of evaporation and convection. In this section, we show that such gradients develop independent on how the precursor is initialized, unless the initial condition is already at equilibrium. We further show, that this effect is likely inherent to the precursor model. First, the simulation of Fig. 4.6 is repeated but with a precursor height that matches the expected equilibrium height $h_p(C = 0.854, \Upsilon = 1, \chi = 1.5, \mu = -1.8)$ according to Eq. (4.19). However, the initial concentration is purposefully kept at $C_0 = 0.3$ which does not match the expected equilibrium concentration.

Figure 4.12 (e.1) shows similarly to the previous simulation for $h_p(t = 0) = 1$ that although the

initial precursor height coincides with the final one, solvent evaporates from the precursor and is resupplied by convection originating from the droplet because C is not at equilibrium. Thus, height, concentration and pressure gradients develop. In the beginning, the precursor thins and then approaches its initial/equilibrium height again but this time with the correct equilibrium concentration.

Another interesting case is when $C_0 = 0.85$, which is close to equilibrium. Figure 4.12 (e.2) shows that the precursor behaves similarly to (e.1) but with less magnitude. It first becomes thinner accompanied by gradients and then relaxes to its equilibrium height. However, due to
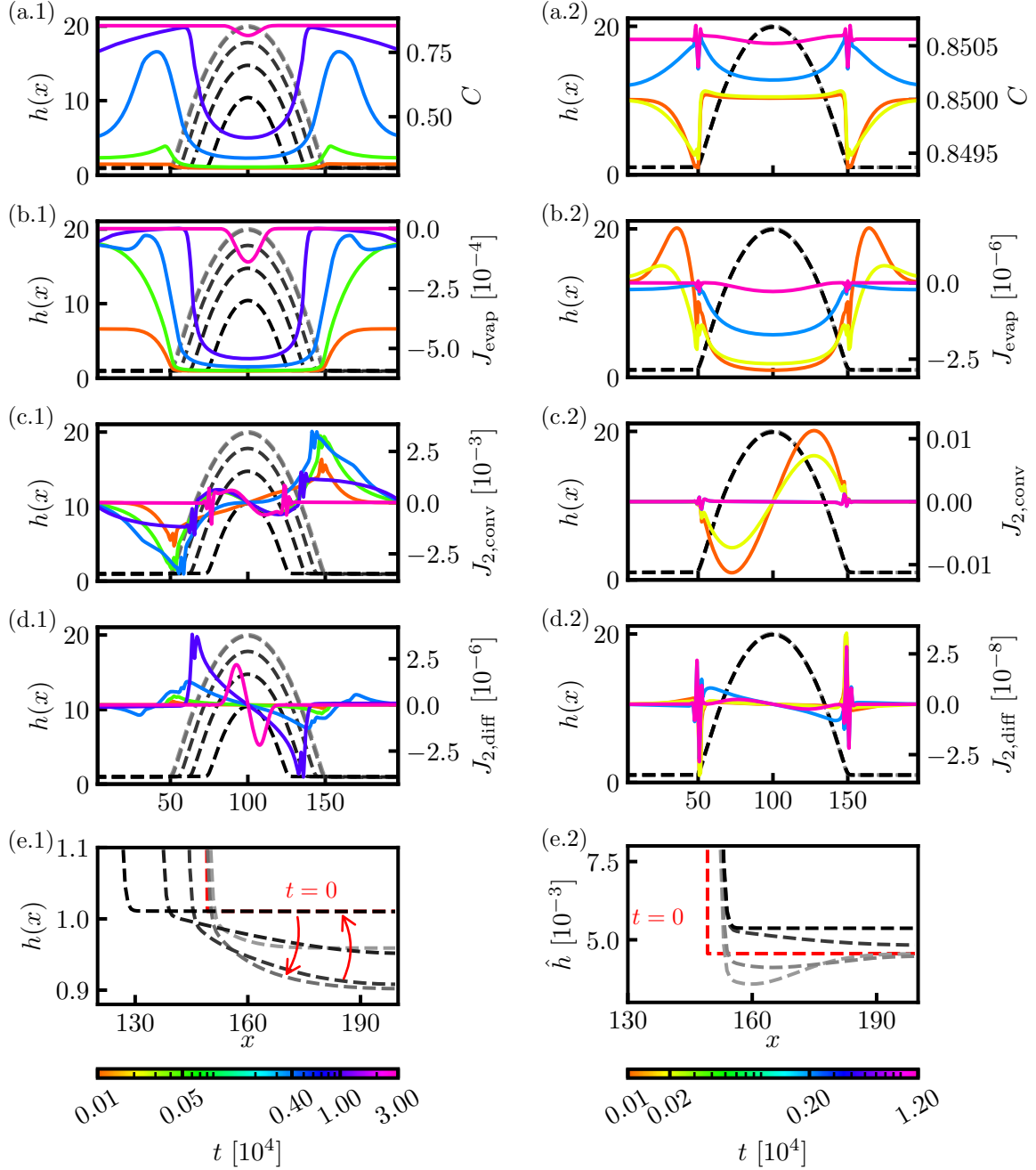
Figure 4.12.: Time evolution of a sessile volatile droplet of a binary mixture described by Eq. (2.126)-(2.127) with $g = 0$, $v = 0$, $\alpha = 0$. Film height h (left axis, gray scale) and other quantities (right axis, colored) are depicted at times labeled on the color bars. In contrast to Fig. 4.6 the precursor is initialized differently. (1) with the expected equilibrium height according to Eq. (4.19) $h_p(C = 0.854, \Upsilon = 1, \chi = 1.5, \mu = -1.8)$ but keeping $C_0 = 0.3$. (2) close to equilibrium with $h_p(C = 0.85, \Upsilon = 1, \chi = 1.5, \mu = -1.8)$ and $C_0 = 0.85$. The gray/black lines follow the same order as the colored ones, meaning that the darker the later the time. (a) solute concentration (b) evaporative flux J_{evap} (c) convective flux of solute $J_{2,\text{conv}}$ (d) diffusive flux of solute $J_{2,\text{diff}}$ (e) zoom of the precursor region, $\hat{h} = h - 1$. The profile at $t = 0$ is separately depicted in red. The remaining parameters are $h_0 = 20$, $\text{Pe}^{-1} = 10^{-4}$, $\chi = 1.5$, $\Omega = 0.001$, $\Upsilon = 1$ and $\mu = -1.8$.

the closeness to equilibrium barely any solute evaporates. Thus, the final state is different from the previous case with a slightly smaller concentration $C \approx 0.8506$, which is still within the predicted range of Eq. (4.24), and much larger h_{max}. Another case has previously been shown in Fig. 4.8.(b). If the initial droplet is smaller at $h_0 = 10$, the final state is a flat film. However, no new observations can be made in terms of precursor dynamics. A breakdown of the simulation is shown in Fig. A.11 in the appendix. Nevertheless, these case studies show that the volatile binary mixture system possesses regions of multistability between at least droplet and flat film states.

The precursor gradients are present in the TFE for a simple liquid as well

$$\partial_t h = -\nabla \cdot \left[\frac{h^3}{3} \nabla \left(\Delta h - f'(h) \right) \right] - \Omega \left[-\Delta h + f'(h) - \mu \right]. \tag{4.26}$$
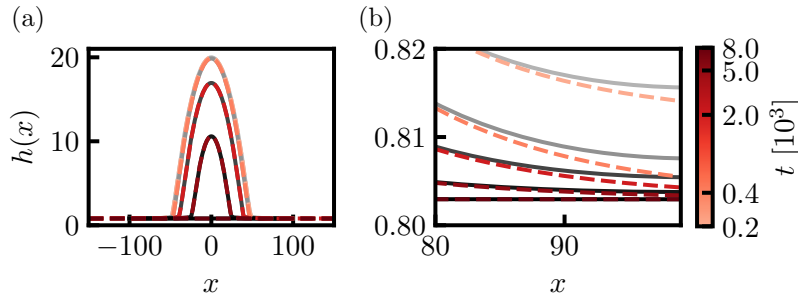
Figure 4.13.: Selected height profiles from a time simulation an evaporating droplet of a simple liquid on a horizontal substrate. Gray scale represents a simulation for $L_x = 200$, $N_x = 256$ while the red scale is for $L_x = 300$, $N_x = 384$. (a) full domains (b) closeup of edge at $x = 100$. The governing equation is Eq. (4.26). The remaining parameters are $h_0 = 20$, $\Omega = 0.001$ and $\mu = -1.8$

Figure 4.13 shows two simulations of an evaporating droplet of a simple liquid for two different domain sizes. The simulation on the smaller domain is depicted in gray scale while the larger one is depicted in red scale. The closeup at the edge of the small domain in (b) shows that the

precursors do not overlap. The gradients depend on domain size, due to the Neumann boundary conditions.

In contrast to the binary mixture system, here, stationary droplets are unstable. Taking a stable stationary droplet from the non-volatile case, perturbing it with some noise and turning on evaporation always results in complete evaporation, see Fig. 4.14. Naturally, evaporation in (a) occurs faster due to $\Omega = 1$ while it takes longer in panel (b) for $\Omega = 0.1$. Due to the computational limitations of FDM simulations, smaller Ω and noise amplitudes than in Fig. 4.14 have been tested by utilizing the FEM library *oomph-lib* [HH06], verifying the unstable droplets[1], see Fig. A.12 which shows the vanishing droplet even at zero noise and $\Omega = 10^{-3}$. Overall, this
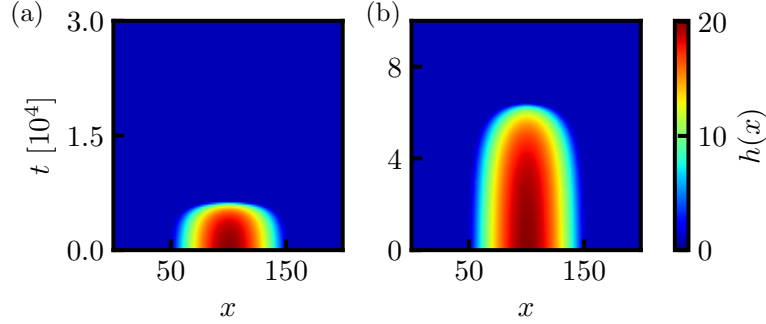

Figure 4.14.: Space-time plots of $h(x)$ for an evaporating droplet of a simple liquid on a horizontal substrate as described by Eq. (4.26). The initial condition is taken from the non-volatile case after the droplet has fully converged and then perturbed by white noise of amplitude (a) 10^{-5} ($\Omega = 1$), (b) 10^{-2} ($\Omega = 0.1$). $\mu = 0.01568$ is chosen as measured from the converged droplet $\mu = \mu_l = -\partial_{xx}h + f'(h)$. The remaining parameters are $L_x = 200$, $N_x = 256$ and $h_0 = 20$.

means that the precursor gradients are not a new effect stemming from extending the TFE to two components but a consequence of evaporation driving the droplet out of equilibrium and the Neumann boundary conditions. As long as both order parameter fields are not in equilibrium, it does not matter how the precursor is initialized. The dynamics introduce gradients to the precursor nonetheless. Further, judging from the previous section, the precursor gradients are not directly related to the local concentration maxima moving out of the droplet.

4.7. Diffusion-limited Precipitation

In contrast to the simulation of the full deposition model in Sec. 4.4 the case of a sessile drop of a volatile binary mixture Sec. 4.5-4.6 does not exhibit stiffness except at vanishing inverse Peclét number. In this section, the phase-field part is isolated by investigating the simpler Xu Meakin system of Sec. 2.4.3 for diffusion-limited precipitation. It models precipitation from a mixture described by a normalized solute concentration field c. Liquid and solid phase are indicated by the phase-field ϕ, i.e., the presence of precipitate is only qualitatively represented by ϕ. The

---

[1]Many thanks to Simon Hartmann for quickly setting up the code and corresponding simulations.

considered model is

$$\partial_t \phi = \frac{1}{\text{Pe}_{\text{xm}}} \left(\Delta\phi - \partial_\phi f_{\text{xm}}(\phi, c, \lambda) - \kappa|\nabla\phi| \right), \tag{4.27}$$

$$\partial_t c = \Delta c + \alpha \partial_t \phi. \tag{4.28}$$

Note, that, with the next section in mind, the relations gained from the thin-interface limit Eq. (2.93),(2.94),(2.101) will not be applicable in the full model due to the different dynamic equations for the solute. The parameters are therefore treated phenomenologically here. All simulations in this section consider precipitation and subsequent formation of fingers from an oversaturated homogeneous liquid for varying control parameters. Circular Dirichlet boundary conditions and a disc of radius r with Gaussian profile with white noise as the IC for ϕ are employed

$$\phi(x, y, 0) = 1 - 2e^{-\ln(2)\frac{(x-L_x)^2 + (y-L_y)^2}{r^2}}, \tag{4.29}$$

$$c(x, y, 0) = c_0. \tag{4.30}$$

As mentioned in Sec. 2.4.1 planar interfaces are unstable due to Mullins-Sekerka instability in this system. In the absence of curvature effects the dispersion relation is simply linear growth which means that the smallest wavelength is limited by grid resolution. Further, the curvature term $|\nabla\phi|\kappa$ needs to be explicitly treated as

$$\lim_{|\nabla\phi|\to 0} \kappa = 0. \tag{4.31}$$
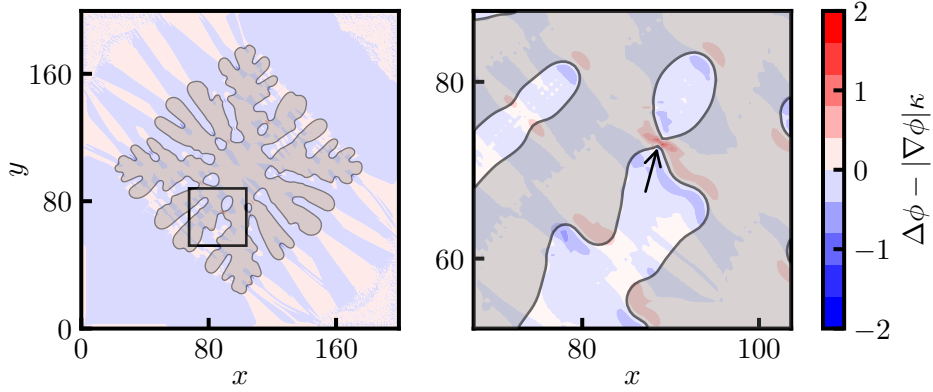
Figure 4.15.: Snapshot of a precipitating mixture limited by diffusion in a 2D domain and described by Eq. (2.97)-(2.98). Initial conditions are a Gaussian disc with white noise for ϕ and constant concentration c_0, cf. Eq. (4.29)-(4.30). Dirichlet boundary conditions on a circular domain. The $\phi = 0$ level set is depicted as solid black line while $\phi = -1$ is shaded in gray. The background is colored from blue to red according to the anisotropic part of the curvature term $\Delta\phi - |\nabla\phi|\kappa$. The right panel is a zoom. The system parameters are: $L_x = L_y = 200$, $N_x = N_y = 384$, $c_0 = 0.5$, $\alpha = 0.5$, $\lambda = 1.8$, $\text{Pe}_{\text{xm}} = 1$.

Furthermore, the curvature term becomes problematic at sharp corners where $\nabla\phi$ is ambiguous [Set99, SB07]. This can be seen in the simulation snapshot in Fig. 4.15. The left panel shows

the $\phi = 0$ contour as a black solid line. The solid phase $\phi = -1$ is slightly grayed while the background is colored according to the anisotropic part of the curvature

$$\Delta\phi - |\nabla\phi|\kappa = \frac{\nabla\phi \cdot \nabla|\nabla\phi|}{|\nabla\phi|}, \tag{4.32}$$

using

$$|\nabla\phi|\kappa = |\nabla\phi|\nabla \cdot \left(\frac{\nabla\phi}{|\nabla\phi|}\right) = \frac{\Delta\phi|\nabla\phi| - \nabla\phi \cdot \nabla|\nabla\phi|}{|\nabla\phi|} = \Delta\phi - \frac{\nabla\phi \cdot \nabla|\nabla\phi|}{|\nabla\phi|}. \tag{4.33}$$

Fingers have emerged from the circular nucleus, followed by tip-splitting. Four main branches are visible pointing to the left, right, top and bottom. This can be classified as a dendrite. A zoom of two sharp corners, which approach each other, is shown in the right panel. The large values indicate how stiff the system becomes as the corners sharpen or approach each other, practically halting the simulation. Sun and Beckermann investigated the behavior of the interface motion in dependence on b' which corresponds to $\frac{1}{\text{Pe}_{\text{xm}}}$ in the Xu Meakin model with a finer grid resolution than is used here and forward Euler method [SB07]. Notice the broken fourfold rotational symmetry of the full contour due to white noise. This symmetry stems from the discretization grid.

The formation of dendrites naturally depends on the system parameters. Figure 4.16 shows a parameter study in α and λ. They control the amount of solute taken upon precipitation and the steepness of the local potential, respectively. Again, $\phi = 0$ contours are shown but for two different times $t_1 = 35$ and $t_2 = 175$. The colored background denotes the $c(x, y, t_2)$ profile. Remember that negative c simply correspond to concentrations below the equilibrium concentration. Some simulations, labeled with κ, are limited by the aforementioned numerical problem of resolving sharp corners. These parameter sets do not always result in a stiff system. Depending on the perturbations such corners may develop early on in the simulation or not at all before the solid phase reaches the circular boundary. Comparing the t_1 contours one can see that simulations start with growth of the circular interface before it becomes unstable due to the Mullins-Sekerka instability. From there, fingers grow and split while extracting solute from the liquid. The onset of instability can be delayed by decreasing α. Since α controls the partition coefficient, larger α deplete more solute which in turn slows down dendrite growth as can be seen by the smaller areas covered by solid for $t = t_2$. Concurrently, the structures become more fractal. λ has a simpler effect, speeding up the dynamics as it increases which is expected since it controls the tilt of the local potential. Parameter sets ($\lambda = 2.0, \alpha = 0.3, 0.4$) in particular exhibit spontaneous precipitation outside of the initial nucleus leaving small islands of enclosed liquid as solute is mostly depleted. These will eventually be covered by solid on a longer time scale due to diffusion of solute from the boundary. Similarly to α, c_0 can affect the occurrence of aggregate growth or spontaneous precipitation as well (not shown here).

The effect of Pe_{xm} on the pattern formation is of interest as well since $\frac{1}{\text{Pe}_{\text{xm}}}$ takes on a similar role to σ in Eq. (2.112) of the full model. Contours of times t_1, t_2, t_3 and t'_1, t'_2, t'_3 are shown in a parameter study in Fig. 4.17. The structures are less fractal as Pe_{xm} increases since diffusion occurs faster and thus c is locally more homogeneous. At very large Pe_{xm} the system undergoes aggregate growth, however, the interface will become unstable on larger time scale unless the boundary is reached faster. Note that Fig. 4.17 (b) is simulated on a larger domain in order to observe longer time scales. In contrast to Fig. 4.15, most of the fractal patterns shown in Fig. 4.16-4.17 are less considered dendrites, but more seaweed-like, due to the absence of clear main branches. These may manifest for larger domain sizes and time scales.

Figure 4.16.: Snapshots of a precipitating mixture limited by diffusion in a 2D domain obtained from a parameter study in the source strength α and coupling parameter λ. The governing equations are Eq. (2.97)-(2.98). See Eq. (4.29)-(4.30) for the initial conditions. $\phi = 0$ level sets are depicted at $t_1 = 35$ and $t_2 = 175$. The background colors denote the $c(x, y, t_2)$ profile. Dirichlet boundary conditions are applied on a circular domain. The system parameters are: $L_x = L_y = 200$, $N_x = N_y = 304$, $c_0 = 0.5$, $\mathrm{Pe_{xm}} = 1$, $\alpha \in \{0.1, 0.2, 0.3, 0.4, 0.5\}$ and $\lambda = \in \{1.5, 1.6, 1.7, 1.8, 1.9, 2.0\}$.
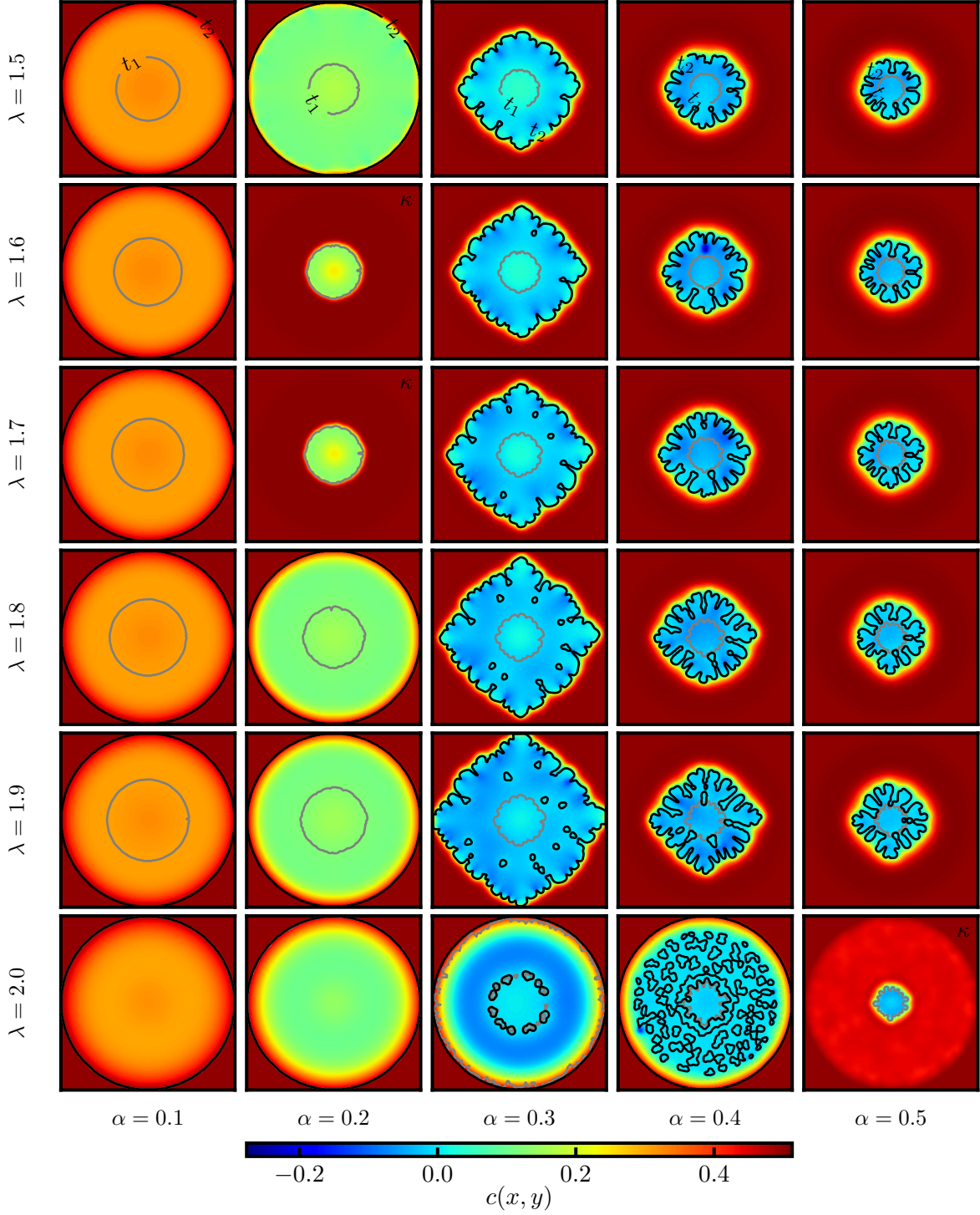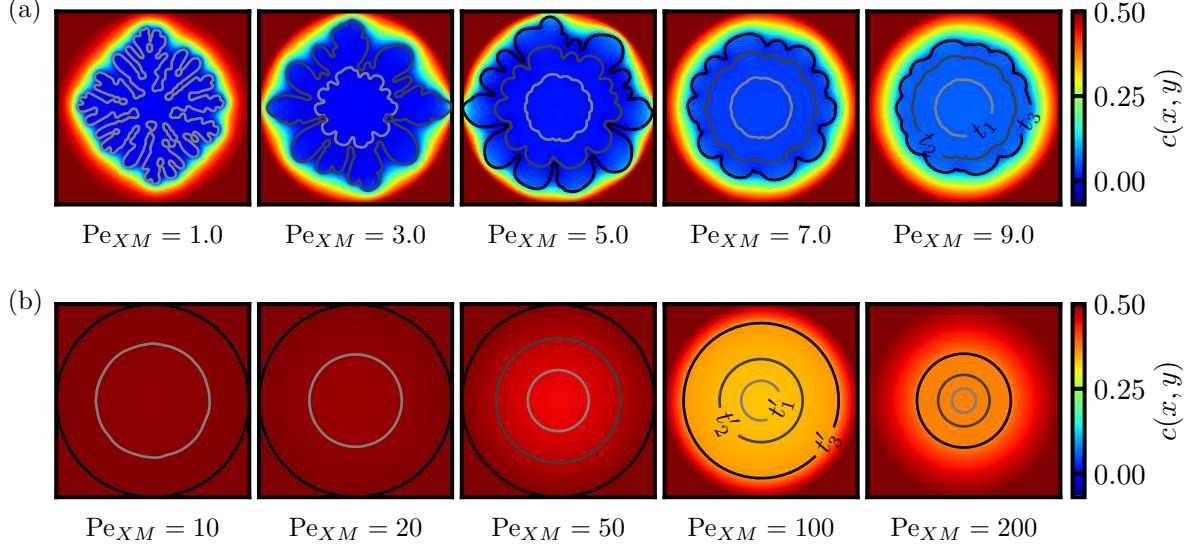
Figure 4.17.: Snapshots of a precipitating mixture limited by diffusion in a 2D domain obtained from a parameter study in the Peclét number $\text{Pe}_{\text{xm}} = 1$. The governing equations are Eq. (2.97)-(2.98). See Eq. (4.29)-(4.30) for the initial conditions. $\phi = 0$ level sets are depicted at times t_i. (a) at $t_1 = 500$, $t_2 = 1500$ and $t_3 = 2250$ on $L_x = L_y = 200$, $N_x = N_y = 304$. (b) at $t'_1 = 2 \cdot 10^4$, $t'_2 = 5 \cdot 10^4$ and $t'_3 = 10^5$ on $L_x = L_y = 600$, $N_x = N_y = 912$. The background colors denote the $c(x, y, t_3)$ profile. The concentration range is different from Fig. 4.16. Dirichlet boundary conditions are applied on a circular domain. The remaining system parameters are: $c_0 = 0.5$, , $\alpha = 0.5$ and $\lambda = 0.5$.

Figure 4.18.: (a) Snapshot of a precipitating liquid in a dip-coating geometry after transients have died out and solute has been deposited homogeneously. The substrate is two-dimensional and the system is described by Eq. (2.126)-(2.129). Film height h and deposit thickness ζ a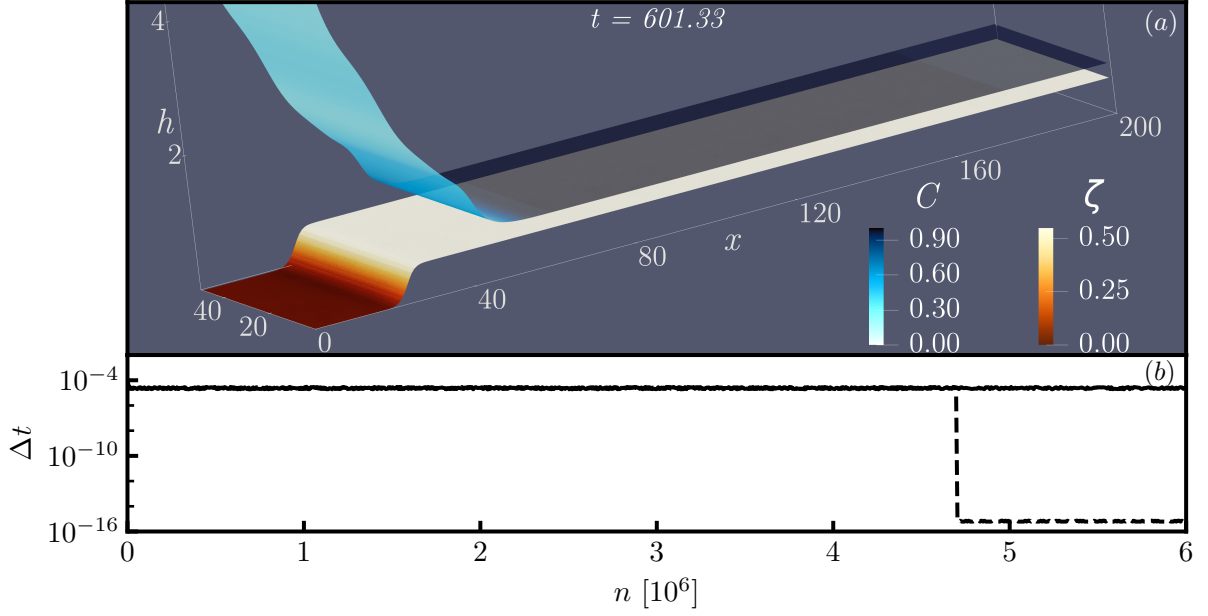re shown as surfaces. Their color mapping corresponds to the solute concentration C and once again the deposit thickness ζ, respectively. The pulling direction points towards positive x. The simulation is equivalent to the one in Fig. 4.4, however the mean curvature κ is turned off. (b) Adaptive time step Δt against the number of integration steps for $\kappa = 0$ (solid line) and $\kappa \neq 0$ (dashed line). The latter exhibits an abrupt drop in Δt at the onset of precipitation. See Sec. 2.5.4 for the initial conditions. The system parameters are $L_x = 200$, $L_y = 50$, $N_x = 256$, $N_y = 64$, $h_0 = 15$, $C_0 = 0.3$, $C_{\mathrm{eq}} = 0.35$, $v = 0.6$, $g = 10^{-3}$, $\beta = 2$, $\mathrm{Pe}^{-1} = 1$, $\chi = 1.5$, $\Omega = 0.008$, $\Upsilon = 1$, $\mu = -6$, $\alpha = 0.1$, $\lambda = 15$, $\Lambda = 1$, $\sigma = 1$.

4.8. Precipitation in a Dip-Coating Geometry

Following the previous investigations of various submodels, the remainder of this chapter is dedicated to the full model describing dip-coating of a volatile binary fluid including a deposition mechanism, see Eq. (2.126)-(2.129). Many results from Sec. 4.5-4.6 can be transferred to the full model since the phase-field dynamics only becomes relevant during deposition, i.e., above certain threshold concentrations.

4.8.1. Mean Curvature and Advection

The results of Sec. 4.5 and 4.7 indicate that the properties of the binary mixture model are mostly not responsible for the stiffness that has been shown in Sec. 4.4, with exceptions related to mixing parameters, i.e. Pe^{-1} or Υ. One source of stiffness is the mean curvature κ in the phase-field when $\nabla\phi$ becomes ambiguous. This can be easily verified by setting $\kappa = 0$. Figure 4.18 (a) shows the final frame of the example shown at the beginning of this chapter in Fig. 4.4 when the mean curvature is turned off. As before, precipitation occurs within the precursor and results in
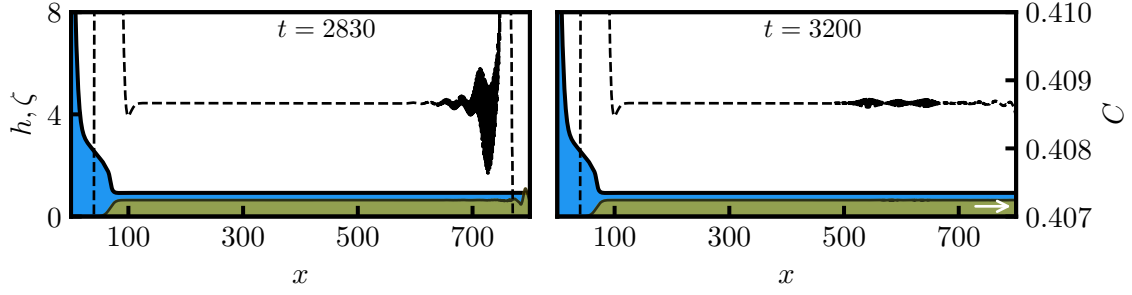
Figure 4.19.: Snapshots of a binary mixture with deposition mechanism in a dip-coating geometry on a 1D substrate described by Eq. (2.126)-(2.129). The state develops towards a homogeneous deposit. Film height h and solute concentration C are shown in blue and dashed black, respectively. The substrate is pulled towards the right. The solution is shown at times after the initial transient front has reached the right boundary. There, a numerical instability develops and propagates to the left, reflects at the left boundary and propagates to the right again. This process repeats until the instability dissipates. The governing equations are Eq. (2.126)-(2.129). The system parameters are $L = 800$, $N = 1024$, $h_0 = 20$, $C_0 = 0.3$, $C_{\text{eq}} = 0.4$, $v = 0.3$, $g = 10^{-3}$, $\beta = 2$, $\text{Pe}^{-1} = 10^{-3}$, $\chi = 1.5$, $\Omega = 0.02$, $\Upsilon = 1$, $\mu = -1.6$, $\alpha = 0.5$, $\lambda = 6$, $\Lambda = 0.2$, $\sigma = 1$.

a deposit of small height. However, no dendrites form. The front is planar and advances while homogeneously depositing solute. No stiffness occurs for the whole duration as can be seen in Fig. 4.18 (b) where the adaptive time step Δt is plotted against the number of integration steps for both cases. The stiffness of the simulation with $\kappa \neq 0$ is clearly depicted by the sudden drop in Δt. The fastest growing mode of the Mullins-Sekerka instability diverges in the absence of curvature effects. Since the grid resolution is fixed, this problem is always present in this model. Note that the preconditioning using a hyperbolic tangent for the signed distance function $n(\mathbf{x}, t)$ analyzed in [SB07, Gla01] is not useful here as it results in a constant positive contribution on the right-hand side of the evolution equation due to the modification of the double-well potential, see App. A.13. A proper asymptotic analysis would be required to identify a good transformation for ϕ. However, since it involves a set of complex equations for the liquid and thus for the concentration C, this is not pursued here. Instead, it is possible to avoid the numeric instability by choosing a sufficiently small [large] domain size [advection velocity] such that the fastest growing mode is still resolvable by the grid discretization before the pattern is advected out of the domain.

The investigation of the 2D domain is continued in Sec. 4.8.4 while the next few sections discuss 2D domains. Besides by the aforementioned the system is affected by more numerical instabilities, one being very typical for advection systems. Naively choosing centered stencils for the advection terms can lead to numerical dispersion as is known for the FTCS scheme (forward in time, centered in space) for the classic advection equation. In our case, the instability becomes noticeable as the initial transient front reaches the right boundary. The instability reflects between both boundaries and decreases in amplitude with time. Such an instability is briefly mentioned in Sec. 3.3. However, the simulation is not stiff here, indicating that the time scale of this transient is not too different from the physical time scale. Snapshots of the instability are shown in Fig. 4.19.

Previous long-wave models did not encounter this problem since the separation of length scales was smaller for the systems considered there, allowing the usage of single-precision second order FDM [KGFC10, Tew13]. Upwind schemes are a common way to deal with such problems but a purely backward differencing stencil results in instabilities developing at the left boundary. Fortunately, an asymmetric stencil that takes three points on the left and one on the right works for our system. On a side note, replacing all first derivatives by this stencil, which makes implementation simpler, does not make a difference here but will not be adopted since central differences are preferred when the x-symmetry is not broken.

4.8.2. Parameter Choices and Modeling Aspects

Since the full model depends on 14 (effective) parameters, excluding the Dirichlet boundary conditions, it is sensible to discuss some of their values or limitations. The transfer velocity v is a very important experimental control parameter. The generalized system is expected to at least possess height profiles similar to the simple liquid case.

The previously shown profiles show very small deposit thicknesses. They are smaller than the precursor which is related to the relatively small bath height h_0, which in turn means that the precursor is much larger than in reality. A no compromise approach would be to increase h_0 on the left boundary which leads to more extracted liquid and thus higher ridges in the region of time-periodic states (TPS). However, the FDM implementation is limited here, allowing at most $h_0 \approx 20$ before resolving the contact line becomes too difficult. Instead a smaller inclination $\beta = 1$ is chosen for a similar effect at smaller h_0. This value for β is also used when simulating ensembles of simple sliding drops [WTEG+17] and lies below values considered in bifurcation analysis of the simple non-volatile liquid case [TWGT19]. We choose the dimensionless gravitational acceleration $g = 10^{-3}$ to be relatively small and do not include its contribution to the evaporative flux. The choice of the mixing parameter $\chi = 1.5$ has been discussed in Sec. 4.5. The equilibrium concentration C_{eq} in Eq. (2.107) does not represent a sharp precipitation threshold as $\lambda(C - C_{eq})$ only tilts the local potential f_{xm}, thereby modeling the deposition process as a first order phase transition. As mentioned in Sec. 2.4.3 the phases $\phi^* = \lambda(C - C_{eq})$ and $\phi = 1$ switch stabilities at $\lambda(C - C_{eq}) = 1$, i.e., for $\lambda(C - C_{eq}) > 1$ the phase transition between $\phi = 1$ and $\phi = \phi^* > 1$ is possible. For that, $\partial_t \phi$ must be positive. This means that solute is extracted from, at that stage, non-existing deposit. This is possible in this model since no mechanism exists that prevents ζ from becoming negative. The resulting unphysical third phase ϕ^* would then possess more solute than initialized or injected from the bath. $\phi^* = \lambda(C - C_{eq}) <= 1$ holds for any $C, C_{eq} \leq 1$ if $\lambda \leq 1$ but then $\phi_s = -1$ never becomes a local maximum and much stronger perturbations would be required. Instead, we adopt $\lambda \geq 3$ and initialize simulations with $\phi(x, y, 0) = 0.99$ which is still physically liquid but primes the phase-field to precipitate once C becomes large enough. Note that the Dirichlet BC is kept at $\phi_0 = \phi(x, y = 0) = 1$. Setting the initial condition not to exactly match an extremum of the local potential has previously been done in first order phase transition models as well, one of which is the reduced model for the Langmuir-Blodgett transfer presented in Sec. 2.6 [KGFT12]. However, it is taken a step further there, i.e., the Dirichlet BC is set to $c_0 = -0.9$. Setting $\phi_0 = 0.99$ in contrast to, for example, $\phi = 0.9999$ does not result in a qualitative difference (not shown here).

Remember the precursor behavior analyzed in Sec. 4.5: Upon evaporation the solute concentration grows mostly in the precursor region. This effect is naturally still present in the full model. In order to exclude this effect we introduce a height dependent switch $m(h)$ that turns $J_{\text{diff},i}$, J_{evap} and $\partial_t \phi$ off as h approaches a chosen height of $h_1 = 1.1$ close to the precursor thickness.
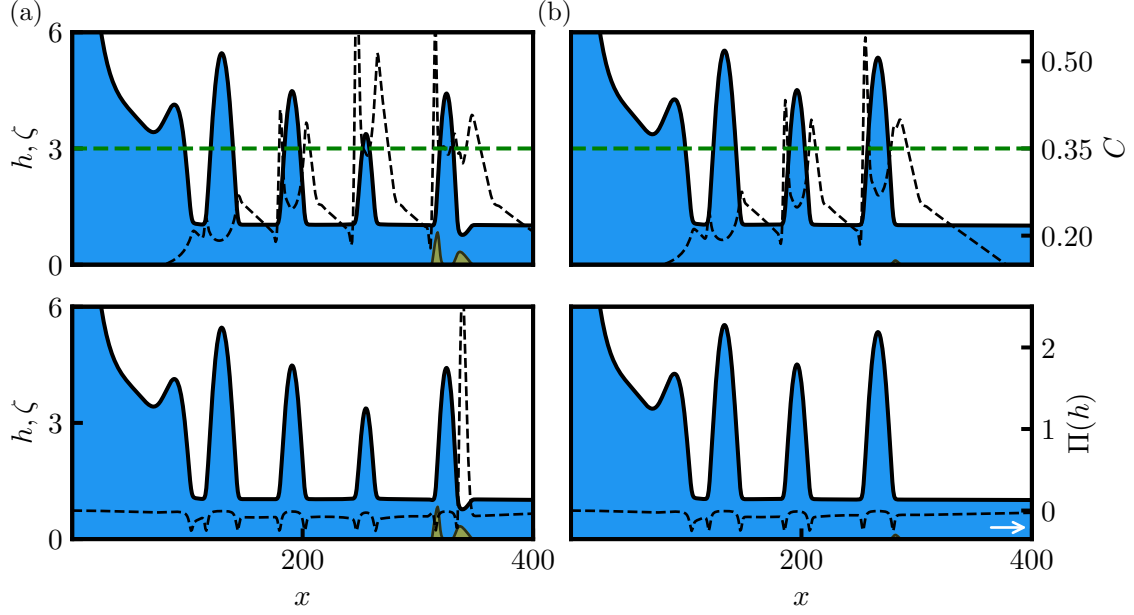
Figure 4.20.: Snapshots of liquid ridges of a binary mixture with deposition mechanism in a dip-coating geometry on a 1D substrate described by Eq. (2.126)-(2.129). The profiles are taken at the onset of deposition. Film height h(blue), solute concentration C (dashed black, top) and disjoining pressure $\Pi(h)$ (dashed black, bottom), respectively. The equilibrium concentration C_{eq} is shown in dashed green. The substrate is pulled towards the right. (a) height dependent switch according to Eq. (4.34)-(4.36) (b) including Eq. (4.37). The system parameters are $L = 800$, $N = 1024$, $h_0 = 20$, $C_0 = 0.1$, $\phi_0 = 0.99$, $v = 0.1$, $g = 0.001$, $\beta = 1$, $\text{Pe}^{-1} = 10^{-3}$, $\chi = 1.5$, $\Omega = 0.004$, $\Upsilon = 1$, $\mu = -1.6$, $C_{\text{eq}} = 0.35$, $\alpha = 0.2$, $\lambda = 20$, $\Lambda = 1$, $\sigma = 5$.

Namely, we use and replace

$$m(h) = \frac{1}{2}(\tanh(35(h - h_1)) + 1) \tag{4.34}$$

$$J_{\text{evap}} \rightarrow m(h)J_{\text{evap}}, \tag{4.35}$$

$$J_{\text{diff,i}} \rightarrow m(h)J_{\text{diff,i}} \qquad i = 1, 2, \tag{4.36}$$

$$\partial_t \phi + \mathbf{v}\nabla\phi \rightarrow m(h)(\partial_t \phi + \mathbf{v}\nabla\phi) \tag{4.37}$$

in Eqs. (2.126)-(2.129).

Figure 4.20 (a) shows 1D profiles of periodic ridges at the onset of precipitation, still without using Eq. (4.37). While the ridges initially grow by taking liquid from the bath, over time their growth is inhibited by evaporation, locally increasing C. Once a ridge detaches , its surrounding precursor possesses higher solute concentrations than in the beginning. As ridges shrink further they leave behind precursors of even higher concentration. Once $C > C_{\text{eq}}$ precipitation becomes possible, particularly in the precursor region. It is first triggered at the front. The film height significantly decreases which causes the disjoining pressure to sharply increase and the system to become stiff. This effect does not always occur. If precipitation and evaporation are slow enough, it is possible that convection fills up the missing liquid such as in the previous examples
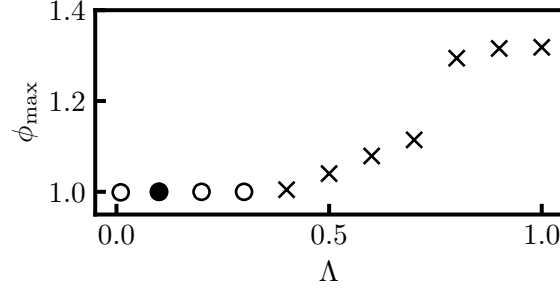
Figure 4.21.: Phase-field maximum $\phi_{\mathrm{max}} = \max(\phi(x,t))$ with varying $\Lambda \in \{0.1, ..., 1.0\}$ for a precipitating liquid in a dip-coating geometry. $\phi_{\mathrm{max}} > 1$, $\phi_{\mathrm{max}} \leq 1$ and $\Lambda = 0.2$ are marked by crosses, circles and a filled circle respectively. The governing equations are Eq. (2.126)-(2.129). The system parameters are $L = 800$, $N = 1024$, $h_0 = 20$, $C_0 = 0.3$, $\phi_0 = 0.99$, $v = 0.1$, $g = 0.001$, $\beta = 1$, $\mathrm{Pe}^{-1} = 10^{-3}$, $\chi = 1.5$, $\Omega = 0.008$, $\Upsilon = 1$, $\mu = -1.6$, $C_{\mathrm{eq}} = 0.4$, $\alpha = 0.5$, $\lambda = 3$, $\sigma = 1$.

in Fig. 4.18 or 4.19 for which v is well within the Landau-Levich regime of the one-component TFE. The simulation is repeated with the addition of Eq. (4.37) in (b), showing that h does not sharply drop anymore. After a transient, the system periodically deposits solute.

Note that the logarithmic term in μ_{osm} diverges as $C \to 1$. Although the term regulates itself by decreasing rate of evaporation, the discretized model can become stiff as C approaches 1. This is the case for small Υ, which weakens the osmotic pressure, i.e., C can become closer to 1 than for larger Υ, see App. A.13 for a corresponding solution snapshot.

Theoretically, $\lambda = 3$ does not prevent ϕ^* from growing beyond 1 which can be observed when varying Λ, see Fig. 4.21. Only for $\Lambda < 0.4$ does the phase-field remain bounded by $[-1, 1]$. Naturally, this threshold will depend on the other parameters which is why $\Lambda = 0.2$ will be adopted for all following simulations. This has the drawback of wider phase-field interfaces. Note that ϕ_{max} does not reach a plateau as $\Lambda \geq 0.9$ may indicate. ϕ_{max} continues in a non-linear fashion as Λ becomes larger (not shown here).

Since all control parameters have been presented, we present the *standard parameter set* that is used in all remaining simulations of this chapter if not stated otherwise.

		Standard parameter set		
$L = 800$	$N = 1024$	$h_0 = 20$	$C_0 = 0.3$	$\phi_0 = 0.99$
$v = 0.1$	$g = 10^{-3}$	$\beta = 1$	$\mathrm{Pe}^{-1} = 10^{-3}$	$\chi = 1.5$
$\Omega = 0.01$	$\Upsilon = 1$	$\mu = -1.6$	$C_{\mathrm{eq}} = 0.4$	$\alpha = 0.5$
$\lambda = 3$	$\Lambda = 0.2$	$\sigma = 1$		

4.8.3. Deposition Patterns in 1D

As mentioned in the introduction 1, primary interest lies in the deposition patterns. Therefore, we consider the dependency of the morphology on various system parameters. Since the occurrence of precipitation is determined by the solute concentration profiles $C(\mathbf{x}, t)$, we first focus on those
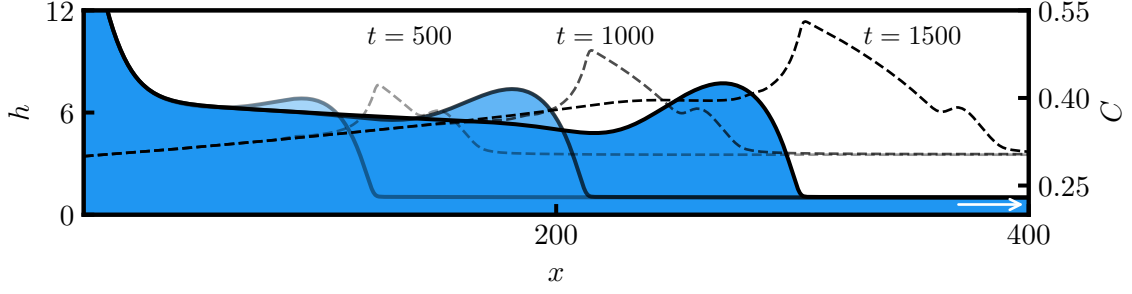
Figure 4.22.: Transient resulting in a Landau-Levich-like film state for a binary mixtrue with deposition mechanism in a dip-coating geometry on a 1D substrate described by Eq. (2.126)-(2.129). The ridge leaves the domain at the right boundary at large time. Film height h and solute concentration C are depicted in blue and dashed black, respectively. Deviating parameters are: $v = 0.22$, $\Omega = 0.004$.
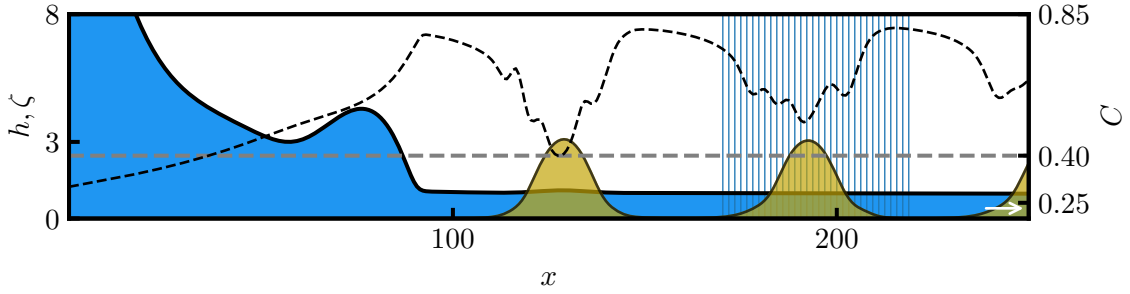

Figure 4.23.: Time-periodic deposition of ridges for a binary mixture in a dip-coating geometry on a 1D substrate described by Eq. (2.126)-(2.129). Film height h, deposit thickness ζ, solute concentration C and equilibrium concentration C_{eq} are depicted in blue, olive, dashed black and dashed gray, respectively. Further, every second grid node is depicted with vertical lines around one of the deposited peaks indicating that the peaks are on a scale larger than Δx.

and then proceed to present the deposition patterns.

Take the case of a homogeneous deposit that is preceded by the extraction of a homogeneous film, meaning flat with a constant small slope due to evaporation. We shall call such states *Landau-Levich-like*. This regime is found at high transfer velocities v. Figure 4.22 shows three corresponding snapshots before the onset of precipitation. A transient ridge is drawn out of the bath and transported across the right boundary. The concentration profile, divided into a uniform section and a growing, widening peak, resembles observations made for advection-diffusion systems where a moving source of increasing strength emits surfactants onto a flat film [WJ01, Wil98]. Periodic ridge states possess concentration profiles like the one shown in Fig. 4.20.(b). There, C is locally maximal at the edges of each ridge. Upon precipitation solute is deposited until the concentration falls again below C_{eq}. The ridges are then advected as solids while precursor with an irregular concentration profile is left on top. Figure 4.23 shows a snapshot of a similar ridge state but with higher deposits. The grid discretization is depicted by vertical lines for every second node, indicating that the peaks possess a length scale larger than

the grid resolution Δx and are therefore no numerical artifact.

Before the onset of precipitation, the local concentration profiles are asymmetric due to the longer evaporation time of each ridge's right flank. Interestingly, there are cases in which the left flank overtakes the right flank in concentration. This can be understood by analyzing $\partial_t C$:

$$
\begin{aligned}
\partial_t C &= \frac{1}{h}\left(\partial_t \psi_2 - C\partial_t h\right) \\
&= \frac{1}{h}\left(-\nabla \cdot \mathbf{J}_{2,\text{conv}} - \nabla \cdot \mathbf{J}_{2,\text{diff}} + C\nabla \cdot \mathbf{J}_h - CJ_{\text{evap}}\right) \\
&= \frac{1}{h}\left(-\nabla \cdot (C\mathbf{J}_h) - \nabla \cdot \mathbf{J}_{2,\text{diff}} + C\nabla \cdot \mathbf{J}_h - CJ_{\text{evap}}\right) \\
&= \frac{1}{h}\left(-\nabla C \cdot \mathbf{J}_h - \nabla \cdot \mathbf{J}_{2,\text{diff}} - CJ_{\text{evap}}\right) \qquad (4.38) \\
&=: \partial_t C^{(\text{conv})} + \partial_t C^{(\text{diff})} + \partial_t C^{(\text{evap})} \qquad (4.39)
\end{aligned}
$$

where we define the flux of the fluid

$$
\mathbf{J}_h := \frac{h^3}{3}\nabla\left[\Delta h - f'(h) - g(h + \beta x)\right] + \mathbf{v}h, \qquad (4.40)
$$

use the fact that the diffusive contributions cancel out when calculating $\partial_t h$ and drop (ϕ, ζ) since we consider solutions before the onset of precipitation. Notice that convection does not create concentration gradients as it contributes as an advection term with "velocity" J_h. We label each of the three contributions by their underlying physical phenomenon and visualize them in Fig. 4.24 which is a snapshot of a ridge solution similar to the previous figure. Here, the onset of precipitation is delayed by employing smaller C_0 and Ω.

Since ridges farther in space correspond to states later in time and vice versa in advected geometries, it is possible to take the ridges at a single time t as a representation of the time evolution of the left-most ridge. Here, we focus on the ones labeled (1) and (3). The right flank of (I) possesses a higher concentration (dashed, black) than the left flank (panel (a)). This interchanges for longer times. $\partial_t C$ (dashed, black) is almost symmetric for (1), the left flank's $\partial_t C$ is slightly smaller than the right flank's (panel (b)). The evaporative contribution $\partial_t C^{(\text{evap})}$ (violet) is symmetric, too, while diffusion (green) and convection (orange) are small in comparison. The location of the concentration maxima x_1 and x_2 are denoted by gray dashed lines. The symmetry of the concentration profile changes for (3). While the evaporation profile becomes smaller on the left, solute has practically ceased evaporating at x_2. Evaporation still continues at x_1 due to diffusive and convective resupply from the bulk. The convective contribution is anti-symmetric around x_1, meaning that it shifts solute even past x_1 into the precursor. This is the same mechanism as discussed in Sec. 4.5. Note that the peaks broaden in time due to the shrinking ridge and the concurrent shift of the contact lines towards the center of each individual ridge from evaporation and convection.

For the remainder of this section the focus lies in the (Ω, v)-space and select studies branching from the standard parameter set. The evaporation constant Ω and transfer velocity v are of particular interest since they strongly affect the time scales of the dynamics. Similar (non-)volatile dip-coating models have been investigated previously, particularly in regards to the transfer velocity [KGFC10, TWGT19, MMT21]. Figure 4.25 shows a phase diagram in the (Ω, v) plane that was obtained by sampling the parameter space. Note that the initial condition remains unchanged, meaning that hysteresis is not visible here.
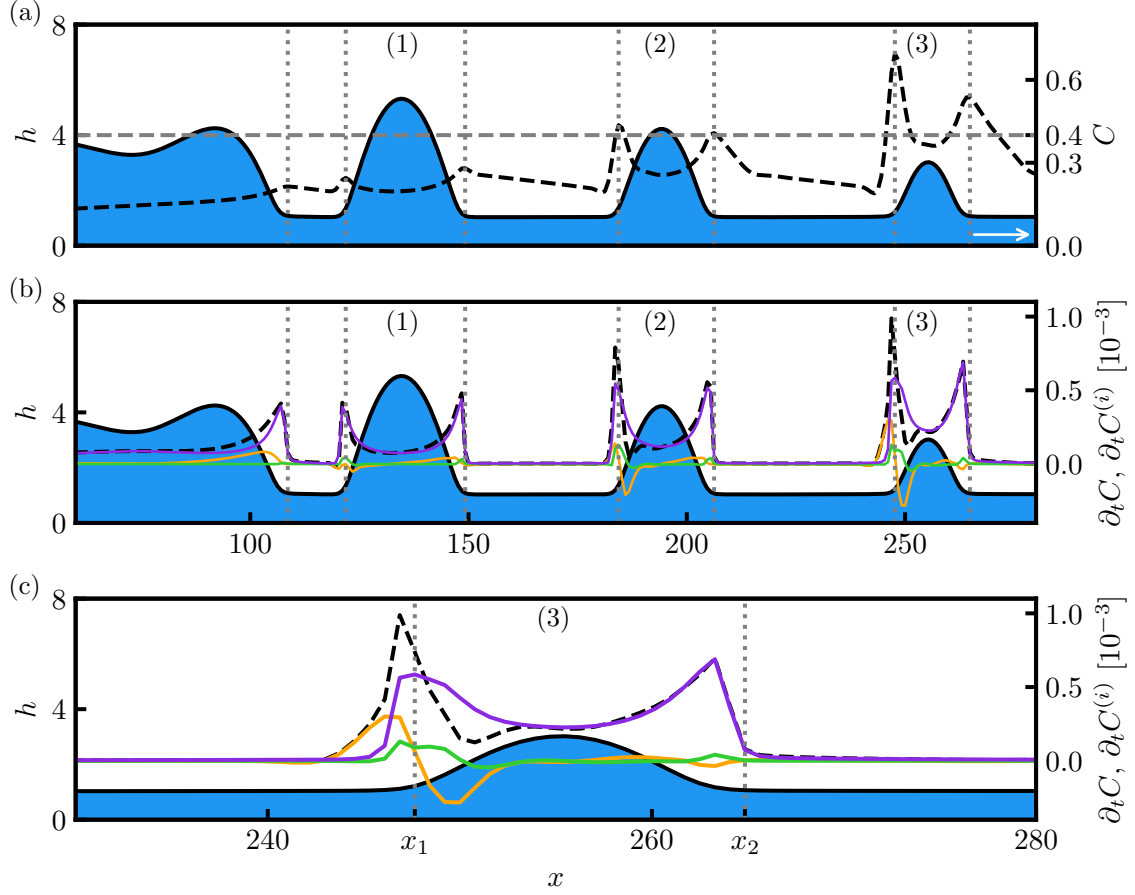
Figure 4.24.: Snapshot of a TPS of liquid ridges of a binary mixture with deposition mechanism in a dip-coating geometry on a 1D substrate described by Eq. (2.126)-(2.129). The snapshot is taken before the onset of precipitation. Extracted ridges are labeleld by (1), (2) and (3). Film height h is depicted in blue. Local concentration maxima are marked by dotted gray vertical lines. (a) solute concentration C (dashed black) and equilibrium concentration C_{eq} (dashed gray). (b) Concentration change $\partial_t C$ (dashed black) and corresponding convective (orange), diffusive (green) or evaporative (violet) contributions $\partial_t C^{(i)}$. (c) Zoom of ridge (3), positions of local concentration maxima are labeled by x_1 and x_2. Deviating parameters are: $C_0 = 0.1$, $\Omega = 0.004$.

We distinguish each region by the occurrence of deposition ((b), (d), (e), enclosed by solid black line) and time-periodicity ((c), (d), (e), enclosed by dotted line). It is known from the non-volatile case of a simple liquid that steady states emerge towards small and high transfer velocities with TPS in between. Estimating the regions of TPS at vanishing Ω one may believe that the v-range should still be of similar size, however it is actually shifted towards smaller velocities and more narrow. The v-range of TPS for $(\Omega, \alpha) = (0,0)$ is depicted in white bars and shifted to $(\Omega = 0.01)$ for comparison. It is much smaller than for the volatile case of $(\Omega, \alpha) = (0.01, 0)$, denoted by the dotted arrows, which in turn is smaller than for $(\Omega, \alpha) = (0.01, 0.5)$ depicted by (d) and (e) at $\Omega = 0.01$.
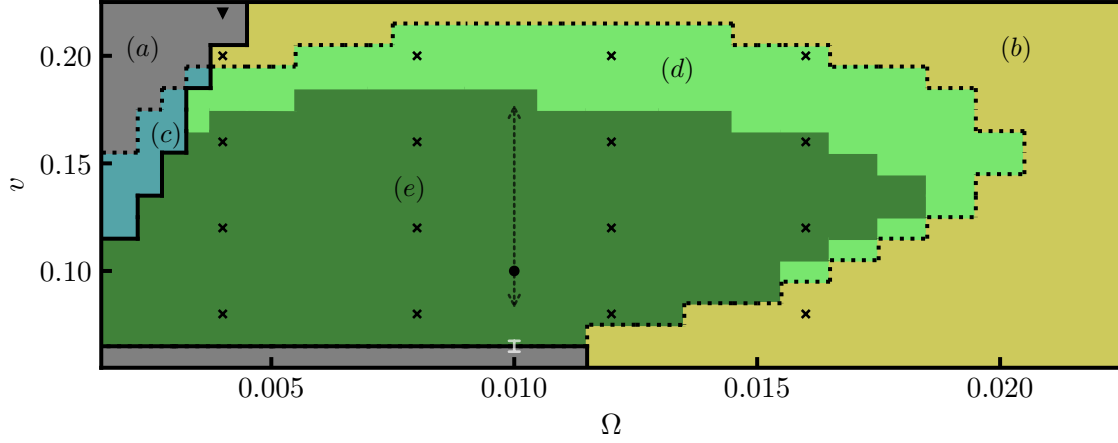
Figure 4.25.: Morphological phase diagram in the (Ω, v) plane for a (precipitating) liquid in a dip-coating geometry on a 1D substrate described by the full model Eq. (2.126)-(2.129). This means especially $\alpha = 0.5$. Regions of TPS are enclosed by a dotted line while regions of deposition are enclosed by a solid line. (a) flat liquid without deposit, (b) flat deposit, (c) liquid ridges without deposit, (d,e) periodic deposits. The deposition in (e) is preceded by existing liquid ridge(s). The v-range of TPS for the case $\Omega = 0.01$, $\alpha = 0$ is marked by dotted arrows while the v-range for $\Omega = 0$, $\alpha = 0$ is marked by white bars. The standard parameter set is marked by $\bullet$. The solution shown in Fig. 4.22 is marked by $\blacktriangledown$. Profiles shown in Fig. 4.26 are marked by $\times$. $\Omega \in \{0.002, ..., 0.022\}$, $v \in \{0.06, ..., 0.22\}$. The sample rates are $\Delta\Omega = 10^{-3}$ and $\Delta v = 0.01$. Around the region of TPS without deposition (c) the sample rate is increased up to $\Delta v = 5 \cdot 10^{-4}$

Naturally, the parameter space is dominated by flat deposition (b) once Ω becomes large enough while at small Ω this is limited by the domain size and v (a). The region of TPS without deposit (c) is expected to extend further towards smaller velocities as Ω approaches 0 since C_{eq} cannot be surpassed without evaporation. Interestingly, for $\Omega \in \{0.002, ..., 0.011\}$ such solutions have not been found at the lower v-boundary of the onset of TPS for the applied sampling rates. Note that the TPS with deposit are further distinguished by a [non-]existing liquid ridge before the onset of precipitation (d,e).

The region of patterned deposits is of particular interest. Figure 4.26 gives an overview of some of the occuring patterns. All presented patterns are regular, meaning neither transient nor chaotic. Above, we distinguished two types of periodic deposits by the [non-]existence of a liquid ridge before the onset of deposition. This criterion can be formulated stricter for the purpose of classifying the deposition patterns. One can distinguish between depositions before and after liquid ridges detach from the meniscus. The latter occurs at small v and Ω, showing deposits with symmetric peaks and vanishing minimum deposit thicknesses. The former shows a variety of patterns that are highly dependent on the meniscus dynamics, ranging from high to low amplitudes and asymmetric peaks. Note that such peaks possess steeper left than right flanks which is to be distinguished from having high left or right tails such as for the parameters $(\Omega, v) = (0.008, 0.16)$ or $(0.012, 0.08)$.
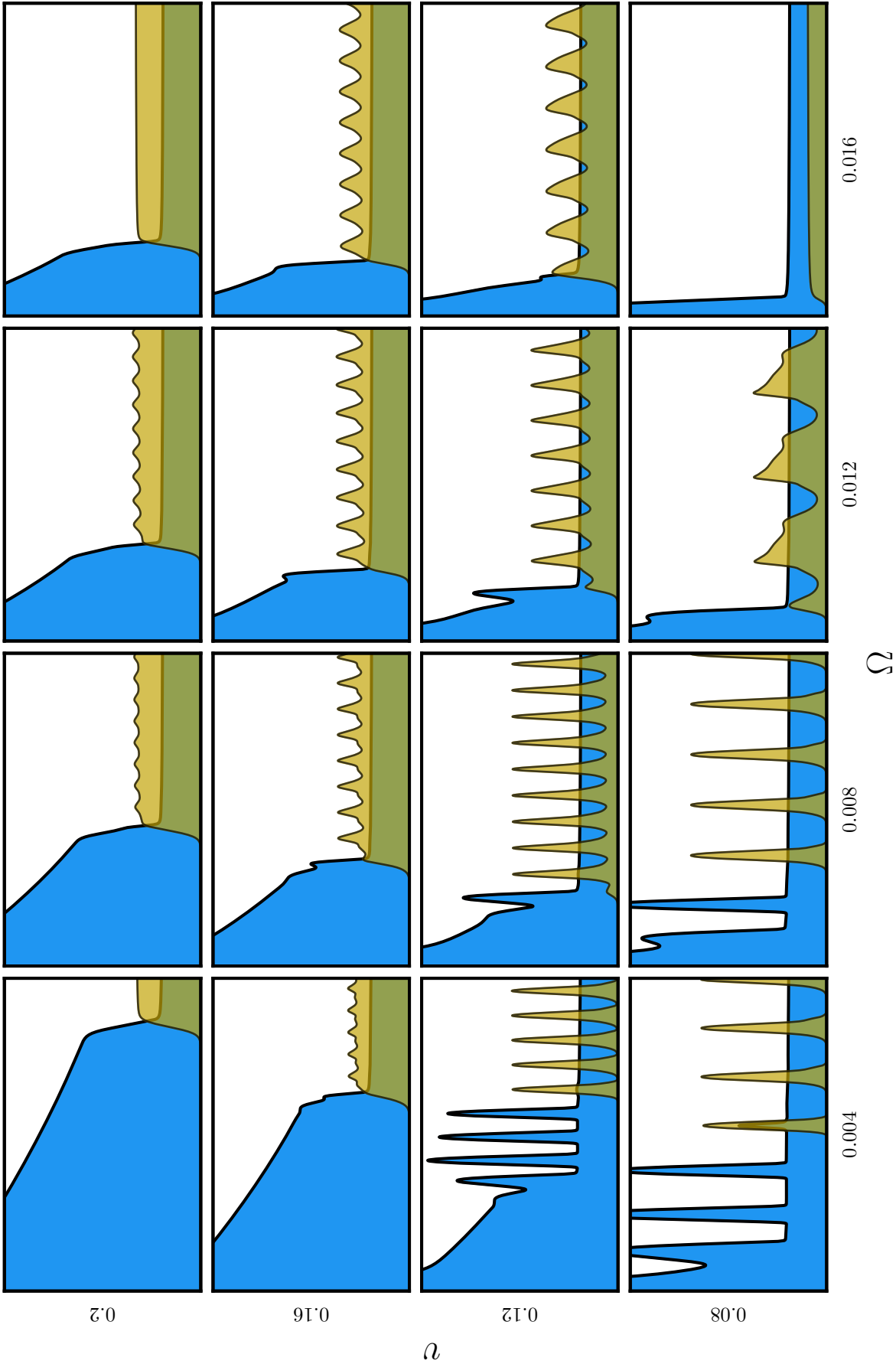
Figure 4.26.: Snapshots of a binary mixture with deposition mechanism in a dip-coating geometry at parameters marked by $\times$ in the (Ω, v)-plane of Fig. 4.25. The governing equations are Eq. (2.126)-(2.129). Film height h and deposit thickness ζ are shown in blue and olive, respectively. The domain is shown until $x = 600$ with axis limits of $(h_0, C_{\max}) = (5, 0.8)$.
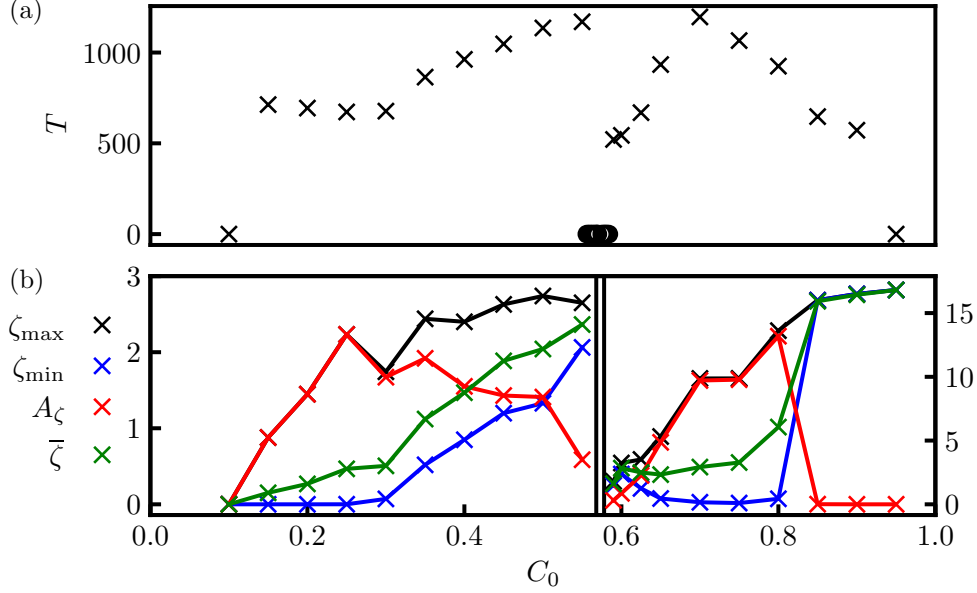

Figure 4.27.: Solution measures of deposition patterns of a precipitating liquid in a dip-coating geometry for varying initial solute concentration C_0. (a) time period T. The deposit is flat at very small and large C_0. The system possesses another flat deposit region($\circ$) at around $C_0 = 0.58$. This solution branch is left out in (b). (b) maximum deposition thickness $\zeta_{\max}$, minimum deposition thickness $\zeta_{\max}$, amplitude or prominence A_ζ and mean thickness $\overline{\zeta}$. Hysteresis is not observed around the intermediate C_0 region of flat deposit down to a parameter resolution of $\Delta C_0 = 0.006$. Note, that the y-axis scale changes at $C_0 = 0.58$. The governing equations are Eq. (2.126)-(2.129). Deviating parameters are: $C_0 = 0.1$, $\Omega = 0.004$.

Besides v, an important parameter is C_0, it controls the solute amount in the system. In Fig. 4.27 we show a study in C_0 for a select parameter set quantifying the deposit ζ and its periodicity T. (a) As C_0 increases the period slightly decreases to a minimum at $C_0 = 0.3$, increases to $T \approx 1100$ at $C_0 = 0.55$, drops on a branch of flat deposit, increases again starting from $T \approx 500$, reaches a maximum and decreases again until once more the deposit is flat. In (b) solution measures maximum deposit thickness $\zeta_{\max}$, minimum deposit thickness $\zeta_{\min}$, amplitude [prominence] A_ζ and mean deposit thickness $\overline{\zeta}$ are depicted. The y-axis scale is increased upon crossing the double line. Note that the branch of flat deposit in the center is left out. In the first half (left y-axis) $\zeta_{\min}$ and $\overline{\zeta}$ increase monotonically. $\zeta_{\max}$ and A_ζ increase until $C_0 = 0.25$ and then behave non-monotonically. Interestingly, the two measures overlap at small C_0 and since $\zeta_{\min}$ is negligibly small which indicates that the deposited ridges increase in height without increase

in base height. In the second half (right y-axis), the oversaturated regime, ζ_{min} decreases as C_0 increases until $C_0 = 0.75$ and slightly increases again at $C_0 = 0.8$. From $C_0 = 0.85$ on the amplitude A_ζ vanishes, i.e., the deposit is flat. Due to the oversaturation deposition is triggered close to the bath, which results in high deposit thicknesses. Note, that the $C_0 = 0.85, 0.9$ states are still time-periodic with regards to the height profile, i.e., the corresponding periods shown in (a) are those of the liquid ridges. In this model two mechanisms can be responsible for arrest of deposition dynamics: Desaturation of the liquid below C_{eq} and h falling to precursor height. The former should be independent of C_0, however in the latter case more solute remains in the precursor after deposition for higher C_0 resulting in a nonlinear relation between $\bar{\zeta}$ and C_0. This is different from precursor models that do not treat the deposit with a separate field such as in [FAT12]. There, the solute in the precursor counts towards the deposit thickness. Hysteresis is not observed around the intermediate C_0 region of flat deposit down to a parameter resolution of $\Delta C_0 = 0.006$.

4.8.4. Deposition in 2D – Outlook

The branched structure shown in the experimental data of Fig. 1.2 with larger length scale indicates the occurrence of a fingering instability due to dewetting. As mentioned in the beginning of this chapter, thin-film models are able to describe such instabilities. However, DNS indicate that a dip-coating geometry may have a stabilizing effect on transversal instabilities, see the appendix of [TWGT19]. In sample simulations of the full model in two spatial dimensions not shown here we perturb the initial ϕ and h fields with white noise or a single cosine mode in an attempt to trigger both a fingering instability of the dewetting and/or the precipitation front. All samples result in homogeneous y-extensions of states shown in the previous section, corroborating the findings for the simple liquid case. Nevertheless, related coating systems, such as the Langmuir-Blodgett transfer, do exhibit transversal instabilities at the lower boundary of the velocity range of TPS [KGFC10].
Finding the transversal instability of the dewetting front is outside of this work's scope and is left for future endeavors. Instead, an example of a sessile droplet geometry, meaning without the driving force of the substrate advection, is discussed. The time evolution of a simulation is shown in 3D in Fig. 4.28. Liquid and deposit height are assigned to the z coordinate. The color scheme of the liquid height represents the solute concentration. As the solute evaporates the local concentration increases. $t = 1120$: Deposition is initialized by oversaturation and spontaneous nucleation. This in turn is triggered by numerical perturbations due to the grid discretization and amplified by Mullins-Sekerka instability as mentioned in [XM11]. Initializing ϕ with white noise facilitates nucleation even further. This leads to inhomogeneous deposition along the contact line. $t = 1520$: The deposition fronts of individual nuclei advance and merge except for the $x = 100$ plane. The four-fold symmetry of the grid is reflected in the onset of instability. The symmetry is broken due to the white noise. $t = 3310$: The front continues to recede exhibiting a transversal instability on the scale of the discretization. $t = 4100$: fingers on a larger length scale emerge in a spiraling manner due to the combination of C being maximal at the contact line and the contact line's receding motion. $t = 4850, 10010$: fingers branch off towards the center and form a mound, i.e., the envelope of the deposit profile monotonically increases radially towards the center. The solvent has mostly evaporated. The pattern can be classified as a combination of mound-type and fingering deposition since the fingers become higher towards the center. Mound-type deposits have also been found both in experiment and theory when the substrate is smooth and the contact line does not pin on the deposit [WBKF10,

ZM16, PK17]. We emphasize that the fingers here result from the unstable liquid-solid interface of the solute and not the dewetting front of the liquid mixture.
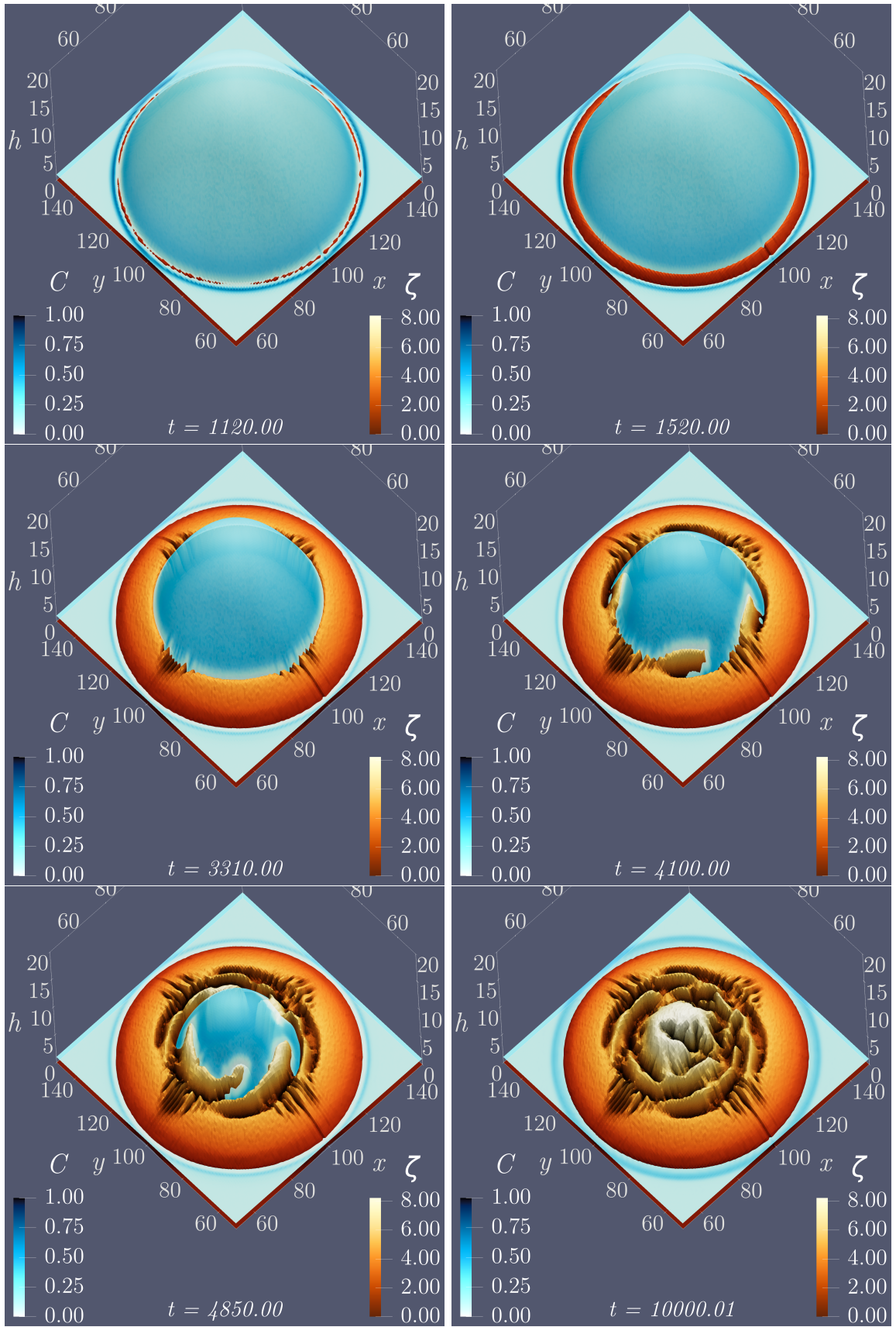
Figure 4.28.: Snapshots from a simulation of evaporative dewetting of a droplet of a binary mixture with deposition mechanism on a 2D substrate. Drop height h and deposit height ζ are given at times $t \in \{1120, 1520, 3310, 4100, 4850, 10010\}$. The color scheme of the liquid height represents the solute concentration C, as can be seen from the smaller concentration (lighter blue) around the propagating deposit. The initial condition is the 2D analog of the parabolic cap used in Sec. 4.5. The homogeneous initial phase-field is perturbed by white noise. $t = 1120$: Since deposition is triggered by nucleation, it is deposited inhomogeneously around the contact line. $t = 1520$: The deposition fronts of individual nuclei advance and merge except for the $x = 100$ plane. $t = 3310$: The front continues to advance inwards exhibiting a transversal instability on the scale of the discretization. $t = 4100$ fingers on a larger length scale emerge in a spiraling manner. $t = 4850, 10010$: fingers branch off towards the center and merge. The solvent has mostly evaporated.

Note that not the full domain is shown in order to focus on the dynamics of the droplet. Deviating parameters are: $C_0 = 0.35$, $v = 0$, $g = 0$, $\Omega = 10^{-3}$, $\Upsilon = 0.1$, $\Lambda = 2$.

5. Pattern Formation in the Langmuir-Blodgett Transfer

A model for another deposition technique, the Langmuir-Blodgett transfer, is presented in Sec. 2.6.1. Recall, that a monolayer of surfactants is deposited from the surface of a liquid bath onto a substrate in this procedure. The two-field thin film model presented in Sec. 2.6 can be reduced to a generalized Cahn-Hilliard equation. The model has recently been extensively studied, ranging from DNS and numerical path-continuation methods to bifurcation analysis and with extensions such as prestructured substrates or a periodic forcing in time [KGFT12, KT14, WG14, ZWHH+16, WZCT+17, Wil16]. The system is relatively well understood for 1D substrates/domains, while 2D studies amount to DNS to our knowledge. Therefore, we briefly summarize part of the cited 1D findings in this introductory part. This also serves as a reference for the analysis of the 2D domain, which is the main focus of this chapter. The order parameter field c is closely related to the surfactant concentration and classifies the state of the surfactant monolayer, in particular, whether the molecules are densely ordered or spread-out disordered, i.e., liquid-condensed (LC, $c > 0$) or liquid-expanded (LE, $c < 0$), respectively. We repeat the dynamic equation (2.158)

$$\partial_t c = \Delta \left[-\Delta c - c + c^3 + \lambda_{\mathrm{SMC}} \zeta_{\mathrm{SMC}}(\mathbf{x}) - \mathbf{v}c \right], \qquad \mathbf{v} = (v, 0)^T \tag{5.1}$$

with transfer velocity v and an external field related to substrate-mediated condensation $\zeta_{\mathrm{SMC}}(\mathbf{x})$. SMC occurs during the transfer of the monolayer from floating on the liquid bath or meniscus on the solid substrate. The monolayer-substrate interaction reduces the free energy of the monolayer and thereby lowers the coexistence pressure between LE and LC phase, facilitating a phase transition from LE to LC phase upon deposition [SR91, RS92, SR94, GR98]. Like in the previous chapter the main control parameter is the transfer velocity v. Figure 5.1 (a) shows a bifurcation branch measured by the L^2-norm

$$||\delta c||^2 = \frac{1}{L_x L_y} \int\limits_{L_x \times L_y} c(\mathbf{x})^2 \mathrm{d}^2\mathbf{x} \tag{5.2}$$

as a function of v for the 1D case. The system possesses three stable, stationary solution sub-branches depicted by solid lines. Unstable ones are marked by dashed lines. Sample solutions $\mathbf{I} - \mathbf{IV}$ are shown in (b). We characterize the states by the c-profile after the meniscus region ($x > x_s$) since the surfactants are in LE phase before ($x < x_s$). The two stable subbranches of high concentration c at low v represent deposits of LC phase (cf. $\mathbf{I}, \mathbf{II}$) whereas the subbranch at smaller c but higher v represents LE phase ($\mathbf{IV}$). This subbranch is populated with subsequent, subcritical Hopf-bifurcations and related time-periodic solution (TPS) branches that end in a variety of bifurcations related to the snaking structure on the left [KT14]. $\mathbf{III}$ shows a sample
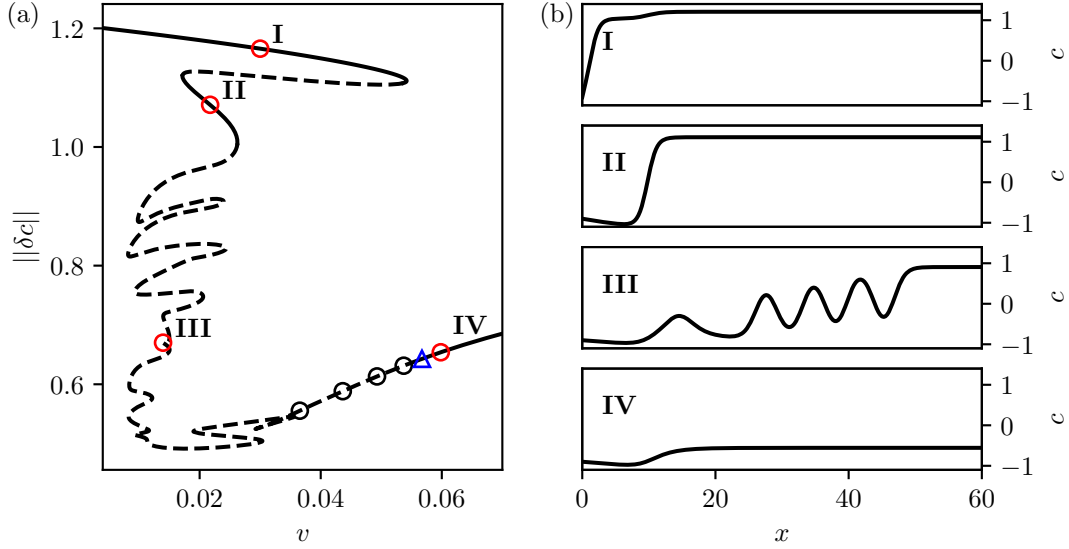
Figure 5.1.: (a) L^2-norm of 1D stationary solutions of Eqs. (2.158)-(2.160) for varying transfer velocity v. The branches are obtained from numerical path-continuation. Solid and dashed lines correspond to stable and unstable solutions, respectively. Sample solution profiles are marked by red ∘ and labelled by $\mathbf{I} - \mathbf{IV}$ and shown in (b). Hopf bifurcations are marked by black ∘. The Hopf bifurcation at which the LE solution gains stability is marked by $\triangle$. Domain size $L_x = 60$. Grid points $N_x = 228$.

solution of this structure. Every other fold that is passed from the top results in an additional peak in the solution profile. Throughout this chapter solutions $\mathbf{I}, \mathbf{II}$ and $\mathbf{III}$ are abbreviated to LC-1, LC-2 and LE solutions, respectively. The Hopf bifurcation at the highest v, marked by $\triangle$ also bifurcates into a branch of TPS. Interestingly, it splits further via a period doubling bifurcation. This branch is linearly stable, ends in a homoclinic bifurcation and conforms to DNS results, showing an extensive patterning region[KGFT12]. In this chapter all control parameters are fixed except for those that are related to the transfer velocity. The fixed values are as follows:

Fixed Parameters

$\lambda_{\mathrm{SMC}} = \dfrac{1}{2}$ $\qquad$ $x_s = 10$ $\qquad$ $l_s = 2$ $\qquad$ $c_0 = -0.9$

For the continuation calculations the Dirichlet BC are weakly imposed with spring constant $s_f = 10^6$. In Sec. 5.1 we present bifurcation diagrams and profiles of 2D states obtained from numerical path continuation by varying the transfer velocity v. In order to characterize the transversal instability of stripes parallel to the contact line, we focus on the small v region where we calculate said branch of TPS, verify the continuation results by DNS and study the behavior of stable steady 2D states under variation of the lateral domain size L_y. Finally, we investigate the behavior of 2D states under time-periodic forcing in Sec. 5.2.

5.1. Solution Structure in 2D

In the following TPS of stripes parallel to the meniscus, i.e., homogeneous in y, are denoted as *horizontal stripes*, cf. Fig. 5.2(a). It is known from both, this model and its hydrodynamic
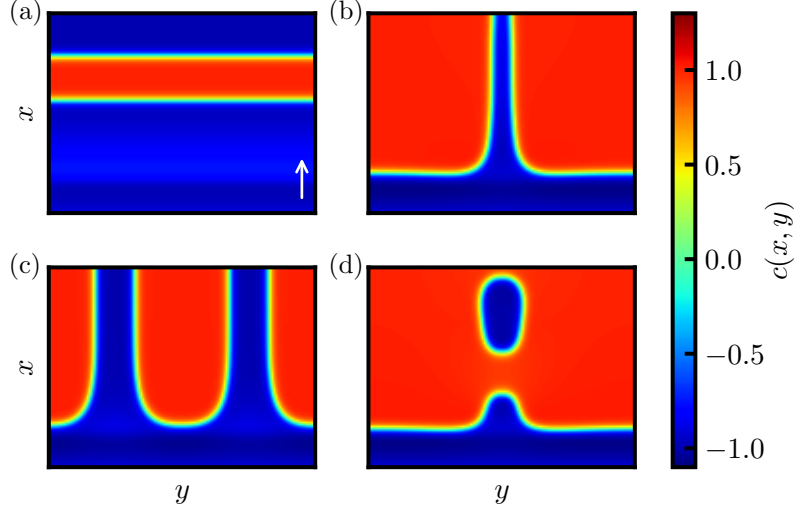

Figure 5.2.: Solution Profiles of 2D DNS obtained with the CUDA framework for the four branches presented in Fig. 5.3(b). (a) Time-periodic horizontal stripes (b) One vertical stripe/LE-finger (c) two vertical stripes (d) ejecting protrusion. Note that patterns are shown in the y-periodic $L_x \times 2L_y = 60 \times 80$ domain with the grid size of $N_x \times 2N_y = 228 \times 122$.

analog, that horizontal stripes become transversally unstable at small v resulting in the formation of vertical stripes, parallel to the transfer direction [KGFC10, KGFT12], cf. Fig. 5.2 (b,c). Both types of stripes are very desirable for applications, especially the latter since stable vertical stripes allow for the formation of, theoretically, infinitely long channels. Another interesting state is the periodic ejection of LE domains from a protrusion of LE bulk as shown in Fig. 5.2 (d). We discuss this state later in this section. Overall, investigating the transversal instability is of particular interest.

We perform the analysis of the transversal instability by two methods: On the one hand, numerical continuation and on the other hand DNS of TPS and transversally inhomogeneous solutions. This allows us to determine the location of instabilities in parameter space and to understand which branches are involved. First, we give an overview of the branch of 2D stationary solutions obtained by transversally extending the domain to $L_x \times L_y = 60 \times 40$ in Fig. 5.3. The solution profiles are discussed in detail afterwards. The majority of the continuation results are published in [LMTG20]. The L^2-norm is depicted as a function of transfer velocity v. The 1D branch of Fig. 5.1 is shown in gray. In Fig. 5.3 (a) Stable [unstable] 2D states are solid turquoise [black]. The LC-1, LE (turquoise), horizontal stripes (red), one-finger (magenta) and two-finger (blue) states obtained from DNS are represented by dashed lines. Analogous to the 1D case the first section consists of the LC-1 solution, translationally invariant in the transversal direction, shortly "y-translation invariant", coinciding with the 1D branch. At about $v = 0.053$ a pitchfork bifurcation occurs where two branches emerge subcritically (their respetive norms coincide). They
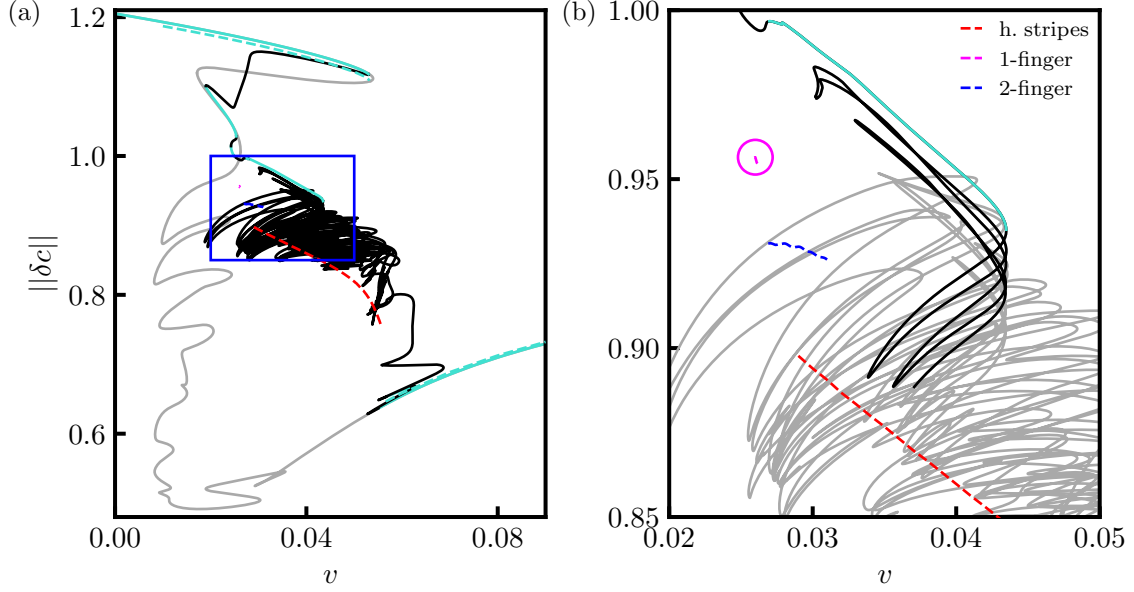
Figure 5.3.: L^2-norm of 2D stationary states of Eq. (2.158)-(2.160) for varying transfer velocity v obtained from numerical continuation (solid turquoise/black for stable/unstable, respectively). The 1D bifurcation curve is depicted in gray. Subbranches of LC-1, LC-2, LE (turquoise) horizontal stripes (red), one-finger (magenta) and two-finger states (blue) obtained from DNS (dashed) are provided. Corresponding profiles are shown in Fig. 5.2(a)-(c). States obtained from DNS related by y-translation by $L_y/2$ exist as well but are not shown here.
(a) overview (b) zoom of the beginning of the 2D criss-crossing section, partially highlighted in black against gray for visual contrast. The small one-finger branch is further marked by a magenta circle. The domain size is $L_x \times 2L_y = 60 \times 80$ with the grid of $N_x \times 2N_y = 228 \times 122$ [LMTG20].

consist of states with broken y-translation symmetry. As we use Neumann boundary conditions (instead of periodic ones) in the lateral direction (y), the two emerging branches are related by a translation in y by $L_y/2$. The emerging branch first extends towards smaller v, undergoes a small number of saddle-node bifurcations before it wildly folds back and forth producing a very dense cluster of sub-branches that overlay and cross each other multiple times. A zoom into part of this region is given in (b) where the first part of the branch is given in blue to allow one to distinguish some of the finer features. Solutions on the 2D branch are mostly unstable. Most of the linearly stable subbranches (turquoise) coincide with stable parts of the 1d branch(cf. Fig. 5.1). Naturally, the solutions regain stability after the final Hopf bifurcation which occurs at almost the same velocity as in 1D.

Moving along the described bifurcation curve a variety of different solutions emerge. A selection is shown in Fig. 5.4. Each profile from left to right and top to bottom corresponds to a solution further along the curve. Stable states are marked by white ∘ which deviates from the stability statements made in [LMTG20]. Stable solutions with broken y-translation symmetry do exist in this system.

The above-mentioned unstable branch emerging from the pitchfork bifurcation on the LC-1 branch consists of (b) a broken y-symmetry solution which (c) laterally extends until the (d)
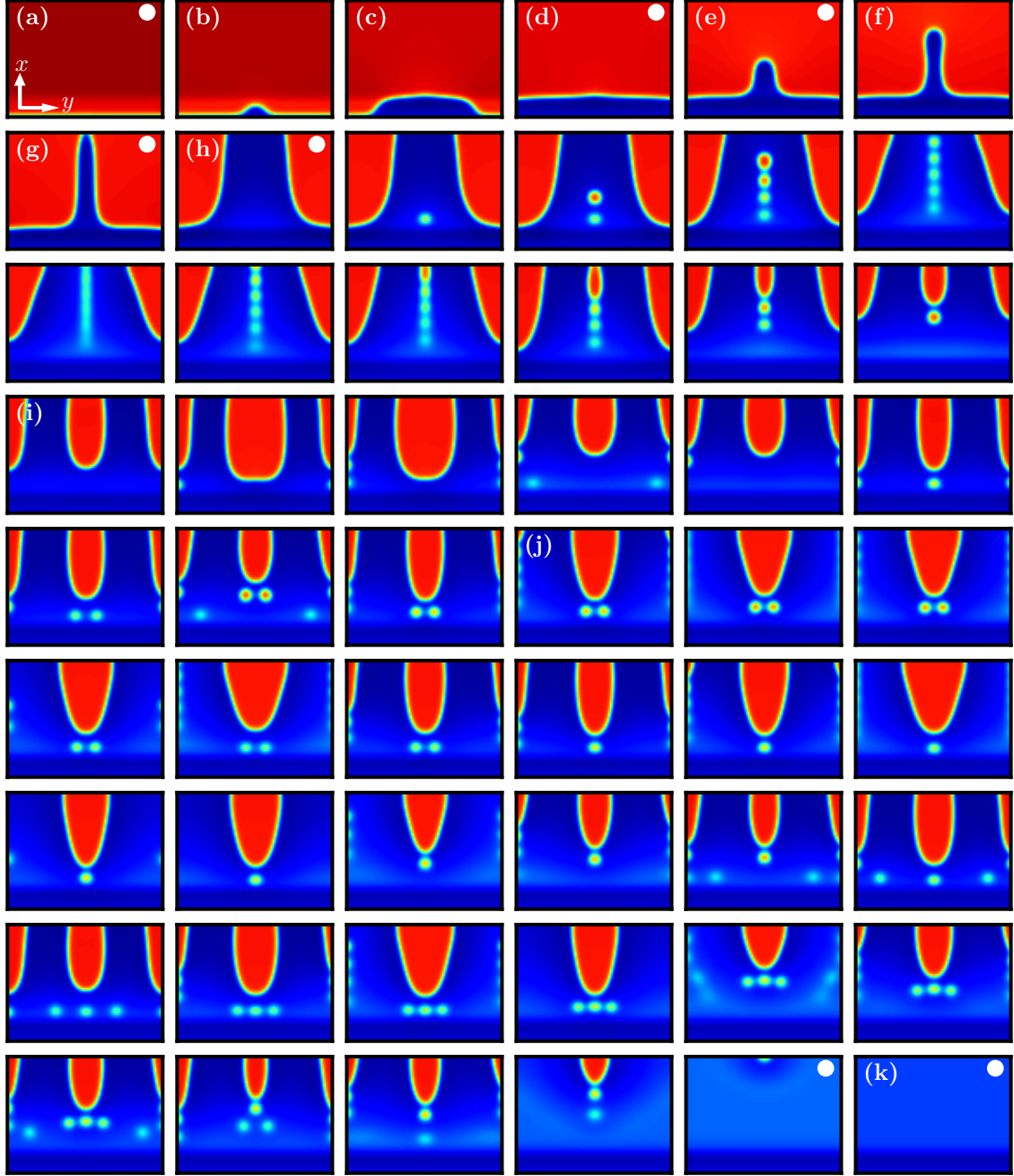
Figure 5.4.: Selected 2D stationary solution profiles of Eq. (2.158)-(2.160) (see Fig. 5.5 for the colorbar) on the branch of fully 2D states in Fig. 5.3. From top left to bottom right we start at $v = 0$ first follow the branch of transversally invariant states, switch to the branch of 2D states and follow it throught the end of Fig. 5.3(a), i.e., we follow the branch with increasing arclength s. All states marked by white $\circ$ are linearly stable. Note that patterns are shown in the y-periodic $L_x \times 2L_y = 60 \times 80$ domain. The remaining labels are used for reference in the main text [LMTG20].

lateral boundaries and becomes linearly stable. The latter manifests from an imperfect pitchfork bifurcation closely related to the LC-2 branch of the 1D curve. The LC-LE interface is not horizontal but slopes towards $y = 0$. From there, another imperfect pitchfork bifurcation is passed which leads to the development of a central LE-finger which (e) briefly gains stability after passing another fold. (f) The finger prolongs until it reaches the upper boundary, (g) becomes stable, briefly loses stability between two folds and (h) increases in width. This so-called "one-stripe" solution exists over a significant velocity interval $[0.0278, 0.0435]$. The short stable section in between the folds surmises $[0.0267, 0.0279]$. This particular branch segment is discussed in more detail below and Fig. 5.6. The stability changes again at the next fold leading into the wild cluster of overlaying, crossing sub-branches caused by the finite system size. These branches would remain disconnected for a system semi-infinite in the y-direction. The different interconnected 2D states combine one or two fingers (blue in red) with different numbers and arrangements of red spots. The branch in Fig. 5.3 forms a rather wild tangle corresponding to a complicated structure with many saddle–node bifurcations, accompanied by the occasional Hopf bifurcation (not shown), eventually ending in the (k) stable y-translation invariant LE solution. A detailed study of the structure and its dependence on parameters cannot be provided here. To give an impression of the complexity we present in Fig.5.5 an alternative representation. Namely, (b) 1D cross-sections $c(x = L_x, y)$ are presented in dependence of the arclength s along the bifurcation curve, i.e., in a space-arclength plot. The accompanying panel (a) shows the values of v which, in particular, allows one to identify at which s saddle-node bifurcations occur. The combination of the two panels allows one to appreciate the type of changes occurring along the bifurcation curve. For instance, one clearly discerns the formation of the first complete blue stripe at $s \approx 0.7$. It then widens and narrows several times accompanied by the emergence of a central line of red spots (not seen in the particular slice shown in Fig. 5.5 (b), cross-sections at a different x-position would be required). The red spots first appear one after another (Fig. 5.4 second row), then nucleate a central red structure at the downstream boundary (third row). This structure then grows from the boundary eating up spot after spot. In this way the original single blue finger is split into two (Fig. 5.4 (j)). The emergence of the central red structure at the boundary is seen at $s \approx 4.42$ in Fig. 5.5. From this point on a varying number of spots emerges and vanishes again at the tips of either of the red (LC) finger-like domains. In addition, from Fig. 5.4 (j) the red domains on the lateral boundaries sometimes recede from the bath, passing through intermediate states in the form of multiple spots. Finally the blue (LE) domain advances everywhere till the branch of 2D states ends in the pitchfork bifurcation on the homogeneous blue(LE) solution (Fig. 5.4 (k)). The intricate sequence of widening and narrowing, advancing and receding fingers is well appreciated in the pattern of the space-arclength plot. The three sections of the 2D branch where the fingers on the lateral boundaries breaks up into a line of spots are easily distinguished and occur in the ranges $s = \{[10.5, 10.9], [11.8, 12.7], [14.3, 15.0]\}$. Along the bifurcation curve profiles Fig. 5.4 (d), (e), (g) and (h) are both stable and have broken y-translation symmetry. Profiles (d) and (e) are not verified with DNS although time-periodic solutions very similar to (e) exist which eject LE spots from the protrusion, see Fig. 5.2 (d). It is possible that the non-ejecting protrusion case exists in a very small parameter region or only establishes after very long transients. (h), and closely related, (g) are the likely branches corresponding to the vertical stripe solutions. The two branches are separated by two subsequent folds which may be the influence of the upper boundary. Figure 5.6 shows two zooms of the one-stripe solution branches for varying lateral domain size L_y [1]. As expected, for small L_y the

---

[1]First calculated by Sebastian Engelnkemper, however, with incorrect stabilities.
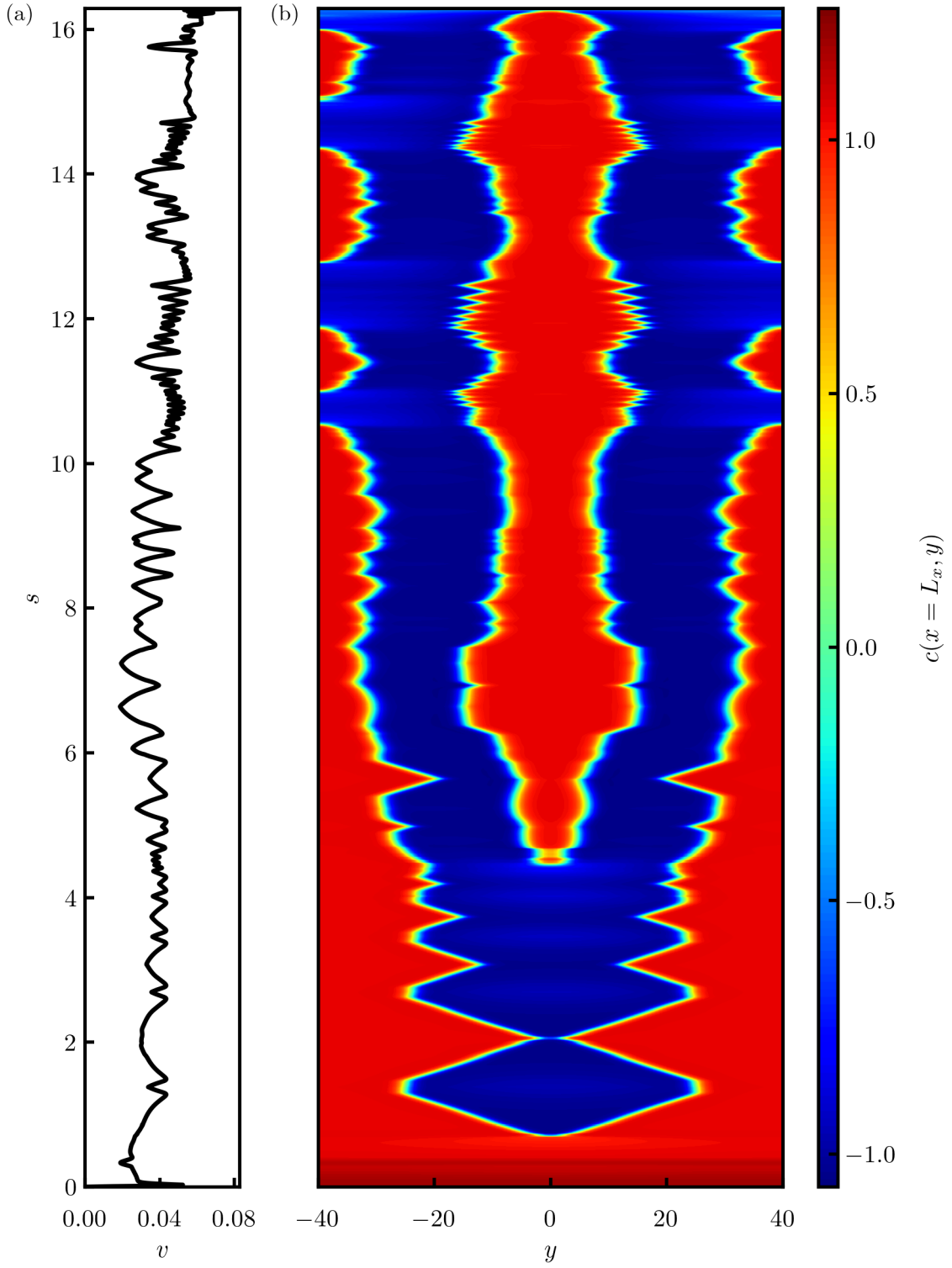
Figure 5.5.: (a) Arclength s vs transfer velocity v along the 2D bifurcation curve in Fig. 5.3 starting from $v = 0$. (b) cross-sections $c(x = L_x, y)$, i.e. at the downstream boundary, of the 2D steady states along the 2D bifurcation curve, ordered by arclength s. The governing equations are Eq. (2.158)-(2.160) [LMTG20].
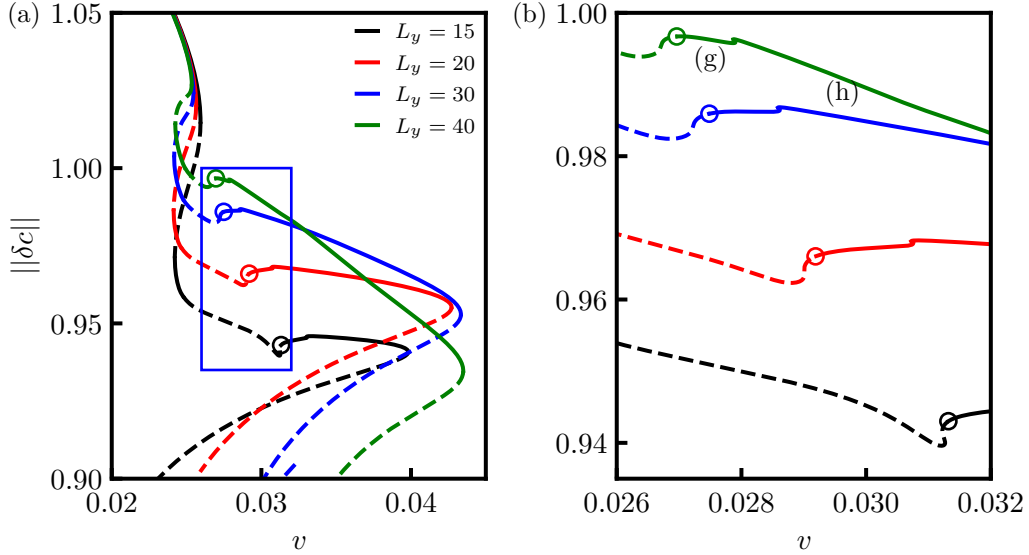
Figure 5.6.: Zooms of the subbranches around the stable one-stripe solutions for varying lateral domain size L_y, see Fig. 5.3. (b) The Hopf-bifurcation at which the steady state gains stability is marked by $\circ$. The respective left stable subbranches consist of profiles (g) of Fig. 5.4 while the right ones, separated by two subsequent folds, corresponds to profiles (h) of Fig. 5.4.

curve converges towards the 1D bifurcation curve, in particular its snaking section. On the other hand the one-stripe branches grow as L_y increases which indicates that these branches are not a finite size phenomenon. Particularly interesting is that subbranch (g) gains stability via a Hopf bifurcation, marked by $\circ$ and subbranch (h) loses stability by a saddle-node bifurcation. However, since many more Hopf bifurcations exist along the bifurcation curve it is unknown which time-periodic branches are related to the horizontal stripe solutions. In an attempt to locate the relevant Hopf bifurcation primitive continuations of horizontal stripes and translationally inhomogeneous solutions are performed and depicted in dashed lines in Fig. 5.3. DNS and continuation greatly differ from each other. Not only is the one-finger stable branch from DNS much smaller but the two-finger solutions are also stable. This indicates a discretization problem. Although both methods converge to some limit for finer discretization, see App. A.14, very fine discretizations are too costly in 2D. Fortunately, we are able to continue with a fine grid size of $N_x \times 2N_y = 456 \times 608$ until past the subbranch of 2-finger solutions. The close up of the 1- and 2-finger solution region is shown in Fig. 5.7. Interestingly, the curve is more regular and does not intersect with itself until past the 2-finger subbranch (blue) instead of the 1-finger branch (magenta) as previously 5.3 (b). The 2-finger subbranch has significantly gained stability while the other is much smaller. The agreement between continuation and DNS is much better here. Especially the multistable region between 2-finger and horizontal stripes is verified. The former gains stability from a Hopf bifurcation. In essence, above findings for the rougher discretization do not change, however, the branches related to the transversal instability are identified more confidently now. Thus, the two simplest cases for the instability of horizontal stripes are: One, a transition from an unstable subbranch of TPS at $v < 0.29$ to the stable 2-finger branch, i.e., horizontal stripes are unstable and appear as a transient state. Two, a
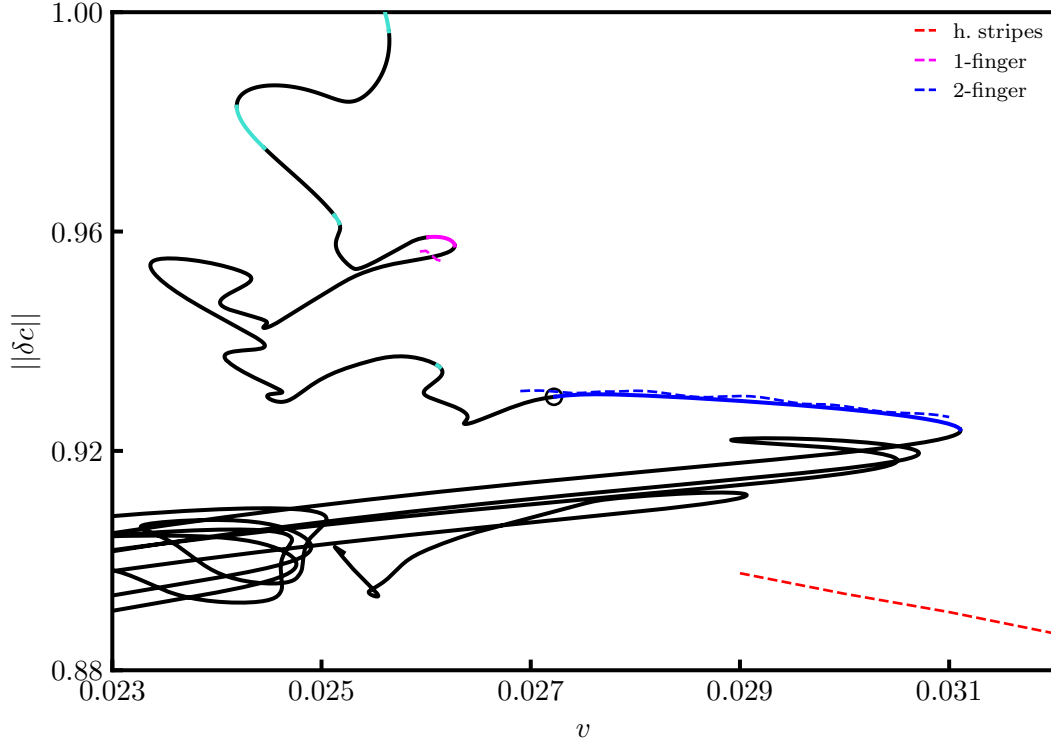
Figure 5.7.: L^2-norm of 2D stationary states of Eq. (2.158)-(2.160) for varying transfer velocity v obtained from numerical continuation (solid turquoise/black for stable/unstable, respectively). Further, branches of horizontal stripes(red), 1-finger (magenta) and 2-finger solutions (blue) obtained from DNS (dashed) are provided. The continuation branches of the latter two are colored the same way. Qualitatively associated profiles are shown in Fig. 5.2(a)-(c). The view is focused on the region of y-symmetry broken stable solution branches. DNS solutions related by y-translation by $L_y/2$ exist as well but are not shown here. The Hopf bifurcation from which the two-finger branch gains stability is marked by $\circ$. Domain size $L_x \times 2L_y = 60 \times 80$, grid size $N_x \times 2N_y = 456 \times 608$.

branch switch occurs within the region of multistability due to perturbation.

Unfortunately, the structure of the bifurcation curve becomes even tighter for finer discretizations which leads to undesired branch switching, thus calculating the complete curve is not pursued here, see App. A.15.

5.2. Time-Periodic Forcing

The period of horizontal stripes depends nonlinearly on the transfer velocity v, i.e., the period can be controlled with v [KGF11, KGFT12]. This control can be taken a step further by applying prestructures to the substrate, i.e., changing its wetting properties periodically in the hydrodynamic model or the external field ζ_{SMC} in the reduced model [KGF11, WG14, WTGK+15, ZWHH+16, WZCT+17]. In practice this is an additional preparatory step during substrate

Figure 5.8.: Synchronization order W of time-periodic 1D solutions for varying mean transfer velocity $\bar{v}$ and forcing amplitude A. The diagram shows structures known as *Arnold tongues*, marking wide regions of equal synchronization orders. Note that $W < 1$ does not occur here. It does, however, occur for different ω. The governing equation is Eq. (2.158). Larger domain sizes $L \in \{1000, ..., 5000\}$ are employed while keeping $\Delta x = 1$ for smaller $\bar{v}$ in order to capture larger stripe distances [Ly17, LTCG19].

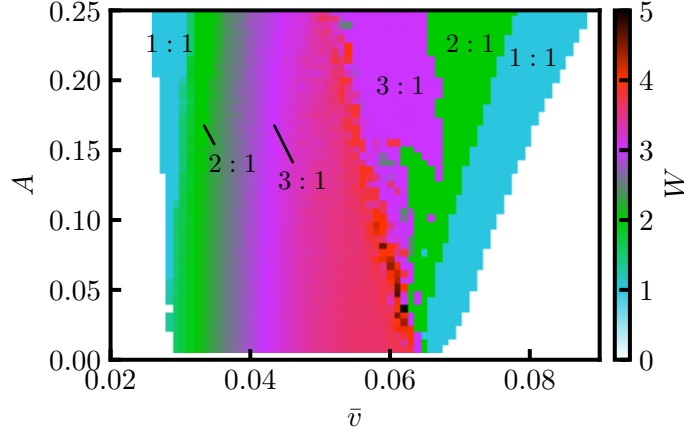fabrication which is justifiable if the resulting pattern is worth the additional costs. Using pre-structures falls under the category of spatial forcing in the hopes that the deposition pattern adjusts its period to multiples or fractions of the prestructure's period. Alternatively, the system can be put under temporal forcing, i.e., periodically changing the transfer velocity v around a mean value [Wil16]

$$v = \bar{v}(1 + A\sin(\omega t)), \tag{5.3}$$

with (angular) frequency ω. In practice this can be performed with a piezomotor. For horizontal stripes this indeed leads to locking between enforced and exhibited stripe distances. Figure 5.8 shows a parameter study in the forcing amplitude A and $\bar{v}$ [LTCG19]. Note that the lateral boundary conditions are periodic here in contrast to the previous sections. The *synchronization order* [*rotation number*]

$$W = \frac{\bar{k}}{k_0} = \frac{2\pi}{\bar{l}}\frac{\bar{v}}{\omega} \tag{5.4}$$

is extracted from each simulation as a solution measure with mean wavenumber $\bar{k}$, enforced wavenumber k_0 and mean stripe distance $\bar{l}$. $W = 1$ and $W = 2$ mean 1:1 and 2:1 synchronization, respectively. The latter meaning that the spatial frequency is double the enforced one. For periodic states W is a rational number $\frac{n}{m}$ for which the phase locking region becomes larger the smaller n and m [PRK03]. In the following such regions are called *major* ones. At small amplitudes major regions of synchronization $W = 2$ and $W = 1$ are present at the v edges of the patterning region, respectively. In between, W changes continuously. As A increases, more frequencies begin to lock and regions such as $W = 3$ grow. The competition between the system's natural (unforced) frequency and the enforced one is clearly visible. The former dominating in the center of the $\bar{v}$ range and the latter at the boundaries. Notably, these boundaries extend with increasing A. The morphological phase diagram takes on the very characteristic form of *Arnold tongues*, meaning, major regions of equal synchronization order, which typically grow when the

forcing amplitude is increased [Arn61]. Unsurprisingly, regions of multistability appear as well which are especially prevalent around the $W = 4$ region, indirectly indicated by the abrupt and frequent changes in W. See [LTCG19] for more details.

In [LTCG19] we have shown that the system exhibits a variety of patterns ranging from horizontal, vertical, oblique stripes, lattice, transient branch to hole and broken horizontal stripe structures. The last two pattern types occur more frequent at high amplitudes which shows that too strong forcing is not necessarily beneficial for stable periodic patterns. Naturally, even higher amplitudes eventually stabilize horizontal stripes again and will lead to extensive $W = 1$ synchronization [LTCG19]. The 1D results can be adopted to the horizontal stripes, however, the influence of forcing on y-symmetry broken patterns is important as well. A parameter study employing DNS and primitive continuation of select branches of 2D states is performed in Fig. 5.9 (c,d). A primitive continuation pertains subsequent DNS which use the final state of the previous simulation as the initial condition. The transfer velocity v is varied per simulation. Fundamental wavenumbers k_x and k_y are extracted from the FFT

$$\hat{c} = |\text{FFT}[c]| \tag{5.5}$$

of the final states of each simulation. By "fundamental", we mean local maxima corresponding to the smallest non-zero harmonic order. For stripe patterns the single and for lattice patterns the two smallest ones are taken. An example lattice pattern with its spectrum are shown in (a) and (b), respectively. Panels (c) and (d) show a parameter study of the horizontal stripes across the patterning regime in black for reference. Note that the patterning range of the horizontal stripes does not match that of the 1D data above because the discretization is different. Due to y-translation symmetry W_y naturally vanishes while regions of 1:1 and 1:2 (red) synchronization are clearly visible in (d). Since the analysis is performed without time averaging, errors from spatial discretization are apparent in the horizontal synchronization plateaus. The example branches of oblique (blue) and lattice (green) structures do not show synchronization in the lateral direction. Interestingly, the oblique branch is not synchronized in x as well which indicates the dominance of the natural frequency, even though it partially overlaps with the 1:2 synchronized horizontal stripe plateau in regards to $\overline{v}$. On the other hand, the lattice structures do exhibit a 1:2 synchronizing plateau. The multistable system possesses many more lattice and oblique solution branches whose investigation exceeds the scope of this work.
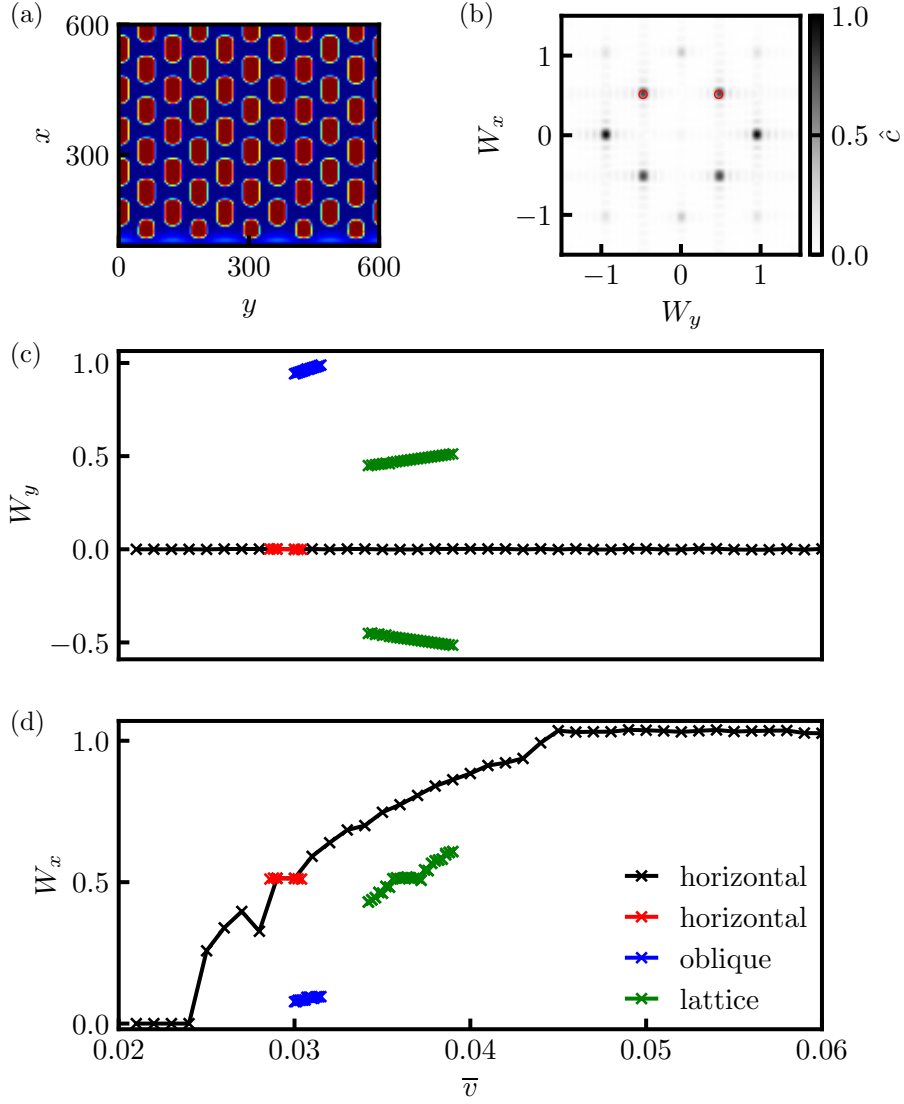
Figure 5.9.: (a) Solution profile of a lattice pattern obtained from DNS of Eq. (2.158)-(2.160). (b) Fourier-transform of the pattern. The wavenumbers $\overline{k}$ are mapped to the synchronization order by Eq. (5.4). Local maxima of $\hat{c} = |\text{FFT}[c]|$ that correspond to the smallest non-zero harmonic order are marked by red ∘. (c) Parameter study of select branches of 2D states. Shown is the synchronization order W_y in the lateral (y) direction for horizontal stripe (black, red), oblique stripe (blue) and lattice solutions (green) with v covering the patterning regime. (d) Order of synchronization in the pulling direction(x) v covering the patterning regime. Stripe patterns possess one fundamental wavenumber and lattice structures two. The analysis is performed without time averaging errors which causes spatial discretization errors to appear in the horizontal synchronization plateaus. Domain size $L_x \times L_y = 600 \times 600$, grid points $N_x \times L_y = 384 \times 384$.

6. Summary and Outlook

Deposition patterns for complex liquids have been modeled and analyzed in this thesis. To this end, a thin film and a Cahn-Hilliard type model for the description of dip-coating and the Langmuir-Blodgett transfer have been formulated. The former has been derived via lubrication approximation and includes capillary, wetting, mixing, evaporation, viscosity and deposition effects. Deposition is explicitly modeled by coupling to a phase-field equation. It is abbreviated as the *full model*. The latter is a known reduced model, derived from hydrodynamic equations describing a surfactant covered liquid.

The full model has first been analyzed by subsequently switching on and off effects such as evaporation, deposition or viscous drag. In the presence of a contact line the interplay of evaporation and convection result in the formation of a local concentration maximum that shifts away from the bulk and even past old contact line positions into the precursor region. Entropic contributions to the bulk free energy of the mixture reduce the rate of evaporation whereas solute-solvent interactions increase it. If a sessile droplet without deposition mechanism is initialized with unsteady concentration or film height, solvent will evaporate and material redistributes by convection, resulting in a stable flat film or droplet solution. Our analysis reveals the existence of stable stationary droplet solutions contrasting the behavior of a volatile simple liquid.

The diffusion-limited precipitation from a homogeneous mixture has been investigated, showing that the solutal solid-liquid interface is prone to a fingering instability and subsequent tip-splitting. Unfortunately, the curvature term κ causes numerical stiffness when two interfacial corners meet and the interface normals become ambiguous. For fast solute diffusion the onset of instability is delayed by longer transient aggregate growth.

These results are relevant for the full model since the dynamics prior to deposition are only governed by the hydrodynamic equations. The instability of the solutal solid-liquid interface exists in both the diffusion-limited as well as the full model.

For the full model we have discussed modeling intricacies such as the value of the mixing parameter χ, taking care that the anti-diffusion regime is avoided, practical parameter ranges for the simulations and introduced a function $m(h)$, which switches off non-convective fluxes for film heights below the precursor. The analysis is mostly performed for 1D substrates for which the homogeneous deposition and ridge deposits are of particular interest. The concentration profiles of the ridges are similar to those of sessile droplets before the onset of deposition, but also slightly different due to the active setup. A morphological phase diagram has been obtained in the (Ω, v) (strength of evaporation, transfer velocity) plane for long simulation times distinguishing between stationary solutions, time-periodic solutions (TPS), presence of deposits and the formation of liquid ridge(s). The existence of TPS is well-known for active setups such as dip-coating. In comparison to the dip-coating of a single component volatile liquid, volatility of the solvent immensely increases the v-range of TPS while deposition extends this even further. We distinguish two types of ridge deposits: One, deposition from detached liquid ridges and two,

deposition before detachment. The latter of which highly depends on the meniscus dynamics and results in a variety of base thicknesses, amplitudes and ridge symmetries. A parameter scan of the initial solute concentration shows that deposit properties depend nonlinearly on C_0, in addition, an intermediate regime of flat deposition exists above the equilibrium solute concentration $C_0 \approx 0.55 < C_{\mathrm{eq}}$. For 2D substrates only projections of 1D long time solutions have been found for the dip-coating geometry. A sessile droplet on a 2D subsstrate has shown aggregate deposition quickly followed by a fingering instability, triggered by initial noise and FDM perturbations. The fingering pattern shows properties of dendrites with side branching and tip-splitting. The final pattern reminds of a fingering pattern with mound-like height profile.

Unfortunately, the disjoining pressure is a source of numerical stiffness. The sudden dip in film height upon deposition results in disjoining pressure values in its diverging regime. The aforementioned switch function avoids this by halting evaporation of the precursor, thereby preventing the solute concentration to become too high.

We have identified FDM stencils causing numerical instability and confirmed the limits of our explicit approximations. In essence, the numerical problems are a consequence of tracking the three-phase contact line and resolving the solutal solid-liquid interface. While FDM are very intuitive to implement, the drawbacks on numerical stability and mass conservation are quite severe and time consuming to work with. The implementation should be switched to the oomph-lib one, i.e., FEM and implicit time-stepping. The implicit scheme will be beneficial for mass conservation and stability while mesh adaptation will help resolving multiscale structures.

We have shown that the full model can capture the fingering instability of the solutal solid-liquid interface for the case of a sessile droplet. The precipitation process is triggered by initializing with a nucleus. This cannot be done for the dip-coating geometry. Since phase-field gradients are energetically punished, any small initial perturbation relaxes before the onset of deposition. Therefore a relatively strong tilt of f_{xm} of $\lambda = 3$, for which the nucleation barrier vanishes at high concentrations, has been chosen. This results in a different problem, namely, the occurrence of a third phase, see Fig. 2.2. In practice the manifestation of the third phase can be well prevented by increasing the solutal solid-liquid interface width, i.e., decreasing the length scale ratio Λ. However, this opposes the purpose of a diffuse interface which should have a relatively small width. Therefore, a different approach must be chosen for the future. There are at least two approaches to this problem. One is keeping the nucleation barrier ($\lambda \leq 1$) for all concentrations and repeatedly introducing noise into the system throughout the simulation. However this shifts the approach to a more stochastic one and introduces an additional parameter. Another is choosing a different potential such that no third phase is possible and the nucleation barrier still vanishes as the equilibrium solute concentration is approached. However, this cannot be done arbitrarily as some physical motivation should be kept.

We further suggest dropping the counter term of the curvature driven interface motion $\kappa(\nabla\phi)$. It is not required for the formation of dendrites. In fact its absence reflects the Gibbs-Thomson relation in the sharp interface limit. The FDM discretization introduces sufficient anisotropy. If an isotropic scheme is chosen, the fingering instability of the solutal solid-liquid interface will result in the formation of seaweed-like patterns. It is possible that viscous drag is enough to result in the regular small scale dendrites as seen in Fig. 1.2. If not, anisotropy can still be reintroduced by modifying the solutal solid-liquid surface tension.

In order to model demixing instabilities of non-vanishing wavelength, a gradient energy term for the solute concentration can be introduced.

Coupling a thin-film model to a phase-field equation is a promising approach for the description of liquid flow and precipitation. The deposition of solid solute is modeled explicitly. Even

dynamics of the deposit itself can be added due to the modular approach. Aside from above suggestions to modify the full model, next steps are going to be finding appropriate parameters for a hydrodynamic fingering instability and then include the deposition mechanism, to see if the expected multiscale patterns appear.

Theoretical investigations of the LB transfer have been performed in literature cited in Chap. 5. We have extended said research by focusing on 2D domains. An analysis of the bifurcation structure for varying transfer velocity v on a small domain with emphasis on fingering patterns, i.e., vertical stripes, has been performed. Aside from known stationary 1D states, stable single and two finger solutions are found, connected by similar but unstable states that possess spots of LC surfactant phase between fingers or at their tips. These states connect the LC and LE type 1D solution branches as well, coexisting with the snaking structure of the 1D unstable states. The curve of 2D states loops and criss-crosses densely through parameter space. We have varied the lateral domain size, showing that the stable vertical stripe solutions found by continuation are not results from finite size effects. FEM (continuation) and FDM (DNS) discretizations have been matched in order to verify the vertical stripe solutions, showing good agreement. Further, the two finger branch forms a region of multistability with the branch of horizontal stripes. Furthermore, the vertical stripe branches gain stability from a Hopf bifurcation.

An interesting next step will be continuing the TPS emerging from the Hopf bifurcations from which the vertical stripe solutions gain stability, see where they end and how they are related to the stable TPS of horizontal stripes. However, the corresponding steady state is two dimensional which makes such an endeavor particularly demanding in computational cost and numerical stability is not guaranteed either.

The stripe distances of horizontal stripes have been controlled by periodically varying v around a mean value and typical synchronization phenomena have been found. Select 2D branches calculated from DNS do not exhibit major synchronization in the transversal direction. The oblique pattern is not synchronized in either direction while the lattice one is solely synchronized in the transfer direction. More fractional synchronization orders are not ruled out. It is possible that synchronization of the transversal direction does occur in very limited parameter regions. The system exhibits multistability and can be controlled by changing forcing amplitude and forcing frequency in addition to the transfer velocity.

Overall, the development of the full model, its analysis and the Langmuir-Blodgett results provide new insights into the dynamics of complex liquids and also transversal instabilities of related interfaces.

A. Appendix

A.1. Hydrodynamic Side Calculations

A.1.1. Derivation of Compressible Navier-Stokes Equations

The following discussion is inspired by Schlichting and Kestin's book on boundary layer theory as well as Leal's book on advanced transport phenomena [SK61, Lea07]. We characterize fluid flow by its velocity field $\tilde{\mathbf{u}}$, pressure $\tilde{p}$ and density $\tilde{\rho}$. These 5 unknowns can be determined by the continuity equation (conservation of mass), equations of motion (conservation of momentum) and the thermodynamic equation of state $\tilde{p} = \tilde{f}(\tilde{\rho})$. The continuity equation reads

$$\partial_{\tilde{t}}\tilde{\rho} + \tilde{\nabla} \cdot (\tilde{\rho}\tilde{\mathbf{u}}) = 0. \tag{A.1}$$

The general momentum equation from Newton's second law reads

$$\tilde{\rho}\frac{D\tilde{\mathbf{u}}}{D\tilde{t}} = \tilde{\mathbf{F}} + \tilde{\mathbf{P}}. \tag{A.2}$$

Momentum changes under the influence of body forces $\tilde{\mathbf{F}}$ and surface forces $\tilde{\mathbf{P}}$. The forces mentioned here have units of force densities. Surface forces can be separated into shear and normal stresses. Thus, $\tilde{\mathbf{P}}$ can be replaced by the stress tensor $\underline{\tilde{\sigma}}$

$$\tilde{\rho}\frac{D\tilde{\mathbf{u}}}{D\tilde{t}} = \tilde{\mathbf{F}} + \tilde{\nabla} \cdot \underline{\tilde{\sigma}}. \tag{A.3}$$

These are also known as *Cauchy's* equations of motion. The material, or advective, derivative is defined as

$$\frac{D\tilde{\rho}}{D\tilde{t}} = \frac{\partial\tilde{\rho}}{\partial\tilde{t}} + \tilde{\mathbf{u}} \cdot \tilde{\nabla}\tilde{\rho}. \tag{A.4}$$

Note that all fields depend on Eulerian coordinates. Thus, the material derivative describes the rate of change in a frame moving with some material volume (Lagrangian). It is useful to consider the deviatoric stresses $\underline{\tilde{\tau}}$, also known as viscous stress tensor, from a reference state in which the fluid is at rest with thermodynamic pressure p. Then the Eq. (A.3) reads

$$\tilde{\rho}\frac{D\tilde{\mathbf{u}}}{D\tilde{t}} = -\tilde{\nabla}p + \tilde{\nabla} \cdot \underline{\tilde{\tau}} + \tilde{\mathbf{F}}. \tag{A.5}$$

Note that $\underline{\tilde{\sigma}}$ and $\underline{\tilde{\tau}}$ are symmetric tensors (if local torque is of order larger than unit volume). At this point $\underline{\tilde{\tau}}$ needs to be specified further. We assume an isotropic Newtonian fluid, thus the stress tensor linearly depends on the strain rate tensor with no preferential direction. Further, the strain rate tensor depends on the velocity gradient. Thus,

$$\underline{\tilde{\tau}} \sim \tilde{\nabla}\tilde{\mathbf{u}}. \tag{A.6}$$

With $\tilde{\nabla}\tilde{\mathbf{u}}$ being the Jacobian of the velocity field. Note, that $\underline{\tilde{\tau}}$ cannot contain elements independent of $\tilde{\nabla}\tilde{\mathbf{u}}$ since stress should vanish for $\tilde{\mathbf{u}} = const$. Although we previously established that $\tilde{\tau}$ is symmetric, it is sensible to analyze why an antisymmetric part would not contribute to the strain. We split the Jacobian into symmetric $\underline{\dot{\tilde{\varepsilon}}}$ and antisymmetric contribution $\underline{\tilde{R}}$

$$\tilde{\nabla}\tilde{\mathbf{u}} = \underline{\dot{\tilde{\varepsilon}}} + \underline{\tilde{R}}. \tag{A.7}$$

$$= \left[\frac{1}{2}(\tilde{\nabla}\tilde{\mathbf{u}} + \tilde{\nabla}\tilde{\mathbf{u}}^{\mathsf{T}})\right] + \left[\frac{1}{2}(\tilde{\nabla}\tilde{\mathbf{u}} - \tilde{\nabla}\tilde{\mathbf{u}}^{\mathsf{T}})\right] \tag{A.8}$$

The antisymmetric part then reads

$$\tilde{R}_{ij} = \left[\frac{1}{2}(\tilde{\nabla}\tilde{\mathbf{u}} - \tilde{\nabla}\tilde{\mathbf{u}}^{\mathsf{T}})\right]_{ij} = \frac{1}{2}\left(\partial_j \tilde{u}_i - \partial_i \tilde{u}_j\right) \tag{A.9}$$

$$= \frac{1}{2}\tilde{\nabla} \times \tilde{\mathbf{u}}. \tag{A.10}$$

This expression can be identified to be the angular velocity $\tilde{\boldsymbol{\omega}}$ of a rigid body rotation

$$\tilde{\boldsymbol{\omega}} = \frac{1}{2}\tilde{\nabla} \times \tilde{\mathbf{u}}. \tag{A.11}$$

In other words: Contributions of the above form to the stress tensor behave exactly like the curl of $\tilde{\mathbf{u}}$. Its components and therefore influence change as $\tilde{\mathbf{u}}$ changes in space. Overall the resulting motion corresponds to a rigid body rotation with angular velocity $\tilde{\boldsymbol{\omega}}$. Obviously, a rigid body rotation does not cause strain. Therefore, $\tilde{\tau}$ has to be a symmetric tensor. Note, that Eq. (A.11) can be easily derived for a rotation around a principal axis z by calculating $\tilde{\nabla} \times \tilde{\mathbf{u}}$ in cylinder coordinates.

The contribution of the symmetric Jacobian $\underline{\dot{\tilde{\varepsilon}}}$ is usually called the *strain rate tensor* or *rate of strain tensor*. In general $\underline{\dot{\tilde{\varepsilon}}}$ will have diagonal and off-diagonal elements. The former results in contraction or expansion of the fluid element where-as the latter represents the strain caused by pure shearing. In order to separately model these effects the stress tensor can be written as

$$\underline{\tilde{\tau}} = 2\eta\underline{\dot{\tilde{\varepsilon}}} + \lambda\tilde{\nabla} \cdot \tilde{\mathbf{u}}\underline{I} \tag{A.12}$$

$$= \tilde{\eta}\left(\nabla\tilde{\mathbf{u}} + \tilde{\nabla}\tilde{\mathbf{u}}^{\mathsf{T}}\right) + \lambda\tilde{\nabla} \cdot \tilde{\mathbf{u}}\underline{I}. \tag{A.13}$$

η is then the dynamic viscosity, sometimes shear viscosity, λ the bulk viscosity and $\underline{I}$ the identity matrix. The compressional contribution naturally vanishes for $\tilde{\nabla} \cdot \tilde{\mathbf{u}} = 0$, which represents the incompressible case. This can be easily shown by expressing the continuity equation in the comoving frame

$$\frac{D\tilde{\rho}}{D\tilde{t}} + \tilde{\rho}\tilde{\nabla} \cdot \tilde{\mathbf{u}} = 0. \tag{A.14}$$

Here, $\frac{D\tilde{\rho}}{D\tilde{t}} = 0$ and $\tilde{\nabla} \cdot \tilde{\mathbf{u}} = 0$ are equivalent, i.e., constant density(in time) in Lagrangian view is equivalent to $\tilde{\nabla} \cdot \tilde{\mathbf{u}} = 0$. In the laboratory frame changes to $\tilde{\rho}$ can then only occur by advection while retaining the spatial density profile. Often, a stronger assumption is made by setting $\tilde{\rho} = const.$ both in time and space. Then $\partial_{\tilde{t}}\tilde{\rho} = 0$ as well. In any case, the condition for incompressibility is

$$\tilde{\nabla} \cdot \tilde{\mathbf{u}} = 0. \tag{A.15}$$

Note that λ is sometimes neglected in the compressible case anyway. If that is not the case, then Stokes' hypothesis

$$\lambda \approx -\frac{2}{3}\eta \tag{A.16}$$

is usually applied [Sto49]. Overall, the compressible momentum Navier-Stokes equations read

$$\tilde{\rho}\frac{D\tilde{\mathbf{u}}}{D\tilde{t}} = -\tilde{\nabla}\tilde{p} + \tilde{\nabla}\cdot\left[\eta\left(\tilde{\nabla}\tilde{\mathbf{u}} + \tilde{\nabla}\tilde{\mathbf{u}}^{\mathsf{T}}\right) + \lambda\tilde{\nabla}\cdot\tilde{\mathbf{u}}\underline{I}\right] + \tilde{\mathbf{F}}. \tag{A.17}$$

For $\eta = const.$ one can further simplify

$$\tilde{\nabla}\cdot\tilde{\nabla}\tilde{\mathbf{u}} = \Delta\tilde{\mathbf{u}} \tag{A.18}$$

$$\tilde{\nabla}\cdot\tilde{\nabla}\tilde{\mathbf{u}}^{\mathsf{T}} = \tilde{\nabla}(\tilde{\nabla}\cdot\tilde{\mathbf{u}}). \tag{A.19}$$

The latter vanishes in the incompressible case.

A.1.2. Derivation of Kinematic Condition

Let

$$\tilde{S}(\tilde{\mathbf{x}}^{(3)}, \tilde{t}) = \tilde{z} - \tilde{h}(\tilde{x}, \tilde{y}, \tilde{t}) = 0 \tag{A.20}$$

denote the liquid-gas interface. It is assumed that no mass transport occurs through this interface, therefore the same fluid particles are part of the surface for all times. Formally, this means that the material derivative of the implicit surface $\tilde{S}$ vanishes [Lea07].

$$
\begin{aligned}
0 &= \left.\frac{D(\tilde{z} - \tilde{h}(\tilde{x}, \tilde{y}, \tilde{t}))}{D\tilde{t}}\right|_{\tilde{z}=\tilde{h}} \\
&= \partial_{\tilde{t}}\tilde{z} + \tilde{\mathbf{u}}^{(3)}\big|_{\tilde{z}=\tilde{h}} \cdot \tilde{\nabla}^{(3)}\tilde{z} - \partial_{\tilde{t}}\tilde{h} - \tilde{\mathbf{u}}^{(3)}\big|_{\tilde{z}=\tilde{h}} \cdot \tilde{\nabla}^{(3)}\tilde{h}(\tilde{x}, \tilde{y}, \tilde{t}) \\
&= u_{\tilde{z}}\big|_{\tilde{z}=\tilde{h}} - \partial_{\tilde{t}}\tilde{h} - \tilde{\mathbf{u}}\big|_{\tilde{z}=\tilde{h}} \cdot \tilde{\nabla}\tilde{h} - u_{\tilde{z}}\big|_{\tilde{z}=\tilde{h}}\partial_{\tilde{z}}\tilde{h}
\end{aligned} \tag{A.21}
$$

$$\Leftrightarrow u_{\tilde{z}}\big|_{\tilde{z}=\tilde{h}} = \partial_{\tilde{t}}\tilde{h} + \tilde{\mathbf{u}}\big|_{\tilde{z}=\tilde{h}} \cdot \tilde{\nabla}\tilde{h}. \tag{A.22}$$

After evaluation of the operators, we arrive at the kinematic boundary condition by utilizing the independence of $\tilde{z}$.

A.2. Binary Mixture Dilute Limit

By applying the symmetric thin-film equations for a binary mixture Eq. (2.57)-(2.58) the dynamic equation for film height h can be easily formulated since the diffusive terms cancel each other.

$$\partial_t h = \partial_t \psi_1 + \partial_t \psi_2 = -\nabla \cdot \left\{ \frac{h^3}{3\eta} \nabla\left[\gamma\Delta h - f'(h)\right] \right\} \tag{A.23}$$

The one for the solute concentration C takes a couple more steps.

$$
\begin{aligned}
\partial_t C_2 = \partial_t \frac{\psi_2}{h} &= \frac{1}{h^2}\left(h\partial_t\psi_2 - \psi_2\partial_t h\right) \\
&= \frac{1}{h^2}\left\{ h\left[-\nabla\cdot\left(\frac{1}{3\eta}\psi_2 h^2 \nabla P\right) + \nabla\cdot\left(Dh(1 - 2\chi C_1 C_2)\right)\nabla C_2\right]\right.
\end{aligned}
$$

$$-\psi_2 \left[-\nabla \cdot \left(\frac{1}{3\eta} h^3 \nabla P \right) \right] \Bigg\} \tag{A.24}$$

$$P = \gamma \Delta h - f'(h) \tag{A.25}$$

Apply

$$\nabla \cdot \left(\psi_2 h^2 \nabla P \right) = \left(h^2 \nabla \psi_2 + 2\psi_2 h \nabla h \right) \cdot \nabla P + \psi_2 h^2 \Delta P \tag{A.26}$$

$$\nabla \cdot \left(h^3 \nabla P \right) = 3h^2 \nabla h \cdot \nabla P + h^3 \Delta P \tag{A.27}$$

for

$$\partial_t C_2 = -\frac{1}{h^2} \left\{ \frac{1}{3\eta} \left(h^3 \nabla \psi_2 - \psi_2 h^2 \nabla h \right) \cdot \nabla P - h \nabla \cdot \left(Dh \left(1 - 2\chi C_1 C_2 \right) \nabla C_2 \right) \right\}, \tag{A.28}$$

factor h^4 out of the convective part and apply the product rule in reverse

$$\nabla C_2 = \nabla \frac{\psi_2}{h} = \frac{h \nabla \psi_2 - \psi_2 \nabla h}{h^2} \tag{A.29}$$

leads to

$$\partial_t C_2 = -\frac{h^2}{3\eta} \nabla C_2 \cdot \nabla \left[\gamma \Delta h - f'(h) \right] + \frac{D}{h} \nabla \cdot \left(h \left(1 - 2\chi C_1 C_2 \right) \nabla C_2 \right). \tag{A.30}$$

Finally, setting $\chi = 0$ results in the binary mixture model in the dilute limit

$$\partial_t h = -\nabla \cdot \left\{ \frac{h^3}{3\eta} \nabla \left[\gamma \Delta h - f'(h) \right] \right\} \tag{A.31}$$

$$\partial_t C = -\frac{h^2}{3\eta} \nabla C \cdot \nabla \left[\gamma \Delta h - f'(h) \right] + \frac{D}{h} \nabla \cdot \left(h \nabla C \right). \tag{A.32}$$

A.3. Non-dimensionalization of Xu and Meakin Model

In this section, a phase-field model for precipitation with diffusive solute flux is non-dimensionalized. We begin by repeating Eq. (2.84) and (2.91) [XM08, XM11].

$$\partial_{\tilde{t}} \tilde{\phi} = -\frac{1}{\tau} \frac{\delta \tilde{\mathcal{F}}_{\mathrm{xm}}}{\delta \tilde{\phi}} - \frac{\varepsilon^2}{\tau} \tilde{\kappa} |\tilde{\nabla} \tilde{\phi}| \tag{A.33}$$

$$\partial_{\tilde{t}} \tilde{c} = D_{\mathrm{xm}} \tilde{\Delta} \tilde{c} + \alpha \partial_{\tilde{t}} \tilde{\phi} \left(1 + \frac{D_{\mathrm{xm}} \tilde{\Delta} \tilde{\phi} - \partial_{\tilde{t}} \tilde{\phi}}{\tilde{k} |\tilde{\nabla} \tilde{\phi}|} \right) \tag{A.34}$$

$$\tilde{\mathcal{F}}_{\mathrm{xm}} = \int \mathrm{d}^2 \tilde{\mathbf{x}} \left(\frac{\varepsilon^2}{2} (\tilde{\nabla} \tilde{\phi})^2 + f_{\mathrm{xm}} \right) \tag{A.35}$$

$$f_{\mathrm{xm}}(\tilde{\phi}, \tilde{c}; \lambda) = f_1(\tilde{\phi}) + \lambda f_2(\tilde{\phi}) \tilde{c} \tag{A.36}$$

$$f_1(\tilde{\phi}) = -\frac{\tilde{\phi}^2}{2} + \frac{\tilde{\phi}^4}{4} \tag{A.37}$$

$$f_2(\tilde{\phi}) = \tilde{\phi} - \frac{\tilde{\phi}^3}{3} \tag{A.38}$$

$$\tilde{\kappa} = \tilde{\nabla} \cdot \frac{\tilde{\nabla}\tilde{\phi}}{|\tilde{\nabla}\tilde{\phi}|} \tag{A.39}$$

We introduce general time T and length scales X which are specified later.

$$\tilde{t} = Tt \qquad \tilde{x}_i = Xx_i \qquad i \in \{1, 2\}. \tag{A.40}$$

$$\frac{\partial}{\partial \tilde{t}} = \frac{1}{T}\frac{\partial}{\partial t} \qquad \tilde{\nabla} = \frac{1}{X}\nabla \qquad \tilde{\kappa} = \frac{1}{X}\kappa \tag{A.41}$$

$$\tilde{\phi}(\tilde{x}, \tilde{y}, \tilde{t}) = \tilde{\phi}(Xx, Xy, Tt) = \phi(x, y, t) \tag{A.42}$$

$$\tilde{c}(\tilde{x}, \tilde{y}, \tilde{t}) = \tilde{c}(Xx, Xy, Tt) = c(x, y, t) \tag{A.43}$$

$$f_{\mathrm{xm}}(\tilde{\phi}, \tilde{c}; \lambda) = f_{\mathrm{xm}}(\phi, c; \lambda) \tag{A.44}$$

$$\tilde{\mathcal{F}}_{\mathrm{xm}} = \int \mathrm{d}x\mathrm{d}y X^2 \left(\frac{\varepsilon^2}{2X^2}(\nabla\phi)^2 + f_{\mathrm{xm}} \right) \tag{A.45}$$

$$= X^2 \mathcal{F}_{\mathrm{xm}}, \qquad E := X^2 \tag{A.46}$$

Since $\tilde{\mathcal{F}}_{\mathrm{xm}}$ has unit of length^2, the "energy" scale E is dimensional accordingly. The variation non-dimensionalizes as

$$\frac{\delta\tilde{\mathcal{F}}_{\mathrm{xm}}}{\delta\tilde{\phi}} = \frac{E}{X^2 \cdot 1}\frac{\delta\mathcal{F}_{\mathrm{xm}}}{\delta\phi} = \frac{\delta\mathcal{F}_{\mathrm{xm}}}{\delta\phi}. \tag{A.47}$$

Applying above relations, the (non-dimensional) ϕ-equation then reads

$$\partial_t\phi = T\partial_{\tilde{t}}\tilde{\phi}(\tilde{x}, \tilde{y}, \tilde{t}) \tag{A.48}$$

$$= \frac{T}{\tau}\left[-\frac{\delta\mathcal{F}_{\mathrm{xm}}}{\delta\phi} - \frac{\varepsilon^2}{X^2}\kappa|\nabla\phi| \right]. \tag{A.49}$$

While the $\tilde{c}$-equation reads

$$\partial_t c = T\partial_{\tilde{t}}\tilde{c} = T\left[D_{\mathrm{xm}}\tilde{\Delta}\tilde{c} + \alpha\partial_{\tilde{t}}\tilde{\phi}\left(1 + \frac{D_{\mathrm{xm}}\tilde{\Delta}\tilde{\phi} - \partial_{\tilde{t}}\tilde{\phi}}{\tilde{k}_r|\tilde{\nabla}\tilde{\phi}|} \right) \right] \tag{A.50}$$

$$= T\left[\frac{D_{\mathrm{xm}}}{X^2}\Delta c + \frac{\alpha}{T}\partial_t\phi\left(1 + \frac{\frac{D_{\mathrm{xm}}}{X^2}\Delta\phi - \frac{1}{T}\partial_t\phi}{\tilde{k}_r\frac{1}{X}|\nabla\phi|} \right) \right] \tag{A.51}$$

$$= \frac{TD_{\mathrm{xm}}}{X^2}\Delta c + \alpha\partial_t\phi\left(1 + \frac{\Delta\phi - \frac{X^2}{D_{\mathrm{xm}}T}\partial_t\phi}{\tilde{k}_r\frac{X}{D_{\mathrm{xm}}}|\nabla\phi|} \right). \tag{A.52}$$

In [XM08] the scales

$$T = \frac{\varepsilon^2}{D_{\mathrm{xm}}} \qquad X = \varepsilon \tag{A.53}$$

are chosen, i.e., a diffusive time scale and length on the scale of the phase-field interface width. This leads to the penultimate equations

$$\partial_t\phi = \frac{\varepsilon^2}{\tau D_{\mathrm{xm}}}\left(\Delta\phi - \partial_\phi f_{\mathrm{xm}}(\phi, c; \lambda) - \kappa|\nabla\phi| \right) \tag{A.54}$$

$$\partial_t c = \Delta c + \alpha \partial_t \phi \left(1 + \frac{\Delta \phi - \partial_t \phi}{k_r |\nabla \phi|} \right) \tag{A.55}$$

in which effective parameters k_r and Péclet number $\mathrm{Pe_{xm}}$

$$k_r = \frac{\varepsilon}{D_{\mathrm{xm}}} \tilde{k}_r \qquad \mathrm{Pe_{xm}} = \frac{\tau D_{\mathrm{xm}}}{\varepsilon^2} \tag{A.56}$$

can be identified. One can make a slightly different choice of parameters by introducing length scale of diffusion l and substitute k by Damköhler number D_a and length scale ratio $s = \frac{\varepsilon}{l}$

$$D_a = \frac{\tilde{k}_r l}{D_{\mathrm{xm}}} = \frac{\tilde{k}_r \varepsilon}{s D_{\mathrm{xm}}} = \frac{k_r}{s}. \tag{A.57}$$

The final equations then read

$$\partial_t \phi = \frac{1}{\mathrm{Pe_{xm}}} \left(\Delta \phi - \partial_\phi f_{\mathrm{xm}}(\phi, c; \lambda) - \kappa |\nabla \phi| \right) \tag{A.58}$$

$$\partial_t c = \Delta c + \alpha \partial_t \phi \left(1 + \frac{\Delta \phi - \partial_t \phi}{D_a s |\nabla \phi|} \right). \tag{A.59}$$

It is further necessary to express Eq. (2.95) in the effective parameters.

$$\tau = \frac{\varepsilon^2}{D_{\mathrm{xm}}} \mathrm{Pe_{xm}} = \alpha \lambda \frac{\varepsilon^2}{D_{\mathrm{xm}}} \left(\frac{5}{3} + \frac{\sqrt{2} D_{\mathrm{xm}}}{\tilde{k}_r \varepsilon} \right) \tag{A.60}$$

$$\Leftrightarrow \mathrm{Pe_{xm}} = \alpha \lambda \left(\frac{5}{3} + \frac{\sqrt{2} D_{\mathrm{xm}}}{\tilde{k}_r \varepsilon} \right) \tag{A.61}$$

$$= \alpha \lambda \left(\frac{5}{3} + \frac{\sqrt{2}}{s D_a} \right) \tag{A.62}$$

$$\Leftrightarrow \lambda = \frac{\mathrm{Pe_{xm}}}{\alpha \left(\frac{5}{3} + \frac{\sqrt{2}}{s D_a} \right)} \tag{A.63}$$

Note that $\mathrm{Pe_{xm}}$ corresponds to P_e' and s to ε' in [XM11].

A.4. Non-dimensionalization of the Full Model

In this section, the precipitation model under complex fluid flow presented in Sec. 2.5 is non-dimensionalized. The dimensional dynamic equations (2.104)-(2.106) read

$$\partial_{\tilde{t}} \begin{pmatrix} \tilde{\psi}_1 \\ \tilde{\psi}_2 \end{pmatrix} = -\tilde{\nabla} \cdot \begin{pmatrix} \tilde{\mathbf{J}}_{1,c} \\ \tilde{\mathbf{J}}_{2,c} \end{pmatrix} + \begin{pmatrix} \tilde{J}_{\mathrm{evap}} \\ \tilde{J}_{\mathrm{source}} \end{pmatrix}$$

$$= \tilde{\nabla} \cdot \left[\left((\underline{\tilde{Q}}^{\mathrm{diff}} + (\underline{\tilde{Q}}^{\mathrm{conv}}) \begin{pmatrix} \tilde{\nabla} \frac{\delta \tilde{\mathcal{F}}_{\mathrm{bm}}}{\delta \tilde{\psi}_1} \\ \tilde{\nabla} \frac{\delta \tilde{\mathcal{F}}_{\mathrm{bm}}}{\delta \tilde{\psi}_2} \end{pmatrix} \right) \right] + \begin{pmatrix} -E_v \left(\frac{\delta \tilde{\mathcal{F}}_{\mathrm{bm}}}{\delta \tilde{\psi}_1} - \tilde{\mu}_g \right) \\ \alpha (\tilde{\psi}_1 + \tilde{\psi}_2) \partial_{\tilde{t}} \tilde{\phi} \end{pmatrix} \tag{A.64}$$

$$\partial_{\tilde{t}} \tilde{\phi} = -\frac{1}{\tau} \frac{\delta \tilde{\mathcal{F}}_{\mathrm{xm}}}{\delta \tilde{\phi}} - \frac{\varepsilon^2}{\tau} \tilde{\kappa} |\tilde{\nabla} \tilde{\phi}| \tag{A.65}$$

$$\partial_{\tilde{t}}\tilde{\zeta} = -\alpha(\tilde{\psi}_1 + \tilde{\psi}_2)\partial_{\tilde{t}}\tilde{\phi} \tag{A.66}$$

$$\tilde{\mathcal{F}}_{\text{bm}}[\tilde{\psi}_1, \tilde{\psi}_2] = \int \mathrm{d}^2\tilde{\mathbf{x}} \left\{ \frac{\gamma}{2}\left[\tilde{\nabla}\tilde{h}\right]^2 + f(h) + n_{\max}k_B\hat{T} \right. \tag{A.67}$$

$$\left. \cdot \left[\tilde{\psi}_1 \log(\tilde{C}_1) + \tilde{\psi}_2 \log(\tilde{C}_2) - \tilde{h} + \chi\frac{\tilde{\psi}_1\tilde{\psi}_2}{\tilde{h}} \right] \right\} \tag{A.68}$$

$$\tilde{\mathcal{F}}_{\text{xm}} = \int \mathrm{d}^2\tilde{\mathbf{x}} \left(\frac{\varepsilon^2}{2}(\tilde{\nabla}\tilde{\phi})^2 + f_{\text{xm}}(\tilde{\phi}, \tilde{C}_2) \right). \tag{A.69}$$

We begin non-dimensionalizing the $\tilde{\psi}_1$ and $\tilde{\psi}_2$ equations by introducing non-dimensional quantities as follows:

$$\tilde{t} = Tt \qquad \tilde{\mathbf{x}} = X\mathbf{x} \qquad \tilde{\psi}_i(\tilde{x}, \tilde{y}, \tilde{t}) = H\psi_i(x, y, t) \qquad \tilde{\mathcal{F}}_{\text{bm}} = F\mathcal{F}_{\text{bm}} \tag{A.70}$$

$$\frac{\partial}{\partial \tilde{t}} = \frac{1}{T}\frac{\partial}{\partial t} \qquad \tilde{\nabla} = \frac{1}{X}\nabla \qquad \frac{\partial}{\partial \tilde{\psi}_i} = \frac{1}{H}\frac{\partial}{\partial \psi_i} \tag{A.71}$$

$$\partial_t \begin{pmatrix} \psi_1 \\ \psi_2 \end{pmatrix} = \frac{T}{H}\partial_{\tilde{t}} \begin{pmatrix} \tilde{\psi}_1 \\ \tilde{\psi}_2 \end{pmatrix} = -\frac{T}{H}\tilde{\nabla} \cdot \begin{pmatrix} \tilde{\mathbf{J}}_{1,c} \\ \tilde{\mathbf{J}}_{2,c} \end{pmatrix} + \frac{T}{H} \begin{pmatrix} \tilde{J}_{\text{evap}} \\ \tilde{J}_{\text{source}} \end{pmatrix}. \tag{A.72}$$

A.4.1. Conserved Fluxes of ψ_1 and ψ_2

Consider the conserved parts first.

$$\partial_t \begin{pmatrix} \psi_1 \\ \psi_2 \end{pmatrix} = -\frac{T}{H}\nabla \cdot \begin{pmatrix} \tilde{\mathbf{J}}_{1,c} \\ \tilde{\mathbf{J}}_{2,c} \end{pmatrix} = \frac{T}{H}\frac{1}{X}\nabla \cdot \left[\left(\underline{\tilde{Q}}^{\text{diff}} + \underline{\tilde{Q}}^{\text{conv}}\right) \frac{F}{X^2H}\frac{1}{X} \begin{pmatrix} \nabla\frac{\delta\mathcal{F}_{\text{bm}}}{\delta\psi_1} \\ \nabla\frac{\delta\mathcal{F}_{\text{bm}}}{\delta\psi_2} \end{pmatrix} \right] \tag{A.73}$$

$$= \frac{TF}{X^4H^2}\frac{1}{X}\nabla \cdot \left[\left(\underline{\tilde{Q}}^{\text{diff}} + \underline{\tilde{Q}}^{\text{conv}}\right) \begin{pmatrix} \nabla\frac{\delta\mathcal{F}_{\text{bm}}}{\delta\psi_1} \\ \nabla\frac{\delta\mathcal{F}_{\text{bm}}}{\delta\psi_2} \end{pmatrix} \right] \tag{A.74}$$

$$\dots$$

Specifically, we apply scales as in thinfilm equations for simple liquids which will leave the convective parts of the equation parameter free [TGT14].

$$X = \sqrt{\frac{3}{5}}\frac{\tilde{h}_{\text{eq}}}{\tilde{\vartheta}_{\text{eq}}} \qquad H = \tilde{h}_{\text{eq}} \qquad T = \frac{9\eta\tilde{h}_{\text{eq}}}{25\gamma\tilde{\vartheta}_{\text{eq}}^4} \left(= \frac{\eta X^4}{\gamma H^3} \right) \tag{A.75}$$

$$F = \gamma\tilde{h}_{\text{eq}}^2 \qquad \tilde{h}_{\text{eq}} = \left(\frac{B}{A}\right)^{\frac{1}{3}} \qquad \tilde{\vartheta}_{\text{eq}} = \sqrt{\frac{-2\tilde{f}(\tilde{h}_{\text{eq}})}{\gamma}} = \sqrt{\frac{3}{5}\frac{A}{\gamma}}\frac{1}{\tilde{h}_{\text{eq}}} \tag{A.76}$$

$$\dots = \frac{\eta}{\tilde{h}_{\text{eq}}^3}\nabla \cdot \left[\left(\underline{\tilde{Q}}^{\text{diff}} + \underline{\tilde{Q}}^{\text{conv}}\right) \begin{pmatrix} \nabla\frac{\delta\mathcal{F}_{\text{bm}}}{\delta\psi_1} \\ \nabla\frac{\delta\mathcal{F}_{\text{bm}}}{\delta\psi_2} \end{pmatrix} \right], \tag{A.77}$$

with stable equilibrium film height $\tilde{h}_{\text{eq}}$, mesoscopic equilibrium contact angle $\tilde{\vartheta}_{\text{eq}}$ and wetting energy coefficients A, B. Next, we identify the dimensionless mobilities

$$\underline{Q}^{\text{conv}} = \frac{\eta}{\tilde{h}_{\text{eq}}^3}\underline{\tilde{Q}}^{\text{conv}} = \frac{\eta}{\tilde{h}_{\text{eq}}^3}\frac{\tilde{h}_{\text{eq}}^3}{3\eta}(\psi_1 + \psi_2) \begin{pmatrix} \psi_1^2 & \psi_1\psi_2 \\ \psi_1\psi_2 & \psi_2^2 \end{pmatrix} \tag{A.78}$$

$$= \frac{\psi_1 + \psi_2}{3} \begin{pmatrix} \psi_1^2 & \psi_1\psi_2 \\ \psi_1\psi_2 & \psi_2^2 \end{pmatrix} \tag{A.79}$$

$$\underline{Q}^{\text{diff}} = \frac{\eta}{\tilde{h}_{\text{eq}}^3} \underline{\tilde{Q}}^{\text{diff}} = \frac{\eta}{\tilde{h}_{\text{eq}}^3} \frac{\tilde{h}_{\text{eq}}}{n_{\max}\hat{\zeta}} (\psi_1 + \psi_2) \frac{\psi_1\psi_2}{(\psi_1 + \psi_2)^2} \begin{pmatrix} 1 & -1 \\ -1 & 1 \end{pmatrix} \tag{A.80}$$

$$=: q \frac{\psi_1\psi_2}{\psi_1 + \tilde{\psi}_2} \begin{pmatrix} 1 & -1 \\ -1 & 1 \end{pmatrix} \tag{A.81}$$

with effective mobility

$$q = \frac{\eta}{\tilde{h}_{\text{eq}}^2 n_{\max}\hat{\zeta}} \tag{A.82}$$

that relates shear viscosity to diffusion related drag. q does not contain all parameters related to either convection or diffusion, thus we make a slight variable change by introducing a different dimensionless parameter, the inverse Péclet number. We define the convective and diffusive time scales τ_{conv} and τ_{diff}, respectively,

$$\tau_{\text{conv}} := T = \frac{\eta X^4}{\gamma H^3} \qquad \tau_{\text{diff}} := \frac{X^2}{D}, \qquad \text{with } D := \frac{k_B\hat{T}}{\hat{\zeta}}, \tag{A.83}$$

in which the diffusion coefficient D is identified by the Einstein relation. The inverse Péclet number is their ratio and Υ is a ratio between thermal and surface energy (volume) density

$$\text{Pe}^{-1} = q\Upsilon = \frac{\tau_{\text{conv}}}{\tau_{\text{diff}}} = \frac{3}{5} \frac{k_B\hat{T}\eta}{\hat{\zeta}\tilde{h}_{\text{eq}}\tilde{\vartheta}_{\text{eq}}^2\gamma} \tag{A.84}$$

$$\Upsilon = n_{\max}k_B\hat{T}\frac{X^2}{\gamma H} = \frac{3}{5}n_{\max}k_B\hat{T}\frac{\tilde{h}_{\text{eq}}}{\gamma\tilde{\vartheta}_{\text{eq}}^2} \tag{A.85}$$

$$\mathcal{F}_{\text{bm}} = \int_\Omega \frac{1}{2}(\nabla h)^2 + f(h) + \Upsilon\left[\psi_1\ln(C_1) + \psi_2\ln(C_2) - h + \chi\frac{\psi_1\psi_2}{h}\right] \, \text{d}x\text{d}y. \tag{A.86}$$

The intermediate steps for identifying the dimensionless free energy and wetting energy are shown in the following:

$$\mathcal{F}_{\text{bm}} = \frac{\tilde{\mathcal{F}}_{\text{bm}}}{F}$$

$$= \frac{1}{F} \int \text{d}^2\tilde{\mathbf{x}} \left\{ \frac{\gamma}{2}\left(\tilde{\nabla}\tilde{h}\right)^2 + \tilde{f}(\tilde{h}) + n_{\max}k_B\hat{T}\left[\tilde{\psi}_1\log(\tilde{C}_1) + \tilde{\psi}_2\log(\tilde{C}_2) - \tilde{h} + \chi\frac{\tilde{\psi}_1\tilde{\psi}_2}{\tilde{h}}\right] \right\}$$

$$= \frac{1}{\gamma H^2} \int \text{d}^2\mathbf{x}X^2 \left\{ \frac{\gamma H^2}{2X^2}(\nabla h)^2 + \tilde{f}(\tilde{h}) + n_{\max}k_B\hat{T}H \right.$$

$$\left. \cdot \left[\psi_1\log(C_1) + \psi_2\log(C_2) - h + \chi\frac{\psi_1\psi_2}{h}\right] \right\}$$

$$= \int \text{d}^2\mathbf{x} \left\{ \frac{1}{2}(\nabla h)^2 + \frac{X^2}{\gamma H^2}\tilde{f}(\tilde{h}) + n_{\max}k_B\hat{T}\frac{X^2}{\gamma H}\left[\psi_1\log(C_1) + \psi_2\log(C_2) - h + \chi\frac{\psi_1\psi_2}{h}\right] \right\}$$

$$= \int \text{d}^2\mathbf{x} \left\{ \frac{1}{2}h^2 + f(h) + \Upsilon\left[\psi_1\log(C_1) + \psi_2\log(C_2) - h + \chi\frac{\psi_1\psi_2}{h}\right] \right\}, \tag{A.87}$$

where the concentration (volume fraction) is

$$C_i(x, y, t) = \frac{\psi_i(x, y, t)}{h(x, y, t)} = \frac{\tilde{\psi}_i(\tilde{x}, \tilde{y}, \tilde{t})}{\tilde{h}(\tilde{x}, \tilde{y}, \tilde{t})} = \tilde{C}_i(\tilde{x}, \tilde{y}, \tilde{t}). \tag{A.88}$$

A dimensionless variation reads as

$$\frac{\delta \mathcal{F}_{\mathrm{bm}}}{\delta h} = \frac{HX^2}{F} \frac{\delta \tilde{\mathcal{F}}_{\mathrm{bm}}}{\delta \tilde{h}}, \tag{A.89}$$

in which $e_{\mathrm{bm}} = \frac{F}{X^2}$ can be called an energy (area) density scale. The non-dimensional wetting energy $f(h)$ is

$$\begin{aligned}
f(h) &= \frac{1}{e_{\mathrm{bm}}} \tilde{f} = \frac{X^2}{\gamma H^2} \left(-\frac{A}{2\tilde{h}^2} + \frac{B}{5\tilde{h}^5} \right) \\
&= \frac{X^2 A}{\gamma H^4} \left(-\frac{1}{2h^2} + \frac{B}{A} \frac{1}{H^3} \frac{1}{5h^5} \right) \qquad \left| \; H = \tilde{h}_{\mathrm{eq}} = \left(\frac{B}{A} \right)^{\frac{1}{3}} \right. \\
&= \frac{X^2 A}{\gamma H^4} \left(-\frac{1}{2h^2} + \frac{1}{5h^5} \right) \\
&= -\frac{1}{2h^2} + \frac{1}{5h^5} \tag{A.90}
\end{aligned}$$

A useful relations may be

$$\tilde{f}(\tilde{h}_{\mathrm{eq}}) = -\frac{3}{10} \frac{A}{\tilde{h}_{\mathrm{eq}}^2}. \tag{A.91}$$

In the following subsections non-dimensionalization of the non-conserved fluxes is considered.

A.4.2. Evaporative Flux

$$\begin{aligned}
J_{\mathrm{evap}} &= \frac{T}{H} \tilde{J}_{\mathrm{evap}} = -E_v \frac{T}{H} \left(\frac{\delta \tilde{\mathcal{F}}}{\delta \tilde{\psi}_1} - \tilde{\mu}_g \right) = -E_v \frac{T}{H} \frac{F}{X^2 H} \left(\frac{\delta \mathcal{F}}{\delta \psi_1} - \frac{X^2 H}{F} \tilde{\mu}_g \right) \\
&= -E_v \frac{T}{H} \frac{\gamma H}{X^2} \left(\frac{\delta \mathcal{F}}{\delta \psi_1} - \frac{X^2}{\gamma H} \tilde{\mu}_g \right) \\
&= -\Omega \left(\frac{\delta \mathcal{F}}{\delta \psi_1} - \mu \right) \tag{A.92}
\end{aligned}$$

The additional effective parameters are then the ratio of convective/evaporative time scales Ω and a dimensionless chemical potential (pressure) μ

$$\Omega = \frac{E_v T \gamma}{X^2} = \frac{\tau_{\mathrm{conv}}}{\tau_{\mathrm{evap}}} = E_v \frac{9\eta \tilde{h}_{\mathrm{eq}}}{25 \gamma \tilde{\vartheta}_{\mathrm{eq}}^4} \frac{\gamma}{\frac{3}{5} \frac{\tilde{h}_{\mathrm{eq}}^2}{\tilde{\vartheta}_{\mathrm{eq}}^2}} = \frac{3}{5} \frac{\eta}{\tilde{h}_{\mathrm{eq}} \tilde{\vartheta}_{\mathrm{eq}}^2} E_v \tag{A.93}$$

$$\mu = \frac{X^2}{\gamma H} \mu_g = \frac{3}{5} \frac{\tilde{h}_{\mathrm{eq}}}{\gamma \tilde{\vartheta}_{\mathrm{eq}}^2} \mu_g. \tag{A.94}$$

Executing the variations, we can see for the ψ_1 equation how the dynamic equation is composed of convective, diffusive and evaporative parts

$$\begin{aligned}
\partial_t \psi_1 = &- \nabla \cdot \left\{ \frac{1}{3} \psi_1 h^2 \nabla \left[\Delta h - f'(h) \right] - \mathrm{Pe}^{-1} h \left(1 - 2\chi C_1 C_2 \right) \nabla C_1 \right\} \\
&- \Omega \left[-\Delta h + f'(h) + \Upsilon \left(\log C_1 - 1 + \chi C_2^2 \right) - \mu \right]. \tag{A.95}
\end{aligned}$$

A.4.3. Source Term

The non-conserved flux density in $\partial_t \psi_2$ is non-dimensionalized as follows:

$$J_{\text{source}} = \frac{T}{H} \tilde{J}_{\text{source}} = \frac{T}{H} \alpha (\tilde{\psi}_1 + \tilde{\psi}_2) \partial_{\tilde{t}} \tilde{\phi} = \alpha (\psi_1 + \psi_2) \partial_t \phi . \tag{A.96}$$

Analogously the non-dimensional ζ-equation reads

$$\partial_t \zeta = -\alpha (\psi_1 + \psi_2) \partial_t \phi. \tag{A.97}$$

A.4.4. Phase-field

We can adopt Eq. (A.49) for the phase-field but this time introduce effective parameters σ and Λ as ratios of time scales of convection/particle mobility and length scales of lateral wetting/phase-field. Obviously, T and X remain unchanged from Eq. (A.75).

$$\sigma := \frac{T}{\tau} \qquad \Lambda := \frac{X}{\varepsilon} \tag{A.98}$$

$$\partial_t \phi = \frac{T}{\tau} \left[\frac{\varepsilon^2}{X^2} \Delta \phi - \partial_\phi f_{\text{xm}} (\phi, C_2 - C_{\text{eq}}; \lambda) - \frac{\varepsilon^2}{X^2} \kappa |\nabla \phi| \right] \tag{A.99}$$

$$= \sigma \left[\Lambda^{-2} \Delta \phi - \partial_\phi f_{\text{xm}} (\phi, C_2 - C_{\text{eq}}; \lambda) - \Lambda^{-2} \kappa |\nabla \phi| \right] \tag{A.100}$$

A.4.5. Generalization to Include Gravity

By adding another contribution $\tilde{\mathcal{F}}_g$ to the free energy of the binary mixture $\tilde{\mathcal{F}}_{\text{bm}}$ one can include gravitational effects

$$\tilde{\mathcal{F}}_g = \int_\Omega \tilde{f}_g(\tilde{h}) \, \mathrm{d}^2 \tilde{\mathbf{x}} = \int_\Omega \frac{1}{2} \tilde{\rho} \tilde{g} \tilde{h}^2 + \tilde{\rho} \tilde{g} \tilde{h} \tilde{\beta} \tilde{x} \, \mathrm{d}^2 \tilde{\mathbf{x}} . \tag{A.101}$$

This contribution accounts for hydrostatic pressure and, if the substrate is inclined, the potential energy depending on the small inclination angle $\tilde{\beta}$. $\tilde{\rho}$ is the constant mass density of the mixture and $\tilde{g}$ the gravitational acceleration. Constant density $\tilde{\rho}$ of the mixture is assumed which is why the gravity terms do not need to be separated into individual solvent and solute contributions. Non-dimensionalization then occurs the same way as in previous sections:

$$\frac{\delta \tilde{\mathcal{F}}_g}{\delta \tilde{\psi}_1} = \frac{\delta \tilde{\mathcal{F}}_g}{\delta \tilde{\psi}_2} = \frac{\partial \tilde{f}_g}{\partial \tilde{h}} - 0 = \tilde{\rho} \tilde{g} \tilde{h} + \tilde{\rho} \tilde{g} \tilde{\beta} \tilde{x} \tag{A.102}$$

$$\Leftrightarrow \frac{\delta \mathcal{F}}{\delta h} = \frac{\delta \mathcal{F}}{\delta \psi_i} = \frac{HX^2}{F} \frac{\delta \tilde{\mathcal{F}}_g}{\delta \tilde{\psi}_i} = \frac{X^2}{\gamma H} \tilde{\rho} \tilde{g} (\tilde{h} + \tilde{\beta} \tilde{x}) = g \left(h + \frac{X}{H} \tilde{\beta} x \right) = g(h + \beta x) . \tag{A.103}$$

The effective parameters g and β are defined using the previously chosen scales:

$$X^2 = \frac{3}{5} \frac{\tilde{h}_{\text{eq}}^2}{\tilde{\vartheta}_{\text{eq}}^2} \tag{A.104}$$

$$\Rightarrow g = \frac{\tilde{\rho} X^2}{\gamma} \tilde{g} = \frac{3}{5} \frac{\tilde{\rho} \tilde{h}_{\text{eq}}^2}{\gamma \tilde{\vartheta}_{\text{eq}}^2} \tilde{g} \tag{A.105}$$

$$\beta = \frac{X}{H}\tilde{\beta} = \sqrt{\frac{3}{5}}\frac{1}{\tilde{\vartheta}_{\text{eq}}}\tilde{\beta}. \tag{A.106}$$

Due to the $\psi_1 \leftrightarrow \psi_2$ symmetry this contribution does not appear in the diffusive part of the dynamic equations. The convective fluxes $\mathbf{J}_{i,c}$ are then supplemented by

$$-\frac{h}{3}\psi_i\left\{\psi_1\nabla\frac{X^2}{\gamma H}\frac{\delta\tilde{\mathcal{F}}_g}{\delta\tilde{\psi}_1} + \psi_2\nabla\frac{X^2}{\gamma H}\frac{\delta\tilde{\mathcal{F}}_g}{\delta\tilde{\psi}_2}\right\} = -\frac{h}{3}\psi_i\left\{\psi_1 g\left(\nabla h + \begin{pmatrix}\beta\\0\end{pmatrix}\right) + \psi_2 g\left(\nabla h + \begin{pmatrix}\beta\\0\end{pmatrix}\right)\right\}$$

$$= -\frac{h^2}{3}\psi_i\left\{g\left(\nabla(\psi_1 + \psi_2) + \begin{pmatrix}\beta\\0\end{pmatrix}\right)\right\} \tag{A.107}$$

A.4.6. Comoving Frame with Source Terms

Here, we show how switching out of the comoving frame affects source terms. Let $R_{c,\hat{\psi}_2}$ denote the conserved expressions on the right-hand side of the $\hat{\psi}_2$ equation in the frame moving with the substrate and $R_{\hat{\phi}}$ the right-hand side of the $\hat{\phi}$ equation.

$$\frac{d\hat{\psi}_2(\hat{x}, \hat{y}, t)}{dt} = R_{c,\hat{\psi}_2} + \alpha h\frac{d\hat{\phi}(\hat{x}, \hat{y}, t)}{dt} \tag{A.108}$$

$$\frac{d\hat{\phi}(\hat{x}, \hat{y}, t)}{dt} = R_{\hat{\phi}}(\hat{\phi}) \tag{A.109}$$

The local coordinates and fields of the substrate are denoted by $\wedge$. The transformations to the stationary laboratory frame then read

$$\hat{x} = x + vt \tag{A.110}$$

$$\hat{\psi}_2(\hat{x}, t) = \hat{\psi}_2(x + vt, t) =: \psi_2(x, t). \tag{A.111}$$

Then,

$$\Rightarrow \partial_t\psi_2(x, t) + v\partial_x\psi_2 = R_{c,\psi_2}(\psi_2) + \alpha h(\partial_t\phi + v\partial_x\phi) \tag{A.112}$$

$$\partial_t\phi(x, t) = R_{\hat{\phi}}(\phi) - v\partial_x\phi(x, t) . \tag{A.113}$$

Formally the source term only depends on $R_{\hat{\phi}}(\phi)$ but the ϕ equation is still advected, as it should be. This can be adopted for ζ as well.

A.5. Macroscopic and Mesoscopic Droplet

The one component thin-film equation reads

$$\partial_t h = -\nabla \cdot \left\{\frac{1}{3}h^3\nabla\left[\Delta h - f'(h)\right]\right\}, \tag{A.114}$$

$$f'(h) = \frac{1}{h^3} - \frac{1}{h^6}. \tag{A.115}$$

Solutions, which fulfill

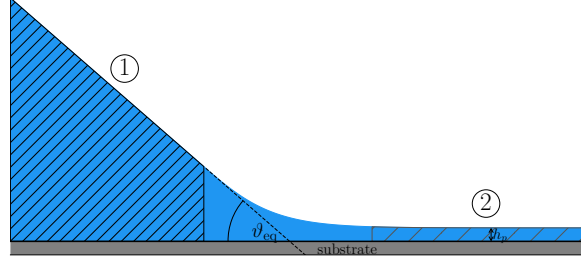$$-\Delta h + f'(h) - \mu = 0, \tag{A.116}$$

Figure A.1.: Sketch of the contact line region of an infinitely high droplet on a horizontal substrate. The rest of the substrate is covered by a precursor of height h_p. Region ① has constant slope $\partial_x h = -\vartheta_{\text{eq}}$ while region ② depicts the precursor region.

are stationary solutions of both the non-volatile (A.114) and volatile (A.117) thin-film equation. μ takes the role of a Lagrange multiplier in the former and a chemical potential in the latter case.

$$\partial_t h = -\nabla \cdot \left\{ \frac{1}{3} h^3 \nabla \left[\Delta h - f'(h) \right] \right\} - \Omega \left[-\Delta h + f'(h) - \mu \right] \tag{A.117}$$

In 1D the variation can be undone by multiplying Eq. (A.116) with $\partial_x h$ and integrating once

$$\frac{1}{2} \left(\partial_x h \right)^2 - f(h) + \mu h = E = const. \tag{A.118}$$

with integration constant or energy E. Consider a droplet of infinite height whose contact line region is depicted in Fig. A.1. Its curvature is zero in both regions ① and ② while the slope in region ① remains unchanged as $h \to \infty$. Equations (A.116) and (A.118) can then be simplified to

$$\begin{array}{cc}
① & ② \\
f'(h_\infty) = 0 = \mu & f'(h_p) = \mu \\
\frac{1}{2}\vartheta_{\text{eq}}^2 - \mu h_\infty = E & -f(h_p) + \mu h_p = E
\end{array}$$

Since $\mu = 0$ and $E = const.$ the equations simplify further to

$$f'(h_p) = 0 \qquad \Rightarrow h_p = 1 \tag{A.119}$$

$$\frac{1}{2}\vartheta_{\text{eq}}^2 = -f(h_p) \quad \Rightarrow \vartheta_{\text{eq}} = \sqrt{-2f(h_p)}. \tag{A.120}$$

Above relations change for a droplet of finite height as depicted in Fig. A.2. A droplet of finite height can be roughly divided into three parts: ① around the maximum h_0 with approximately constant curvature $\partial_{xx}h_0$, ② the inflection point that defines the contact angle $\partial_x h_i = \tilde{\vartheta}_{\text{eq}}$ and ③ the precursor region. The inflection point goes to infinity for an infinite droplet. Here, equations (A.116) and (A.118) evaluate to

$$\begin{array}{ccc}
① & ② & ③ \\
f'(h_p) = \mu & f'(h_i) = \mu & -\Delta h_0 + f'(h_0) = \mu \\
-f(h_p) + \mu h_p = E & \frac{1}{2}\tilde{\vartheta}_{\text{eq}}^2 - f(h_i) + \mu h_i = E & -f(h_0) + \mu h_0 = E
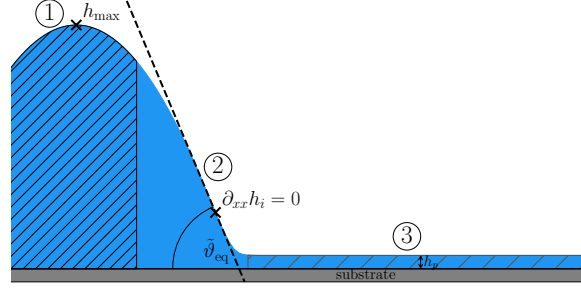\end{array}$$

Figure A.2.: Sketch of a finite droplet on a horizontal substrate. The rest of the substrate is covered by a precursor of height h_p. Region ① is around the maximum with approximately constant curvature. ② marks the inflection point while region ③ depicts the precursor region.
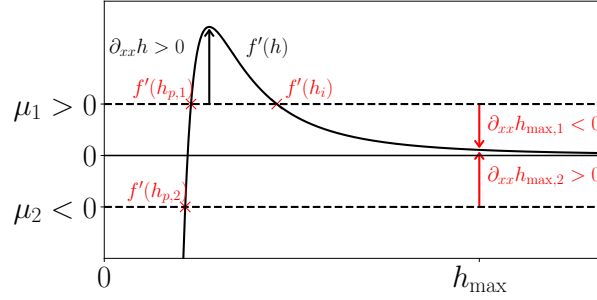
Figure A.3.: Sketch of the derivative of the wetting energy $f'(h)$ (black solid line). Chemical potentials $\mu_1 > 0$ and $\mu_2 < 0$ are depicted as black dashed lines, signifying condensation or evaporation. Precursor heights $h_{p,1}$, $h_{p,2}$ and height at inflection point h_i are marked in red. The curvatures required to fulfill Eq. (A.123) for some maximum height h_0 are depicted as well as the maximal curvature at the contact line.

After using the fact that μ and E are constant this system of equations can be reduced to a set of 4 equations with 5 unknowns: h_p, h_i, h_0, $\partial_{xx}h_0$ and $\tilde{\vartheta}_{\text{eq}}$

$$f'(h_p) = f'(h_i) = -\Delta h_0 + f'(h_0)[= \mu] \tag{A.121}$$

$$-f(h_p) + \mu h_p = \frac{1}{2}\tilde{\vartheta}_{\text{eq}}^2 - f(h_i) + \mu h_i = -f(h_0) + \mu h_0[= E] \tag{A.122}$$

If one were to choose an initial condition, one could set for example h_0 or $\partial_{xx}h_0$. The problem is finding an initial condition that fulfills Eq. (A.121)-(A.122). A parabolically shaped cap on a precursor cannot fulfill the conditions for ②. Still, one can deduce information on the existence of stationary solutions for varying μ with these equations. A necessary condition is for Eq. (A.121) to be true.

$$\partial_{xx}h_0 = f'(h_0) - \mu. \tag{A.123}$$

This can be well understood graphically by consulting Figure A.3. There, $f'(h)$ is depicted as a solid black line. In a volatile system μ acts as a chemical potential, it is an imposed property. For $\max(f'(h)) > \mu_1 > 0$ and some maximum height h_0 a stationary droplet solution will adopt precursor height $h_{p,1}$ and height at inflection point h_i while the curvature of the droplet fulfills Eq. (A.123). Since $f'(h_0) - \mu_1 < 0$, $\partial_{xx}h_0$ has the correct sign for a droplet. In the case of $\mu_2 < 0$

a stationary droplet solution cannot exist. However, a meniscus solution can since it does not have an inflection point but the right curvature. The argumentation is similar in the non-volatile case with the main difference being that μ is not imposed but takes the role of a Lagrange multiplier, adopting a value corresponding to the amount of liquid present in the system. This subtlety may lead to different stabilities depending on whether the conserved or non-conserved system is investigated as has been discussed for Allen-Cahn and Cahn-Hilliard type systems in Sec. 3 of [EGUW+19]. The aforementioned reference contains a bifurcation diagram on the TFE as well.

Equation (A.123) must still hold which means that stationary droplet solutions in a non-volatile case will never adopt $\mu < 0$. Note that the case of an infinite droplet corresponds to $\mu = 0$. The inflection point as well as the maximum height go to infinity. Obviously, stationary solutions do not exist for $\mu > \max(f'(h))$. The contribution of curvature can further be motivated by imagining the coarsening of multiple droplets. The droplets exchange liquid by increasing or decreasing the surrounding precursors. These deductions change when switching to a two-component system as is shown in Sec. 4.5.

A.6. Derivation of Parabolically Shaped Cap

In this section, the expression for a parabolically shaped cap is derived, basically calculating coefficients of a polynomial. The cap will be fully determined by precursor height h_p, maximum height h_0 and some contact angle ϑ. A radially symmetric parabola centered at $r = 0$ reads as

$$h(r) = ar^2 + b \tag{A.124}$$

The parabola shall reach precursor height at $r = R$ and the slope at that point is determined by ϑ while the height at $r = 0$ is set as well. The conditions then read

$$\partial_r h(R) = -\vartheta \tag{A.125}$$
$$h(R) = h_p \tag{A.126}$$
$$h(0) = h_0 \tag{A.127}$$

Equation (A.125) sets

$$\partial_r h(r = R) = 2aR = -\vartheta$$
$$a = -\frac{\vartheta}{2R} \tag{A.128}$$

which results in

$$h(r) = -\frac{\vartheta}{2R}r^2 + b. \tag{A.129}$$

Then Eq. A.126 determines b to

$$b = \frac{\vartheta}{2}R + h_p. \tag{A.130}$$

With Eq. (A.127) the remaining unknown variable R can be calculated.

$$h(r) = \frac{1}{2}\vartheta\left(-\frac{r^2}{R} + R\right) + h_p \tag{A.131}$$

$$h(0) = h_0$$

$$\Leftrightarrow \frac{1}{2}\vartheta R + h_p = h_0$$

$$\Leftrightarrow R = \frac{2(h_0 - h_p)}{\vartheta} \tag{A.132}$$

Inserting R results in

$$h(r) = \frac{1}{2}\vartheta\left(-r^2\frac{\vartheta}{2(h_0 - h_p)} + \frac{2(h_0 - h_p)}{\vartheta}\right) + h_p$$

$$= -\frac{\vartheta^2}{4(h_0 - h_p)}r^2 + h_0\,. \tag{A.133}$$

For the actual implementation the parabola is shifted to the center of the domain and cut off at $r \geq R$. We use the short hand notation $r = \sqrt{\left(x - \frac{L_x}{2}\right)^2 + \left(y - \frac{L_y}{2}\right)^2}$

$$h(x, y, 0) = \begin{cases} -\frac{\vartheta^2}{4(h_0 - h_p)}r^2 + h_0 & \text{for } r \leq R \\ h_p & \text{else} \end{cases}. \tag{A.134}$$

In the not rescaled formulation the slope at the contact line is approximately given by the equilibrium contact angle $\tilde{\vartheta}_{\text{eq}}$. Let us calculate this angle for the dimensionless formulation:

$$\partial_r h = \frac{X}{H}\partial_{\tilde{r}}\tilde{h}(\tilde{R}) \tag{A.135}$$

$$= \frac{X}{H}\sqrt{-2\frac{\gamma H^2}{X^2\gamma}f(h_{\text{eq}})} \tag{A.136}$$

$$= \sqrt{-2f(h_{\text{eq}})} \tag{A.137}$$

$$= -\vartheta_{\text{eq}} \tag{A.138}$$

A.7. Mullins-Sekerka Instability

We repeat the equations of Sec. 2.4.2:

$$\partial_{\tilde{t}}\tilde{C}_i = D_i\tilde{\Delta}\tilde{C}_i, \qquad\qquad i = s, l, \tag{A.139}$$

$$\mathbf{n}\cdot\left(D_l\tilde{\nabla}\tilde{C}_l - D_s\tilde{\nabla}\tilde{C}_s\right) = \left(\tilde{C}_s - \tilde{C}_l\right)\tilde{\mathbf{v}}\cdot\mathbf{n} \qquad\qquad \text{at } \tilde{\mathbf{x}} = \tilde{\xi}, \tag{A.140}$$

$$\tilde{C}_s = K\tilde{C}_l \qquad\qquad \text{at } \tilde{\mathbf{x}} = \tilde{\xi}, \tag{A.141}$$

$$T_l = T_m + m_l\tilde{C}_l - \frac{\hat{\gamma}T_m}{\tilde{\rho}L}\kappa \qquad\qquad \text{at } \tilde{\mathbf{x}} = \tilde{\xi}, \tag{A.142}$$

$$\tilde{C}_s \xrightarrow{\tilde{x}\to-\infty} C_\infty, \qquad\qquad \tilde{C}_l \xrightarrow{\tilde{x}\to\infty} C_\infty, \qquad\qquad \tilde{C}_i \xrightarrow{\tilde{x}\to 0} C_{\text{eq},i}. \tag{A.143}$$

See Sec. 2.4.2 for the definitions of the quantities. Equation (A.139) in the comoving frame reads

$$\partial_{\tilde{t}}\tilde{C}_i = D_i\tilde{\Delta}\tilde{C}_i - \tilde{v}\partial_{\tilde{x}}\tilde{C}_i. \tag{A.144}$$

With the Ansatz

$$\tilde{C}_i^*(\tilde{x}) = e^{-q\tilde{x}} \tag{A.145}$$

and Eq. (A.143) we find the steady state

$$\tilde{C}_l^* = C_\infty + (C_{\text{eq},l} - C_\infty)e^{-\frac{\tilde{v}}{D_l}\tilde{x}}, \qquad \tilde{C}_s^* = KC_{\text{eq},l}. \tag{A.146}$$

In case of a planar interface $\tilde{x} > 0$ denotes the liquid and $\tilde{x} < 0$ the solid phase. The interface advances towards $\tilde{x} \to +\infty$ We perform a linear stability analysis of this state by making the Ansatz

$$\tilde{C}_i(\tilde{x}, \tilde{y}) = \tilde{C}_i^* + \epsilon\tilde{C}_{i\tilde{k}}^{(1)}(\tilde{x})b(\tilde{t}, \tilde{y}), \tag{A.147}$$

$$\tilde{\xi}(\tilde{y}, \tilde{t}) = \epsilon\tilde{\xi}_{\tilde{k}}^{(1)}b(\tilde{t}, \tilde{y}), \tag{A.148}$$

$$\text{with } b(\tilde{t}, \tilde{y}) = e^{\tilde{\omega}\tilde{t}}e^{i\tilde{k}y}. \tag{A.149}$$

Eq. (A.139) then reads

$$\tilde{\omega}\epsilon\tilde{C}_{i\tilde{k}}^{(1)}b(\tilde{t}, \tilde{y}) = D_i\epsilon\partial_{\tilde{x}\tilde{x}}\tilde{C}_{i\tilde{k}}^{(1)}b(\tilde{t}, \tilde{y}) - \epsilon\tilde{k}^2 D_i\tilde{C}_{i\tilde{k}}^{(1)}b(\tilde{t}, \tilde{y}) - \epsilon\tilde{v}\partial_{\tilde{x}}\tilde{C}_{i\tilde{k}}^{(1)}b(\tilde{t}, \tilde{y}) \tag{A.150}$$

$$\Leftrightarrow \qquad \tilde{\omega}\tilde{C}_{i\tilde{k}}^{(1)} = D_i\partial_{\tilde{x}\tilde{x}}\tilde{C}_{i\tilde{k}}^{(1)} - \tilde{k}^2 D_i\tilde{C}_{i\tilde{k}}^{(1)} - \tilde{v}\partial_{\tilde{x}}\tilde{C}_{i\tilde{k}}^{(1)}. \tag{A.151}$$

We make another exponential Ansatz

$$\tilde{C}_{i\tilde{k}}^{(1)}(\tilde{x}) = e^{\tilde{q}\tilde{x}}, \tag{A.152}$$

which leads to the quadratic equation

$$\tilde{\omega} = D_i\tilde{q}^2 - \tilde{k}^2 D_i - \tilde{v}\tilde{q} \tag{A.153}$$

$$\Leftrightarrow \qquad \tilde{q}^2 = \frac{\tilde{\omega}}{D_i} + \tilde{k}^2 + \frac{\tilde{v}}{D_i}\tilde{q}. \tag{A.154}$$

Next, we apply the quasi-stationary approximation. It would be more rigorous to keep above equation as it is, i.e., denoting $\tilde{q}$ as the solutions of Eq. (A.154) and introduce the quasi-stationary approximation at the end of the derivation. However, doing this beforehand leads to simpler intermediate calculations, the result does not change. The quasi-stationary approximation assumes fast diffusive dynamics, i.e., the front moves slow enough for the concentration fields to adjust instantaneously:

$$\omega \ll D_i\tilde{k}^2, \qquad \tilde{k} \gg \frac{D_i}{\tilde{v}}. \tag{A.155}$$

Then Eq. (A.154) simplifies to

$$\tilde{q} = \pm\tilde{k}. \tag{A.156}$$

The solute concentration in each phase must converge to C_∞ as the distance from the interface increases, leading to

$$\tilde{C}_{s\tilde{k}}^{(1)}(\tilde{x}) = a_{s\tilde{k}}e^{\tilde{k}\tilde{x}}, \qquad \tilde{C}_{l\tilde{k}}^{(1)}(\tilde{x}) = a_{l\tilde{k}}e^{-\tilde{k}\tilde{x}}. \tag{A.157}$$

with coefficients $a_{i\tilde{k}}$, which we determine from the Gibbs-Thomson relation (A.142). First we realize that the temperature $\hat{T}$ of the isothermal system is

$$\hat{T} = \hat{T}_m + m_i C_{\text{eq},i}. \tag{A.158}$$

Of course this also holds at the interface

$$\hat{T}_l = \hat{T}_m + m_l C_{\text{eq},l}, \tag{A.159}$$

and Eq. (A.142) becomes

$$\tilde{C}_l = C_{\text{eq},l} + \frac{\hat{\gamma}\hat{T}_m}{\tilde{\rho}Lm_l}\tilde{\kappa}. \tag{A.160}$$

In 2D the curvature $\tilde{\kappa}$ reads

$$\tilde{\kappa} = -\frac{\partial_{\tilde{x}\tilde{x}}\tilde{\xi}}{\left(1 + \partial_{\tilde{x}}^2\right)^{\frac{3}{2}}} = -\partial_{\tilde{x}\tilde{x}}\tilde{\xi} + \mathcal{O}(\epsilon^2), \tag{A.161}$$

since $\tilde{\xi}$ is of order ϵ. On the solid side of the interface we then get with Eq. (A.141)

$$\tilde{C}_s^* + \epsilon a_{s\tilde{k}} e^{\tilde{k}\tilde{\xi}} b(\tilde{t}, \tilde{y}) = K C_{\text{eq},l} + K \frac{\hat{\gamma}\hat{T}_m}{\tilde{\rho}Lm_l}\left(-\partial_{\tilde{x}\tilde{x}}\tilde{\xi}\right). \tag{A.162}$$

Since $\tilde{\xi} = \mathcal{O}(\epsilon)$, we can approximate the exponential function on the left-hand side to zeroth order and get with $\tilde{C}_s^* = K C_{\text{eq},l}$ in the last step

$$\tilde{C}_s^* + \epsilon a_{s\tilde{k}} b(\tilde{t}, \tilde{y}) = K C_{\text{eq},l} + K \frac{\hat{\gamma}\hat{T}_m}{\tilde{\rho}Lm_l} k^2 \epsilon \tilde{\xi}_{\tilde{k}}^{(1)} b(\tilde{t}, \tilde{y}) \tag{A.163}$$

$$\Rightarrow \qquad a_{s\tilde{k}} = K \frac{\hat{\gamma}\hat{T}_m}{\tilde{\rho}Lm_l} k^2 \tilde{\xi}_{\tilde{k}}^{(1)}. \tag{A.164}$$

On the liquid side we similarly get

$$C_\infty + (C_{\text{eq},l} - C_\infty)\, e^{-\frac{v}{D_l}\tilde{\xi}} + \epsilon a_{l\tilde{k}} b(\tilde{t}, \tilde{y}) = C_{\text{eq},l} + \frac{\hat{\gamma}\hat{T}_m}{\tilde{\rho}Lm_l}\tilde{k}^2 \epsilon \tilde{\xi}_{\tilde{k}}^{(1)} b(\tilde{t}, \tilde{y}) \tag{A.165}$$

$$\Rightarrow C_\infty + (C_{\text{eq},l} - C_\infty)\left(1 - \frac{v}{D_l}\epsilon\tilde{\xi}_{\tilde{k}}^{(1)} b(\tilde{t}, \tilde{y})\right) + \epsilon a_{l\tilde{k}} b(\tilde{t}, \tilde{y}) = C_{\text{eq},l} + \frac{\hat{\gamma}\hat{T}_m}{\tilde{\rho}Lm_l}\tilde{k}^2 \epsilon \tilde{\xi}_{\tilde{k}}^{(1)} b(\tilde{t}, \tilde{y}) \tag{A.166}$$

$$\Leftrightarrow -(C_{\text{eq},l} - C_\infty)\frac{v}{D_l}\epsilon\tilde{\xi}_{\tilde{k}}^{(1)} b(\tilde{t}, \tilde{y}) + \epsilon a_{l\tilde{k}} b(\tilde{t}, \tilde{y}) = \frac{\hat{\gamma}\hat{T}_m}{\tilde{\rho}Lm_l}\tilde{k}^2 \epsilon \tilde{\xi}_{\tilde{k}}^{(1)} b(\tilde{t}, \tilde{y}) \tag{A.167}$$

$$\Leftrightarrow a_{l\tilde{k}} = \tilde{\xi}_{\tilde{k}}^{(1)}\left[(C_{\text{eq},l} - C_\infty)\frac{v}{D_l} + \frac{\hat{\gamma}\hat{T}_m}{\tilde{\rho}Lm_l}\tilde{k}^2\right]. \tag{A.168}$$

This leaves us with one unknown: $\tilde{\xi}_{\tilde{k}}^{(1)}$. We utilize Eq. (A.140) to eliminate it. The interface normal reads

$$n_{\tilde{x}} = \left(1 + \left(\partial_{\tilde{y}}\tilde{\xi}\right)^2\right)^{-\frac{1}{2}} = 1 + \mathcal{O}(\epsilon^2) \tag{A.169}$$

$$n_{\tilde{y}} = -\partial_{\tilde{y}}\tilde{\xi}\left(1 + \left(\partial_{\tilde{y}}\tilde{\xi}\right)^2\right)^{-\frac{1}{2}} = -\partial_{\tilde{y}}\tilde{\xi} + \mathcal{O}(\epsilon^3) \tag{A.170}$$

The solute gradient components at the interface read

$$\partial_{\tilde{x}}\tilde{C}_l(\tilde{\xi}) = -\frac{\tilde{v}}{D_l}(C_{\text{eq},l} - C_\infty)\left(1 - \frac{\tilde{v}}{D_l}\epsilon\tilde{\xi}_{\tilde{k}}^{(1)} b(\tilde{t}, \tilde{y})\right) - \tilde{k}\epsilon a_{l\tilde{k}} b(\tilde{t}, \tilde{y}), \tag{A.171}$$

$$\partial_{\tilde{y}}\tilde{C}_l(\tilde{\xi}) = \epsilon a_{l\tilde{k}} i\tilde{k} e^{-\tilde{k}\tilde{\xi}} b(\tilde{t},\tilde{y}) = \epsilon a_{l\tilde{k}} i\tilde{k} b(\tilde{t},\tilde{y}) + \mathcal{O}(\epsilon^2),\tag{A.172}$$

$$\partial_{\tilde{x}}\tilde{C}_s(\tilde{\xi}) = \tilde{k}\epsilon a_{s\tilde{k}} b(\tilde{t},\tilde{y}) + \mathcal{O}(\epsilon^2),\tag{A.173}$$

$$\partial_{\tilde{y}}\tilde{C}_s(\tilde{\xi}) = i\tilde{k}\epsilon a_{s\tilde{k}} b(\tilde{t},\tilde{y}).\tag{A.174}$$

The perturbed interface velocity $\tilde{V}$ is

$$\tilde{V} = \tilde{v} + \dot{\tilde{\xi}}.\tag{A.175}$$

Inserting above relations into Eq. (A.140) gives

$$-D_l\frac{\tilde{v}}{D_l}\left(C_{\text{eq},l} - C_\infty\right)\left(1 - \frac{\tilde{v}}{D_l}\epsilon\tilde{\xi}_{\tilde{k}}^{(1)}b(\tilde{t},\tilde{y})\right) - D_l\tilde{k}\epsilon a_{l\tilde{k}}b - D_s\tilde{k}\epsilon a_{s\tilde{k}}b$$
$$-i\tilde{k}\epsilon\tilde{\xi}_{\tilde{k}}^{(1)}b\left[D_l i\tilde{k}\epsilon a_{l\tilde{k}}b - D_s i\tilde{k}\epsilon a_{s\tilde{k}}b\right] = \left(\tilde{C}_s^* + \epsilon a_{s\tilde{k}}b - \tilde{C}_l^* - \epsilon a_{l\tilde{k}}b\right)\left(\tilde{v} + \tilde{\omega}\epsilon\tilde{\xi}_{\tilde{k}}^{(1)}b\right).\tag{A.176}$$

Note, that

$$\tilde{C}_s^*(\tilde{\xi}) - \tilde{C}_l^*(\tilde{\xi}) = C_{\text{eq},s} - C_{\text{eq},l} + \frac{\tilde{v}}{D_l}\left(C_{\text{eq},l} - C_\infty\right)\tilde{\xi} + \mathcal{O}(\epsilon^2)\tag{A.177}$$

$$= C_{\text{eq},s} - C_{\text{eq},l} + \frac{\tilde{v}}{D_l}\left(C_{\text{eq},l} - C_\infty\right)\epsilon\tilde{\xi}_{\tilde{k}}^{(1)}b + \mathcal{O}(\epsilon^2).\tag{A.178}$$

We collect all terms of order 0:

$$-D_l\frac{\tilde{v}}{D_l}\left(C_{\text{eq}} - C_\infty\right) = \tilde{v}\left(C_\infty - C_{\text{eq}}\right) = \left(C_{\text{eq},s} - C_{\text{eq},l}\right)\tilde{v} =: \tilde{v}\Delta C,\tag{A.179}$$

where we introduce the concentration gap ΔC. This means, we can identify $C_{\text{eq},s} = C_\infty$. The last term on the left-hand side of Eq. (A.176) is $\mathcal{O}(\epsilon^2)$ and thus neglected. The ϵ^1 terms amount to

$$-\Delta C\frac{\tilde{v}^2}{D_l}\epsilon\tilde{\xi}_{\tilde{k}}^{(1)}b - \tilde{k}\epsilon b\left(D_l a_{l\tilde{k}} + D_s a_{s\tilde{k}}\right) = \tilde{v}\epsilon b\left(a_{s\tilde{k}} - a_{l\tilde{k}}\right) - \Delta C\frac{\tilde{v}^2}{D_l}\epsilon\tilde{\xi}_{\tilde{k}}^{(1)}b + \Delta C\tilde{\omega}\epsilon\tilde{\xi}_{\tilde{k}}^{(1)}b\tag{A.180}$$

$$\Leftrightarrow -\tilde{k}\left(D_l a_{l\tilde{k}} + D_s a_{s\tilde{k}}\right) = \tilde{v}\left(a_{s\tilde{k}} - a_{l\tilde{k}}\right) + \Delta C\tilde{\omega}\tilde{\xi}_{\tilde{k}}^{(1)}\tag{A.181}$$

$$\xrightarrow{\text{(A.164),(A.168)}} -\tilde{k}\left\{D_l\tilde{\xi}_{\tilde{k}}^{(1)}\left[(C_{\text{eq},l} - C_\infty)\frac{\tilde{v}}{D_l} + \frac{\hat{\gamma}\hat{T}_m}{\tilde{\rho}Lm_l}\tilde{k}^2\right] + D_s K\frac{\hat{\gamma}\hat{T}_m}{\tilde{\rho}Lm_l}k^2\tilde{\xi}_{\tilde{k}}^{(1)}\right\}$$
$$= \tilde{v}\left\{K\frac{\hat{\gamma}\hat{T}_m}{\tilde{\rho}Lm_l}k^2\tilde{\xi}_{\tilde{k}}^{(1)} - \tilde{\xi}_{\tilde{k}}^{(1)}\left[(C_{\text{eq},l} - C_\infty)\frac{\tilde{v}}{D_l} + \frac{\hat{\gamma}\hat{T}_m}{\tilde{\rho}Lm_l}\tilde{k}^2\right]\right\} + \Delta C\tilde{\omega}\tilde{\xi}_{\tilde{k}}^{(1)}\tag{A.182}$$

$$\Leftrightarrow -\tilde{k}\left\{D_l\left[-\Delta C\frac{v}{D_l} + \frac{\hat{\gamma}\hat{T}_m}{\tilde{\rho}Lm_l}\tilde{k}^2\right] + D_s K\frac{\hat{\gamma}\hat{T}_m}{\tilde{\rho}Lm_l}k^2\right\}$$
$$= \tilde{v}\left\{K\frac{\hat{\gamma}\hat{T}_m}{\tilde{\rho}Lm_l}k^2 - \left[-\Delta C\frac{\tilde{v}}{D_l} + \frac{\hat{\gamma}\hat{T}_m}{\tilde{\rho}Lm_l}\tilde{k}^2\right]\right\} + \Delta C\tilde{\omega}\tag{A.183}$$

$$\xrightarrow{K=1} -\tilde{k}\left\{-\Delta C\tilde{v} + \frac{\hat{\gamma}\hat{T}_m}{\tilde{\rho}Lm_l}\tilde{k}^2\left(D_l + D_s\right)\right\} = \tilde{v}\Delta C\frac{\tilde{v}}{D_l} + \Delta C\tilde{\omega}\tag{A.184}$$

$$\Leftrightarrow \tilde{\omega} = -\tilde{k}\tilde{v}\left\{-1 + \frac{\hat{\gamma}\hat{T}_m}{\tilde{\rho}Lm_l\Delta C}\tilde{k}^2\frac{D_l}{\tilde{v}}\left(1 + \frac{D_s}{D_l}\right)\right\} - \frac{\tilde{v}^2}{D_l}\tag{A.185}$$

$$\Leftrightarrow \tilde{\omega}(\tilde{k}) = \tilde{k}\tilde{v}\left(1 - d_c d_d \tilde{k}^2\left(1+n\right)\right) - \frac{\tilde{v}^2}{D_l}. \tag{A.186}$$

We introduce the capillary length

$$d_c = \frac{\hat{\gamma}\hat{T}_m}{\tilde{\rho}Lm_l \Delta C}, \tag{A.187}$$

the diffusive length

$$\frac{D_l}{\tilde{v}} \tag{A.188}$$

and the ratio of the diffusivities

$$n = \frac{D_s}{D_l}. \tag{A.189}$$

Finally, we apply the quasi-stationary approximation again which allows us to neglect the constant term:

$$\tilde{\omega}(\tilde{k}) = \tilde{k}\tilde{v}\left(1 - d_c d_d \tilde{k}^2\left(1+n\right)\right). \tag{A.190}$$

Although the curvature term in Eq. (A.160) has a different sign in comparison to the Gibbs-Thomson equation for the temperature field utilized in the calculation for the pure material [MS64], this cancels out due to the swapped terms of the concentration gradients on the left-hand side of Eq. (A.140). Thus, capillarity still acts stabilizing. The reader must have realized that $K = 1$ results in a vanishing right-hand side of Eq. (A.140) and also $\Delta C = 0$. Setting $K = 1$ is only done for convenience. Qualitatively, the dispersion relation does not change, when keeping $K \neq 1$, as can be seen in Eq. (A.183), i.e, it still contains a linear destabilizing and a cubic stabilizing term.

A.8. Analytical Calculations for the Binary Mixture System

Here, we calculate possible precursor height h_p and height at inflection point h_i for a stationary droplet of a binary mixture with constant solute concentration C.

$$0 = J_{\text{evap}}$$

$$\Leftrightarrow 0 = -\Omega\left[f'(h) + \tilde{\mu}\right]$$

$$\Leftrightarrow 1 - h^3 = h^6 \tilde{\mu}$$

$$\xrightarrow{h^3 \equiv w} 0 = w^2 + \frac{w-1}{\tilde{\mu}}$$

$$\Rightarrow w = \frac{1}{2\tilde{\mu}}\left(-1 \pm \sqrt{1+4\tilde{\mu}}\right) \tag{A.191}$$

$$= 2\frac{-1 \pm \sqrt{1+4\tilde{\mu}}}{4\tilde{\mu}} \tag{A.192}$$

$$= 2\frac{-1 \pm \sqrt{1+4\tilde{\mu}}}{1+4\tilde{\mu}-1} \tag{A.193}$$

$$= 2\frac{-1 \pm \sqrt{1+4\tilde{\mu}}}{\left(\sqrt{1+4\tilde{\mu}}-1\right)\left(\sqrt{1+4\tilde{\mu}}+1\right)} \tag{A.194}$$

$$= \frac{2}{1 \pm \sqrt{1+4\tilde{\mu}}} \tag{A.195}$$

$$\Rightarrow h = \left(\frac{2}{1 \pm \sqrt{1 + 4\tilde{\mu}}}\right)^{\frac{1}{3}} \tag{A.196}$$

$$h_p = \left(\frac{2}{1 + \sqrt{1 + 4\tilde{\mu}}}\right)^{\frac{1}{3}} = \left(\frac{2}{1 + \sqrt{1 + 4\left(\Upsilon\left(\ln(1 - C) - 1 + \chi C^2\right) - \mu\right)}}\right)^{\frac{1}{3}} \tag{A.197}$$

$$h_i = \left(\frac{2}{1 - \sqrt{1 + 4\tilde{\mu}}}\right)^{\frac{1}{3}} = \left(\frac{2}{1 - \sqrt{1 + 4\left(\Upsilon\left(\ln(1 - C) - 1 + \chi C^2\right) - \mu\right)}}\right)^{\frac{1}{3}} \tag{A.198}$$

A.9. Linear Stability Analysis of the Full Model

Since the ϕ equation depends on the solute concentration C and not directly on the thickness ψ_2 it is more convenient to analyze the linear stability of the full model with $g = v = 0$ in a different basis, i.e., (h, C, ϕ)., which is also more intuitive. See Sec. 2.5.1 for the original basis. The ζ equation is dropped since it is directly proportional to the ϕ equation. The dynamic equations then read

$$\partial_t h = -\nabla \cdot \mathbf{J}_h + J_{\text{evap}} \tag{A.199}$$

$$\partial_t C = \frac{1}{h}\left(-\mathbf{J}_h \cdot \nabla C - \nabla \cdot \mathbf{J}_{2,\text{diff}} - C J_{\text{evap}}\right) + \alpha \partial_t \phi \tag{A.200}$$

$$\partial_t \phi = \sigma\left(\Lambda^{-2}\Delta\phi - f'_{\text{xm}}(\phi, C - C_{\text{eq}}) - \Lambda^{-2}|\nabla\phi|\kappa(\phi)\right) \tag{A.201}$$

$$\mathbf{J}_h = -\frac{h^3}{3}\nabla P = \frac{h^3}{3}\nabla\left(\Delta h - f'(h)\right) \tag{A.202}$$

$$J_{\text{evap}} = -\Omega\left(P + \Upsilon\mu_{\text{osm}} - \mu\right) \tag{A.203}$$

$$\mu_{\text{osm}}(C) = \ln(1 - C) - 1 + \chi C^2 \tag{A.204}$$

$$\mu'_{\text{osm}}(C) = -\frac{1}{1 - C} + 2\chi C \tag{A.205}$$

$$\mathbf{J}_{2,\text{diff}} = -\text{Pe}^{-1}h\left(1 - 2\chi(1 - C)C\right)\nabla C \tag{A.206}$$

$$= \text{Pe}^{-1}h(1 - C)\mu'_{\text{osm}}(C)\nabla C \tag{A.207}$$

$$f'_{\text{xm}}(\phi, C - C_{\text{eq}}) = f'_{\text{xm},1}(\phi) + \lambda f'_{\text{xm},2}(\phi)\left(C - C_{\text{eq}}\right) \tag{A.208}$$

$$= -\phi + \phi^3 + \lambda(1 - \phi^2)\left(C - C_{\text{eq}}\right). \tag{A.209}$$

The prime denotes derivation by ϕ if ambiguous. We make the ansatz

$$h(\mathbf{x}, t) = h^* + \epsilon h_1(\mathbf{x}, t) = h^* + \epsilon a_h e^{\omega t + i\mathbf{kx}} \tag{A.210}$$

$$C(\mathbf{x}, t) = C^* + \epsilon C_1(\mathbf{x}, t) = C^* + \epsilon a_c e^{\omega t + i\mathbf{kx}} \tag{A.211}$$

$$\phi(\mathbf{x}, t) = \phi^* + \epsilon \phi_1(\mathbf{x}, t) = \phi^* + \epsilon a_\phi e^{\omega t + i\mathbf{kx}} \tag{A.212}$$

with homogeneous stationary solutions (h^*, C^*, ϕ^*), perturbation amplitudes a_i and growth rate ω. For the h equation we linearize the operators $\mathbf{J}_h$ and J_{evap} which contain P and μ_{osm}:

$$P = -\Delta h + f'(h) = k^2 \epsilon h_1 + f'(h^*) + \epsilon f''(h^*)h_1 + \mathcal{O}(\epsilon^2) \tag{A.213}$$

$$\Rightarrow \mathbf{J}_h = -\frac{h^3}{3}\nabla P = -\left(\frac{h^{*3}}{3} + \epsilon h^{*2}h_1\right)\left(k^2\epsilon\nabla h_1 + \epsilon f''(h^*)\nabla h_1\right) + \mathcal{O}(\epsilon^2)$$

$$= -\frac{h^{*3}}{3}\epsilon i\mathbf{k}\left(k^2 + f''(h^*)\right)h_1 + \mathcal{O}(\epsilon^2) \tag{A.214}$$

$$\mu_{\mathrm{osm}} = \mu_{\mathrm{osm}}(C^*) + \epsilon\mu'_{\mathrm{osm}}(C^*)C_1 + \mathcal{O}(\epsilon^2) \tag{A.215}$$

$$= \ln(1 - C^*) - 1 + \chi C^{*2} + \epsilon C_1 \left(-\frac{1}{1 - C^*} + 2\chi C^*\right) + \mathcal{O}(\epsilon^2)$$

Plugging Eq. (A.213)- (A.215) into (A.199) gives

$$\omega\epsilon h_1 = -\frac{h^{*3}}{3}\epsilon k^2\left(k^2 + f''(h^*)\right)h_1 - \Omega\left[\epsilon h_1\left(k^2 + f''(h^*)\right) + f'(h^*)\right. \tag{A.216}$$

$$\left. + \Upsilon\left(\mu_{\mathrm{osm}}(C^*) + \epsilon\mu'_{\mathrm{osm}}(C^*)C_1\right) - \mu\right] + \mathcal{O}(\epsilon^2) \tag{A.217}$$

$$= \epsilon h_1\left[-\frac{h^{*3}}{3}k^2\left(k^2 + f''(h^*)\right) - \Omega\left(k^2 + f''(h^*)\right)\right] - \epsilon C_1\Omega\Upsilon\mu'_{\mathrm{osm}}(C^*) + \mathcal{O}(\epsilon^2) \tag{A.218}$$

$$= \epsilon h_1\left[\left(-\frac{h^{*3}}{3}k^2 - \Omega\right)\left(k^2 + f''(h^*)\right)\right] - \epsilon C_1\Omega\Upsilon\mu'_{\mathrm{osm}}(C^*) + \mathcal{O}(\epsilon^2) \tag{A.219}$$

where we demand

$$f'(h^*) + \Upsilon\mu_{\mathrm{osm}}(C^*) - \mu = 0 \tag{A.220}$$

in Eq. (A.218) for the stationary solutions, i.e., homogeneous solutions that hold $J_{\mathrm{evap}} = 0$. Since the source term of the C-equation depends directly on the ϕ-equation, we proceed with linearization of such. This requires linearizing the operators f'_{xm} and $|\nabla\phi|\kappa$:

$$\begin{aligned}f'_{\mathrm{xm}} &= f'_{\mathrm{xm,1}}(\phi^*) + \epsilon f''_{\mathrm{xm,1}}(\phi^*)\phi_1 \\ &\quad + \lambda\left(f'_{\mathrm{xm,2}}(\phi^*) + \epsilon f''_{\mathrm{xm,2}}(\phi^*)\phi_1\right)\left(C^* + \epsilon C_1 - C_{\mathrm{eq}}\right) + \mathcal{O}(\epsilon^2) \\ &= f'_{\mathrm{xm,1}}(\phi^*) + \lambda f'_{\mathrm{xm,2}}(\phi^*)(C - C_{\mathrm{eq}}) + \epsilon\phi_1\left(f''_{\mathrm{xm,1}}(\phi^*) + f''_{\mathrm{xm,2}}(\phi^*)(C^* - C_{\mathrm{eq}})\right) \\ &\quad + \epsilon C_1\lambda f'_{\mathrm{xm,2}}(\phi^*) + \mathcal{O}(\epsilon^2) \\ &= \epsilon\phi_1\left(f''_{\mathrm{xm,1}}(\phi^*) + f''_{\mathrm{xm,2}}(\phi^*)(C^* - C_{\mathrm{eq}})\right) + \epsilon C_1\lambda f'_{\mathrm{xm,2}}(\phi^*) + \mathcal{O}(\epsilon^2).\end{aligned} \tag{A.221}$$

In the last step, we further demand ϕ^* to be an extremum of f_{xm} which solves

$$f'_{\mathrm{xm}}(\phi^*, C^* - C_{\mathrm{eq}}) = 0 \tag{A.222}$$

without constraining C^* further. For the curvature term we utilize Eq. (4.33)

$$|\nabla\phi|\kappa = \Delta\phi - \frac{\nabla\phi\cdot\nabla|\nabla\phi|}{|\nabla\phi|} \tag{A.223}$$

$$\frac{\nabla\phi\cdot\nabla|\nabla\phi|}{|\nabla\phi|} = \frac{i\mathbf{k}\epsilon\cdot\nabla\left(k\epsilon|\phi_1|\right)}{k\epsilon|\phi_1|} + \mathcal{O}(\epsilon^2). \tag{A.224}$$

The numerator requires differentiating the complex norm

$$\nabla|\phi_1| = \frac{\phi_1^*\nabla\phi_1 + \phi_1\nabla\phi_1^*}{|\phi_1|} + \mathcal{O}(\epsilon^2) = i\mathbf{k}\frac{|\phi_1|^2}{|\phi_1|} + \mathcal{O}(\epsilon^2) = i\mathbf{k}|\phi_1| + \mathcal{O}(\epsilon^2) \tag{A.225}$$

with $\phi_1 \neq 0$. Plugging Eq. (A.224)-(A.225) into (A.223) gives

$$|\nabla\phi|\kappa = -k^2\phi_1 + k^2\phi_1 + \mathcal{O}(\epsilon^2) = \mathcal{O}(\epsilon^2). \tag{A.226}$$

Unsurprisingly, the curvature term only contributes non-linearly. Applying Eq. (A.221) and (A.226) to (A.201) gives the linearized ϕ-equation

$$\omega\epsilon\phi_1 = \sigma\left[-\Lambda^{-2}k^2\epsilon\phi_1 - \epsilon\phi_1 f''_{\mathrm{xm}}(\phi^*, C^*-C_{\mathrm{eq}}) - \epsilon C_1\lambda f'_{\mathrm{xm},2}(\phi^*)\right] + \mathcal{O}(\epsilon^2)$$

$$= \epsilon\phi_1\sigma\left[-\frac{1}{\Lambda^2}k^2 - f''_{\mathrm{xm}}(\phi^*, C^*-C_{\mathrm{eq}})\right] - \epsilon C_1\sigma\lambda f'_{\mathrm{xm},2}(\phi^*) + \mathcal{O}(\epsilon^2). \tag{A.227}$$

For the C-equation Eq. (A.200) the first term $-\frac{1}{h}\mathbf{J}_h\nabla C$ vanishes in first order since $\mathbf{J}_h = \mathcal{O}(\epsilon)$ and ∇C as well. The diffusive flux contribution linearizes to:

$$\mathbf{J}_{2,\mathrm{diff}} = \mathrm{Pe}^{-1}h^*(1-C^*)\mu'_{\mathrm{osm}}(C^*)i\mathbf{k}\epsilon C_1 + \mathcal{O}(\epsilon^2)$$

$$\Rightarrow \frac{1}{h}\left(-\nabla\cdot\mathbf{J}_{2,\mathrm{diff}}\right) = \left(\frac{1}{h^*} + \epsilon h_1\left(-\frac{1}{h^{*2}}\right)\right)\left[\mathrm{Pe}^{-1}h^*(1-C^*)\mu'_{\mathrm{osm}}(C^*)k^2\epsilon C_1\right]$$
$$+ \mathcal{O}(\epsilon^2) \tag{A.228}$$

$$= \mathrm{Pe}^{-1}(1-C^*)\mu'_{\mathrm{osm}}(C^*)k^2\epsilon C_1 + \mathcal{O}(\epsilon^2). \tag{A.229}$$

The linearized evaporative contribution, taken from Eq. (A.218), reads

$$J_{\mathrm{evap}} = -\epsilon h_1\Omega\left(k^2 + f''(h^*)\right) - \epsilon C_1\Omega\Upsilon\mu'_{\mathrm{osm}}(C^*) + \mathcal{O}(\epsilon^2) \tag{A.230}$$

$$\Rightarrow -\frac{C}{h}J_{\mathrm{evap}} = \frac{C^*}{h^*}\Omega\epsilon h_1\left(k^2 + f''(h^*)\right) + \epsilon C_1\frac{C^*}{h^*}\Omega\Upsilon\mu'_{\mathrm{osm}}(C^*) + \mathcal{O}(\epsilon^2). \tag{A.231}$$

Then Eq. (A.200) to first order in ϵ is

$$\omega\epsilon C_1 = \mathrm{Pe}^{-1}(1-C^*)\mu'_{\mathrm{osm}}(C^*)k^2\epsilon C_1$$
$$+ \frac{C^*}{h^*}\Omega\epsilon h_1\left(k^2 + f''(h^*)\right) + \epsilon C_1\frac{C^*}{h^*}\Omega\Upsilon\mu'_{\mathrm{osm}}(C^*) \tag{A.232}$$
$$+ \epsilon\phi_1\alpha\sigma\left[-\frac{1}{\Lambda^2}k^2 - f''_{\mathrm{xm}}(\phi^*, C^*-C_{\mathrm{eq}})\right] - \epsilon C_1\alpha\sigma\lambda f'_{\mathrm{xm},2}(\phi^*) + \mathcal{O}(\epsilon^2)$$

In the following the function arguments are omitted for convenience. The perturbation's exponential functions in Eq (A.219),(A.232) and (A.227) can be eliminated which results in an eigenvalue problem for the Jacobian $\underline{J}$:

$$\begin{pmatrix} \left(-\frac{h^{*3}}{3}k^2 - \Omega\right)\left(k^2+f''\right) & \Omega\Upsilon\mu'_{\mathrm{osm}} & 0 \\ \frac{C^*}{h^*}\Omega\left(k^2+f''\right) & \mu'_{\mathrm{osm}}\left[\mathrm{Pe}^{-1}(1-C^*)k^2 + \frac{C^*}{h^*}\Omega\Upsilon\right] - \alpha\sigma\lambda f'_{\mathrm{xm},2} & \alpha\sigma\left(-\Lambda^{-2}k^2 - f''_{\mathrm{xm}}\right) \\ 0 & \sigma\lambda f'_{\mathrm{xm},2} & \sigma\left(-\Lambda^{-2}k^2 - f''_{\mathrm{xm}}\right) \end{pmatrix} \tag{A.233}$$

We can recognize several features previously seen in the dynamic equations. The third column shows the connection between phase-field and source term. Entry J_{ch} reflects concentration growth due to evaporation. Influence of wetting or osmosis can be easily identified by f'' or μ'_{osm} contributions.

$$\omega\begin{pmatrix} a_h \\ a_c \\ a_\phi \end{pmatrix} = \underline{J}\begin{pmatrix} a_h \\ a_c \\ a_\phi \end{pmatrix} \tag{A.234}$$

$$\Rightarrow \det\left(\underline{J} - \omega\underline{I}\right) = 0. \tag{A.235}$$

Since two corners of $\underline{J}$ are 0, i.e., h is not directly coupled to ϕ and vice versa, the calculation simplifies to:

$$0 = (J_{hh} - \omega)(J_{cc} - \omega)(J_{\phi\phi} - \omega) - J_{hc}J_{ch}(J_{\phi\phi} - \omega) - (J_{hh} - \omega)J_{c\phi}J_{\phi c} \tag{A.236}$$

$$\Rightarrow 0 = \left[\left(-\frac{h^{*3}}{3}k^2 - \Omega\right)(k^2 + f'') - \omega\right]\left[\sigma\left(-\Lambda^{-2}k^2 - f''_{\mathrm{xm}}\right) - \omega\right] \tag{A.237}$$

$$\cdot \left\{\mu'_{\mathrm{osm}}\left[\mathrm{Pe}^{-1}(1 - C^*)k^2 + \frac{C^*}{h^*}\Omega\Upsilon\right] - \alpha\sigma\lambda f'_{\mathrm{xm},2} - \omega\right\} \tag{A.238}$$

$$- \Omega\Upsilon\mu'_{\mathrm{osm}}\frac{C^*}{h^*}\Omega(k^2 + f'')\left[\sigma\left(-\frac{1}{\Lambda^2}k^2 - f''_{\mathrm{xm}}\right) - \omega\right] \tag{A.239}$$

$$- \left[\left(-\frac{h^{*3}}{3}k^2 - \Omega\right)(k^2 + f'') - \omega\right]\alpha\sigma\left(-\Lambda^{-2}k^2 - f''_{\mathrm{xm}}\right)\sigma\lambda f'_{\mathrm{xm},2} \tag{A.240}$$

This characteristic polynomial is of third order. The solution is not trivial [BSMM05]. Let us evaluate the more compact Eq. (A.236) and sort the terms by ω to bring the equation in the form

$$0 = a\omega^3 + b\omega^2 + c\omega + d : \tag{A.241}$$

$$0 = \omega^3 - \omega^2(J_{hh} + J_{cc} + J_{\phi\phi}) - \omega(J_{hc}Jch + J_{c\phi}J_{\phi c} - J_{cc}J_{\phi\phi} - J_{\phi\phi}J_{hh} - J_{cc}J_{hh})$$
$$- J_{hh}J_{cc}J_{\phi\phi} + J_{hc}J_{ch}J_{\phi\phi} + J_{hh}J_{c\phi}J_{\phi c}. \tag{A.242}$$

Here, we have already divided by $a = -1$. Cubic equations can be solved via Cardan's formulas, however the resulting expressions contain complex numbers even in cases when the solutions are actually real, see *casus irreducibilis*. The sign of the discriminant gives information on the nature of the solutions. With the transformation

$$\omega = x - \frac{b}{3a} \stackrel{a=1}{=} x - \frac{b}{3} \tag{A.243}$$

the equation can be reduced to the depressed cubic equation

$$x^3 + px + q = 0 \tag{A.244}$$

with

$$p = \frac{3ac - b^2}{3a^2} \stackrel{a=1}{=} c - \frac{b^2}{3} \tag{A.245}$$

$$q = \frac{1}{27a^3}\left(2b^3 - 9abc + 27a^2d\right) \stackrel{a=1}{=} \frac{2}{27}b^3 - \frac{bc}{3} + d. \tag{A.246}$$

The discriminant then reads

$$D = 27q^2 + 4p^3 \tag{A.247}$$

$$= 4b^3d - b^2c^2 - 18bcd + 4c^3 + 27d^2. \tag{A.248}$$

For $D > 0$ one real and two complex, $D < 0$ three real and $D = 0$ also three real but degenerate solutions exist. Note that $D < 0$ can only be negative if $p < 0$. The compressed cubic can be solved by transcendental expressions, they are Viete's trigonometric solutions [Zuc08]:

$$x_i = 2\sqrt{-\frac{p}{3}}\cos\left(\frac{1}{3}\arccos\left(\frac{3q}{2p}\sqrt{\frac{-3}{p}}\right) - \frac{2\pi i}{3}\right), i = 0, 1, 2. \tag{A.249}$$
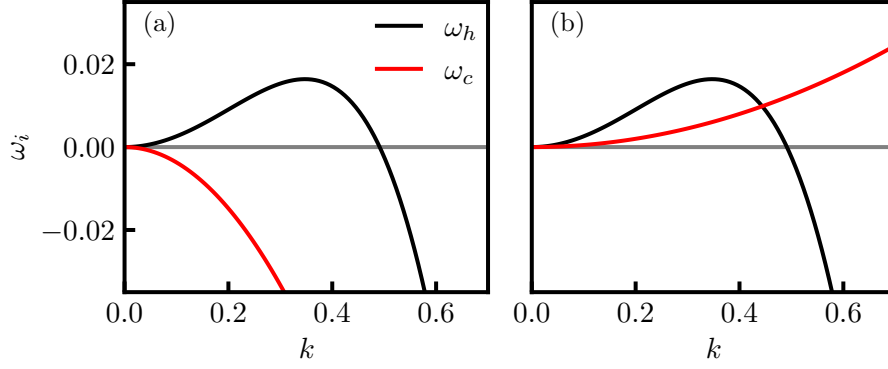
Figure A.4.: Growth rates of perturbations of homogeneous states in linearized symmetric binary mixtures without evaporation and deposition. The dispersion relations are Eq. (A.250)-(A.250). The utilized parameters are: $h^* = 1.5$, $C^* = 0.3$, $\mathrm{Pe}^{-1} = 1$, $\chi_a, \chi_b = 1.5, 2.5$.

The reader may be familiar with these from stationary solutions for the cubic Allen-Cahn equation. This expression is is real for $D < 0$ and also correct for $D > 0$, however, unsurprisingly, it becomes complex then. Applying Eq. (A.243)-(A.246) to (A.242) we formally have the dispersion relations for our problem. Unfortunately, first attempts at simplifying the resulting extensive expressions with *Mathematica* [Wol22] have been unsuccessful. For future work one can simplify the Jacobian in order to get managable dispersion relations. A strong simplification would be for example $\Omega = \sigma = 0$ which is the non-volatile case without deposit and directly results in a diagonal 2×2 Jacobian. The growth rates can then be directly associated with film height h and solute concentration C, i.e., instabilities are decoupled:

$$\omega_h = -\frac{h^{*3}}{3}k^2 \left(k^2 + f''(h^*)\right) \tag{A.250}$$

$$\omega_c = -\mathrm{Pe}^{-1}k^2 \left[1 - 2\chi \left(1 - C^*\right) C^*\right]. \tag{A.251}$$

Instability examples are shown in Fig. A.4. In both panels the homogeneous film height h^* is above the critical one, thus, h develops a well-known finite wavelength instability. In panel (a) the C-mode is within the linearly stable regime since $\chi_a = 1.5 < 2$. However for $\chi = 2.5$ the sign in front of k^2 changes. The concentration becomes unstable, i.e., the system is in the anti-diffusive regime and the system exhibits a vanishing wavelength instability. Since the instability is not stabilized by for example a k^4 term in the dispersion relation, this means that demixing instabilities cannot be properly caught in the current version of the model and require for example adding gradient energy terms for C.

A.10. Binary Mixture Results
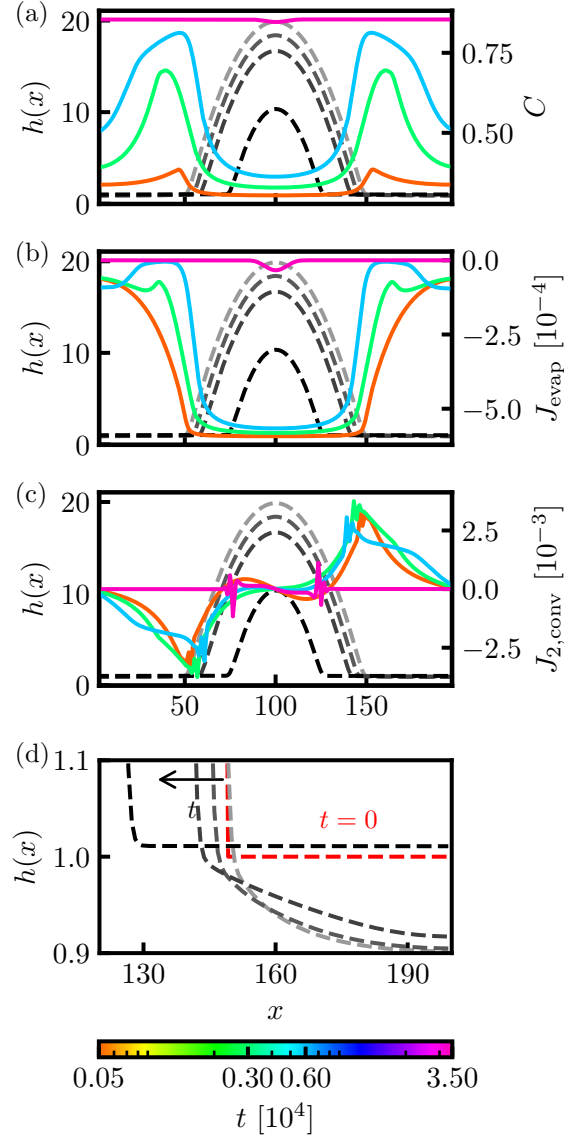
Figure A.5.: Time evolution of a volatile droplet of a binary mixture. Film height h (left axis, gray scale) and other quantities (right axis, colored) are depicted at times $t\,[10^4] =$ 0.05, 0.3, 0.6, 3.5. The gray/black lines follow the same order as the colored ones, meaning that the darker the later the time. (a) solute concentration (b) evaporation rate J_{evap} (c) convective flux $J_{2,\text{conv}}$ (d) zoom of the precursor region. The profile at $t = 0$ is separately depicted in red. The governing equations are Eq. (2.126)-(2.127) with $g = 0$, $v = 0$, $\alpha = 0$. The remaining parameters are $\text{Pe}^{-1} = 0$, $\chi = 1.5$, $\Omega = 0.001$, $\Upsilon = 1$ and $\mu = -1.8$.
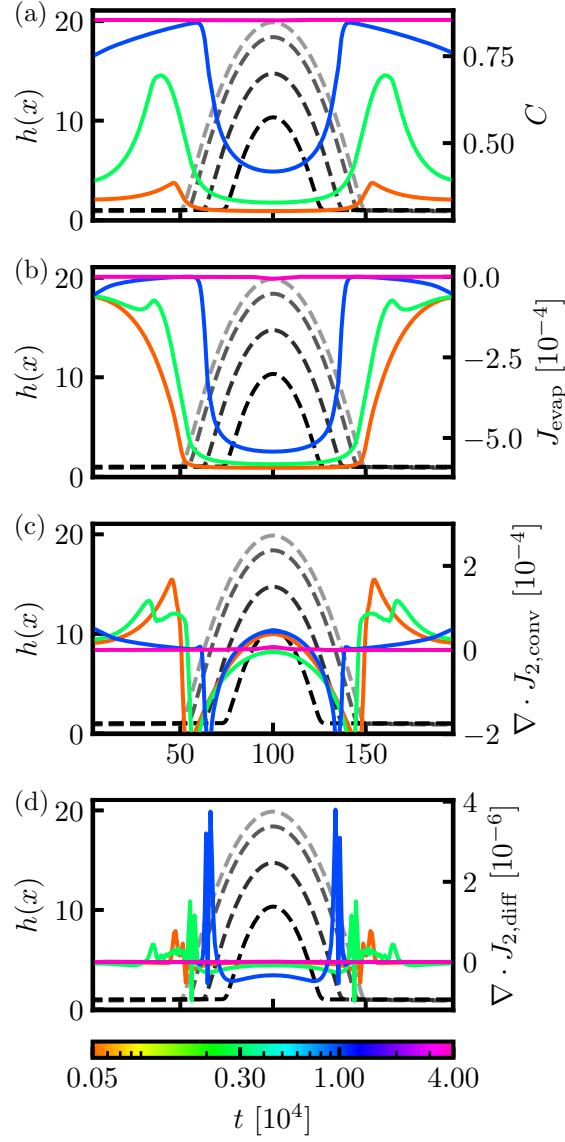
Figure A.6.: Time evolution of a volatile droplet of a binary mixture. Film height h (left axis, gray scale) and other quantities (right axis, colored) are depicted at times $t\,[10^4] = 0.05,\ 0.3,\ 1.0,\ 4.0$. The gray/black lines follow the same order as the colored ones, meaning that the darker the later in time. (a) solute concentration (b) evaporation rate J_{evap} (c) rate of convection of solute $\nabla \cdot J_{2,\text{conv}}$ (d) rate of diffusion of solute $\nabla \cdot J_{2,\text{diff}}$. The governing equations are Eq. (2.126)-(2.127) with $g = 0$, $v = 0$, $\alpha = 0$. The remaining parameters are $\text{Pe}^{-1} = 10^{-4}$, $\chi = 1.5$, $\Omega = 0.001$, $\Upsilon = 1$ and $\mu = -1.8$.

A study of Ω is performed in Fig. A.7, along with a comparison of mean height $\bar{h}(t)$ in Fig. A.8 showing that the solutions will converge to equal states, independent of Ω.
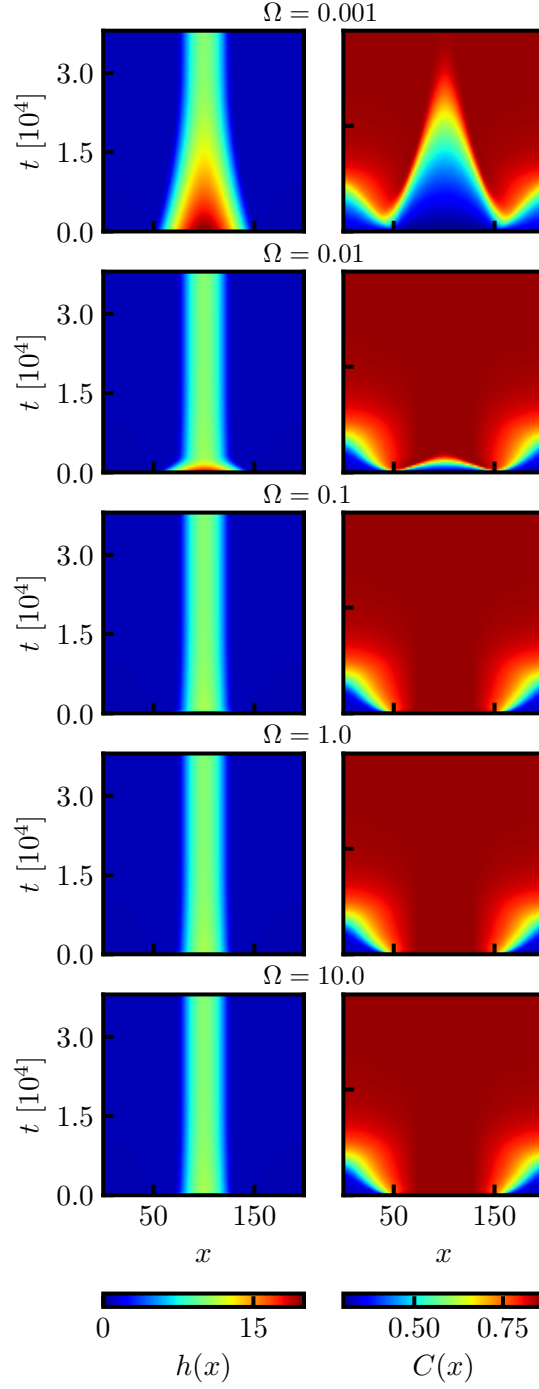
Figure A.7.: Space-time plots of a volatile droplet of a binary mixture. Shown are film height h(left) and solute concentration C(right) for increasing evaporation strength Ω. The governing equations are Eq. (2.126)-(2.127) with $g = 0$, $v = 0$, $\alpha = 0$. Other parameters are $h_0 = 20$, $C_0 = 0.3$, $\chi = 1.5$, $Pe^{-1} = 10^{-4}$, $\Upsilon = 1$, $\mu = -1.8$
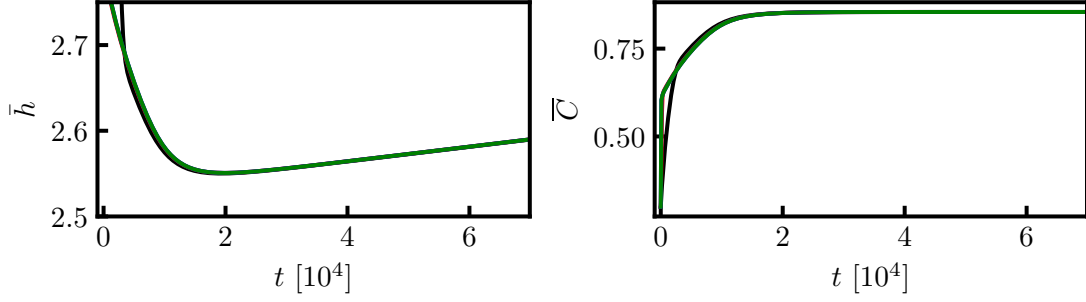
Figure A.8.: Time evolution of mean height $\bar{h}$ and mean solute concentration $\overline{C}$ of a volatile, sessile droplet of a binary mixture for evaporation rates $\Omega = 0.01\,(\text{black}),\ 0.1\,(\text{red}),\ 1.0\,(\text{blue}),\ 10.0\,(\text{green})$. Some colors are not visible due to overlap. The initial condition is a parabolically shaped cap. The governing equations are Eq. (2.126)-(2.127) with $g = 0$, $v = 0$, $\alpha = 0$. The remaining parameters are $h_0 = 20$, $C_0 = 0.3$, $\text{Pe}^{-1} = 10^{-4}$, $\chi = 1.5$, $\Upsilon = 1$ and $\mu = -1.8$.

While it is likely that the droplet solutions in Sec. 4.5 are stable due to the simulation being direct and starting from a non-stationary state, it is sensible to specifically test their stability. We show this for a similar parameter set as in Fig. 4.6 but with faster evaporation rate for convenience. Figure A.9 shows fluxes and mean height $\bar{h}$ of an evaporating droplet that has been perturbed by white noise of amplitude 0.01. The initial condition is taken from the $\Omega = 0.1$ simulation at $t = 5 \cdot 10^4$. Both convection and evaporation have not reached equilibrium yet indicating that the initial condition was not fully converged. Solvent is condensing mostly in the droplet region and very slightly in the precursor region while some material convects from the contact line region into the droplet. The fluxes behave not smooth in the contact line region. Overall the system gains mass over time which can be attributed to condensation and FDM error. However, it is likely that the droplet shape will persist since the initial perturbation is not amplified. The concentration profile barely changes around $C = 0.854$, see the space-time plot in Fig. A.10.
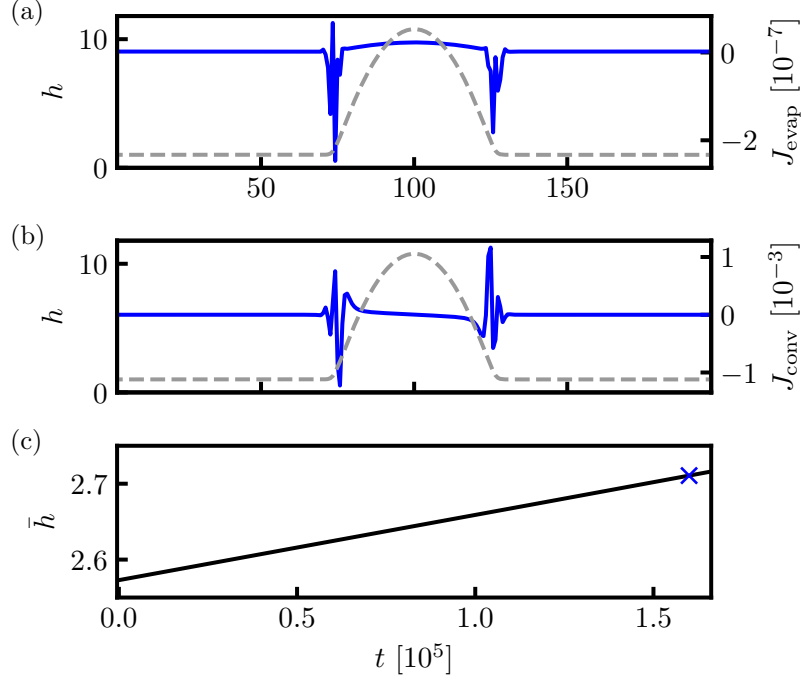
Figure A.9.: Simulation data of a perturbed evaporating droplet. The initial condition is taken from the simulation in Fig. A.7 with $\Omega = 0.1$ at $t_{\text{previous}} = 5 \cdot 10^4$ and then perturbed by white noise of amplitude 0.01. (a) evaporative flux J_{evap} (blue) (b) convective flux J_{conv} (blue) at $t = 1.6 \cdot 10^5$. Film height h is shown in dashed gray. (c) time evolution of mean film height $\bar{h}$. The governing equations are Eq. (2.126)-(2.127) with $g = 0$, $v = 0$, $\alpha = 0$. The system parameters are unchanged from the original simulation $\text{Pe}^{-1} = 10^{-4}$, $\chi = 1.5$, $\Omega = 0.1$, $\Upsilon = 1$ and $\mu = -1.8$.
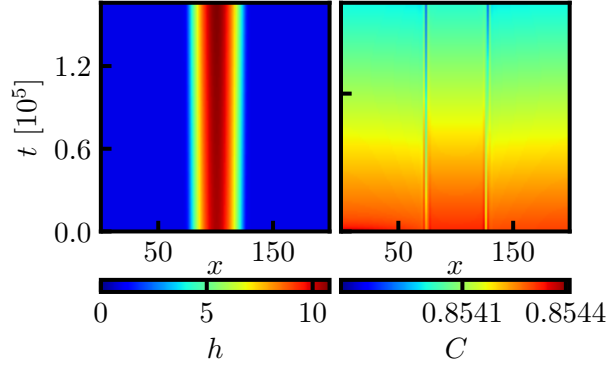
Figure A.10.: Space-time data of a perturbed evaporating droplet of a binary mixture. The initial condition is taken from the simulation in Fig. A.7 with $\Omega = 0.1$ at $t = 5 \cdot 10^4$ and then perturbed by white noise of amplitude 0.01. Shown are film height h and solute concentration C. The governing equations are Eq. (2.126)-(2.127) with $g = 0$, $v = 0$, $\alpha = 0$. The system parameters are $\text{Pe}^{-1} = 10^{-4}$, $\chi = 1.5$, $\Omega = 0.1$, $\Upsilon = 1$ and $\mu = -1.8$.
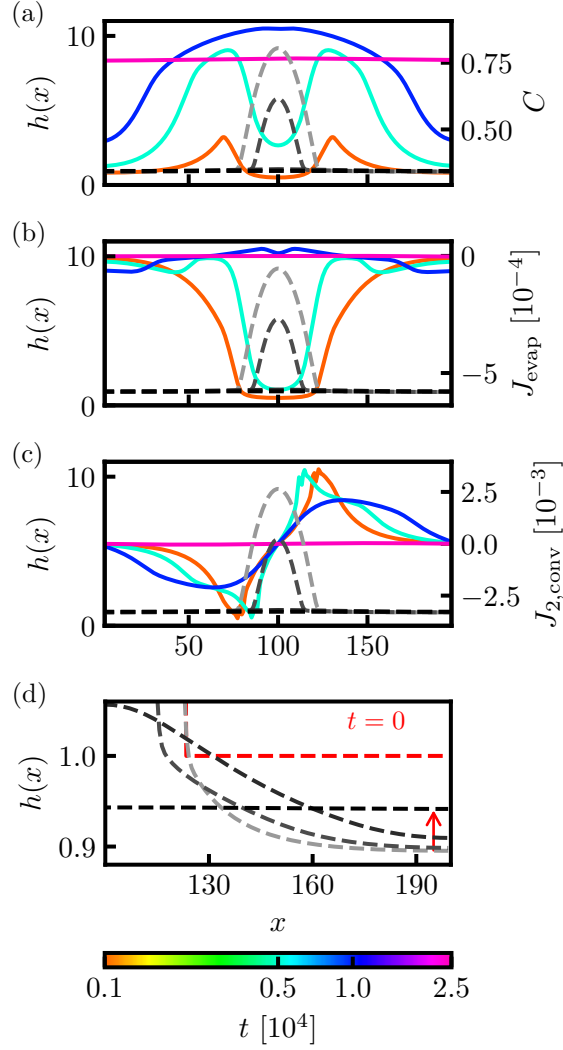
Figure A.11.: Time evolution of a sessile volatile binary mixture droplet. This simulation is qualitatively similar to the one at the top of Fig. 4.8.(b) whose final state is a flat film. Film height h (left axis, gray scale) and other quantities (right axis, colored) are depicted at times labeled on the color bars. The gray/black lines follow the same order as the colored ones, meaning that the darker the later the time. (a) solute concentration (b) evaporative flux J_{evap} (c) convective flux of solute $J_{2,\text{conv}}$ (d) zoom of the precursor region. The profile at $t = 0$ is separately depicted in red. The governing equations are Eq. (2.126)-(2.127) with $g = 0$, $v = 0$, $\alpha = 0$. The remaining parameters are $h_0 = 10$, $\text{Pe}^{-1} = 10^{-4}$, $\chi = 1.5$, $\Omega = 0.001$, $\Upsilon = 1$ and $\mu = -1.8$.

A.11. Simple Liquid Results
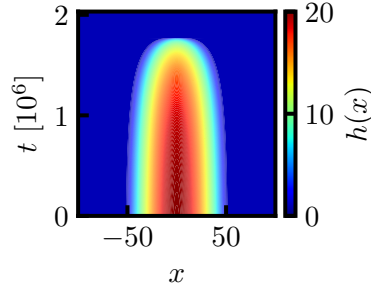
Figure A.12.: Space-time plot of $h(x)$ for an evaporating sessile, simple droplet on a horizontal substrate. The initial condition is taken from the non-volatile case after the droplet has fully converged. $\mu = 0.01568$ is chosen as measured from the converged droplet $\mu = \mu_l = -\partial_{xx}h + f'(h)$. The governing equation is Eq. (4.26). The remaining parameters are $\Omega = 10^{-3}$, $L = 100$, $h_0 = 20$. The calculation is executed via FEM spatial discretization and implicit time-stepping utilizing *oomph-lib* with Neumann boundary conditions [HH06]. For visualization the simulated droplet half is mirrored. Many thanks to Simon Hartmann for quickly setting up the code and corresponding simulations.

A.12. Full Model Results

A.12.1. Small Osmotic Pressure
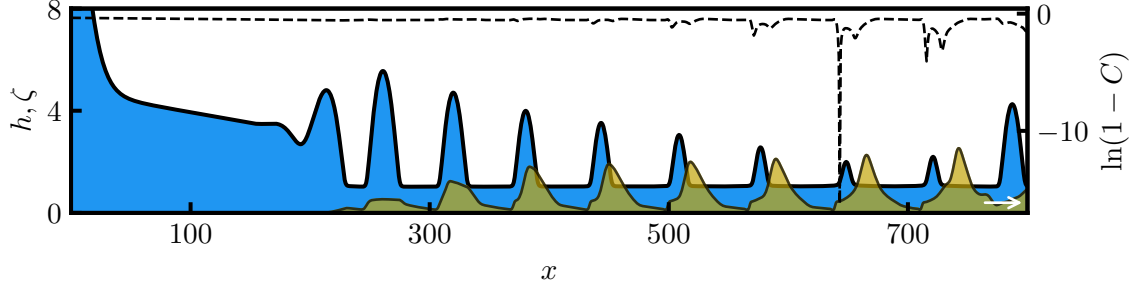
Figure A.13.: Snapshot of a precipitating binary mixture in a dip-coating geometry on a 1D substrate described by Eq. (2.126)-(2.129) and Eq. (4.34)-(4.36). Shown are film height h, logarithmic term $\ln(1-C)$ within J_{evap} and the deposit thickness ζ in blue, dashed black and olive, respectively. The substrate is pulled towards the right. Due to the small α only a small amount is deposited and the liquid ridges persist. Thus, they continue to evaporate. However since the phase-field has recorded a phase transition already, i.e. $\phi = -1$ around each ridge, precipitation is not triggered a second time. C is allowed to approach 1 and the logarithm diverges. One can avoid this scenario by choosing larger α since in reality precipitation is expected to only occur once and to deposit the majority of the solute. This effect should be independent of the switch applied to the ϕ equation. The system parameters are $L = 1600$, $N = 2048$, $h_0 = 20$, $C_0 = 0.3$, $\phi_0 = 0.99$, $v = 0.1$, $g = 0.001$, $\beta = 1$, $\text{Pe}^{-1} = 0.001$, $\chi = 1.5$, $\Omega = 0.001$, $\Upsilon = 0.01$, $\mu = -0.7$, $C_{\text{eq}} = 0.4$, $\alpha = 0.2$, $\lambda = 20$, $\Lambda = 1$, $\sigma = 10$.

A.12.2. Dip-Coating Periodic Solution Measures

The solution measures in Fig. 4.27 are obtained as follows: The onset of deposition x_{onset} is defined at the location where the effective deposit thickness ζ first becomes positive. A measure point is chosen as

$$x_{\text{mp}} = \min\left(x_{\text{onset}} + 100, \frac{x_{\text{onset}} + L_x}{2}\right) \tag{A.252}$$

such that patterns are given enough time to relax. A time series $\zeta(x_{\text{mp}}, t)$ is extracted from the solution data. Each period can then be processed for maximum thickness ζ_{max}, minimum thickness ζ_{min}, amplitude A_ζ and mean thickness $\overline{\zeta}$. After averaging over all periods, the data points shown in Fig. 4.27 are obtained. In the absence of deposition the measure point is defined by

$$x_{\text{mp}} = 0.9 L_x. \tag{A.253}$$

A.13. Preconditioning

The sign in front of tanh is irrelevant as one can redefine $n \to -n$.

$$\phi(\mathbf{x}, t) = -\tanh\left(\frac{n(\mathbf{x}, t)\Lambda}{\sqrt{2}}\right) \tag{A.254}$$

$$n(\mathbf{x}, t) = -\frac{\sqrt{2}}{\Lambda}\tanh^{-1}(\phi) \tag{A.255}$$

$$\frac{\partial}{\partial x}\tanh(x) = 1 - \tanh(x)^2 \tag{A.256}$$

$$\partial_t \phi = -\frac{\Lambda}{\sqrt{2}}(1 - \phi^2)\partial_t n \tag{A.257}$$

$$\Rightarrow \partial_t n = -\frac{\sqrt{2}}{\Lambda}\left(1 - \phi^2\right)^{-1}\partial_t \phi \tag{A.258}$$

$$\partial_t \phi = \sigma\left(\Lambda^{-2}\Delta\phi - \partial_\phi f_{\mathrm{xm}} - \Lambda^{-2}\kappa|\nabla\phi|\right) \tag{A.259}$$

We substitute each of the ϕ terms with Eq. (A.254) in the following, only keeping $(1 - \phi^2)$ or polynomials of ϕ expressions as the former will cancel out when applying Eq. (A.258) and the latter can be directly substituted with Eq. (A.254).

$$\mathcal{N} := \frac{n(\mathbf{x}, t)\Lambda}{\sqrt{2}} \tag{A.260}$$

$$\nabla\phi = -\nabla\tanh(\mathcal{N}) \tag{A.261}$$

$$= -(1 - \phi^2)\nabla\mathcal{N} \tag{A.262}$$

$$= -(1 - \phi^2)\frac{\Lambda}{\sqrt{2}}\nabla n \tag{A.263}$$

$$\Delta\phi = -(1 - \phi^2)\Delta\mathcal{N} - \nabla\mathcal{N} \cdot \nabla\phi(-2\phi) \tag{A.264}$$

$$= -\frac{\Lambda}{\sqrt{2}}(1 - \phi^2)\Delta n + 2\phi\frac{\Lambda}{\sqrt{2}}\nabla n \cdot \nabla\phi \tag{A.265}$$

$$= -\frac{\Lambda}{\sqrt{2}}(1 - \phi^2)\Delta n + \sqrt{2}\Lambda\phi\nabla n\left(-\frac{\Lambda}{\sqrt{2}}\nabla n(1 - \phi^2)\right) \tag{A.266}$$

$$= -\frac{\Lambda}{\sqrt{2}}(1 - \phi^2)\Delta n - \Lambda^2\phi|\nabla n|^2(1 - \phi^2) \tag{A.267}$$

$$\frac{\nabla\phi}{|\nabla\phi|} = -\frac{\nabla\tanh(\mathcal{N})}{|\nabla\tanh(\mathcal{N})|} = -\frac{(1 - \phi^2)\nabla\mathcal{N}}{|1 - \phi^2||\nabla\mathcal{N}|} \stackrel{|\phi|\leq 1}{=} -\frac{\nabla\mathcal{N}}{|\nabla\mathcal{N}|} = -\frac{\nabla n}{|\nabla n|} \tag{A.268}$$

$$\Rightarrow \nabla \cdot \frac{\nabla\phi}{|\nabla\phi|} = -\nabla \cdot \frac{\nabla n}{|\nabla n|} \tag{A.269}$$

$$|\nabla\phi| = |\nabla\mathcal{N}||1 - \phi^2| = \frac{\Lambda}{\sqrt{2}}|\nabla n|(1 - \phi^2) \tag{A.270}$$

The local potential can be left unchanged. Inserting Eq. (A.267),(A.269),(A.270) into Eq. (A.259) and then into Eq. (A.258) results in

$$\partial_t n = -\frac{\sqrt{2}}{\Lambda}\left(1 - \phi^2\right)^{-1}\sigma\left\{-\frac{\Lambda}{\Lambda^2\sqrt{2}}(1 - \phi^2)\Delta n - \frac{\Lambda^2}{\Lambda^2}\phi|\nabla n|^2(1 - \phi^2)\right.$$

$$-(1-\phi^2)(\lambda c - \phi) + \frac{1}{\Lambda^2}\frac{\Lambda}{\sqrt{2}}|\nabla n|(1-\phi^2)\nabla\cdot\frac{\nabla n}{|\nabla n|}\Bigg\}\tag{A.271}$$

$$= \sigma\left\{\Lambda^{-2}\Delta n + \frac{\sqrt{2}}{\Lambda}\phi|\nabla n|^2 + \frac{\sqrt{2}}{\Lambda}(\lambda c - \phi) - \Lambda^{-2}|\nabla n|\nabla\cdot\frac{\nabla n}{|\nabla n|}\right\}\tag{A.272}$$

$$= \sigma\left\{\Lambda^{-2}\Delta n + \frac{\sqrt{2}}{\Lambda}\left[\lambda c - \phi\left(1 - |\nabla n|^2\right)\right] - \Lambda^{-2}|\nabla n|\nabla\cdot\frac{\nabla n}{|\nabla n|}\right\}\tag{A.273}$$

$$= \sigma\left\{\Lambda^{-2}\Delta n + \frac{\sqrt{2}}{\Lambda}\left[\lambda c + \tanh\left(\frac{n\Lambda}{\sqrt{2}}\right)\left(1 - |\nabla n|^2\right)\right] - \Lambda^{-2}|\nabla n|\nabla\cdot\frac{\nabla n}{|\nabla n|}\right\}\tag{A.274}$$

For the Xu-Meakin model the phase-field equation reads

$$\partial_t\phi = \frac{1}{\mathrm{Pe}_{\mathrm{xm}}}\left(\Delta\phi - \partial_\phi f_{\mathrm{xm}}(\phi, c, \lambda) - \kappa|\nabla\phi|\right)\tag{A.275}$$

and the equation for the signed distance function can be written down by formally substituting

$$\sigma \to \mathrm{Pe}_{\mathrm{xm}}^{-1} \qquad \Lambda \to 1\tag{A.276}$$

$$\phi(\mathbf{x}, t) = -\tanh\left(\frac{n(\mathbf{x}, t)}{\sqrt{2}}\right)\tag{A.277}$$

resulting in

$$\partial_t n = \mathrm{Pe}_{\mathrm{xm}}^{-1}\left\{\Delta n + \sqrt{2}\left[\lambda c + \tanh\left(\frac{n}{\sqrt{2}}\right)\left(1 - |\nabla n|^2\right)\right] - |\nabla n|\nabla\cdot\frac{\nabla n}{|\nabla n|}\right\}.\tag{A.278}$$

A.14. Discretization Analysis of LB Continuation Data

pde2path and the CUDA code utilize finite element and finite difference method for spatial discretization, respectively. Both methods are expected to converge with increasing number of nodes, provided floating point precision is not an issue. As a benchmark for finding practical discretizations for both methods the LC-1 branch (see Fig. 5.1) of stable stationary solutions is chosen, see the introduction of Chapter 5 and 5.1 for an overview of the solution space. Figure A.14 shows said branch for varying FEM and FDM discretizations in gray/black and red, respectively. Both methods approach each other quite well as the number of nodes is increased. However, it is apparent that a systematic discrepancy persists even at finer discretizations. A higher order FDM would be required for a more conclusive comparison. Alternatively, one can switch to direct numerics with FEM, such as *oomph-lib*. Nevertheless, $L_x = 60$, $N_x = 400$ is about the practical limit for single core 2D pde2path calculations while $L_x = 60$, $N_x = 100$ is the limit for second order FDM with the concerned generalized Cahn-Hilliard model.

While the 2D bifurcation curve for rough discretizations such as Fig. 5.3 can be obtained without too much trouble the increasingly tightening structures result in undesired branch switching at finer discretizations. Figure A.15 shows a section of the 2D bifurcation curve for a discretization of $L_x \times L_y = 60 \times 30$, $N_x \times N_y = 400 \times 200$. The curve is depicted in dashed gray scale. The darker the dashes, the further along the curve the solution and the larger the arclength s is. (a) In this region the curve first follows the blue arrows, a fold, undergoes a section of wild criss-crossing again and then follows the red arrows, overlapping with the blue arrows. (b) However, here, it passes the fold. Depending on the stepsize undesired branch switching can occur, possibly resulting in closed loops.
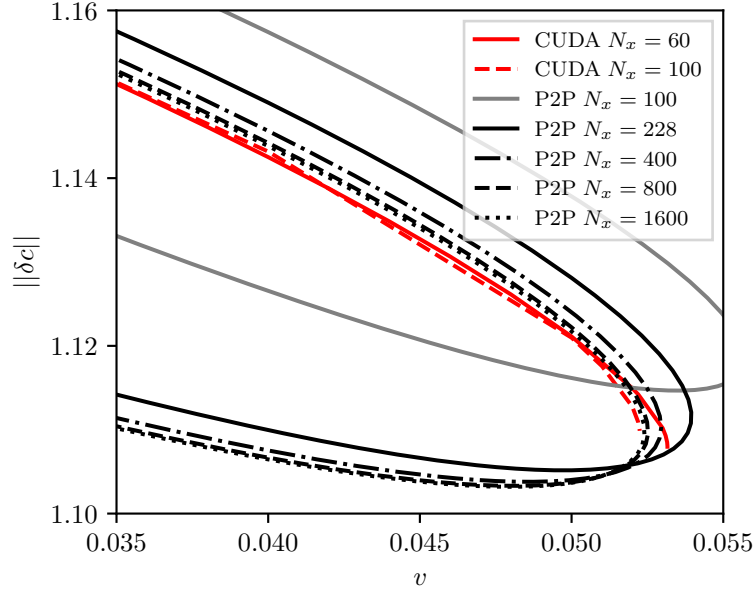
Figure A.14.: L^2-norm of the 1D stable stationary liquid-condensed solution (LC-1, see Fig. 5.1) for varying transfer velocity v. The branches are obtained from numerical continuation (gray/black) and direct numerical simulations (red) using pde2path and CUDA, respectively. The spatial discretization is applied by FEM and FDM, respectively. The branches become unstable past their folds. Note that the Dirichlet boundary condition is imposed on node $c(0, y) = -0.9$ for FEM but $c(-\Delta x, y) = -0.9$ for FDM. In order to match both methods the ghost point is prepended to c for FDM when calculating the norm. Further, for FEM the Dirichlet BC is imposed by a harmonic term that only acts on $x = 0$ on the right-hand side. Its spring constant (p.nc.sf in PDE2PATH) is set to a high value of 10^6. The governing equations are Eq. (2.158)-(2.160). Domain size $L_x = 60$.
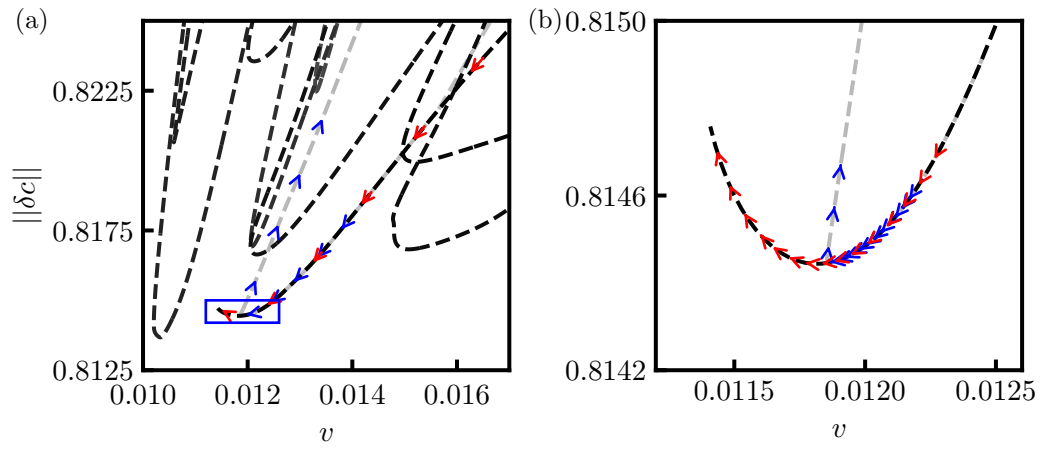
Figure A.15.: L^2-norm of 2D steady states for varying transfer velocity v obtained from numerical path continuation of Eq. (2.158)-(2.160). The curve is depicted in dashed gray scale. The darker the dashes the further along the curve the solution and the larger the arclength s is. Blue arrows (earlier) denote the section that follows the fold while red arrows (later) denote the section that passes it. (a) overview (b) zoom. Discretization $L_x \times 2L_y = 60 \times 60, N_x \times 2N_y = 400 \times 400$.

A.15. Finite Difference Stencils

$$\times \frac{1}{144\Delta x^2}$$

$$\times \frac{1}{72\Delta x^2}$$

$$\frac{\partial^2}{\partial x \partial y}$$

$$\times \frac{1}{144\Delta x^3}$$
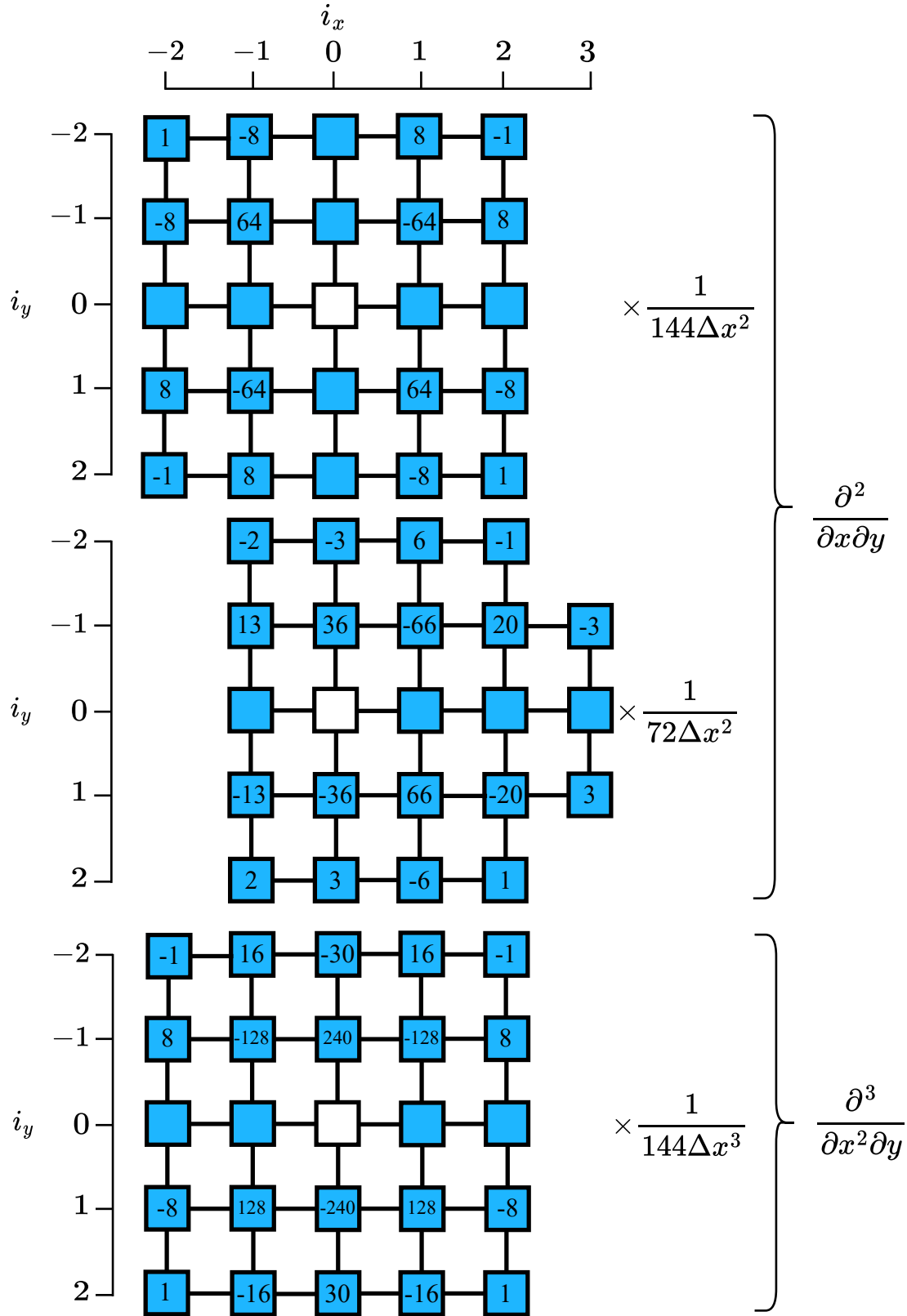
$$\frac{\partial^3}{\partial x^2 \partial y}$$

Figure A.16.: Fourth order FDM stencils of $\frac{\partial^2}{\partial x \partial y}$ and $\frac{\partial^3}{\partial x^2 \partial y}$. Other orientations of the non-centered $\frac{\partial^2}{\partial x \partial y}$ are obtained by rotation. The centered $\frac{\partial^3}{\partial x \partial y^2}$ stencil is obtained by swapping x and y. The node for which the derivative is calculated is marked by a white box.
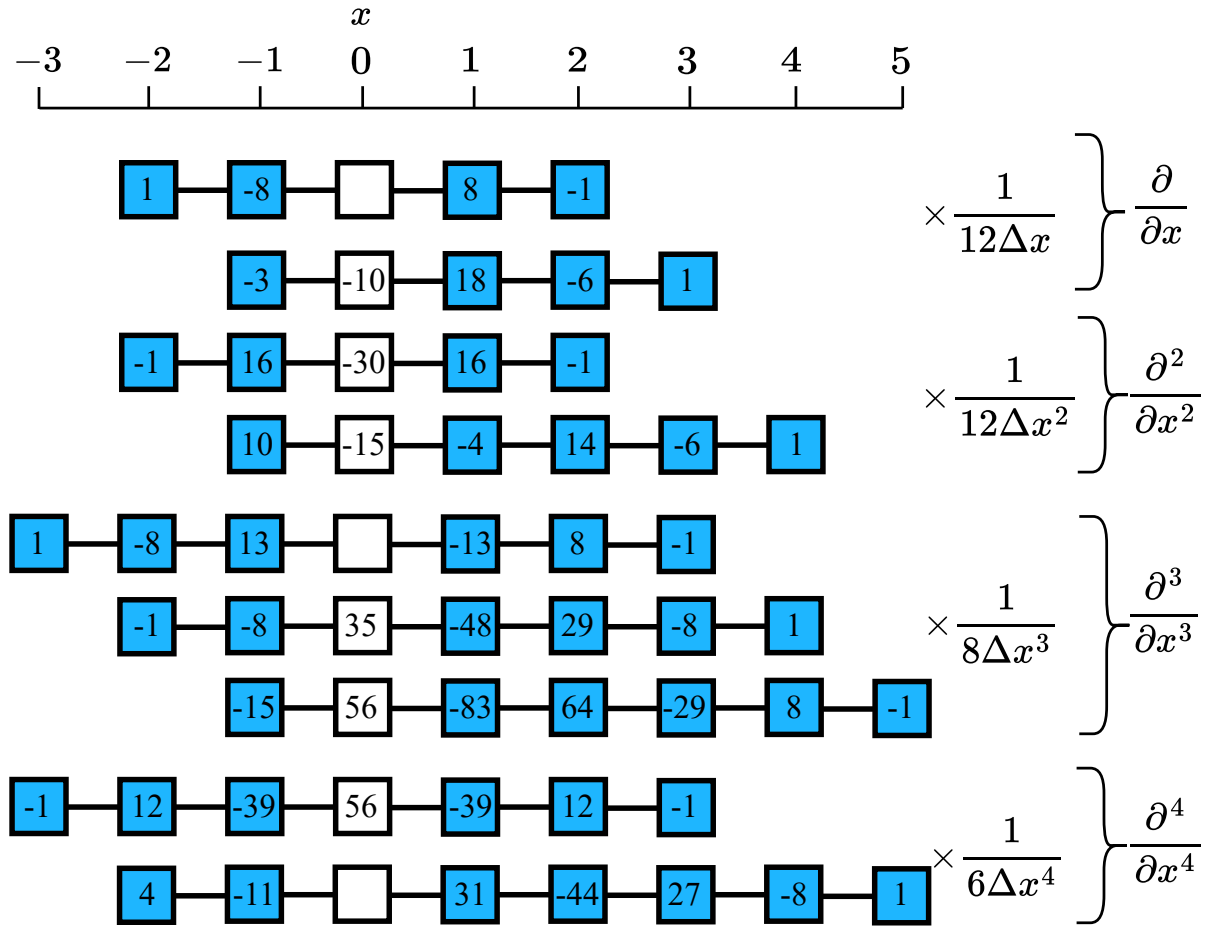
Figure A.17.: Fourth order FDM stencils of one-dimensional derivatives. Other orientations of the non-centered stencils are obtained by flipping the stencil and each sign. The node for which the derivative is calculated is marked by a white box.
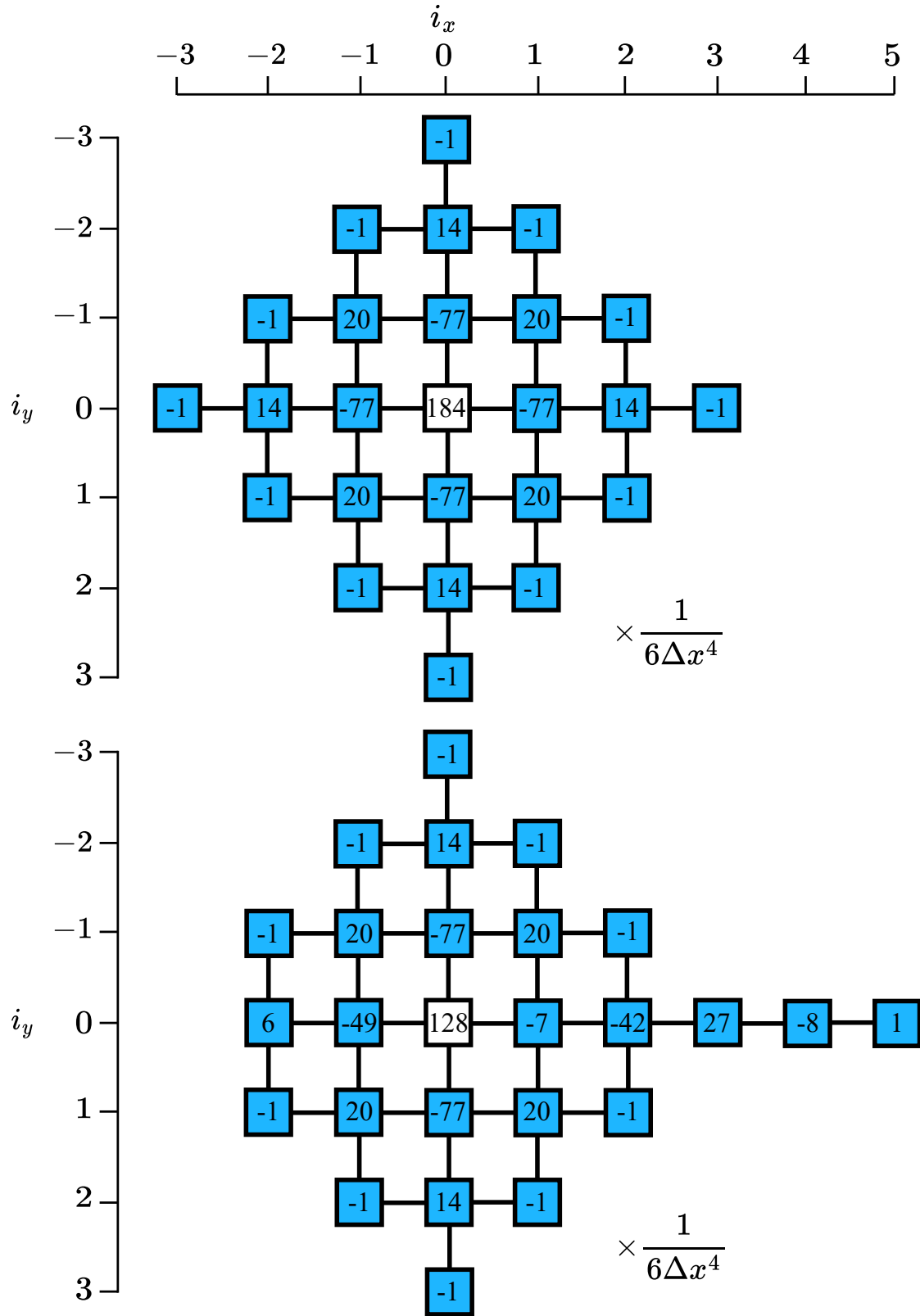
Figure A.18.: Fourth order FDM stencils of the biharmonic operator Δ^2 as a centered and non-centered variant with the latter having three nodes on the top and bottom but only two nodes on the left. The stencils for other orientations are easily obtained by rotation. The signs do not change. The node for which the derivative is calculated is marked by a white box.

List of Recurrent Symbols

Symbol	Description	Unit	First appearance/ definition
A	coefficient of long-range interactions	J	p. 12
A	forcing amplitude	1	p. 90
α	strength of source term	1	p. 20
A_ζ	amplitude [prominence] of deposit	1	p. 75
B	coefficient of short-range interactions	Jm^3	p. 12
$\tilde{\beta}$	substrate inclination	rad	p. 25
β	effective substrate inclination	1	p. 25
C	solute concentration	1	p. 26
$\hat{c}$	magnitude of Fourier transform of c	1	p. 91
$\tilde{c}$	normalized solute concentration, dimensional arguments	1	p. 19
c	normalized solute concentration	1	p. 21
c	surfactant concentration	1	p. 28
C_0	solute concentration at $x = 0$	1	p. 26
c_0	surfactant concentration at $x = 0$	1	p. 29
$\tilde{C}_1$	solvent concentration, dimensional arguments	1	p. 13
C_1	solvent concentration	1	p. 23
$C_{1,0}$	solvent concentration at $x = 0$	1	p. 26
$\tilde{C}_2$	solute concentration, dimensional arguments	1	p. 13
C_2	solute concentration	1	p. 23
$C_{2,0}$	solute concentration at $x = 0$	1	p. 26
Ca	capillary number	1	p. 11
C_{eq}	local equilibrium solute concentration	1	p. 20
χ	mixing parameter	1	p. 13
D	diffusion coefficient	m^2/s	p. 14
D_a	Damköhler number	1	p. 21
$||\delta c||$	L^2-norm of c	1	p. 81
$\partial_t C^{(\text{conv})}$	convective contribution to rate of change of C	1	p. 71
$\partial_t C^{(\text{diff})}$	diffusive contribution to rate of change of C	1	p. 71
$\partial_t C^{(\text{evap})}$	evaporative contribution to rate of change of C	1	p. 71
D_{xm}	diffusion coefficient in the Xu-Meakin model	m^2/s	p. 20
ε	length scale related to interface thickness	m	p. 20
η	dynamic [shear] viscosity	Js/m^3	p. 8

Symbol	Description	Unit	First appearance/ definition
E_v	strength of evaporation	m^3/Js	p. 22
$\mathbf{e}_x$	basis vector in x	1	p. 43
F	energy scale	J	p. 23
$\tilde{\mathcal{F}}$	free energy functional	J	p. 15
$\mathcal{F}$	free energy functional	1	p. 12
$\tilde{f}$	wetting energy [local potential]	Jm^2	p. 12
f	wetting energy [local potential]	1	p. 24
f_1	double-well potential	1	p. 15
f_2	odd function for tilting the local potential	1	p. 15
f_3	primitive function of the source term	1	p. 15
$\tilde{\mathcal{F}}_{\mathrm{bm}}$	free energy functional for a passive geometry	J	p. 13
$\mathcal{F}_{\mathrm{bm}}$	free energy functional for a passive geometry	1	p. 25
$\tilde{f}_{\mathrm{FH}}$	Flory-Huggins type local potential	J/m^2	p. 13
$\mathcal{F}_g$	gravitative contribution to $\mathcal{F}$	1	p. 25
$\mathcal{F}_{\mathrm{xm}}$	phase-field functional	1	p. 25
$\tilde{\mathcal{F}}_{\mathrm{xm}}$	functional of the phase-field equation	m^2	p. 19
f_{xm}	local potential of $\mathcal{F}_{\mathrm{xm}}$	1	p. 19
$\tilde{g}$	gravitational acceleration	m/s^2	p. 25
g	effective gravitational acceleration	1	p. 25
γ	liquid-gas surface tension	J/m^2	p. 9
$\tilde{\Gamma}$	surfactant concentration, hydrodynamic	1	p. 27
γ_{lg}	liquid-gas surface tension	J/m^2	p. 11
γ_{sg}	solid-gas surface tension	J/m^2	p. 11
γ_{sl}	solid-liquid surface tension	J/m^2	p. 11
$\tilde{h}$	film height [height of the liquid-gas interface]	m	p. 9
h	film height [height of the liquid-gas interface]	1	p. 23
H	vertical length scale	m	p. 10
h_0	film height at $x = 0$ or initial height of droplet	1	p. 25
$\tilde{h}_{\mathrm{eq}}$	equilibrium height	m	p. 12
h_p	precursor height	1	p. 26
$\underline{\underline{I}}$	identity matrix	1	p. 9
$\tilde{\mathbf{J}}_1$	solvent flux	m^2/s	p. 13
$\tilde{\mathbf{J}}_{1,c}$	conserved solvent flux	m^2/s	p. 22
$\mathbf{J}_{1,c}$	conserved solvent flux	1	p. 24
$\tilde{\mathbf{J}}_2$	solute flux	m^2/s	p. 13
$\tilde{\mathbf{J}}_{2,c}$	conserved solute flux	m^2/s	p. 22
$\mathbf{J}_{2,c}$	conserved solute flux	1	p. 24
$\mathbf{J}_{2,\mathrm{conv}}$	convective solute flux	1	p. 71
$\mathbf{J}_{2,\mathrm{diff}}$	diffusive solute flux	1	p. 71
$\tilde{J}_{\mathrm{evap}}$	evaporative flux	m/s	p. 22
J_{evap}	evaporative flux	1	p. 24
$\mathbf{J}_h$	flux of the liquid (conserved)	1	p. 71
$\tilde{J}_{\mathrm{source}}$	source term	m/s	p. 22

Symbol	Description	Unit	First appearance/ definition
J_{source}	source term	1	p. 24
$\overline{k}$	mean wavenumber	1	p. 90
$\tilde{k}$	wavenumber	1/m	p. 18
k_0	enforced wavenumber	1	p. 90
$\tilde{\kappa}$	mean curvature of the interface	1/m	p. 9
κ	mean curvature of the interface	1	p. 21
k_B	Boltzmann constant	J/K	p. 13
$\tilde{k}_r$	reaction rate	m/s	p. 21
L	domain size	1	p. 25
$\overline{l}$	mean stripe distance	1	p. 90
Λ	length scale ratio of dewetting and interface	1	p. 24
$\tilde{\lambda}$	coupling parameter	J/m^2	p. 15
λ	coupling parameter	1	p. 20
λ_{SMC}	strength of SMC-term	1	p. 29
l_s	width of transition region	1	p. 29
$\tilde{M}$	part of $\underline{\tilde{Q}}^{\text{diff}}$	m^5/Js	p. 14
μ	effective chemical potential of the gas phase	1	p. 24
$\tilde{\mu}_g$	chemical potential of gas	J/m^2	p. 22
$\tilde{\mu}_l$	chemical potential of liquid	J/m^2	p. 22
N	number of grid points	1	p. 31
$\mathbf{n}$	interface normal	1	p. 9
n_{max}	particle number density of the mixture	1/m^3	p. 13
Ω	time scale ratio of evaporation to convection	1	p. 24
ω	forcing frequency (angular)	1	p. 90
$\tilde{\omega}$	growth rate of linear perturbations	1/s	p. 18
$\tilde{p}$	pressure	J/m^3	p. 8
p	pressure	1	p. 10
Pe^{-1}	inverse Peclét number	1	p. 24
Pe_{xm}	Péclet number, diffusion-limited precipitation	1	p. 21
$\tilde{\phi}$	phase-field, dimensional arguments	1	p. 15
ϕ	phase-field	1	p. 21
ϕ_0	phase-field at $x = 0$	1	p. 25
$\tilde{\Pi}$	disjoining pressure	J/m^3	p. 9
Π	disjoining pressure	1	p. 11
$\tilde{\psi}_1$	solvent thickness	m	p. 13
ψ_1	solvent thickness	1	p. 23
$\tilde{\psi}_2$	solute thickness	m	p. 13
ψ_2	solute thickness	1	p. 23
$\tilde{Q}$	mobility	1/Js	p. 15
Q^{c}	mobility matrix of conserved flux	1	p. 12
$\underline{\tilde{Q}}^{\text{conv}}$	mobility matrix of convective flux	m^6/Js	p. 13
$\underline{Q}^{\text{conv}}$	mobility matrix of convective flux	1	p. 24
$\underline{\tilde{Q}}^{\text{diff}}$	mobility matrix of diffusive flux	m^6/Js	p. 13

Symbol	Description	Unit	First appearance/ definition
$\underline{Q}^{\mathrm{diff}}$	mobility matrix of diffusive flux	1	p. 24
$\underline{Q}^{\mathrm{nc}}$	mobility matrix of non-conserved flux	1	p. 12
Re	Reynolds number	1	p. 10
$\tilde{\rho}$	mass density	$\mathrm{kg/m^3}$	p. 8
S	spreading parameter	$\mathrm{J/m^2}$	p. 11
s	arclength	1	p. 86
σ	time scale ratio of convection and particle mobility	1	p. 24
$\underline{\tilde{\sigma}}_{\mathrm{gas}}$	stress tensor of the gas phase	$\mathrm{J/m^3}$	p. 9
$\underline{\tilde{\sigma}}$	stress tensor	$\mathrm{J/m^3}$	p. 9
T	time period	1	p. 75
$\hat{T}$	temperature	K	p. 13
T	time scale	s	p. 10
$\tilde{t}$	time	s	p. 8
$\mathbf{t}$	interface tangent	1	p. 10
t	time	1	p. 10
τ	time scale of particle mobility	s	p. 20
θ	macroscopic contact angle	rad	p. 11
$\tilde{\vartheta}_{\mathrm{eq}}$	mesoscopic equilibrium contact angle	rad	p. 12
ϑ_{eq}	mesoscopic equilibrium contact angle	1	p. 27
θ_{eq}	macroscopic equilibrium contact angle	rad	p. 11
$\hat{T}_m$	melting temperature	K	p. 15
U	velocity scale	m/s	p. 10
$\tilde{\bar{\mathbf{u}}}$	mean flow velocity	m/s	p. 10
$\bar{\mathbf{u}}$	mean flow velocity	1	p. 10
$\tilde{u}$	normalized temperature	1	p. 15
$\mathbf{u}$	flow velocity	1	p. 10
Υ	ratio of thermal and surface energy	1	p. 24
$\tilde{u}_{\tilde{x}}, \tilde{u}_{\tilde{z}}, \tilde{u}_{\tilde{z}}$	flow velocity in $\tilde{x},\tilde{y},\tilde{z}$-direction	m/s	p. 8
u_z	flow velocity in z-direction	1	p. 10
$\bar{v}$	mean transfer velocity	1	p. 90
$\mathbf{v}$	transfer velocity	1	p. 25
v	magnitude of $\mathbf{v}$	1	p. 25
W	interface width	m	p. 16
W	synchronization order [rotation number]	1	p. 90
$\tilde{\mathbf{x}}$	position vector	m	p. 9
$\tilde{x}$	coordinate in the plane of the substrate	m	p. 8
X	lateral length scale	m	p. 10
$\mathbf{x}$	position vector	1	p. 10
x_s	meniscus position	1	p. 29
$\tilde{y}$	coordinate in the plane of the substrate	m	p. 8
$\tilde{z}$	coordinate normal to the substrate	m	p. 8
$\tilde{\zeta}$	deposit thickness	m	p. 23
ζ	deposit thickness	1	p. 23

Symbol	Description	Unit	First appearance/ definition
$\hat{\zeta}$	drag [friction] coefficient	Js/m^2	p. 14
$\bar{\zeta}$	mean deposit thickness	1	p. 75
ζ_{max}	minimum deposit thickness	1	p. 75
ζ_{min}	minimum deposit thickness	1	p. 75
ζ_{SMC}	external field modeling substrate-monolayer interactions	1	p. 29

Bibliography

[ABKK+09] M. Asta, C. Beckermann, A. Karma, W. Kurz, R. Napolitano, M. Plapp, G. Purdy, M. Rappaz, and R. Trivedi. "Solidification microstructures and solid-state parallels: recent developments, future directions". *Acta Mater.* 57 (2009), 941–971.

[AEZT+18] M. Abo Jabal, A. Egbaria, A. Zigelman, U. Thiele, and O. Manor. "Connecting monotonic and oscillatory motions of the meniscus of a volatile polymer solution to the transport of polymer coils and deposit morphology". *Langmuir* 34 (2018), 11784–11794.

[AG20] K. Ankit and M. E. Glicksman. "Growth competition during columnar solidification of seaweed microstructures". *Eur. Phys. J. E* 43 (2020), 14.

[Aja05] V. S. Ajaev. "Evolution of dry patches in evaporating liquid films". *Phys. Rev. E* 72 (2005), 031605.

[Alm99] R. F. Almgren. "Second-order phase field asymptotics for unequal conductivities". *SIAM J. Appl. Math.* 59 (1999), 2086–2107.

[AMW98] D. M. Anderson, G. B. McFadden, and A. A. Wheeler. "Diffuse-interface methods in fluid mechanics". *Annu. Rev. Fluid Mech.* 30 (1998), 139–165.

[AP10] H. A. Atwater and A. Polman. "Plasmonics for improved photovoltaic devices". *Nat. Mater.* 9 (2010), 205–213.

[Arn61] V. I. Arnol'd. "Small denominators. I. Mapping the circle onto itself". *Izv. Akad. Nauk SSSR Ser. Mat.* 25 (1961), 21–86.

[BDG10] H. Bodiguel, F. Doumenc, and B. Guerrier. "Stick-slip patterning at low capillary numbers for an evaporating colloidal suspension". *Langmuir* 26 (2010), 10758–10763.

[BDM19] M. Bonacini, E. Davoli, and M. Morandotti. "Analysis of a perturbed Cahn-Hilliard model for Langmuir-Blodgett films". *Nonlinear Differ. Equ. Appl.* 26 (2019), 36.

[BDSK+99] C. Beckermann, H.-J. Diepers, I. Steinbach, A. Karma, and X. Tong. "Modeling melt convection in phase-field simulations of solidification". *J. Comput. Phys.* 154 (1999), 468–496.

[BJM18] P. Bollada, P. Jimack, and A. Mullis. "A numerical approach to compensate for phase field interface effects in alloy solidification". *Computational Materials Science* 151 (2018), 338–350.

[Blo35] K. B. Blodgett. "Films built by depositing successive monomolecular layers on a solid surface". *J. Am. Chem. Soc.* 57 (1935), 1007–1022.

[BM03]   T. Biben and C. Misbah. "Tumbling of vesicles under shear flow within an advected-field approach". *Phys. Rev. E* 67 (2003), 031908.

[BMLV03]   T. Biben, C. Misbah, A. Leyrat, and C. Verdier. "An advected-field approach to the dynamics of fluid interfaces". *EPL* 63 (2003), 623–630.

[BMS89]   D. E. Bornside, C. W. Macosko, and L. E. Scriven. "Spin coating: one-dimensional model". *J. Appl. Phys.* 66 (1989), 5185–5193.

[BRSB+04]   J. Beaucourt, F. Rioual, T. Séon, T. Biben, and C. Misbah. "Steady to unsteady dynamics of a vesicle in a flow". *Phys. Rev. E* 69 (2004), 011906.

[BSMM05]   I. Bronstein, K. Semendjajew, G. Musiol, and H. Mühlig. *Taschenbuch der Mathematik*. Verlag Harri Deutsch, 2005.

[BWMM94]   W. Boettinger, A. Wheeler, B. Murray, and G. McFadden. "Prediction of solute trapping at high solidification rates using a diffuse interface phase-field theory of alloy solidification". *Mater. Sci. Eng. A* 178 (1994), 217–223.

[Cag86]   G. Caginalp. "An analysis of a phase field model of a free boundary". *Arch. Ration. Mech. Anal.* 92 (1986), 205–245.

[CBH07]   B. P. Cook, A. L. Bertozzi, and A. E. Hosoi. "Shock solutions for particle-laden thin films". *SIAM J. Appl. Math.* 68 (2007), 760–783.

[CCDT+86]   Y. Couder, O. Cardoso, D. Dupuy, P. Tavernier, and W. Thom. "Dendritic growth in the Saffman-Taylor experiment". *EPL* 2 (1986), 437–443.

[CCR92]   B. Caroli, C. Caroli, and B. Roulet. "Instabilities of planar solidification fronts". *Solids Far from Equilibrium*. Cambridge University Press, 1992.

[CG10]   A. M. Cazabat and G. Guena. "Evaporation of macroscopic sessile droplets". *Soft Matter* 6 (2010), 2591–2612.

[CL87]   G. Caginalp and J. T. Lin. "A numerical analysis of an anisotropic phase field model". *IMA J. Appl. Math.* 39 (1987), 51–66.

[CMS13]   C. E. Colosqui, J. F. Morris, and H. A. Stone. "Hydrodynamically driven colloidal assembly in dip coating". *Phys. Rev. Lett.* 110 (2013), 188302.

[CS88]   J. T. Cheung and H. Sankur. "Growth of thin films by laser-induced evaporation". *Crit. Rev. Solid State Mater. Sci.* 15 (1988), 63–109.

[CS91]   G. Caginalp and E. Socolovsky. "Computation of sharp phase boundaries by spreading: the planar and spherically symmetric cases". *J. Comput. Phys.* 95 (1991), 85–100.

[CSA17]   C. Chalmers, R. Smith, and A. J. Archer. "Dynamical density functional theory for the evaporation of droplets of nanoparticle suspension". *Langmuir* 33 (2017), 14490–14501.

[CSE12]   T. S. Chan, J. H. Snoeijer, and J. Eggers. "Theory of the forced wetting transition". *Phys. Fluids* 24 (2012), 072104.

[DBDH+97]   R. D. Deegan, O. Bakajin, T. F. Dupont, G. Huber, S. R. Nagel, and T. A. Witten. "Capillary flow as the cause of ring stains from dried liquid drops". *Nature* 389 (1997), 827–829.

[DDG16]   M. Dey, F. Doumenc, and B. Guerrier. "Numerical simulation of dip-coating in the evaporative regime". *Eur. Phys. J. E* 39 (2016), 19.

[Dee00]   R. D. Deegan. "Pattern formation in drying drops". *Phys. Rev. E* 61 (2000), 475–485.

[Der75]   B. V. Derjaguin. "Untersuchungen des Spaltdruckes dünner Filme, deren Entwicklung, Ergebnisse und zu lösende aktuelle Probleme". *Colloid. Polym. Sci.* 253 (1975), 492–499.

[DG10]   F. Doumenc and B. Guerrier. "Drying of a solution in a meniscus: a model coupling the liquid and the gas phases". *Langmuir* 26 (2010), 13959–13967.

[DG13]   F. Doumenc and B. Guerrier. "Self-patterning induced by a solutal Marangoni effect in a receding drying meniscus". *EPL* 103 (2013), 14001.

[DGGR+21]   J. A. Diez, A. G. González, D. A. Garfinkel, P. D. Rack, J. T. McKeown, and L. Kondic. "Simultaneous decomposition and dewetting of nanoscale alloys: a comparison of experiment and theory". *Langmuir* 37 (2021), 2575–2585.

[DK02]   J. A. Diez and L. Kondic. "Computing three-dimensional thin film flows including contact lines". *J. Comput. Phys.* 183 (2002), 274–306.

[DK07]   J. A. Diez and L. Kondic. "On the breakup of fluid films of finite and infinite extent". *Phys. Fluids* 19 (2007), 072107.

[DKB00]   J. A. Diez, L. Kondic, and A. Bertozzi. "Global models for moving contact lines". *Phys. Rev. E* 63 (2000), 011208.

[DLH16]   X. Ding, J. Liu, and T. A. L. Harris. "A review of the operating limits in slot die coating processes". *AIChE J.* 62 (2016), 2508–2524.

[DSZZ19]   C.-a. Di, H. Shen, F. Zhang, and D. Zhu. "Enabling multifunctional organic transistors with fine-tuned charge transport". *Acc. Chem. Res.* 52 (2019), 1113–1124.

[DY99]   C. Denniston and J. Yeomans. "Diffuse interface simulation of Marangoni convection". *Phys. Chem. Chem. Phys.* 1 (1999), 2157–2161.

[EFKP04]   B. Echebarria, R. Folch, A. Karma, and M. Plapp. "Quantitative phase-field model of alloy solidification". *Phys. Rev. E* 70 (2004), 061604.

[EGUW+19]   S. Engelnkemper, S. V. Gurevich, H. Uecker, D. Wetzel, and U. Thiele. "Continuation for thin film hydrodynamics and related scalar problems". *Computational Modeling of Bifurcations and Instabilities in Fluid Mechanics*. Edited by A. Gelfgat. Computational Methods in Applied Sciences, vol 50. Springer, 2019, 459–501.

[Emm08]   H. Emmerich. "Advances of and by phase-field modelling in condensed-matter physics". *Adv. Phys.* 57 (2008), 1–87.

[Eng17]   S. Engelnkemper. "Nichtlineare Analyse Physikochemisch Getriebener Entnetzung - Statik und Dynamik". PhD thesis. Westfälische Wilhelm-Universität Münster, 2017.

[EPBS+07]   K. R. Elder, N. Provatas, J. Berry, P. Stefanovic, and M. Grant. "Phase-field crystal modeling and classical density functional theory of freezing". *Phys. Rev. B* 75 (2007), 064107.

[Erb12]   H. Erbil. "Evaporation of pure liquid sessile and spherical suspended drops: a review". *Adv. Colloid Interface Sci.* 170 (2012), 67–86.

[Erb21]   H. Y. Erbil. "Dependency of contact angles on three-phase contact line: a review". *Colloids and Interfaces* 5 (2021).

[ESR00]   M. H. Eres, L. W. Schwartz, and R. V. Roy. "Fingering phenomena for driven coating films". *Phys. Fluids* 12 (2000), 1278–1295.

[FAT11]   L. Frastia, A. J. Archer, and U. Thiele. "Dynamical model for the formation of patterned deposits at receding contact lines". *Phys. Rev. Lett.* 106 (2011), 077801.

[FAT12]   L. Frastia, A. J. Archer, and U. Thiele. "Modelling the formation of structured deposits at receding contact lines of evaporating solutions and suspensions". *Soft Matter* 8 (2012), 11363–11386.

[FCH00]   R. Folch, J. Casademunt, and A. Hernández-Machado. "Viscous fingering in liquid crystals: anisotropy and morphological transitions". *Phys. Rev. E* 61 (2000), 6632–6638.

[FCHR99a]   R. Folch, J. Casademunt, A. Hernández-Machado, and L. Ramírez-Piscina. "Phase-field model for Hele-Shaw flows with arbitrary viscosity contrast. ii. Numerical study". *Phys. Rev. E* 60 (1999), 1734–40.

[FCHR99b]   R. Folch, J. Casademunt, A. Hernández-Machado, and L. Ramírez-Piscina. "Phase-field model for Hele-Shaw flows with arbitrary viscosity contrast. i. Theoretical approach". *Phys. Rev. E* 60 (1999), 1724–1733.

[FFDR13]   J. Friedli, J. L. Fife, P. Di Napoli, and M. Rappaz. "Dendritic growth morphologies in Al-Zn alloys–part I: X-ray tomographic microscopy". *Metall. Mater. Trans. A* 44 (2013), 5522–5531.

[FTBC+01]   R. Folch, T. Tóth-Katona, Á. Buka, J. Casademunt, and A. Hernández-Machado. "Periodic forcing in viscous fingering of a nematic liquid crystal". *Phys. Rev. E* 64 (2001), 056225.

[GCF00]   M. Gleiche, L. Chi, and H. Fuchs. "Nanoscopic channel lattices with controlled anisotropic wetting". *Nature* 403 (2000), 173–175.

[Gen85]   P. G. de Gennes. "Wetting: statics and dynamics". *Rev. Mod. Phys.* 57 (1985), 827–863.

[GFS07]   M. Ghosh, F. Fan, and K. J. Stebe. "Spontaneous pattern formation by dip coating of colloidal suspensions on homogeneous surfaces". *Langmuir* 23 (2007), 2180–2183.

[Gla01]   K. Glasner. "Nonlinear preconditioning for diffuse interfaces". *J. Comput. Phys.* 174 (2001), 695–711.

[GLFD+16]   P. Gao, L. Li, J. J. Feng, H. Ding, and X.-Y. Lu. "Film deposition and transition on a partially wetting plate in dip coating". *J. Fluid Mech.* 791 (2016), 358–383.

[GLR02]   G. Grün, M. Lenz, and M. Rumpf. "A finite volume scheme for surfactant driven thin film flow". *Finite Volumes for Complex Applications Iii*. Edited by R. Herbin and D. Kröner. Hermes Penton Sciences, 2002, 567–574.

[GR00]   G. Grün and M. Rumpf. "Nonnegativity preserving convergent schemes for the thin film equation". *Numer. Math.* 87 (2000), 113–152.

[GR01]   G. Grün and M. Rumpf. "Simulation of singularities and instabilities arising in thin film flow". *Eur. J. Appl. Math.* 12 (2001), 293–320.

[GR98]   K. Graf and H. Riegler. "Molecular adhesion interactions between Langmuir monolayers and solid substrates". *Colloids Surf., A* 131 (1998), 215–224.

[Grä01]   M. Grätzel. "Photoelectrochemical cells". *Nature* 414 (2001), 338–344.

[Grü99]   G. Grün. "On the numerical simulation of wetting phenomena". *Proceedings of the 15th Gamm-seminar Kiel, Numerical Methods of Composite Materials*. Edited by S. S. W. Hackbusch. Vieweg-Verlag, 1999.

[GTHT14]   M. Galvagno, D. Tseluiko, L. H., and U. Thiele. "Continuous and discontinuous dynamic unbinding transitions in drawn film flow". *Phys. Rev. Lett.* 112 (2014), 137803.

[HAQ99]   S. W. Husain, M. S. Ahmed, and I. Qamar. "Dendritic morphology observed in the solid-state precipitation in binary alloys". *Metall. Mater. Trans. A* 30 (1999), 1529–1534.

[HC61]   G. Horvay and J. Cahn. "Dendritic and spheroidal growth". *Acta Metall.* 9 (1961), 695–705.

[HDJT22]   S. Hartmann, C. Diddens, M. Jalaal, and U. Thiele. "Sessile drop evaporation in a gap - cross over between diffusion-limited and phase transition-limited regime". *arXiv preprint:2206.14595* (2022).

[HH06]   M. Heil and A. L. Hazel. "Oomph-lib – an object-oriented multi-physics finite-element library". *Fluid-structure Interaction*. Edited by H.-J. Bungartz and M. Schäfer. Springer Berlin Heidelberg, 2006, 19–49.

[HH77]   P. C. Hohenberg and B. I. Halperin. "Theory of dynamic critical phenomena". *Rev. Mod. Phys.* 49 (1977), 435–479.

[HL12]   W. Han and Z. Lin. "Learning from "coffee rings": ordered structures enabled by controlled evaporative self-assembly". *Angew. Chem. Int. Ed.* 51 (2012), 1534–1546.

[HLBE+06] U. Helmersson, M. Lattemann, J. Bohlmark, A. P. Ehiasarian, and J. T. Gudmundsson. "Ionized physical vapor deposition (IPVD): a review of technology and applications". *Thin Solid Films* 513 (2006), 1–24.

[HMD22]   C. Hu, S. Martin, and R. Dingreville. "Accelerating phase-field predictions via recurrent neural networks learning the microstructure evolution in latent space". *Comput. Methods Appl. Mech. Eng.* 397 (2022), 115128.

[Hor98]   G. Horowitz. "Organic field-effect transistors". *Adv. Mater.* 10 (1998), 365–377.

[HWMD17]   S. Hu, Y. Wang, X. Man, and M. Doi. "Deposition patterns of two neighboring droplets: Onsager variational principle studies". *Langmuir* 33 (2017), 5965–5972.

[Iva47]   G. Ivantsov. "The temperature field around a spherical, cylindrical, or pointed crystal growing in a cooling solution". *Dokl. Akad. Nauk Sssr*. Volume 58. 1947, 567–569.

[JLFH21]   D. Ji, L. Li, H. Fuchs, and W. Hu. "Engineering the interfacial materials of organic field-effect transistors for efficient charge transport". *Acc. Mater. Res.* 2 (2021), 159–169.

[JS09]   M. Juntunen and R. Stenberg. "Nitsche's method for general boundary conditions". *Math. Comput.* 78 (2009), 1353–1374.

[JYWM20]   Z. Jiang, X. Yang, M. Wu, and X. Man. "The drying of liquid droplets*". *Chin. Phys. B* 29 (2020), 096803.

[Kal00]   S. Kalliadasis. "Nonlinear instability of a contact line driven by gravity". *J. Fluid Mech.* 413 (2000), 355–378.

[Kar01]   A. Karma. "Phase-field formulation for quantitative modeling of alloy solidification". *Phys. Rev. Lett.* 87 (2001), 115701.

[KB20]   K. Kolegov and L. Barash. "Applying droplets and films in evaporative lithography". *Adv. Colloid Interface Sci.* 285 (2020), 102271.

[Kel77]   H. Keller. "Numerical solution of bifurcation and nonlinear eigenvalue problems". *Applications of Bifurcation Theory.* Edited by P. Rabinowitz. Academic Press, New York, 1977, 359–384.

[KGF09]   M. H. Köpf, S. V. Gurevich, and R. Friedrich. "Thin film dynamics with surfactant phase transition". *EPL* 86 (2009), 66003.

[KGF11]   M. H. Köpf, S. V. Gurevich, and R. Friedrich. "Controlled nanochannel lattice formation utilizing prepatterned substrates". *Phys. Rev. E* 83 (2011), 016212.

[KGFC10]   M. H. Köpf, S. V. Gurevich, R. Friedrich, and L. Chi. "Pattern formation in monolayer transfer systems with substrate - mediated condensation". *Langmuir* 26 (2010), 10444.

[KGFT12]   M. H. Köpf, S. V. Gurevich, R. Friedrich, and U. Thiele. "Substrate-mediated pattern formation in monolayer transfer: a reduced model". *New J. Phys.* 14 (2012), 023016.

[KHNK+22]   M. Kasichke, S. Hartmann, K. Niermann, D. Kostyrin, U. Thiele, and E. L. Gurevich. "Pattern formation in slot-die coating". *arXiv preprint:2101.01614* (2022).

[KKLS+12]   B.-H. Kim, S.-I. Kim, J.-C. Lee, S.-J. Shin, and S.-J. Kim. "Dynamic characteristics of a piezoelectric driven inkjet printhead fabricated using MEMS technology". *Sens. Actuators Phys.* 173 (2012), 244–253.

[KKS99]   S. G. Kim, W. T. Kim, and T. Suzuki. "Phase-field model for binary alloys". *Phys. Rev. E* 60 (1999), 7186–7197.

[KLR17]   S. Karpitschka, F. Liebig, and H. Riegler. "Marangoni contraction of evaporating sessile droplets of binary mixtures". *Langmuir* 31 (2017), 4682–4687.

[KN87]   H. B. Keller and A. Nandakumaran. *Lectures on Numerical Methods in Bifurcation Problems.* Edited by A. Nandakumaran and M. Ramaswamy. Volume 79. Springer, 1987.

[Kob93]   R. Kobayashi. "Modeling and numerical simulations of dendritic crystal growth". *Physica D* 63 (1993), 410–423.

[Köp11]   M. H. Köpf. "On the Dynamics of Surfactant Covered Thin Liquid Films and the Formation of Stripe Patterns in Langmuir-Blodgett Transfer". PhD thesis. 2011.

[KR14]   S. Karpitschka and H. Riegler. "Sharp transition between coalescence and non-coalescence of sessile drops". *J. Fluid Mech.* 743 (2014).

[KR96]   A. Karma and W.-J. Rappel. "Phase-field method for computationally efficient modeling of solidification with arbitrary interface kinetics". *Phys. Rev. E* 53 (1996), R3017–R3020.

[KR98]   A. Karma and W.-J. Rappel. "Quantitative phase-field modeling of dendritic growth in two and three dimensions". *Phys. Rev. E* 57 (1998), 4323–4349.

[Kre09]   F. C. Krebs. "Fabrication and processing of polymer solar cells: a review of printing and coating techniques". *Sol. Energ. Mat. Sol.* 93 (2009), 394–412.

[KT14]   M. H. Köpf and U. Thiele. "Emergence of the bifurcation structure of a Langmuir-Blodgett transfer model". *Nonlinearity* 27 (2014), 2711–2734.

[KT16]   A. Karma and D. Tourret. "Atomistic to continuum modeling of solidification microstructures". *Curr. Opin. Solid State Mater. Sci.* 20 (2016), 25–36.

[LAMB+16]   M. Li, C. An, T. Marszalek, M. Baumgarten, K. Müllen, and W. Pisula. "Impact of interfacial microstructure on charge carrier transport in solution-processed conjugated polymer field-effect transistors". *Adv. Mater.* 28 (2016), 2245–2252.

[Lan80]   J. S. Langer. "Instabilities and pattern formation in crystal growth". *Rev. Mod. Phys.* 52 (1980), 1–28.

[Lan87]   J. S. Langer. "Lectures in the theory of pattern formation". *Chance and Matter.* Edited by J. V. J. Souletie and R. Stora. Proceedings of the Les Houches Summer School, Session XLVI. North-Holland, New York, 1987.

[LAPM14]   M. Li, C. An, W. Pisula, and K. Müllen. "Alignment of organic semiconductor microstripes by two-phase dip-coating". *Small* 10 (2014), 1926–1931.

[Lar14]   R. G. Larson. "Transport and deposition patterns in drying sessile droplets". *AIChE J.* 60 (2014), 1538–1571.

[LB13]   M. G. Larson and F. Bengzon. *The Finite Element Method: Theory, Implementation, and Applications.* Edited by T. Barth, M. Griebel, D. Keyes, R. Nieminen, D.Roose, and T.Schlick. Springer Berlin, Heidelberg, 2013.

[LC00]   E. Lajeunesse and Y. Couder. "On the tip-splitting instability of viscous fingers". *J. Fluid Mech.* 419 (2000), 125–149.

[Lea07]   L. G. Leal. *Advanced Transport Phenomena: Fluid Mechanics and Convective Transport Processes.* Cambridge Series in Chemical Engineering. Cambridge University Press, 2007.

[LEGA+88]   L. Leger, M. Erman, A. M. Guinet-Picard, D. Ausserre, and C. Strazielle. "Precursor film profiles of spreading liquid drops". *Phys. Rev. Lett.* 60 (1988), 2390–2393.

[LeV07]   R. J. LeVeque. *Finite Difference Methods for Ordinary and Partial Differential Equations.* Society for Industrial and Applied Mathematics, 2007.

[LGP02]   A. V. Lyushnin, A. A. Golovin, and L. M. Pismen. "Fingering instability of thin evaporating liquid films". *Phys. Rev. E* 65 (2002), 021602.

[LGSO+10]   L. Li, P. Gao, K. C. Schuermann, S. Ostendorp, W. Wang, C. Du, Y. Lei, H. Fuchs, L. D. Cola, K. Müllen, and L. Chi. "Controllable growth and field-effect property of monolayer to multilayer microstripes of an organic semiconductor". *J. Am. Chem. Soc.* 132 (2010), 8807–8809.

[LGWM+13]   L. Li, P. Gao, W. Wang, K. Müllen, H. Fuchs, and L. Chi. "Growth of ultrathin organic semiconductor microstripes with thickness control in the monolayer precision". *Angew. Chem. Int. Ed.* 52 (2013), 12530–12535.

[LL42]   L. Landau and V. Levich. "Dragging of a liquid by a moving plate". *Acta Physic-ochim. U.R.S.S.* (1942).

[LM77]   J. Langer and J. Müller-Krumbhaar. "Stability effects in dendritic crystal growth". *J. Cryst. Growth* 42 (1977), 11–14.

[LM78a]   J. Langer and H. Müller-Krumbhaar. "Theory of dendritic growth—I. Elements of a stability analysis". *Acta Metall.* 26 (1978), 1681–1687.

[LM78b]   J. Langer and H. Müller-Krumbhaar. "Theory of dendritic growth—II. Instabilities in the limit of vanishing surface tension". *Acta Metall.* 26 (1978), 1689–1695.

[LMTG20]   P.-M. T. Ly, K. D. J. Mitas, U. Thiele, and S. V. Gurevich. "Two-dimensional patterns in dip coating - first steps on the continuation path". *Physica D* 409 (2020), 132485.

[LRH22]   X. Liu, H. Riegler, and J. Hao. "Diphenylalanine deposition by dip-coating from acidic solutions: fibers and closed homogeneous films". *Langmuir* 38 (2022), 13055–13064.

[LS06]   R. Levy and M. Shearer. "The motion of a thin liquid film driven by surfactant and gravity". *SIAM J. Appl. Math.* 66 (2006), 1588–1609.

[LTCG19]   P.-M. T. Ly, U. Thiele, L. Chi, and S. V. Gurevich. "Effects of time-periodic forcing in a Cahn-Hilliard model for Langmuir-Blodgett transfer". *Phys. Rev. E* 99 (2019), 062212.

[Ly17]   P.-M. T. Ly. "Time-periodic forcing in a Cahn-Hilliard model for Langmuir-Blodgett transfer". Master's thesis. 2017.

[MBN19]   L. K. Malla, R. Bhardwaj, and A. Neild. "Analysis of profile and morphology of colloidal deposits obtained from evaporating sessile droplets". *Colloids Surf., A* 567 (2019), 150–160.

[MD16]   X. Man and M. Doi. "Ring to mountain transition in deposition pattern of drying droplets". *Phys. Rev. Lett.* 116 (2016), 066101.

[MDBS+19]   L. Merklein, D. Daume, F. Braig, S. Schlisske, T. Rödlmeier, M. Mink, D. Kourkoulos, B. Ulber, M. Di Biase, K. Meerholz, G. Hernandez-Sosa, U. Lemmer, H. M. Sauer, E. Dörsam, P. Scharfer, and W. Schabel. "Comparative study of printed multilayer oled fabrication through slot die coating, gravure and inkjet printing, and their combination". *Colloids and Interfaces* 3 (2019).

[ME18]   D. Mampallil and H. B. Eral. "A review on suppression and utilization of the coffee-ring effect". *Adv. Colloid Interface Sci.* 252 (2018), 38–54.

[MHJN+14]   C. S. Moore, J. Hennessy, A. D. Jewell, S. Nikzad, and K. France. "Recent developments and results of new ultraviolet reflective mirror coatings". Volume 9144. 2014, 91444H.

[ML78]   H. Müller-Krumbhaar and J. Langer. "Theory of dendritic growth—III. Effects of surface tension". *Acta Metall.* 26 (1978), 1697–1708.

[MMT21]   K. D. J. Mitas, O. Manor, and U. Thiele. "Bifurcation study for a surface-acoustic-wave-driven meniscus". *Phys. Rev. Fluids* 6 (2021), 094002.

[MS64]   W. W. Mullins and R. F. Sekerka. "Stability of a planar interface during solidification of a dilute binary alloy". *J. Appl. Phys.* 35 (1964), 444–451.

[Muc06]   M. Muccini. "A bright future for organic field-effect transistors". *Nature Materials* 5 (2006), 605–613.

[NGL05]   K. Norrman, A. Ghanbari-Siahkali, and N. B. Larsen. "6 studies of spin-coated polymer films". *Annu. Rep. Prog. Chem. Sect. C: Phys. Chem.* 101 (2005), 174–201.

[NPCB+15]   T. M. Nobre, F. J. Pavinatto, L. Caseli, A. Barros-Timmons, P. Dynarowicz-Łątka, and O. N. Oliveira. "Interactions of bioactive molecules & nanomaterials with Langmuir monolayers as cell membrane models". *Thin Solid Films* 593 (2015), 158–188.

[NS15]   M. Net and J. Sánchez. "Continuation of bifurcations of periodic orbits for large-scale systems". *SIAM J. Appl. Dyn. Syst.* 14 (2015), 674–698.

[NT10]   L. Ó. Náraigh and J. L. Thiffeault. "Nonlinear dynamics of phase separation in thin films". *Nonlinearity* 23 (2010), 1559–1583.

[NVI22]   NVIDIA. *CUDA C Programming Guide Version 11.6*. Accessed on August 29th 2022. 2022.

[NZ95]   B. Nadiga and S. Zaleski. "Investigations of a two-phase fluid model". *Eur. J. Mech. B Fluids* 15 (1995).

[ODB97]   A. Oron, S. H. Davis, and S. G. Bankoff. "Long-scale evolution of thin liquid films". *Rev. Mod. Phys.* 69 (1997), 931–980.

[OKD09]   T. Okuzono, M. Kobayashi, and M. Doi. "Final shape of a drying thin film". *Phys. Rev. E* 80 (2009), 021603.

[OM09]   M. Ohno and K. Matsuura. "Quantitative phase-field modeling for dilute alloy solidification involving diffusion in the solid". *Phys. Rev. E* 79 (2009), 031603.

[Ons31a]   L. Onsager. "Reciprocal relations in irreversible processes. I." *Phys. Rev.* 37 (1931), 405–426.

[Ons31b]   L. Onsager. "Reciprocal relations in irreversible processes. Ii." *Phys. Rev.* 38 (1931), 2265–2279.

[PB19]   N. D. Patil and R. Bhardwaj. "Recent developments on colloidal deposits obtained by evaporation of sessile droplets on a solid surface". *J. Indian Inst. Sci.* 99 (2019), 143–156.

[PE10]   N. Provatas and K. Elder. *Phase-field Methods in Materials Science and Engineering*. 1st. Wiley-VCH, 2010.

[PF90]   O. Penrose and P. C. Fife. "Thermodynamically consistent models of phase-field type for the kinetic of phase transitions". *Physica D* 43 (1990), 44–62.

[PGD98]   N. Provatas, N. Goldenfeld, and J. Dantzig. "Efficient computation of dendritic microstructures using adaptive mesh refinement". *Phys. Rev. Lett.* 80 (1998), 3308–3311.

[PK17]   T. Pham and S. Kumar. "Drying of droplets of colloidal suspensions on rough substrates". *Langmuir* 33 (2017), 10061–10076.

[Pla11]   M. Plapp. "Unified derivation of phase-field models for alloy solidification from a grand-potential functional". *Phys. Rev. E* 84 (2011), 031601.

[Pla12]   M. Plapp. "Multiphase microfluidics: the diffuse interface model". Edited by R. Mauri. Volume 538. CISM Courses and Lectures. Springer Vienna, 2012. Chapter Phase-field models, 129–175.

[Pla15]   M. Plapp. "15 - phase-field models". *Handbook of Crystal Growth*. Edited by T. Nishinaga. Second Edition. Boston: Elsevier, 2015, 631–668.

[PP00]   L. M. Pismen and Y. Pomeau. "Disjoining potential and spreading of thin liquid layers in the diffuse-interface model coupled to hydrodynamics". *Phys. Rev. E* 62 (2000), 2480–2492.

[PRK03]   A. Pikovsky, M. Rosenblum, and J. Kurths. *Synchronization: A Universal Concept in Nonlinear Science*. Cambridge: Cambridge University Press, 2003.

[RARF+20]   M. Richard, A. Al-Ajaji, S. Ren, A. Foti, J. Tran, M. Frigoli, B. Gusarov, Y. Bonnassieux, E. G. Caurel, P. Bulkin, R. Ossikovski, and A. Yassar. "Large-scale patterning of π-conjugated materials by meniscus guided coating methods". *Adv. Colloid Interface Sci.* 275 (2020), 102080.

[RAT11]   M. J. Robbins, A. J. Archer, and U. Thiele. "Modelling the evaporation of thin films of colloidal suspensions using dynamical density functional theory". *J. Phys.: Condens. Matter* 23 (2011), 415102.

[RBKD04]   J. C. Ramirez, C. Beckermann, A. Karma, and H.-J. Diepers. "Phase-field modeling of binary alloy solidification with coupled heat and solute diffusion". *Phys. Rev. E* 69 (2004), 051607.

[Rei65]   F. Reif. *Fundamentals of Statistical and Thermal Physics*. Fundamentals of Physics Series. McGraw-Hill, 1965.

[RS92]   H. Riegler and K. Spratte. "Structural changes in lipid monolayers during the Langmuir-Blodgett transfer due to substrate/monolayer interactions". *Thin Solid Films* 210-211 (1992), 9–12.

[RSWD+18]   S. M. Raupp, M. Schmitt, A.-L. Walz, R. Diehm, H. Hummel, P. Scharfer, and W. Schabel. "Slot die stripe coating of low viscous fluids". *J. Coat. Technol. Res.* 15 (2018), 899–911.

[SADF07]   J. Snoeijer, B. Andreotti, G. Delon, and M. Fermigier. "Relaxation of a dewetting contact line. Part 1. A full-scale hydrodynamic calculation". *J. Fluid Mech.* 579 (2007), 63–83.

[SB07]   Y. Sun and C. Beckermann. "Sharp interface tracking using the phase-field equation". *J. Comput. Phys.* 220 (2007), 626–653.

[Sch89]   L. W. Schwartz. "Viscous flows down an inclined plane: instability and finger formation". *Phys. Fluids A* 1 (1989), 443–445.

[Scr88]   L. E. Scriven. "Physics and applications of dip coating and spin coating". *MRS Online Proceedings Library* 121 (1988), 717–729.

[SD20]   J. A. Stewart and R. Dingreville. "Microstructure morphology and concentration modulation of nanocomposite thin-films during simulated physical vapor deposition". *Acta Mater.* 188 (2020), 181–191.

[SES20]   A. S. Sarkın, N. Ekren, and Ş. Sağlam. "A review of anti-reflection and self-cleaning coatings on photovoltaic panels". *Sol. Energy* 199 (2020), 63–73.

[Set99]   J. Sethian. *Level Set Methods and Fast Marching Methods: Evolving Interfaces in Computational Geometry, Fluid Mechanics, Computer Vision and Material Science.* Cambridge University Press, 1999.

[SFSS19]   A. Salehi, X. Fu, D.-H. Shin, and F. So. "Recent advances in OLED optical design". *Adv. Funct. Mater.* 29 (2019), 1808803.

[SG70]   R. J. Schaefer and M. E. Glicksman. "Initiation of dendrites by crystal imperfections". *Metall. Trans.* 1 (1970), 1973–1978.

[SH96]   M. A. Spaid and G. M. Homsy. "Stability of Newtonian and viscoelastic dynamic contact lines". *Phys. Fluids* 8 (1996), 460–478.

[SJJ08]   C.-H. Sun, P. Jiang, and B. Jiang. "Broadband moth-eye antireflection coatings on silicon". *Appl. Phys. Lett.* 92 (2008), 061112.

[SK61]   H. Schlichting and J. Kestin. *Boundary Layer Theory.* Volume 121. Springer, 1961.

[SMPM+08]   A. Stannard, C. P. Martin, E. Pauliac-Vaujour, P. Moriarty, and U. Thiele. "Dual-scale pattern formation in nanoparticle assemblies". *J. Phys. Chem. C* 112 (2008), 15195–15203.

[SO88]   C.-W. Shu and S. Osher. "Efficient implementation of essentially non-oscillatory shock-capturing schemes". *J. Comput. Phys.* 77 (1988), 439–471.

[Šol05]   P. Šolín. *Partial Differential Equations and the Finite Element Method.* John Wiley & Sons, Ltd, 2005.

[Spi96]   M. Spijker. "Stiffness in numerical initial-value problems". *J. Comput. Appl. Math.* 72 (1996), 393–406.

[SR91]   K. Spratte and H. Riegler. "Fluorescence microscopy studies of layer/substrate interaction during the Langmuir-Blodgett transfer: fractional condensation and local layer modification in lipid monolayers at the three-phase line". *Makromolekulare Chemie. Macromolecular Symposia* 46 (1991), 113–123.

[SR94]   K. Spratte and H. Riegler. "Steady state morphology and composition of mixed monomolecular films (Langmuir monolayers) at the air/water interface in the vicinity of the three-phase line: model calculations and experiments". *Langmuir* 10 (1994), 3161–3173.

[SREP01]   L. W. Schwartz, R. Roy, R. R. Eley, and S. Petrash. "Dewetting patterns in a drying liquid film". *J. Colloid Interface Sci.* 234 (2001), 363–374.

[SS07]   B. W. Smith and K. Suzuki. *Microlithography: Science and Technology.* Edited by B. W. Smith and K. Suzuki. CRC, 2007.

[SS08]   I. Singer-Loginova and H. M. Singer. "The phase field technique for modeling multiphase materials". *Rep. Progr. Phys.* 71 (2008), 106501.

[SS16]   J. A. Stewart and D. E. Spearot. "Phase-field models for simulating physical vapor deposition and grain evolution of isotropic single-phase polycrystalline thin films". *Computational Materials Science* 123 (2016), 111–120.

[SS18]   J. A. Stewart and D. E. Spearot. "Physical vapor deposition of multiphase materials with phase nucleation via a coupled phase-field approach". *Computational Materials Science* 143 (2018), 71–79.

[SSVR11]   S. Semenov, V. Starov, M. Velarde, and R. Rubio. "Droplets evaporation: problems and solutions". *Eur. Phys. J.-Spec. Top.* 197 (2011), 265–278.

[ST58]   P. G. Saffman and G. I. Taylor. "The penetration of a fluid into a porous medium or Hele-Shaw cell containing a more viscous liquid". *Proc. R. Soc. Lond. A* 245 (1958), 312–329.

[Sta11]   A. Stannard. "Dewetting-mediated pattern formation in nanoparticle assemblies". *J. Phys.: Condens. Matter* 23 (2011), 083001.

[Ste09]   I. Steinbach. "Phase-field models in materials science". *Modelling Simul. Mater. Sci. Eng.* 17 (2009), 073001.

[Ste13]   I. Steinbach. "Phase-field model for microstructure evolution at the mesoscopic scale". *Annu. Rev. Mater. Res.* 43 (2013), 89–107.

[Sto49]   G. Stokes. "On the theories of the internal friction of fluids in motion, and of the equilibrium and motion of elastic solids". Volume 8. Trans. Cambr. Phil. Soc., 1849, 287–319.

[SZAF+08]   J. H. Snoeijer, J. Ziegler, B. Andreotti, M. Fermigier, and J. Eggers. "Thick films of viscous fluid coating a plate withdrawn from a liquid reservoir". *Phys. Rev. Lett.* 100 (2008), 244502.

[Szi04]   R. Szilard. *Theories and Applications of Plate Analysis : Classical, Numerical, and Engineering Methods.* English. Hoboken, NJ: John Wiley, 2004.

[TAP12]   U. Thiele, A. J. Archer, and M. Plapp. "Thermodynamically consistent description of the hydrodynamics of free surfaces covered by insoluble surfactants of high concentration". *Phys. Fluids* 24 (2012), 102107.

[TAP16]   U. Thiele, A. Archer, and L. Pismen. "Gradient dynamics models for liquid films with soluble surfactant". *Phys. Rev. Fluids* 1 (2016), 083903.

[Tew13]   W. Tewes. "A theoretical description of pattern formation in thin solution layers". Master's thesis. 2013.

[TGT14]   D. Tseluiko, M. Galvagno, and U. Thiele. "Collapsed heteroclinic snaking near a heteroclinic chain in dragged meniscus problems". *Eur. Phys. J. E* 37 (2014).

[Thi07]   U. Thiele. "Structure formation in thin liquid films". *Thin Films of Soft Matter.* Edited by S. Kalliadasis and U. Thiele. Vienna: Springer Vienna, 2007, 25–93.

[Thi10]   U. Thiele. "Thin film evolution equations from (evaporating) dewetting liquid layers to epitaxial growth". *J. Phys.: Condens. Matter* 22 (2010), 084019.

[Thi14]   U. Thiele. "Patterned deposition at moving contact line". *Adv. Colloid Interface Sci.* 206 (2014), 399–413.

[Thi18]   U. Thiele. "Recent advances in and future challenges for mesoscopic hydrodynamic modelling of complex wetting". *Colloids Surf., A* 553 (2018), 487–495.

[Tho95]   J. W. Thomas. *Numerical Partial Differential Equations: Finite Difference Methods.* Springer New York, NY, 1995.

[TLT16]   M. C. Traub, W. Longsine, and V. N. Truskett. "Advances in nanoimprint lithography". *Annu. Rev. Chem. Biomol. Eng.* 7 (2016), 583–604.

[TPMM21]   J. G. Thakare, C. Pandey, M. M. Mahapatra, and R. S. Mulik. "Thermal barrier coatings–a state of the art review". *Met. Mater. Int.* 27 (2021), 1947–1968.

[TTL13]   U. Thiele, D. V. Todorova, and H. Lopez. "Gradient dynamics description for films of mixtures and suspensions: dewetting triggered by coupled film height and concentration fluctuations". *Phys. Rev. Lett.* 111 (2013), 117801.

[TTP12]   D. Todorova, U. Thiele, and L. M. Pismen. "The relation of steady evaporating drops fed by an influx and freely evaporating drops". *J. Eng. Math.* 73 (2012), 17–30.

[TV87]   C. W. Tang and S. A. VanSlyke. "Organic electroluminescent diodes". *Appl. Phys. Lett.* 51 (1987), 913–915.

[TVAR+09]   U. Thiele, I. Vancea, A. J. Archer, M. J. Robbins, L. Frastia, A. Stannard, E. Pauliac-Vaujour, C. P. Martin, M. O. Blunt, and P. J. Moriarty. "Modelling approaches to the dewetting of evaporating thin films of nanoparticle suspensions". *J. Phys.: Condens. Matter* 21 (2009), 264016.

[TVI11]   Y. Y. Tarasevich, I. V. Vodolazskaya, and O. P. Isakova. "Desiccating colloidal sessile drop: dynamics of shape and concentration". *Colloid. Polym. Sci.* 289 (2011), 1015–1023.

[TWGT19]   W. Tewes, M. Wilczek, S. V. Gurevich, and U. Thiele. "Self-organized dip-coating patterns of simple, partially wetting, nonvolatile liquids". *Phys. Rev. Fluids* 4 (2019), 123903.

[UB05]   B. Utter and E. Bodenschatz. "Double dendrite growth in solidification". *Phys. Rev. E* 72 (2005), 011601.

[Uec18]   H. Uecker. "Hopf bifurcation and time periodic orbits with pde2path - algorithms and applications". *Commun. Comput. Phys.* 25 (2018), 812–852.

[Uec21]   H. Uecker. *Numerical Continuation and Bifurcation in Nonlinear PDEs.* Philadelphia, PA: Society for Industrial and Applied Mathematics, 2021.

[UWR14]   H. Uecker, D. Wetzel, and J. D. M. Rademacher. "pde2path - a matlab package for continuation and bifurcation in 2d elliptic systems". *NM-TMA* 7 (2014), 58–106.

[VSSP+20]   V. K. Vlasko-Vlasov, M. Sulwer, E. V. Shevchenko, J. Parker, and W. K. Kwok. "Ring patterns generated by an expanding colloidal meniscus". *Phys. Rev. E* 102 (2020), 052608.

[VTPS+08]   I. Vancea, U. Thiele, E. Pauliac-Vaujour, A. Stannard, C. Martin, M. Blunt, and P. Moriarty. "Front instabilities in evaporatively dewetting nanofluids". *Phys. Rev. E* 78 (2008), 041601.

[WBKF10]   D. Willmer, K. A. Baldwin, C. Kwartnik, and D. J. Fairhurst. "Growth of solid conical structures during multistage drying of sessile poly(ethylene oxide) droplets". *Phys. Chem. Chem. Phys.* 12 (2010), 3998–4004.

[WBM92]   A. A. Wheeler, W. J. Boettinger, and G. B. McFadden. "Phase-field model for isothermal phase transitions in binary alloys". *Phys. Rev. A* 45 (1992), 7424–7439.

[WBM93]   A. A. Wheeler, W. J. Boettinger, and G. B. McFadden. "Phase-field model of solute trapping during solidification". *Phys. Rev. E* 47 (1993), 1893–1909.

[WCM03]   M. Warner, R. Craster, and O. Matar. "Surface patterning via evaporation of ultrathin films containing nanoparticles". *J. Colloid Interface Sci.* 267 (2003), 92–110.

[WE99]   P. K. Wright and A. G. Evans. "Mechanisms governing the performance of thermal barrier coatings". *Curr. Opin. Solid State Mater. Sci.* 4 (1999), 255–265.

[WG14]   M. Wilczek and S. V. Gurevich. "Locking of periodic patterns in Cahn-Hilliard models for Langmuir-Blodgett transfer". *Phys. Rev. E* 90 (2014), 042926.

[WHK07]   Z.-y. Wang, E.-h. Han, and W. Ke. "Fire-resistant effect of nanoclay on intumescent nanocomposite coatings". *J. Appl. Polym. Sci.* 103 (2007), 1681–1689.

[Wil16]   M. Wilczek. "Pattern Formation in Driven Thin Layers of Simple and Complex Liquids". PhD thesis. Westfälische Wilhelms-Universität Münster, 2016.

[Wil98]   H. A. R. Williams. "Two-dimensional Surfactant-driven Flows of Thin Liquid Films". PhD thesis. Cambridge, 1998.

[WJ01]   H. A. R. Williams and O. E. Jensen. "Two-dimensional nonlinear advection-diffusion in a model of surfactant spreading on a thin liquid film". *IMA J. Appl. Math.* 66 (2001), 55–82.

[WLLZ+16] K. Wu, H. Li, L. Li, S. Zhang, X. Chen, Z. Xu, X. Zhang, W. Hu, L. Chi, X. Gao, and Y. Meng. "Controlled growth of ultrathin film of organic semiconductors by balancing the competitive processes in dip-coating for organic transistors". *Langmuir* 32 (2016), 6246–6254.

[WMD18]   M. Wu, X. Man, and M. Doi. "Multi-ring deposition pattern of drying droplets". *Langmuir* 34 (2018), 9572–9578.

[Wol22]   I. Wolfram Research. *Mathematica*. Wolfram Research, Inc. 2022.

[WSWM+93] S.-L. Wang, R. Sekerka, A. Wheeler, B. Murray, S. Coriell, R. Braun, and G. McFadden. "Thermodynamically-consistent phase-field models for solidification". *Physica D* 69 (1993), 189–200.

[WTEG+17] M. Wilczek, W. Tewes, S. Engelnkemper, S. V. Gurevich, and U. Thiele. "Sliding drops – ensemble statistics from single drop bifurcations". *Phys. Rev. Lett.* 119 (2017), 204501.

[WTGK+15] M. Wilczek, W. B. Tewes, S. V. Gurevich, M. H. Köpf, L. Chi, and U. Thiele. "Modelling pattern formation in dip-coating experiments". *Math. Model. Nat. Phenom.* 10 (2015), 44–60.

[WWHL+20] Z. Wang, S. Wang, L. Huang, L. Li, and L. Chi. "Microstructured ultrathin organic semiconductor film via dip-coating: precise assembly and diverse applications". *Acc. Mater. Res.* 1 (2020), 201–212.

[WYQ18]   H. Wang, D. Yan, and T. Qian. "A phenomenological approach to the deposition pattern of evaporating droplets with contact line pinning". *J. Phys.: Condens. Matter* 30 (2018), 435001.

[WZCT+17] M. Wilczek, J. Zhu, L. Chi, U. Thiele, and S. V. Gurevich. "Dip-coating with prestructured substrates: transfer of simple liquids and langmuir–blodgett monolayers". *J. Phys.: Condens. Matter* 29 (2017), 014002.

[WZHT+15] B. Wang, T. Zhu, L. Huang, T. L. D. Tam, Z. Cui, J. Ding, and L. Chi. "Addressable growth of oriented organic semiconductor ultra-thin films on hydrophobic surface by direct dip-coating". *Org. Electron.* 24 (2015), 170–175.

[XM08]   Z. Xu and P. Meakin. "Phase-field modeling of solute precipitation and dissolution". *J. Chem. Phys.* 129 (2008), 014705.

[XM11]   Z. Xu and P. Meakin. "Phase-field modeling of two-dimensional solute precipitation/dissolution: solid fingers and diffusion-limited precipitation". *J. Chem. Phys.* 134 (2011), 044137.

[XTQ15]   X. Xu, U. Thiele, and T. Qian. "A variational approach to thin film hydrodynamics of binary mixtures". *J. Phys.: Condens. Matter* 27 (2015), 085005.

[YJLD+21] X. Yang, Z. Jiang, P. Lyu, Z. Ding, and X. Man. "Deposition pattern of drying droplets". *Commun. Theor. Phys. (Beijing)* 73 (2021), 047601.

[You05]   T. Young. "An essay on the cohesion of fluids". *Phil. Trans. R. Soc. Lond. A* 95 (1805), 65–87.

[YR06]   G. Yosef and E. Rabani. "Self-assembly of nanoparticles into rings: a lattice-gas model". *J. Phys. Chem. B* 110 (2006), 20965–20972.

[ZAM19]   A. Zigelman, M. Abo Jabal, and O. Manor. "Analysis of the oscillatory wetting–dewetting motion of a volatile drop during the deposition of polymer on a solid substrate". *Soft Matter* 15 (2019), 3580–3587.

[ZB00]   L. Zhornitskaya and A. L. Bertozzi. "Positivity-preserving numerical schemes for lubrication-type equations". *SIAM J. Numer. Anal.* 37 (2000), 523–555.

[ZGL07]   M. Zayat, P. Garcia-Parejo, and D. Levy. "Preventing UV-light damage of light sensitive materials using a highly protective uv-absorbing coating". *Chem. Soc. Rev.* 36 (2007), 1270–1281.

[ZM16]   A. Zigelman and O. Manor. "A model for pattern deposition from an evaporating solution subject to contact angle hysteresis and finite solubility". *Soft Matter* 12 (2016), 5693–5707.

[ZS16]   Y.-T. Zhang and C.-W. Shu. "Chapter 5 - ENO and WENO schemes". *Handbook of Numerical Methods for Hyperbolic Problems.* Edited by R. Abgrall and C.-W. Shu. Volume 17. Handbook of Numerical Analysis. Elsevier, 2016, 103–122.

[ZSE09]   J. Ziegler, J. H. Snoeijer, and J. Eggers. "Film transitions of receding contact lines". *Eur. Phys. J. Spec. Top.* 166 (2009), 177–180.

[ZTTD+19] D. Zang, S. Tarafdar, Y. Y. Tarasevich, M. Dutta Choudhury, and T. Dutta. "Evaporation of a droplet: from physics to applications". *Phys. Rep.* 804 (2019), 1–56.

[Zuc08]   I. J. Zucker. "92.34 the cubic equation - a new look at the irreducible case". *Math. Gaz.* 92 (2008), 264–268.

[ZWHH+16] J. Zhu, M. Wilczek, M. Hirtz, J. Hao, W. Wang, H. Fuchs, and S. V. Gurevich. "Branch suppression and orientation control of Langmuir-Blodgett patterning on prestructured surfaces". *Adv. Mater. Interfaces* 3 (2016), 1600478.

[ZYBH+09] J. Zhu, Z. Yu, G. F. Burkhard, C.-M. Hsu, S. T. Connor, Y. Xu, Q. Wang, M. McGehee, S. Fan, and Y. Cui. "Optical absorption enhancement in amorphous silicon nanowire and nanocone arrays". *Nano Lett.* 9 (2009), 279–282.

Danksagung

An dieser Stelle möchte ich allen danken, die mich während meines Promotionsstudiums unterstützt haben. Vor allem danke ich:

- PD Dr. Svetlana Gurevich und Prof. Dr. Uwe Thiele für die Betreuung, hilfreichen Diskussionen und ihre Geduld.

- Dem PAK943 Projekt für die finanzielle Unterstützung.

- Tobias Frohoff-Hülsmann für Diskussionen und Hilfe mit pde2path.

- Sebastian Engelnkemper für die Vorarbeit der 2D-Kontinuierung.

- Kevin Mitas für die Zusammenarbeit über transversale Instabilitäten.

- Simon Hartmann für Diskussionen, Hilfe mit oomphlib und der besagten Verifizierungssimulationen.

- Walter Tewes und Markus Wilczek für Wissenstransfer und die CUDA Basiscodes.

- Christoph Henkel, Martin Heßler, Max P. Holl, Fenna Stegemerten und Dat-Minh Kevin Ly für Hilfsbereitschaft und Diskussionen.

- meinen Korrekturlesern: Uwe Thiele, Svetlana Gurevich und Simon Hartmann.

- Fabian Dohmen für die Überprüfung von ein paar analytischen Rechnungen.

- meinen Freunden und meiner Familie für ihre endlose Unterstützung und ihr Verständnis.

Lebenslauf

Name	Phong-Minh Timmy Ly
Geburtsdatum	20.10.1992
Geburtsort	Münster
Staatsangehörigkeit	Deutsch
Familienstand	ledig

Schulbildung

1999 – 2003	Grundschule Willibrord Steinfurt
2003 – 2012	Gymnasium Arnoldinum Steinfurt
29.06.2012	Allgemeine Hochschulreife (Note 1,0)

Studium

10/2012 – 09/2015	Bachelorstudium der Physik an der Westfälischen Wilhelms-Universität Münster
14.09.2015	Abschluss Bachelor of Science Physik (Note 1,8) Thema der Bachelorarbeit: Quantummechanical calculations of absorption spectra of organic solar cells
10/2015 – 09/2017	Masterstudium der Physik an der Westfälischen Wilhelms-Universität Münster
29.09.2017	Abschluss Master of Science Physik (Note 1,4) Thema der Masterarbeit: Time-periodic forcing in a Cahn-Hilliard model for Langmuir-Blodgett transfer

Promotionsstudium

seit 10/2017	Promotionsstudium am Institut für Theoretische Physik der Westfälischen Wilhelms-Universität Münster unter der Betreuung von PD Dr. Svetlana V. Gurevich und Prof. Dr. Uwe Thiele

Berufstätigkeit

10/2016 – 03/2017	Studentische Hilfskraft am Institut für Theoretische Physik der Universität Münster
04/2017 – 09/2017	Studentische Hilfskraft am Institut für Theoretische Physik der Universität Münster
10/2017 – 06/2021	Wissenschaftlicher Mitarbeiter am Institut für Theoretische Physik der Universität Münster